



**Singlet excitation energy transfer in covalently bridged
and non-bridged bichromophoric systems**

INAUGURAL-DISSERTATION

zur

Erlangung des Doktorgrades der
Mathematisch-Naturwissenschaftlichen Fakultät
der Heinrich-Heine-Universität Düsseldorf

vorgelegt von

JAN DOMINIK SPIEGEL

aus Neuss

Düsseldorf, Oktober 2016

aus dem Institut für Theoretische Chemie und Computerchemie
der Heinrich-Heine-Universität Düsseldorf

Gedruckt mit Genehmigung der
Mathematisch-Naturwissenschaftlichen Fakultät der
Heinrich-Heine-Universität Düsseldorf

Referentin: Univ.-Prof. Dr. Christel M. Marian
Korreferent: Univ.-Prof. Dr. Holger Gohlke

Tag der mündlichen Prüfung: 11. November 2016

Eidesstattliche Erklärung

Ich versichere an Eides statt, dass die Dissertation von mir selbst verfasst und ohne unzulässige fremde Hilfe unter Beachtung der Grundsätze zur Sicherung der guten wissenschaftlichen Praxis an der Heinrich-Heine-Universität erstellt worden ist. Die aus fremden Quellen direkt oder indirekt übernommenen Gedanken sind als solche kenntlich gemacht. Die Dissertation wurde in der vorgelegten oder in ähnlicher Form noch bei keiner anderen Prüfungsbehörde eingereicht. Es wurden keine früheren erfolglosen Promotionsversuche unternommen.

Neuss, den 28.09.2016

Contents

List of papers	IX
Summary	X
Zusammenfassung	XI
1 Introduction	1
1.1 Excitons	1
1.2 Excitation energy transfer	2
1.3 Importance and applications	4
1.3.1 Photosynthesis	4
1.3.2 Organic photovoltaics	5
1.3.3 Structure determination of biomolecules	6
1.4 State of the art	7
1.5 Motivation and objectives	8
2 Theory	11
2.1 Photophysical processes and Franck-Condon principle	11
2.1.1 Absorption	12
2.1.2 Deactivation of electronically excited states	14
2.2 EET rate	15
2.2.1 Fermi's Golden rule	15
2.2.2 Franck-Condon weighted density of states	19
2.2.3 Spectral overlap integral	21
2.3 Density matrix theory	22
2.3.1 Density function of an N-electron system	22
2.3.2 Reduced density functions	23
2.3.3 Expectation values of one- and two-electron operators	24
2.3.4 Transition density functions	26
2.3.5 From density functions to density matrices	27

2.3.6 Configuration interaction	28
2.3.7 Second quantization	29
2.3.8 Extension to group-function theory: Molecular dimers	29
2.3.9 Analysis of the excited-state wave functions	31
2.4 Excitonic coupling matrix element	32
2.4.1 The two-state system	32
2.4.2 Molecular heterodimer	34
2.4.3 Davydov splitting: The molecular homodimer	37
2.4.4 Ideal dipole approximation	38
2.4.5 Monomer transition density approach	43
2.4.6 Supermolecular transition density approach: Consideration of CT contributions	44
2.5 Förster theory	46
3 Implementations	51
4 Results and discussion	59
4.1 BODIPY/anthracene-based EET cassettes	59
4.1.1 Direct contribution and the role of the molecular linker	59
4.1.2 Charge transfer contributions	60
4.2 Distance-dependent validity of IDA-based FRET model	65
5 Outlook	69
5.1 Extension of the MTD method to triplet-triplet couplings	69
5.2 Optimization of the STD code	72
5.3 Enhancement of the sampling procedure	73
5.4 Enhancement of the alignment procedure	73
Literature	82
Acknowledgment	83

List of papers

Included as part of this thesis:

1. *Quantum chemical studies on excitation energy transfer in BODIPY-based donor-acceptor systems*
J. Dominik Spiegel, Martin Kleinschmidt, Alexander Larbig, Jörg Tatchen, and Christel M. Marian, *J. Chem. Theory Comput.* **2015**, *11*, 4316-4327
Own contribution: Implementation of the MTD and IDA approaches; parallelization of the MTD code; benchmark calculations; quantum chemical calculations; vibrationally resolved spectra; spectral overlap integral; ECMEs and the EET rates; ab initio MD simulations; first draft of manuscript
2. *Charge-transfer contributions to the excitonic coupling matrix element in BODIPY-based energy transfer cassettes*
J. Dominik Spiegel, Igor Lyskov, Martin Kleinschmidt, and Christel M. Marian, *Chem. Phys.* **2016**, (submitted)
Own contribution: Derivation and implementation of the STD formalism; benchmark calculations; quantum chemical calculations; ECMEs; first draft of manuscript
3. *Failure of the IDA in FRET systems at close inter-dye distances is moderated by frequent low κ^2 values*
J. Dominik Spiegel, Simone Fulle, Martin Kleinschmidt, Holger Gohlke, and Christel M. Marian, *J. Phys. Chem. B* **2016**, *120*, 8845-8862
Own contribution: Implementation of the structure alignment algorithm; enhancement of the MTD method; quantum chemical calculations of Cy5; spectral overlap integral and vibrationally resolved spectra; ECMEs, orientation factors and EET rates; sampling and statistical analysis; first draft of manuscript

Not included as part of this thesis:

1. *Singlet fission in quinoidal oligothiophenes*
Nikolai Elfers, Igor Lyskov, J. Dominik Spiegel, and Christel M. Marian, *J. Phys. Chem. C* **2016**, *120*, 13901-13910
Own contribution: Creation of figures for the supplementary information
2. *On the significance of the ${}^1\text{L}_\text{a}$ / ${}^1\text{L}_\text{b}$ nomenclature for fluoro-substituted indole derivates*
Josefin Wilke, Martin Wilke, Christian Brand, J. Dominik Spiegel, Christel M. Marian, and Michael Schmitt, *J. Phys. Chem. A*, (to be published)
Own contribution: DFT/MRCI calculations

Summary

Excitation energy transfer (EET) is an important photophysical process which describes the non-radiative transfer of electron-hole pairs between molecules. The process has various applications ranging from organic photovoltaics to methods for the structure determination of biomolecules. Most quantum chemical approaches for the prediction of the EET rate are based on Fermi's Golden rule. Here, the EET rate is proportional to the square of the excitonic coupling matrix element (ECME) between the appropriate electronic states. In this work, the monomer transition density (MTD) approach for the computation of the ECME between two excited singlet states was implemented, adapted to the DFT/MRCI code and extended to exchange contributions. Furthermore, the method was refined by introducing a mechanism which ensures that only the orbitals are considered which refer to non-vanishing elements of the transition density matrices. To overcome the approximation of treating the supermolecular EET system as two artificially isolated monomers and in order to consider charge-transfer (CT) contributions to the ECME, the MTD method was extended to the supermolecular transition density (STD). Both methods were applied to a number of EET cassettes in which BODIPY serves as exciton acceptor and is linked to anthracene by a molecular bridge. Using the MTD approach and in presence of the linker, the experimental EET rates in the range of picoseconds could fairly be reproduced. In absence of the bridge, MTD and STD provide similar results while the MTD seems to overestimate the ECME in presence of the linker due to the neglect of the CT contributions. It could be shown that the experimentally observed highly efficient EET in a cassette with perpendicular donor acceptor transition dipole moment orientation can be traced back to dynamic effects. To study the validity of the Förster EET model at small donor acceptor distances in a realistic system, a method was developed making a large number of snapshots, obtained from molecular dynamics (MD) simulations, accessible to a transition density-based method for the computation of the ECME. By the use of a quaternion-based approach preoptimized structures of the two subsystems were aligned to the MD snapshots such that a costly relaxation of the structures and recomputation of the transition density matrices is avoided. The method was applied to a pair of dyes attached to a double-stranded RNA. Due to certain preferred relative arrangements of the dyes, substantial deviations from an isotropic transition dipole moment distribution and a Gaussian distance vector distribution could be found. However, the EET rates remain unaffected because the periods in which the failure of the ideal dipole approximation (IDA) is large, have a minor statistical weight.

Zusammenfassung

Exzitonischer Energietransfer (EET) ist ein bedeutender photophysikalischer Prozess, der den strahlungslosen Transfer von Elektronen-Loch-Paaren zwischen Molekülen beschreibt. Anwendungen reichen von der organischen Photovoltaik bis hin zur Strukturaufklärung von Biomolekülen. Die meisten quantenchemischen Methoden zur Berechnung der EET-Rate basieren auf Fermis Goldener Regel. Dabei ist die EET-Rate proportional zum Quadrat des exzitonischen Kopplungsmatrixelements (ECME). In der vorliegenden Arbeit wurde die MTD-Methode zur Berechnung des ECME auf die DFT/MRCI Methode angepasst und um einen Austauschterm erweitert. Durch einen neuen Mechanismus, werden nur solche Orbitale berücksichtigt, die sich auf nicht verschwindend kleine Elemente der Übergangsdichtematrizen beziehen. Um Charge-Transfer (CT) Beiträge berücksichtigen zu können und die Subsysteme nicht isoliert betrachten zu müssen, wurde eine zum MTD Ansatz analoge Methode entwickelt, die auf den Übergangsdichten des Supermoleküls basiert. Beide Methoden wurden auf eine Reihe von EET-Kassetten angewendet, in denen ein Anthracen-Donor über eine molekulare Brücke mit einem BODIPY-Akzeptor verbunden ist. Unter Anwendung des MTD Ansatzes und Berücksichtigung der Brücke konnten die experimentellen EET-Raten in der Größenordnung von Picosekunden reproduziert werden. In Abwesenheit der Brücke liefern MTD und STD ähnliche Ergebnisse, während MTD aufgrund der Vernachlässigung der CT Beiträge das ECME in Anwesenheit der Brücke überschätzt. Weiterhin konnte gezeigt werden, dass der effiziente EET in einer der Kassetten, in der die Übergangsdipolmomente von Donor und Akzeptor rechtwinklig angeordnet sind, auf dynamische Effekte zurückzuführen ist. Um die Richtigkeit des EET-Modells von Förster in einem realistischen System zu untersuchen, wurde eine Methode entwickelt, mit der eine große Anzahl von Schnapschüssen aus einer Molekulardynamiksimulation (MD) einer Übergangsdichte-basierten Methode zur Berechnung des ECME zugänglich gemacht werden kann. Durch die Anpassung voroptimierter Strukturen der Farbstoffe an die Strukturen der MD Schnapschüsse kann eine aufwendige Relaxierung der Strukturen und somit eine erneute Berechnung der Übergangsdichtematrizen vermieden werden. Die Methode wurde auf ein Farbstoffpaar angewendet, wobei die beiden Farbstoffe jeweils kovalent an eine doppelsträngige RNA gebunden waren. Aufgrund bestimmter, bevorzugter relativer Anordnungen der Farbstoffe konnten Abweichungen von einer perfekten Gauß-förmigen Abstandsverteilung und von einer perfekten isotropischen Verteilung des Übergangsdipolmoments gefunden werden. Trotzdem bleibt die EET-Rate nahezu unverändert, da die Zeiträume, in denen der Fehler der idealen Dipolnäherung (IDA) groß ist, einen geringen statistischen Einfluss haben.

Chapter 1

Introduction

1.1 Excitons

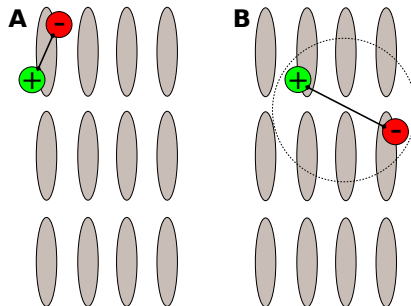


Figure 1.1: Schematic illustration of Frenkel (A) and Wannier-Mott (B) excitons in a lattice.

An exciton is a quasi-particle defined as a coupled electron-hole pair. The term has its origin in solid-state physics. The process of excitation energy transfer, which is treated in this work, refers to the migration of such electron-hole pairs within a molecular aggregate, a polymer or a molecular dimer and is not restricted to the solid state. However, to get an insight into the formation and behavior of electron-hole pairs, a basic understanding of the chemical composition of solids is required.

In a solid, atoms are periodically arranged on a 3-dimensional lattice. Solids characterized by a long-range order of this lattice are called crystals. The electronic structure of crystalline solids can be described by the band model. [1] In the case of only two interacting atoms, atomic orbitals (AOs) of the same kind (1s, 2s, 2p, ...) split into pairs of binding and anti-binding molecular orbitals (MOs). Adding more and more atoms, the number of resulting MOs increases while the energetic distance becomes smaller and smaller, finally resulting in a band structure. The highest occupied energy band is called valence

band while the lowest unoccupied energy band is called conduction band. As long as a band is not fully occupied, the electrons are fully delocalized such that the charge-carriers can move freely from atom to atom within the lattice. Excitation of an electron from the valence band to the conduction band leads to a coupled electron-hole pair — a so-called exciton. Due to the band structure, the electron-hole-pair can move freely within the three-dimensional lattice. The binding energy between the electron in the conduction band and the hole in the valence band depends on their distance according to which excitons can be classified (Fig. 1.1). In honor of the Russian physicist Jakow Iljitsch Frenkel, local, tightly-bound excitons are called **Frenkel excitons**. [2] They are characterized by small electron-hole separations in the range of 1 nm and high binding energies of up to 1 eV. [3] In contrast, excitons with a substantially larger electron-hole distance and smaller binding energy, respectively, are named after the Swiss and English physicists Gregory Hugh Wannier and Nevill Francis Mott (**Wannier-Mott excitons**). [4] In the special case in which the electron and the hole are located on adjacent molecules of the lattice, the exciton is called charge-transfer (CT) exciton and can be regarded as an intermediate state between a Frenkel and a Wannier-Mott exciton. [5]

In the case of single organic molecules instead of crystalline solids, the situation is more straightforward since a band structure does not exist. Therefore, each electronically excited state can be regarded as an exciton. [6] An excitation which is perfectly localized on one molecule is treated as Frenkel exciton while a charge transfer excitation between two molecules is regarded as Wannier-Mott exciton. In larger multichromophoric ensembles and periodic polymeric structures the situation is similar to the one in crystalline solids. Here, the monomer units of the polymer play a role comparable to the atoms within the lattice of a solid. The interaction between two excitons is called excitonic coupling (EC). Restricting our considerations to the interaction between single molecules in bichromophoric systems and small ensembles of chromophores, the EC is equivalent to the interaction between two electronically excited states.

1.2 Excitation energy transfer

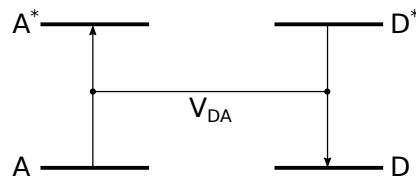


Figure 1.2: EET can in the simplest case be understood as simultaneous excitation of the acceptor and a deexcitation of the donor.

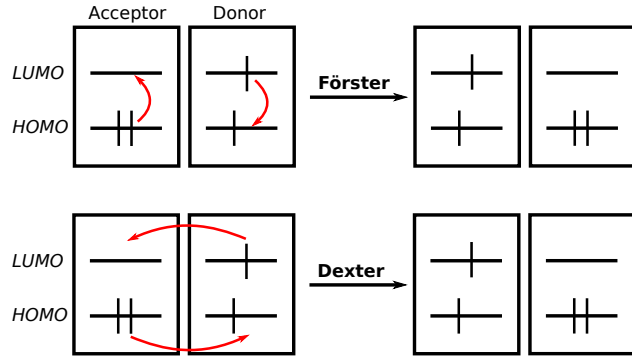


Figure 1.3: Illustration of the Förster and the Dexter EET mechanisms in a HOMO-LUMO-model.

Excitation energy transfer (EET) is a photophysical process which describes the non-radiative transfer of an exciton between two molecular systems. These systems can either be individual molecules, monomeric units of a di- or polymeric structure or elements of a large molecular ensemble. EET was first described by Theodor Förster in the 1940s considering two individual chromophores which can be independently photoexcited. [7, 8] Förster described the process as a simultaneous excitation and deexcitation process of the acceptor and the donor, respectively, without emission and reabsorption of a photon (Fig. 1.2). In a four-electron-four-orbital model the Förster mechanism can be explained as a local transition of an electron from the highest occupied molecular orbital (HOMO) to the lowest unoccupied molecular orbital (LUMO) in the acceptor which is coupled to the appropriate opposite transition in the exciton donor (Fig. 1.3). It is important to mention that both transitions are strongly localized on the individual molecules and that no exchange of charge carriers takes place. According to the Förster mechanism EET can only take place if both transitions are allowed. Strictly speaking, this is only the case if both excited states have the same multiplicity as the appropriate electronic ground state. However, formally spin-forbidden processes can become allowed in the case of strong spin-orbit coupling. Therefore, EET can take place, according to the Förster mechanism, between a triplet and a singlet state if the donor phosphorescence is strong. Nevertheless, the term Förster resonance energy transfer (FRET) usually describes the transfer of excitation energy between two excited singlet states. Since the vehicle of the coupling between the two transitions is the dipole-dipole interaction which decreases with r^{-3} , the donor acceptor separation can reach values in the range of 30-80 Å and higher. [9] In the 1960s, David L. Dexter developed a mechanism describing EET at short donor acceptor distances requiring an overlap of the MOs. [10] In contrast to Förster, Dexter described the EET processes as simultaneous migration of an electron from the donor to

the acceptor and of another electron from the acceptor back to the donor (Fig. 1.3). The Dexter exchange mechanism is able to describe triplet-triplet energy transfer for which the Förster term is vanishing, and explains additional contributions in the case of short-range singlet-singlet EET where the spatial overlap of the MOs of interacting molecules is not negligible. To achieve a high EET efficiency E_{EET} , the EET rate k_{EET} has to be significantly larger than the rates of the competing processes [11]

$$E_{EET} = \frac{k_{EET}}{k_{EET} + k_{fl} + k_{nr}} \quad (1.1)$$

where k_{fl} and k_{nr} are the donor fluorescence rate and non-radiative decay rate, respectively. Typical EET rates are found in the range of picoseconds. It is important to mention that EET always denotes the formal transfer of an electron-hole pair between two molecules. The migration of single electrons is described by the Marcus theory [12] and will not be discussed in this work.

1.3 Importance and applications

EET is an important photophysical process which is exploited for numerous technical and scientific applications based on optoelectronics. In nature, it was originally found as a key step of photosynthesis which takes place in the light-harvesting complexes (LHC) of plants. [13] In an attempt to imitate this highly efficient process of energy conversion, solar cells have been developed. [14] Furthermore, EET is exploited in biophysical chemistry for the investigation of the molecular structure and the dynamics of biomolecular systems. [15, 16] In the following, an overview of the most important applications of EET will be given.

1.3.1 Photosynthesis

Phototropic organisms such as plants, algae and some bacteria are able to convert electromagnetic radiation into a chemical potential. [17] During photosynthesis in plants, single chlorophyll molecules located in the LHCs in the chloroplasts are photoexcited. To cover a large part of the visible spectrum, the LHCs not only contain chlorophyll-a but also chlorophyll-b and various carotenoids. The created excitons are transferred between adjacent chlorophyll molecules towards the reaction centers where the charge separation takes place by various redox reactions in photosystem I and II creating a H^+ gradient between stroma and lumen of the cell. The gradient is exploited to drive the biosynthesis of ATP which is the universal energy carrier of living organisms.

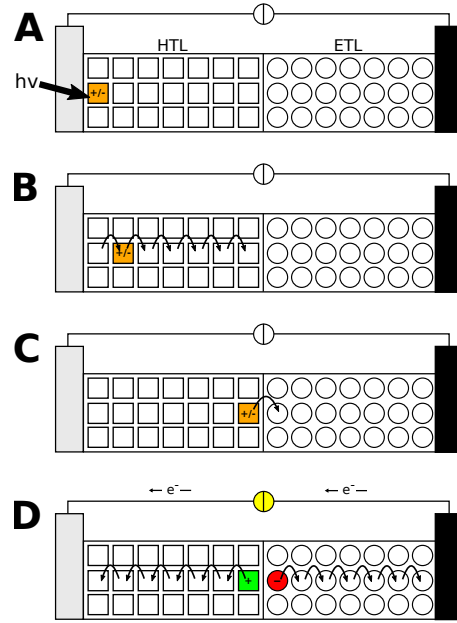


Figure 1.4: Schematic design and working principle of an organic solar cell. A: Photon absorption, B: Exciton migration, C: Charge separation, D: Charge carrier migration. HTL: hole transport layer (reception layer), ETL: electron transport layer.

1.3.2 Organic photovoltaics

In organic photovoltaics, inorganic semiconductors such as silicon dioxide or titanium dioxide are replaced by cheaper organic compounds. [18] The working principle is closely related to the process of photosynthesis in nature. An organic solar cell is generally composed of two electrodes, a reception layer (also termed hole transport layer, HTL) and an electron transport layer (ETL) (Fig. 1.4). [14, 19] One electrode is composed of indium tin oxide or another transparent electronically conductive material such that sun light can reach the excitation layer. Both, excitation layer and ETL, consist of different polymeric materials which are arranged in a way maximizing the interface area. The process of energy conversion can be separated into four major steps (Fig. 1.4). In the first step, a photon is absorbed by a monomer unit of the polymeric excitation layer material. During absorption, the monomer unit is photoexcited and passes over to an electronically excited state representing an exciton. In a second step, the exciton migrates from monomer unit to monomer unit via EET towards the intersection area between excitation and electron transport layer. To achieve a high efficiency of the solar cell, the process of exciton migration has to be much faster than the competing processes such as spontaneous fluorescence or recombination of the electron and the hole. At the intersection between the two layers the exciton is separated into two free charge carriers. In a last step,

hole and electron migrate from monomer unit towards the electrodes creating a voltage which can be used to run an electrical consumer. Hole and electron recombine via the circuit, resetting the system to the initial state.

1.3.3 Structure determination of biomolecules

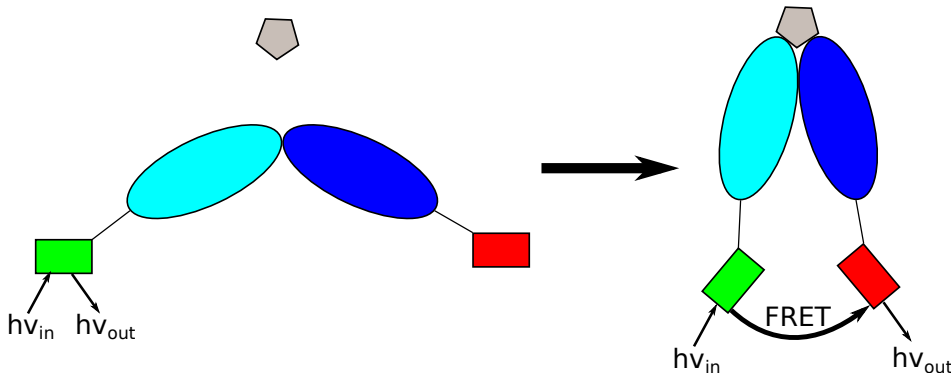


Figure 1.5: Example of FRET used for the detection of the structural change of a protein upon substrate binding.

In biophysical chemistry, the phenomenon of EET is used for the investigation of the structure and the dynamics of biomolecules such as enzymes and nucleic acids. [15] In the most straightforward scenario, a suitable pair of fluorescent dyes is covalently bound to different sites of the target molecule (Fig. 1.5). [20] Since EET takes place between the fluorescent singlet states of the dyes in this context, the term FRET is used in particular, where the "F" refers to the Förster theory. The dyes and linkers are chosen in a way ensuring that the structure and activity of the enzyme remain largely unaffected. Changes of the molecular structure of the target molecule induced by the binding of a substrate or a biochemical reaction can be monitored via changes of the EET rate due to the altered distances between donor and acceptor. When photoexciting the donor, almost exclusively donor fluorescence will be detected when the dyes are well separated. Due to a decreased donor acceptor distance induced by a structural change of the target system, EET becomes more efficient. In this case, acceptor fluorescence can be detected as well upon photoexcitation of the donor. Over the last four decades, highly demanding setups have been developed allowing, e.g., the real-time monitoring of biochemical reactions *in vivo* and *in vitro*. [16, 20]

1.4 State of the art

Experimentally, EET rates can be determined by ultra-fast laser spectroscopy in the picosecond or femtosecond regime. [21, 22] One possibility to access EET rates in quantum chemistry is the application of Fermi's Golden rule. In this context, the EET rate is proportional to the square of the ECME between the interacting electronically excited states. [6] It is important to underline that a high ECME is a necessary but not a sufficient condition for an efficient EET as the pairs of donor deexcitation and acceptor excitation have to be energy-conserving. Alternatively, EET rates can be obtained by excited state molecular dynamics (MD) simulations which is beyond the scope of this work. From a quantum chemical point of view, the challenge is to find an efficient way to accurately compute the EC for molecular systems in which donor and acceptor are not identical. Otherwise the total coupling can directly be calculated from half of the energy splitting (Davydov splitting) between the interacting states as will be shown later. [23] Methods for computing the EC can be separated into monomeric and supermolecular approaches.

In monomeric approaches both subsystems are calculated separately. The wave function of the supermolecular system is approximated as the product of the wave functions of the two individual subsystems. The simplest monomeric approach is directly based on the Förster theory, calculating the EC as a distance-dependent interaction of two transition dipole moments. [6, 7, 8] More accurate results can be achieved if the full transition densities are used instead. In the transition density cube (TDC) method, the transition densities are numerically integrated using a three-dimensional grid. [24] Another way is provided by the distributed transition monopole (DTM) approach approximating the transition densities as a set of point charges located on the two subsystems between which the interaction takes place. [25] The monomer transition density (MTD) approach constitutes a further development of the TDC method expanding the transition densities within the MO basis. [26, 27] The MTD approach is the major approximation used within this work and will be treated in detail later on. Furthermore, Mennucci and coworkers developed a monomeric approach including solvation effects represented by a continuum model. [28, 29] In the 1990s, Harcourt et al. presented a minimal four-electron-four-orbital model providing the opportunity of a separate consideration of local, exchange and CT contributions to the EC in a homodimer. [30, 31, 32] Russo et al. generalized the model to an arbitrary number of orbitals. [33] A method for the consideration of CT contributions which is not restricted to homodimers was developed by Fujimoto. [34, 35] Introducing two ionic intermediate states the EET process can take place according to four different pathways. While the direct part of the EC between the pure locally excited initial and the pure

locally excited final states is calculated in analogy to the MTD method, CT excitations are approximated in a HOMO-LUMO-based approach. Additionally, Fujimoto considers the presence of the respective other monomer by using a frozen-density-embedding formalism. A similar approach based on subsystem-density functional theory (DFT) has been presented by Neugebauer et al. [36, 37] A method which aims for the approximation of the influence of the molecular linker between the donor and the acceptor subsystems was introduced by Caprasecca and Mennucci. [38]

In contrast to monomer based methods, the electronic wave function of the total system is used for further analysis in all supermolecular-based approaches. The simplest approach of this kind is the use of the Davydov splitting for the calculation of the EC which is only possible in the case of a homodimer. [23] Although the calculated EC is exact with respect to the accuracy of the quantum chemical method, its separation into the individual contributions is not straightforward. In supermolecular-based methods suitable for the treatment of molecular heterodimers, diabatization techniques are applied. The calculation is performed by finding the correct unitary transformation which converts the diagonal adiabatic Hamiltonian into the non-diagonal Hamiltonian of the interacting diabatic states. In this case, the EC is equivalent to the off-diagonal elements of the diabatic Hamiltonian. Exploiting a physical quantity which is known for both, the excited states of the isolated monomers and for the corresponding excited states of the supermolecular system, a unitary transformation can be deduced. In a second step this unitary transformation is used for the transformation of the adiabatic Hamiltonian. By this means, the fragment excitation difference (FED) and the fragment spin difference (FSD) methods developed by Hsu et al. enable the calculation of the EC between two singlet and two triplet states, respectively. [39, 40, 41, 42] In 2014, Blancafort and Voityuk developed a similar model using a quantity for the exciton delocalization within the supermolecular arrangement introduced by Lischka and coworkers [43] to find the correct unitary transformation. [44] In order to account for additional CT contributions, the formalism has been extended to a three-state model. Irrespective of the higher computational cost in comparison to monomer based calculations, supermolecule approaches often provide less accurate results. [45] The problem is that the adiabatic states are not solely composed of energetically lowest local transitions but comprise significant additional contributions of higher diabatic states.

1.5 Motivation and objectives

EET is an important photophysical process with numerous applications in chemistry and physics. A detailed understanding of the process is the basis of technological advance in the field of optoelectronics. Research particularly aims for the development of new chemical compounds enhancing the still low efficiency of organic solar cells. Theoretical

calculations can make a decisive contribution predicting the EC and EET rates. By this means, the expensive and demanding synthesis of new compounds can be concentrated on theoretically promising candidates. By the study of model systems, the detailed coupling mechanism, the importance of the molecular geometries and certain substitutes as well as the influence of the architecture of the molecular linker can be understood. A detailed understanding of the processes in model systems provides a valuable basis for the development of new materials.

The primary objective of this work was the implementation of a transition density-based method for the calculation of the EC between two excited singlet states in bichromophoric systems which is adapted to the DFT/MRCI code [46]. The program was devised for the investigation of a number of EET cassettes focussing on the influence of the molecular linker between the donor and the acceptor subsystems. Furthermore, an efficient method connecting to molecular dynamics (MD) simulations was to be provided to be able to study also the dynamics of EET. The method was applied to a well-known FRET model system investigating the validity of the IDA-based Förster theory in the case of very small donor acceptor distances.

The use of monomer-based approaches implies the necessity of splitting the considered supermolecular donor-acceptor system into two isolated subsystems. In the case of a molecular bridge between the donor and the acceptor moiety, a covalent bond has to be split and the resulting fragments have to be saturated with hydrogen atoms. Both, the artificial treatment of the donor and the acceptor as isolated systems and the modification of the chemical structure only allow an approximate study of the original system. To overcome this problem, the initial objective was to use the fragment molecular orbital (FMO) method [47, 48] as implemented in the GAMESS US suite of programs [49] to split the supermolecule into donor and acceptor subsystems. The method was originally developed for the description of large molecules in the electronic ground state and provides excellent results for polypeptides and proteins. [50] In the FMO method, the target system is split into fragments whose energies are determined variationally considering the electrostatic interaction between the fragments by an iterative computation scheme fully relaxing the fragment electron densities. The energy of the unperturbed system can directly be calculated from the sum of the energies of the fragments. In a second step, the interaction energies between each pair of fragments is calculated and added as perturbational correction. Therefore, the electronic ground state energy of the total system (E) is obtained from the appropriate energies of the individual fragments (E_i) and fragment pairs (E_{ij}).

$$E = \sum_i E_i + \sum_{i>j} (E_{ij} - E_i - E_j) \quad (1.2)$$

Due to the dimer correction (second term in Eq. 1.2) the methods is not fully variational. [50] In the FMO method, covalent bonds are split heterolytically. A capping of the resulting fragments is performed effectively by adding the Coulomb field of all other fragments to the considered fragment. Therefore, a saturation with hydrogen atoms is not necessary. An extension of the method to the multi-configuration self-consistent field (MC-SCF) approach enables the description of electronically excited states. [51] To calculate the EC in molecular dimers, the FMO method was planned to be used to compute a set of perfectly donor and acceptor localized MOs. These orbitals were intended for the calculation of the one- and two-electron integrals required by the DFT/MRCI method providing the transition densities. However, it showed that the FMO method in its present form is incompatible with the DFT/MRCI approach. The orbitals obtained by the FMO method are not canonical (diagonal Fock matrix) which is explicitly required in DFT/MRCI. Furthermore, the systems to be studied are characterized by molecular linkers leading to a delocalization of the MOs beyond the borders of the donor and acceptor moieties. The FMO fragmentation principle refers to the splitting of single bonds preserving the electron density within each fragment as most as possible. Therefore it particularly cannot be applied to π -conjugated systems.

Chapter 2

Theory

This section is particularly based on refs. [6, 52, 53].

2.1 Photophysical processes and Franck-Condon principle

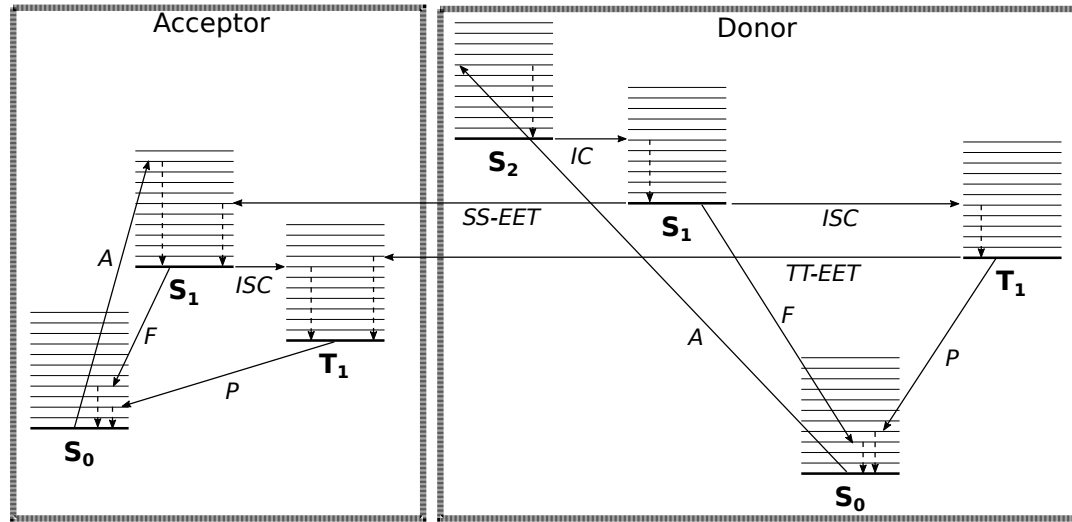


Figure 2.1: Jablonski diagram schematically illustrating the most important photophysical processes. A: absorption, F: fluorescence, P: phosphorescence, IC: internal conversion, ISC: intersystem crossing, SS-EET: singlet-singlet excitation energy transfer, TT-EET: triplet-triplet excitation energy transfer. Dashed arrows denote non-radiative relaxation processes.

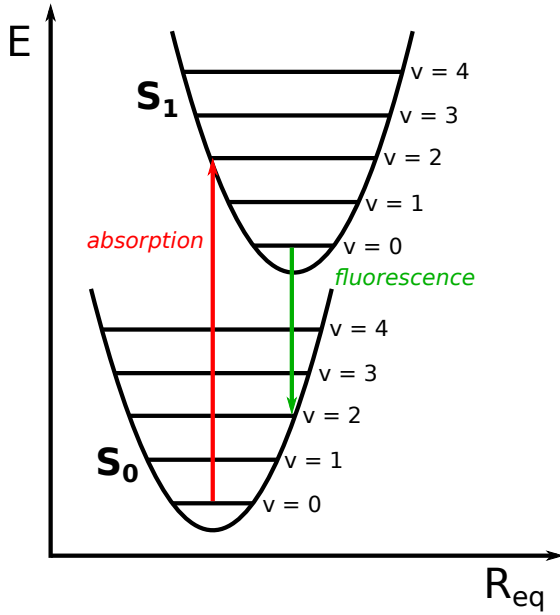


Figure 2.2: Absorption and fluorescence according to the Franck-Condon approximation using the harmonic approximation.

2.1.1 Absorption

The term absorption refers to the excitation of a molecular system due to interaction with resonant electromagnetic radiation. While low energetic radiation in the microwave and infrared (IR) region gives rise to molecular vibrations and rotations, respectively, resonant radiation in the visible (Vis) and the ultraviolet (UV) region ($14000 - 50000 \text{ cm}^{-1}$) causes a reorganization of the electron density within the molecule. In the electronically excited state, which usually has the same spin-multiplicity as the electronic ground state, the electron density as well as the positions of the nuclei in space has changed compared to the electronic ground state. The Franck-Condon principle [54, 55, 56] states that the reorganization of the nuclei takes place on a slower time-scale than the electronic transition due to the much higher mass of the nuclei compared to the electrons. Therefore, each electronic state can be regarded as being composed of a number of vibrational substates, where the combination of an electronic and a certain vibrational substate is called vibronic state (Fig. 2.2). A vibronic transition refers to a transition between a certain vibrational substate of a certain electronic state and a certain vibrational substate of a different electronic state. The difference between the equilibrium molecular geometries of the electronic ground state and the electronically excited state is described by the coordinate ΔR_{eq} . According to the thermal occupation of the vibrational substates of the electronic ground state, an excitation takes place vertically leading to the occupation of different vibrational

substates of a certain electronically excited state which depends on the excitation energy. The vibrational progression of the absorption spectrum can be explained by the different probabilities of these vibronic transitions which depend on the overlap of the vibrational wave functions. The intensity of a vibronic transition is proportional to the absolute square of the transition dipole moment $|\mu_{fi}|^2$ between the initial Ψ_i and the final vibronic states Ψ_f which are defined as the product of the appropriate electronic and vibrational wave functions. [1]

$$|\Psi_i(\vec{r}_1, \vec{r}_2, \dots, \vec{r}_N, \vec{R}_1, \vec{R}_2, \dots, \vec{R}_M)\rangle = |\psi_i(\vec{r}_1, \vec{r}_2, \dots, \vec{r}_N, \vec{R}_1, \vec{R}_2, \dots, \vec{R}_M)\rangle \times |\chi_i(\vec{R}_1, \vec{R}_2, \dots, \vec{R}_M)\rangle \quad (2.1)$$

$$\langle\Psi_f(\vec{r}_1, \vec{r}_2, \dots, \vec{r}_N, \vec{R}_1, \vec{R}_2, \dots, \vec{R}_M)| = \langle\psi_f(\vec{r}_1, \vec{r}_2, \dots, \vec{r}_N, \vec{R}_1, \vec{R}_2, \dots, \vec{R}_M)| \times \langle\chi_f(\vec{R}_1, \vec{R}_2, \dots, \vec{R}_M)| \quad (2.2)$$

In atomic units, the molecular dipole operator is given by

$$\mu = -\underbrace{\sum_{i=1}^N \vec{r}_i}_{\mu_{el}} + \underbrace{\sum_{j=1}^M Z_j \vec{R}_j}_{\mu_{nuc}} \quad (2.3)$$

where r_i and R_j are the cartesian coordinates of the i-th electron and the j-th nucleus, respectively, and where Z_j is the atomic number of the j-th nucleus. The absolute square of the expectation value of the transition dipole moment between the initial and the final vibronic states reads

$$|\mu_{fi}|^2 = |\langle\Psi_f|\mu|\Psi_i\rangle|^2 \quad (2.4)$$

$$= |\langle\Psi_f|\mu_{el}|\Psi_i\rangle + \langle\Psi_f|\mu_{nuc}|\Psi_i\rangle|^2 \quad (2.5)$$

$$= |\langle\psi_f\chi_f|\mu_{el}|\psi_i\chi_i\rangle + \langle\psi_f\chi_f|\mu_{nuc}|\psi_i\chi_i\rangle|^2 \quad (2.6)$$

Applying the Condon approximation Eq. 2.6 can further be decomposed to

$$|\mu_{fi}|^2 = \left| \langle\chi_f|\chi_i\rangle \langle\psi_f|\mu_{el}|\psi_i\rangle |_{R=R_{eq}} + \underbrace{\langle\psi_f|\psi_i\rangle |_{R=R_{eq}} \langle\chi_f|\mu_{nuc}|\chi_i\rangle}_{=0} \right|^2 \quad (2.7)$$

Due to the orthogonality of the electronic states, the term which depends on the nuclear coordinates vanishes such that the expression becomes

$$|\mu_{fi}|^2 = |\langle\chi_f|\chi_i\rangle \langle\psi_f|\mu_{el}|\psi_i\rangle|^2 \quad (2.8)$$

$$= |\langle\chi_f|\chi_i\rangle|^2 \cdot |\langle\psi_f|\mu_{el}|\psi_i\rangle|^2 \quad (2.9)$$

where the absolute square of the overlap integral between the vibrational wave functions is defined as so-called **Franck-Condon factor** which is a measure for the probability of the appropriate vibronic transition. The Franck-Condon principle not only holds true in the framework of absorption but can also be applied to emission as long as the reorganization of the nuclei is slower than the reorganization of the electrons.

2.1.2 Deactivation of electronically excited states

Due to the higher energy of the electronically excited state compared to the electronic ground state, the system returns to the electronic ground state as fast as possible. Due to the existence of different radiating and non-radiating photophysical processes, more than only one pathway is possible for deactivation. [1] Which processes actually take place in a certain molecular system depends on the appropriate rate constants. According to the Franck-Condon principle, the excitation takes place vertically from thermally occupied substates of the electronic ground state populating different vibrational substates of the electronically excited state with a different probability. In solution or in the solid state where the excited molecule can exchange energy with the surrounding molecules, the system relaxes to the vibrational ground state of the current electronically excited state by **vibrational relaxation**. During this process, parts of the excitation energy are converted to thermal energy due to molecular vibrations and due to collisions with solvent molecules. From the vibrational ground state, the system can undergo a transition to an isoenergetic vibrational substate of a different electronic state of either the same spin multiplicity (typically singlet to singlet or triplet to triplet transitions) or a different spin multiplicity (transitions between singlet and triplet states). Such transitions between two states of the same spin multiplicity are called **internal conversion (IC)** while transitions between two states of different spin multiplicity requiring a spin flip are called **intersystem crossing (ISC)**. While IC is spin-allowed, ISC is a spin-forbidden process which only takes place in molecular systems with high spin-orbit coupling (SOC) causing a mixture of singlet and triplet states. SOC is important in all compounds which comprise at least one heavy atom such as sulfur or a transition metal. Furthermore, a **radiative deactivation** can theoretically take place vertically from the lowest vibrational level of each electronically excited state by either **fluorescence** or **phosphorescence**, respectively. The resulting emission spectrum has a vibrational progression which corresponds to Franck-Condon factors between the different vibronic states. Since IC and ISC usually are faster than fluorescence and phosphorescence, respectively, Kasha's rule states that fluorescence and phosphorescence always takes place from the lowest excited state of a given multiplicity (S_1 and T_1). [57] This rule is true for most but not for all molecular systems. Since phosphorescence is a spin-forbidden process, it usually occurs on a much slower time scale

than fluorescence. Similar to ISC, phosphorescence is only possible in molecules with non-zero SOC. If a second, suitable molecule is located next to an electronically excited state, the excitation energy may also be transferred to the second molecule. A detailed quantum chemical description of this non-radiating process known as **excitation energy transfer (EET)** is the main scope of this work and will be treated in detail. EET can take place between electronic states with the same (singlet to singlet, or triplet to triplet) or a different spin-multiplicity (singlet to triplet, or triplet to singlet). In this work, we restrict our considerations to the EET between two excited singlet states. Excitation of a molecule may also induce a photochemical reaction which is beyond the scope of this work. Typical time scales of the most important photophysical processes are listed in Tab. 2.1.

Photophysical Process	Lifetime	Rate (s^{-1})
absorption	fs	10^{-15}
internal conversion	ps	10^{-14}
internal conversion (to GS)	ns - μs	10^{-9} - 10^{-7}
intersystem crossing	ns	10^{-11} - 10^{-8}
fluorescence	ns - μs	10^{-11} - 10^{-6}
phosphorescence	ms - s	10^{-3} - 10^{+2}
excitation energy transfer	ps - ns	

Table 2.1: Typical time scales of photophysical processes. [11] GS: electronic ground state.

2.2 EET rate

2.2.1 Fermi's Golden rule

Under specific conditions which will become clear in the course of this section, the EET rate can be calculated using Fermi's Golden rule. [52] The formula derived by Enrico Fermi and Paul Dirac [58, 59] generally provides a rate constant for the transition from a certain energy eigenstate into a continuum of eigenstates and is based on a perturbational treatment of the Hamiltonian \mathcal{H} of the target system. [6, 60, 61] In the framework of EET, the non-perturbed Hamiltonian \mathcal{H}_0 represents the non-interacting donor and acceptor molecules. To obtain the Hamiltonian \mathcal{H} of the interacting chromophores, the interaction $\mathcal{V}(t)$ is introduced as a time-dependent perturbation of the non-interacting system.

$$\mathcal{H} = \mathcal{H}_0 + \mathcal{V}(t) \quad (2.10)$$

The time-independent Schrödinger equation of the non-interacting system reads

$$\mathcal{H}_0 |\phi_n\rangle = E_n |\phi_n\rangle \quad (2.11)$$

where ϕ_n are the eigenstates of \mathcal{H}_0 with eigenenergies E_n . The eigenstates $|\psi_n(t)\rangle$ of the corresponding time-dependent Schrödinger equation of the non-interacting system are composed of a time-independent term which is equivalent to the eigenstates of \mathcal{H}_0 and a time-dependent term represented by an imaginary exponential function.

$$|\psi_n(t)\rangle = |\phi_n\rangle e^{\frac{-iE_n t}{\hbar}} \quad (2.12)$$

The solutions $|\Psi(t)\rangle$ of the time-dependent Schrödinger equation of the interacting system \mathcal{H}

$$\mathcal{H} |\Psi(t)\rangle = (\mathcal{H}_0 + \mathcal{V}(t)) |\Psi(t)\rangle = i\hbar \frac{d}{dt} |\Psi(t)\rangle \quad (2.13)$$

are assumed to be linear combinations of the eigenstates $|\psi_n(t)\rangle$ of the non-interacting system \mathcal{H}_0 .

$$|\Psi(t)\rangle = \sum_n c_n(t) |\psi_n(t)\rangle \quad (2.14)$$

$$= \sum_n c_n(t) |\phi_n(t)\rangle e^{\frac{-iE_n t}{\hbar}} \quad (2.15)$$

Substituting Eq. 2.15 into Eq. 2.13, one obtains

$$\mathcal{H}_0 \sum_n c_n(t) |\phi_n\rangle e^{\frac{-iE_n t}{\hbar}} + \mathcal{V}(t) \sum_n c_n(t) |\phi_n\rangle e^{\frac{-iE_n t}{\hbar}} = \frac{d}{dt} i\hbar \sum_n c_n(t) |\phi_n\rangle e^{\frac{-iE_n t}{\hbar}} \quad (2.16)$$

Using Eq. 2.11 the expression simplifies to

$$\sum_n c_n(t) E_n |\phi_n\rangle e^{\frac{-iE_n t}{\hbar}} + \mathcal{V}(t) \sum_n c_n(t) |\phi_n\rangle e^{\frac{-iE_n t}{\hbar}} = \frac{d}{dt} i\hbar \sum_n c_n(t) |\phi_n\rangle e^{\frac{-iE_n t}{\hbar}} \quad (2.17)$$

Applying the product rule to derive the right hand side of the equation, we obtain

$$\begin{aligned} \sum_n c_n(t) E_n |\phi_n\rangle e^{\frac{-iE_n t}{\hbar}} &+ \mathcal{V}(t) \sum_n c_n(t) |\phi_n\rangle e^{\frac{-iE_n t}{\hbar}} \\ &= i\hbar \sum_n \left(\frac{d}{dt} c_n(t) |\phi_n\rangle \right) e^{\frac{-iE_n t}{\hbar}} + \sum_n c_n(t) E_n |\phi_n\rangle e^{\frac{-iE_n t}{\hbar}} \end{aligned} \quad (2.18)$$

Multiplying with $\langle \phi_k |$, the expression reads

$$\sum_n c_n(t) \langle \phi_k | \mathcal{V}(t) |\phi_n\rangle e^{\frac{-iE_n t}{\hbar}} = i\hbar \sum_n \left(\frac{d}{dt} c_n(t) \langle \phi_k | \phi_n \rangle \right) e^{\frac{-iE_n t}{\hbar}} \quad (2.19)$$

Introducing the perturbation matrix element V_{kn}

$$V_{kn}(t) = \langle \phi_k | \mathcal{V}(t) |\phi_n\rangle \quad (2.20)$$

and using the orthogonality of the eigenstates ϕ_k and ϕ_n ($\langle \phi_k | \phi_n \rangle = \delta_{kn}$), one obtains

$$\sum_n c_n(t) V_{kn}(t) e^{\frac{-iE_n t}{\hbar}} = i\hbar \left(\frac{d}{dt} c_k(t) \right) e^{\frac{-iE_k t}{\hbar}} \quad (2.21)$$

Rearranging the expression and defining the energy difference between the eigenstates ϕ_k and ϕ_n as

$$\omega_{kn} = \frac{E_k - E_n}{\hbar} \quad (2.22)$$

leads to

$$\frac{d}{dt} c_k(t) = \frac{1}{i\hbar} \sum_n c_n(t) V_{kn}(t) e^{i\omega_{kn} t} \quad (2.23)$$

The differential equation can be solved approximately by a **perturbation expansion** which is truncated after the first-order term. Here, the solution of order $(p+1)$ is obtained iteratively from the solution of order p . [61]

$$\frac{d}{dt} c_k^{(p+1)}(t) \approx \frac{1}{i\hbar} \sum_n c_n^{(p)}(t) V_{kn}(t) e^{i\omega_{kn} t} \quad (2.24)$$

Suppose that for $t = 0$ the system is in the initial state $|i\rangle$ such that

$$c_k^{(0)}(t=0) = \delta_{ki} \begin{cases} 1 & \text{for } k = i \\ 0 & \text{for } k \neq i \end{cases} \quad (2.25)$$

which is the zeroth-order solution of Eq. 2.23 since all expansion coefficients c_k remain constant in time in absence of a perturbation. The first-order solution describes the situation in which the perturbation is switched on and is obtained by substituting the zeroth-order solution (Eq. 2.25) into Eq. 2.23 and solving the resulting differential equation.

$$\frac{d}{dt} c_k^{(1)}(t) = \frac{1}{i\hbar} V_{ki} \cdot e^{i\omega_{ki} t} \quad (2.26)$$

Since the perturbation is supposed to describe the electrostatic interaction between two excitons, it can be assumed to be time-independent

$$V_{ki}(t) = V_{ki} = \text{const.} \quad (2.27)$$

Therefore, the differential equation can simply be solved by integration of the exponential function such that the first-order solution yields

$$c_k^{(1)}(t) = \frac{1}{i\hbar} V_{ki} \int_0^t e^{i\omega_{ki}t} dt \quad (2.28)$$

$$= \frac{1}{i\hbar} V_{ki} \left(\frac{e^{i\omega_{ki}t} - 1}{i\omega_{ki}} \right) \quad (2.29)$$

Truncating the perturbation expansion after the first-order term, it follows that

$$c_k(t) \approx \underbrace{c_k^{(0)}}_{\delta_{ki}} + \underbrace{\frac{1}{i\hbar} V_{ki} \left(\frac{e^{i\omega_{ki}t} - 1}{i\omega_{ki}} \right)}_{c_k^{(1)}} \quad (2.30)$$

The probability of finding the system in state $|k\rangle$ different from the initial state $|i\rangle$ at time t is given by

$$\mathcal{P}_{ki}(t) = |c_k(t)|^2 = \frac{1}{\hbar^2} |V_{ki}|^2 \left| \frac{e^{i(\omega_{ki})t} - 1}{i\omega_{ki}} \right|^2 \quad (2.31)$$

$$= \frac{1}{\hbar^2} |V_{ki}|^2 \left| e^{i(\omega_{ki})\frac{t}{2}} \cdot \frac{e^{i(\omega_{ki})\frac{t}{2}} - e^{-i(\omega_{ki})\frac{t}{2}}}{i\omega_{ki}} \right|^2 \quad (2.32)$$

$$= \frac{1}{\hbar^2} |V_{ki}|^2 \left| e^{i(\omega_{ki})\frac{t}{2}} \cdot \frac{2 \sin(\omega_{ki}\frac{t}{2})}{\omega_{ki}} \right|^2 \quad (2.33)$$

$$= \frac{4}{\hbar^2} |V_{ki}|^2 \frac{\sin^2(\omega_{ki}\frac{t}{2})}{\omega_{ki}^2} \quad (2.34)$$

The average rate is given by the transition probability per time

$$\frac{P_{ki}(t)}{t} = \frac{4}{\hbar^2} |V_{ki}|^2 \cdot \underbrace{\frac{\sin^2(\frac{\omega_{ki}t}{2})}{t \cdot \omega_{ki}^2}}_{f(t, \omega_{ki})} \quad (2.35)$$

Finding the system in the final state k after a long time ($t \rightarrow \infty$) forces energy conservation due to the strong peaking of $f(t, \omega_{ki})$ at $\omega_{ki} \approx 0$.

$$\lim_{t \rightarrow \infty} f(t, \omega_{ki}) = \frac{\pi}{2} \delta(\omega_{ki}) \quad (2.36)$$

Defining dn as the number of states in the energy interval $d\omega_{ki}$, the density of states *near* E_k is

$$\rho(E_k) = \frac{dn}{dE_k} \quad (2.37)$$

Therefore, the total transition rate k_{ki} only refers to final states k' near state k with an energy close to E_k .

$$k_{ki} = \frac{1}{t} \sum_{k' \text{ near } k} \mathcal{P}_{k'i}(t) \quad (2.38)$$

$$= \frac{1}{t} \int \mathcal{P}_{k'i}(t) \cdot \rho(E_k) dE_k \quad (2.39)$$

Here, the sum is replaced by an integral and the condition k' near k is fulfilled by the density of states. Substituting Eq. 2.34 into Eq. 2.39 and using the angular frequency ω instead of the energy E , the expression becomes

$$k_{ki} = \frac{1}{t} \int \frac{4}{\hbar^2} |V_{ki}|^2 \frac{\sin^2(\omega_{ki} \frac{t}{2})}{\omega_{ki}^2} \cdot \rho(\omega_k) d\hbar\omega_{ki} \quad (2.40)$$

$$= \frac{4}{\hbar} |V_{ki}|^2 \rho(\omega_k) \int \frac{1}{t} \frac{\sin^2(\omega_{ki} \frac{t}{2})}{(\omega_{ki})^2} d\omega_{ki} \quad (2.41)$$

$$\approx \frac{4}{\hbar} |V_{ki}|^2 \rho(\omega_k) \int_{-\infty}^{+\infty} \frac{1}{t} \frac{\sin^2(\omega_{ki} \frac{t}{2})}{(\omega_{ki})^2} d\omega_{ki} \quad (2.42)$$

$$= \frac{4}{\hbar} |V_{ki}|^2 \rho(\omega_k) \cdot \frac{\pi}{2} \quad (2.43)$$

$$= \frac{2\pi}{\hbar} \cdot |V_{ki}|^2 \cdot \rho(\omega_k) \quad (2.44)$$

Eq. 2.44 is known as Fermi's Golden rule and is generally valid for an arbitrary photo-physical process in the weak-coupling limit ($\mathcal{P}_{ki}(t) \ll 1$).

2.2.2 Franck-Condon weighted density of states

Generally, the density of states $\rho(E)$ is formally defined as the derivative of the number of quantum states N with respect to the energy E and describes the number of quantum states within a certain energy interval $[E_1; E_2]$.

$$\rho(E) = \frac{dN}{dE} \quad (2.45)$$

$$\Leftrightarrow dN = \rho(E)dE \quad (2.46)$$

$$\Leftrightarrow N = \int_{E_1}^{E_2} \rho(E)dE \quad (2.47)$$

In the framework of EET, the so-called *Franck-Condon weighted density of states* has to be used to calculate the rate constant.

$$k_{EET} = \frac{2\pi}{\hbar} \cdot |V_{DA}|^2 \cdot (FCWD) \quad (2.48)$$

The following derivation is primarily based on ref. [62]. The vibronic wave functions (Φ) of the donor and the acceptor are defined as the product of the appropriate electronic (ϕ) and vibrational wave functions (χ)

$$|\Phi_{D^*N}(r_D, R_D)\rangle = |\phi_{D^*}(r_D, R_D)\rangle \cdot |\chi_{D^*N}(R_D)\rangle \quad (2.49)$$

$$|\Phi_{DM}(r_D, R_D)\rangle = |\phi_D(r_D, R_D)\rangle \cdot |\chi_{DM}(R_D)\rangle \quad (2.50)$$

$$|\Phi_{A^*L}(r_A, R_A)\rangle = |\phi_{A^*}(r_A, R_A)\rangle \cdot |\chi_{A^*L}(R_A)\rangle \quad (2.51)$$

$$|\Phi_{AK}(r_A, R_A)\rangle = |\phi_A(r_A, R_A)\rangle \cdot |\chi_{AK}(R_A)\rangle \quad (2.52)$$

where N and M denote the vibrational states of the electronically excited donor molecule D^* and the donor molecule in the electronic ground state D , respectively. Likewise, K denotes the vibrational state of the acceptor molecule in the electronic ground state A , while L denotes the vibrational state of electronically excited acceptor molecule A^* . The initial and the final vibronic states of the total system (Ψ_I and Ψ_F) are defined as the product of the appropriate vibronic states of the donor and the acceptor, respectively.

$$|\Psi_I\rangle = |\Phi_{D^*N}\rangle \cdot |\Phi_{AK}\rangle \quad (2.53)$$

$$|\Psi_F\rangle = |\Phi_{DM}\rangle \cdot |\Phi_{A^*L}\rangle \quad (2.54)$$

During the EET process, the donor undergoes a vibronic transition from a vibrational substate N with energy E_{D^*N} of the relevant excited state to a vibrational substate M with energy E_{DM} of the electronic ground state. Simultaneously, the exciton acceptor undergoes a transition from a vibrational substate K of its electronic ground state with energy E_{AK} to a vibrational substate L of the excited state with energy E_{A^*L} . For the EET process to be energy-conserving, the initial energy of the total system $E_{D^*N} + E_{AK}$ needs to be equivalent to the energy of the final total system $E_{DM} + E_{A^*L}$. In other words, the amount of energy which is set free by the donor ($E_{D^*N} - E_{DM}$) as well as the amount of energy which is received by the acceptor ($E_{AK} - E_{A^*L}$) have to be equivalent to the amount of transferred energy E (energy of the exciton [6]). Considering *all* combinations of *vibronic* transitions associated with the initial and the final electronic states i (D^*A) and k (DA^*), the EET rate becomes

$$\begin{aligned} k_{EET} = \frac{2\pi}{\hbar} \sum_{M,N} \sum_{K,L} f(E_{D^*N}) f(E_{AK}) & \times \left| \langle \Phi_{DM} \Phi_{A^*L} | \mathcal{V} | \Phi_{D^*N} \Phi_{AK} \rangle \right|^2 \\ & \times \delta(E_{D^*N} + E_{AK} - E_{DM} - E_{A^*L}) \end{aligned} \quad (2.55)$$

where the δ -distribution ensures energy conservation and where $f(E_{D^*N})$ and $f(E_{AK})$ describe the thermal populations of the appropriate vibrational states of the donor excited

and acceptor ground state, respectively, according to a Boltzmann distribution. Introducing the Condon approximation (see Sec. 2.1.1), the coupling matrix element is separated into an electronic term and a vibrational term

$$\langle \Phi_{DM} \Phi_{A^*L} | \mathcal{V} | \Phi_{D^*N} \Phi_{AK} \rangle = \langle \phi_D \phi_{A^*L} | \mathcal{V} | \phi_{D^*} \phi_A \rangle \times \langle \chi_{DM} | \chi_{D^*N} \rangle \langle \chi_{A^*L} | \chi_{AK} \rangle \quad (2.56)$$

such that the coupling between the two vibronic states Ψ_k and Ψ_i can be described as coupling between the appropriate electronic states $\phi_D \phi_A$ and $\phi_{D^*} \phi_{A^*}$ weighted by a measure of the transition probability between the appropriate vibrational states which is provided by the overlap integrals between the vibrational wave functions $\langle \chi_{D^*N} | \chi_{DM} \rangle$ and $\langle \chi_{AK} | \chi_{A^*L} \rangle$. As already mentioned in Sec. 2.1.1 the squares of these overlap integrals are called Franck-Condon factors. Substituting Eq. 2.56 into Eq. 2.55 the EET rate becomes

$$k_{EET} = \frac{2\pi}{\hbar} \left| \langle \phi_D \phi_{A^*} | \mathcal{V} | \phi_{D^*} \phi_A \rangle \right|^2 \sum_{M,N} \sum_{K,L} f(E_{D^*N}) f(E_{AK}) \times \left| \langle \chi_{DM} | \chi_{D^*N} \rangle \langle \chi_{A^*L} | \chi_{AK} \rangle \right|^2 \times \delta(E_{D^*N} + E_{AK} - E_{DM} - E_{A^*L}) \quad (2.57)$$

2.2.3 Spectral overlap integral

The spectral overlap integral is a crude approximation of the FCWD which is based on the lineshape of the emission spectrum of the donor [62]

$$E_D(\omega) = \sum_{M,N} f(E_{D^*N}) |\langle \chi_{D^*N} | \chi_{DM} \rangle|^2 \times \delta(E_{D^*N} + E_{DM} - \hbar\omega) \quad (2.58)$$

and the lineshape of the absorption spectrum of the acceptor

$$A_A(\omega) = \sum_{K,L} f(E_{AK}) |\langle \chi_{AK} | \chi_{A^*L} \rangle|^2 \times \delta(E_{AK} + E_{A^*L} + \hbar\omega) \quad (2.59)$$

where both spectra have to be normalized to unit area. Substituting Eqs. 2.58 and 2.59 into Eq. 2.57 and using

$$\delta(E_{D^*N} + E_{AK} - E_{DM} - E_{A^*L}) = \int_{-\infty}^{+\infty} \delta(E_{D^*N} - E_{DM} - E) \delta(E_{AK} - E_{A^*L} - E) dE \quad (2.60)$$

where E is the energy of the exciton (see sec. 2.2.2), the EET rate can be rewritten as

$$k_{EET} = \frac{2\pi}{\hbar} \cdot |V_{DA}|^2 \cdot \int_0^{\infty} A_A(\omega) E_D(\omega) d\omega \quad (2.61)$$

where the integral is termed spectral overlap integral. Note that the spectral overlap integral used in Förster theory is different from the quantity introduced here. In Förster

theory, the spectral overlap integral not only covers the density of states but also comprises parts of the ECME as will be shown later (see Sec. 2.5). Since the δ -function is a probability distribution, the density of states and therefore the spectral overlap integral is given in units of inverse energy.

2.3 Density matrix theory

The electronic wave function of a molecule consists of a large number of Slater determinants or configuration state functions (CSF) based on MOs that are again linear combinations of basis functions (i.e. a set of AOs). Although the wave function covers all information concerning the target molecule, it does not provide a simple picture of the electron distribution determining its physical and chemical properties. The electron distribution can easily be described in terms of density and transition density functions providing a valuable tool to derive the molecular properties from the electronic wave function. Transition densities play a key role for the calculation of the ECME and therefore for the description of EET.¹

2.3.1 Density function of an N-electron system

Taking the simplest case of a system with only a single electron with spin $+\frac{1}{2}$ in orbital ϕ_A , the wave function is directly given by the wave function of the corresponding spin orbital ψ_A .

$$\psi_A(\vec{x}) = \phi_A(\vec{r})\alpha(s) \quad (2.62)$$

where \vec{x} comprises the three spatial coordinates as well as the spin of the electron. In this case, the probability of finding the electron with spin $+\frac{1}{2}$ in the volume element $d\vec{r}$ (spin-space volume element $d\vec{x}$) is given by

$$\rho(\vec{x}) d\vec{x} = |\psi_A(\vec{x})|^2 d\vec{x} \quad (2.63)$$

$$= |\phi_A(\vec{r})|^2 |\alpha(s)|^2 d\vec{r} ds \quad (2.64)$$

where the $\rho(\vec{x})$ is called **density function**. The corresponding spin-free density function $P(\vec{r})$ relates to the probability of finding the electron with any spin in the volume element $d\vec{r}$ and is obtained from the density function by integration over the spin.

$$P(\vec{r}) = \int_s \rho(\vec{x}) ds \quad (2.65)$$

¹Sec. 2.3 is essentially based on ref. [53]

These considerations which have been made for the minimal system depending on only one electron, can be generalized to an arbitrary system of N electrons. Here, the probability of finding electron 1 in the spin-space volume element $d\vec{x}_1$ and simultaneously electron 2 in the spin-space volume element $d\vec{x}_2$, etc. is given by

$$\rho(\vec{x}_1, \vec{x}_2, \dots, \vec{x}_N) d\vec{x}_1 d\vec{x}_2 \dots d\vec{x}_N = |\Psi(\vec{x}_1, \vec{x}_2, \dots, \vec{x}_N)|^2 d\vec{x}_1 d\vec{x}_2 \dots d\vec{x}_N \quad (2.66)$$

such that the **density function of the entire system** is defined as

$$\rho_{sys}(\vec{x}_1, \vec{x}_2, \dots, \vec{x}_N) = \Psi(\vec{x}_1, \vec{x}_2, \dots, \vec{x}_N) \Psi^*(\vec{x}_1, \vec{x}_2, \dots, \vec{x}_N) \quad (2.67)$$

2.3.2 Reduced density functions

Considering only the location of electron 1 explicitly, one needs the probability of finding electron 1 in the spin-space volume-element $d\vec{x}_1$ and all other ($N-1$) electrons anywhere.

$$d\vec{x}_1 \int \Psi(\vec{x}_1, \vec{x}_2, \dots, \vec{x}_N) \Psi^*(\vec{x}_1, \vec{x}_2, \dots, \vec{x}_N) d\vec{x}_2, \dots, d\vec{x}_N \quad (2.68)$$

Since electrons cannot be distinguished, the probability of finding any of the N electrons in the spin-space volume element $d\vec{x}_1$ and all remaining ($N-1$) electrons anywhere can be expressed as

$$\rho_1(\vec{x}_1) d\vec{x}_1 = N \cdot d\vec{x}_1 \int \Psi(\vec{x}_1, \vec{x}_2, \dots, \vec{x}_N) \Psi^*(\vec{x}_1, \vec{x}_2, \dots, \vec{x}_N) d\vec{x}_2, \dots, d\vec{x}_N \quad (2.69)$$

where $\rho_1(\vec{x}_1)$ is defined as the **reduced one-electron density function**. The corresponding density function without reference to the spin is defined as the **spin-free reduced one-electron density function**.

$$P_1(\vec{r}_1) = \int_s \rho(\vec{x}_1) ds_1 \quad (2.70)$$

$$= N \cdot \int_s \int \Psi(\vec{x}_1, \vec{x}_2, \dots, \vec{x}_N) \Psi^*(\vec{x}_1, \vec{x}_2, \dots, \vec{x}_N) d\vec{x}_2, \dots, d\vec{x}_N d\vec{s}_1 \quad (2.71)$$

For the sake of simplicity all reduced one-electron density functions will be referred to as $\rho(\vec{x}_1)$ and $P(\vec{r}_1)$ in the following omitting the index of 1. By analogy, the **reduced two-electron density function** refers to the probability of finding any two of the N electrons in the spin-space volume elements $d\vec{x}_1$ and $d\vec{x}_2$ and all remaining $N-2$ electrons anywhere.

$$\pi(\vec{x}_1, \vec{x}_2) = N \cdot (N - 1) \int \Psi(\vec{x}_1, \vec{x}_2, \dots, \vec{x}_N) \Psi^*(\vec{x}_1, \vec{x}_2, \dots, \vec{x}_N) d\vec{x}_3, \dots, d\vec{x}_N \quad (2.72)$$

The spin-free variant can again be obtained by integration over the spin.

$$\Pi(\vec{r}_1, \vec{r}_2) \int_s \pi(\vec{x}_1, \vec{x}_2) \, ds_1 ds_2 \quad (2.73)$$

2.3.3 Expectation values of one- and two-electron operators

Taking again the simplest case of a system with only a single electron in spin orbital ψ_A (electron with spin $+\frac{1}{2}$ in the spatial orbital ϕ), the expectation value of an arbitrary operator \mathcal{O} is given by

$$\langle \mathcal{O} \rangle = \int \psi_A^*(\vec{x}) \cdot \mathcal{O} \cdot \psi_A(\vec{x}) \, d\vec{x} \quad (2.74)$$

If the operator does not involve differentiation or integration, one may also write

$$\langle \mathcal{O} \rangle = \int \mathcal{O} \cdot \psi_A(\vec{x}) \psi_A^*(\vec{x}) \, d\vec{x} \quad (2.75)$$

$$= \int \mathcal{O} \cdot \rho(\vec{x}) \, d\vec{x} \quad (2.76)$$

Since operators usually involve differentiation or integration in quantum chemistry, an auxiliary coordinate x' is introduced with

$$\psi^*(\vec{x}') = \psi^*(\vec{x}) \quad (2.77)$$

to avoid \mathcal{O} to act on ψ^* and

$$\langle \mathcal{O} \rangle = \int \mathcal{O} \cdot \psi_A(\vec{x}) \psi_A^*(\vec{x}') \, d\vec{x} \quad (2.78)$$

$$= \int \mathcal{O} \cdot \rho(\vec{x}; \vec{x}') \, d\vec{x} \quad (2.79)$$

is obtained where it is understood that x' is replaced by x after acting with the operator \mathcal{O} but before integration.² Generalizing these considerations to an arbitrary N -electron system, the **density function of the entire system**

$$\rho(\vec{x}_1, \vec{x}_2, \dots, \vec{x}_N; \vec{x}'_1, \vec{x}'_2, \dots, \vec{x}'_N) = \Psi(\vec{x}_1, \vec{x}_2, \dots, \vec{x}_N) \Psi^*(\vec{x}'_1, \vec{x}'_2, \dots, \vec{x}'_N) \quad (2.80)$$

the **reduced one-electron density function**

$$\rho(\vec{x}_1; \vec{x}'_1) = N \cdot \int \Psi(\vec{x}_1, \vec{x}_2, \dots, \vec{x}_N) \Psi^*(\vec{x}'_1, \vec{x}_2, \dots, \vec{x}_N) d\vec{x}_2, \dots, d\vec{x}_N \quad (2.81)$$

²If explicitly only the "diagonal elements" ($\vec{x} = \vec{x}'$) should be considered, it is possible to use the short notation $\rho(\vec{x})$ instead of $\rho(\vec{x}; \vec{x}')$ which will be avoided in this work for the sake of consistency.

and its spin-free variant

$$P(\vec{r}_1; \vec{r}'_1) = N \cdot \int \Psi(\vec{x}_1, \vec{x}_2, \dots, \vec{x}_N) \Psi^*(\vec{x}'_1, \vec{x}_2, \dots, \vec{x}_N) d\vec{x}_2, \dots, d\vec{x}_N ds_1 \quad (2.82)$$

are rewritten. Thus, the expectation value of an arbitrary one-electron operator $\mathcal{O}_1 = \sum_i h(\vec{x}_i)$ of a many-electron system can be written in terms of the reduced one-electron density function

$$\langle \mathcal{O}_1 \rangle = \int \Psi^*(\vec{x}_1, \vec{x}_2, \dots, \vec{x}_N) \left[\sum_i h(\vec{x}_i) \right] \Psi(\vec{x}_1, \vec{x}_2, \dots, \vec{x}_N) d\vec{x}_1, d\vec{x}_2, \dots, d\vec{x}_N \quad (2.83)$$

$$= N \cdot \int h(\vec{x}_1) \Psi(\vec{x}_1, \vec{x}_2, \dots, \vec{x}_N) \Psi^*(\vec{x}'_1, \vec{x}_2, \dots, \vec{x}_N) d\vec{x}_1, d\vec{x}_2, \dots, d\vec{x}_N \quad (2.84)$$

$$= \int h(\vec{x}_1) \rho(\vec{x}_1; \vec{x}'_1) d\vec{x}_1 \quad (2.85)$$

By analogy, the **reduced two-electron density function** and its spin-free variant are rewritten

$$\pi(\vec{x}_1, \vec{x}_2; \vec{x}'_1, \vec{x}'_2) = N(N-1) \int \Psi(\vec{x}_1, \vec{x}_2, \vec{x}_3, \dots, \vec{x}_N) \Psi^*(\vec{x}'_1, \vec{x}'_2, \vec{x}_3, \dots, \vec{x}_N) d\vec{x}_3 \dots d\vec{x}_N \quad (2.86)$$

$$\pi(\vec{r}_1, \vec{r}_2; \vec{r}'_1, \vec{r}'_2) = \int_s \pi(\vec{x}_1, \vec{x}_2; \vec{x}'_1, \vec{x}'_2) ds_1 ds_2 \quad (2.87)$$

Thus, the expectation value of an arbitrary two-electron operator $\mathcal{O}_2 = \sum_{ij} g(\vec{x}_i, \vec{x}_j)$ can also be expressed in terms of the reduced two-electron density function.

$$\langle \mathcal{O}_2 \rangle = \int g(\vec{x}_i, \vec{x}_j) \pi(\vec{x}_1, \vec{x}_2; \vec{x}'_1, \vec{x}'_2) d\vec{x}_1 d\vec{x}_2 \quad (2.88)$$

If the electronic states are represented by single Slater determinants (1-determinant approximation), the reduced two-electron density function can be written in terms of reduced one-electron density functions.

$$\pi(\vec{x}_1, \vec{x}_2; \vec{x}'_1, \vec{x}'_2) = \rho(\vec{x}_1; \vec{x}'_1) \rho(\vec{x}_2; \vec{x}'_2) - \rho(\vec{x}_2; \vec{x}'_1) \rho(\vec{x}_1; \vec{x}'_2) \quad (2.89)$$

$$\Pi(\vec{r}_1, \vec{r}_2; \vec{r}'_1, \vec{r}'_2) = P(\vec{r}_1; \vec{r}'_1) P(\vec{r}_2; \vec{r}'_2) - \frac{1}{2} P(\vec{r}_2; \vec{r}_1) P(\vec{r}_1; \vec{r}_2) \quad (2.90)$$

Eq. 2.90 holds true for a closed shell system where all spatial orbitals are doubly occupied with one electron with α spin and one electron with β spin according to the Pauli principle. The factor $\frac{1}{2}$ can be traced back to the fact that there is no exchange interaction between electrons of anti-parallel spin. In this case, the expectation value of an arbitrary two-

electron operator becomes

$$\begin{aligned}\langle \mathcal{O}_2 \rangle &= \int g(\vec{x}_1, \vec{x}_2) (\rho(\vec{x}_1; \vec{x}'_1)\rho(\vec{x}_2; \vec{x}'_2) - \rho(\vec{x}_2; \vec{x}'_1)\rho(\vec{x}_1; \vec{x}'_2)) d\vec{x}_1 d\vec{x}_2 \\ &= \int \rho(\vec{x}_1; \vec{x}'_1)g(\vec{x}_1, \vec{x}_2)\rho(\vec{x}_2; \vec{x}'_2) d\vec{x}_1 d\vec{x}_2 - \int \rho(\vec{x}_2; \vec{x}'_1)g(\vec{x}_1, \vec{x}_2)\rho(\vec{x}_1; \vec{x}'_2) d\vec{x}_1 d\vec{x}_2\end{aligned}\quad (2.91)$$

and in the spin-free case

$$\langle \mathcal{O}_2 \rangle = \int P(\vec{r}_1; \vec{r}'_1)g(\vec{r}_1, \vec{r}_2)P(\vec{r}_2; \vec{r}'_2) d\vec{r}_1 d\vec{r}_2 - \frac{1}{2} \int P(\vec{r}_2; \vec{r}_1)g(\vec{r}_1, \vec{r}_2)P(\vec{r}_1; \vec{r}_2) d\vec{r}_1 d\vec{r}_2 \quad (2.92)$$

For the two-electron operator being the Coulomb operator r_{12}^{-1} , it becomes obvious that the first integral refers to the Coulomb contribution J while the second integral refers to the exchange contribution K .

$$\langle \Psi_K | \sum_{ij} r_{ij}^{-1} | \Psi_K \rangle = \underbrace{\int \frac{P(\vec{r}_1; \vec{r}'_1)P(\vec{r}_2; \vec{r}'_2)}{r_{12}} d\vec{r}_1 d\vec{r}_2}_J - \underbrace{\frac{1}{2} \int \frac{P(\vec{r}_2; \vec{r}_1)P(\vec{r}_1; \vec{r}_2)}{r_{12}} d\vec{r}_1 d\vec{r}_2}_K \quad (2.93)$$

This expression will become important later on, when the formalism is extended to group-function theory.

2.3.4 Transition density functions

While density functions describe physical properties which depend on a single electronic state (e.g. static dipole moments), transition density functions describe properties which depend on two electronic states (e.g. transition dipole moments). This is particularly important for the analysis of excitation and deexcitation processes. Transition density functions are defined in analogy to their corresponding density functions. The **reduced one-electron transition density function** between two electronic states K and L and its spin-free variant are given by

$$\rho(KL|\vec{x}_1; \vec{x}'_1) = N \cdot \int \Psi_K(\vec{x}_1, \vec{x}_2, \dots, \vec{x}_N) \Psi_L^*(\vec{x}'_1, \vec{x}_2, \dots, \vec{x}_N) d\vec{x}_2 \dots d\vec{x}_N \quad (2.94)$$

$$P(KL|\vec{r}_1; \vec{r}'_1) = \int_s \rho(KL|\vec{x}_1; \vec{x}'_1) ds_1 \quad (2.95)$$

while the **reduced two electron density function** and its spin-free variant read

$$\pi(KL|\vec{x}_1, \vec{x}_2; \vec{x}'_1, \vec{x}'_2) = N(N-1) \int \Psi_K(\vec{x}_1, \vec{x}_2, \vec{x}_3, \dots, \vec{x}_N) \Psi_L^*(\vec{x}'_1, \vec{x}'_2, \vec{x}_3, \dots, \vec{x}_N) d\vec{x}_3 \dots d\vec{x}_N \quad (2.96)$$

$$\Pi(KL|\vec{r}_1, \vec{r}_2; \vec{r}'_1, \vec{r}'_2) = \int_s \pi(KL|\vec{x}_1, \vec{x}_2; \vec{x}'_1, \vec{x}'_2) ds_1 ds_2 \quad (2.97)$$

In the framework of transition density functions, the transition matrix elements for arbitrary one- and two-electron operators ($\mathcal{O}_1 = \sum_i h(\vec{x}_i)$ and $\mathcal{O}_2 = \sum_{ij} g(\vec{x}_i, \vec{x}_j)$) are given by

$$\langle \Psi_L | \mathcal{O}_1 | \Psi_K \rangle = \int h(\vec{x}_1) \rho(KL | \vec{x}_1; \vec{x}'_1) d\vec{x}_1 \quad (2.98)$$

$$\langle \Psi_L | \mathcal{O}_2 | \Psi_K \rangle = \int g(\vec{x}_1, \vec{x}_2) \pi(KL | \vec{x}_1, \vec{x}_2; \vec{x}'_1, \vec{x}'_2) d\vec{x}_1 d\vec{x}_2 \quad (2.99)$$

It should be mentioned that in the special case of $K = L$ all expressions become equivalent to the corresponding density function equations. In the case of 1-determinantal wave functions, the reduced two-electron transition density functions can again be written in terms of reduced one-electron transition density functions

$$\pi(KL | \vec{x}_1, \vec{x}_2; \vec{x}'_1, \vec{x}'_2) = \rho(KL | \vec{x}_1; \vec{x}'_1) \rho(KL | \vec{x}_2; \vec{x}'_2) - \rho(KL | \vec{x}_2; \vec{x}'_1) \rho(KL | \vec{x}_1; \vec{x}'_2) \quad (2.100)$$

$$\Pi(KL | \vec{r}_1, \vec{r}_2; \vec{r}'_1, \vec{r}'_2) = P(KL | \vec{r}_1; \vec{r}'_1) P(KL | \vec{r}_2; \vec{r}'_2) - \frac{1}{2} P(KL | \vec{r}_2; \vec{r}'_1) P(KL | \vec{r}_1; \vec{r}'_2) \quad (2.101)$$

such that the transition matrix element of the Coulomb operator reads

$$\begin{aligned} \langle \Psi_L | \sum_{ij} \vec{r}_{ij}^{-1} | \Psi_K \rangle &= \underbrace{\int \frac{P(KL | \vec{r}_1; \vec{r}'_1) P(KL | \vec{r}_2; \vec{r}'_2)}{\vec{r}_{12}} d\vec{r}_1 d\vec{r}_2}_J \\ &- \underbrace{\frac{1}{2} \int \frac{P(KL | \vec{r}_2; \vec{r}'_1) P(KL | \vec{r}_1; \vec{r}'_2)}{\vec{r}_{12}} d\vec{r}_1 d\vec{r}_2}_K \end{aligned} \quad (2.102)$$

2.3.5 From density functions to density matrices

The density functions defined in Eqs. 2.81 and 2.86 and the transition density functions defined in Eqs. 2.94 and 2.96 often are referred to as density matrices or transition density matrices, respectively. These "unfortunate" [53] and mathematically wrong terms, coined by von Neumann and Dirac, can be traced back to the notation $\rho(\vec{x}; \vec{x}')$ of the density functions which is similar to the notation of matrix elements M_{ij} . However, x and x' are continuous variables while the indices i and j are discrete numbers. This means that the density matrix is not a real matrix since its definition is based on improper basis vectors. Only if the density matrix refers to a finite dimensional Hilbert space such as a set of orthonormal spin orbitals as it is used in the case of quantum chemical calculations, does the density matrix become a true matrix. Assuming single Slater determinantal wave function for each electronic state, the one- and two-electron (transition) density functions

can be expanded in the basis of (spin) orbitals $\{\psi_i\}$.

$$\rho(KL|\vec{x}_1) = \rho(KL|\vec{x}_1; \vec{x}_1) = \sum_{ij} \rho_{ij}^{KL} \cdot \psi_i(\vec{x}_1) \psi_j^*(\vec{x}_1) \quad (2.103)$$

$$\pi(KL|\vec{x}_1, \vec{x}_2) = \pi(KL|\vec{x}_1, \vec{x}_2; \vec{x}_1, \vec{x}_2) = \sum_{ijkl} \rho_{ijkl}^{KL} \cdot \psi_i(\vec{x}_1) \psi_j(\vec{x}_2) \psi_k^*(\vec{x}_1) \psi_l^*(\vec{x}_2) \quad (2.104)$$

The set of expansion coefficients ρ_{ij}^{KL} is defined as matrix representation of the newly introduced density operator ρ

$$\langle \psi_i | \rho | \psi_j \rangle = \rho_{ij} \quad (2.105)$$

and is denoted as **reduced one-electron (transition) density matrix**. The short term (one-electron) **density** is used synonymously. Having expanded the one- and two-electron densities in the basis of spin orbitals, the expectation values for arbitrary one- and two electron operators are given by

$$\langle \Psi_L | \sum_i h(\vec{x}_i) | \Psi_K \rangle = \sum_{ij} \rho_{ij}^{KL} \langle \psi_j | h | \psi_i \rangle = \text{tr}(\rho h) \quad (2.106)$$

$$\langle \Psi_L | \sum_{ij} g(\vec{x}_i, \vec{x}_j) | \Psi_K \rangle = \sum_{ijkl} \pi_{ijkl}^{KL} \langle \psi_k \psi_l | g | \psi_i \psi_j \rangle \quad (2.107)$$

2.3.6 Configuration interaction

A common way to overcome the simple 1-determinantal representation of electronic states neglecting electron correlation is the configuration interaction (CI) formalism. Here, the wave functions of the electronic states (Ψ_K , Ψ_L) are expanded in terms of Slater determinants (Φ_κ , Φ_λ). Instead of Slater-determinants, configuration state functions (CSFs) can be used to speed up the calculation which will not be considered here.

$$\Psi_K = \sum_{\kappa} C_{\kappa}^K \Phi_{\kappa} \quad (2.108)$$

$$\Psi_L = \sum_{\lambda} C_{\lambda}^L \Phi_{\lambda} \quad (2.109)$$

The expansion coefficients C_{κ}^K and C_{λ}^L representing the contribution of each determinant are termed CI coefficients. In the framework of CI, the elements of the reduced one-electron transition density matrix ρ_{ij}^{KL} describing the one-electron transitions between the CI states Ψ_K and Ψ_L can be obtained by the weighted sum of the appropriate reduced one-electron transition density matrix elements $\rho_{ij}^{\kappa\lambda}$.

$$\rho_{ij}^{KL} = \sum_{\kappa, \lambda} C_{\kappa}^K C_{\lambda}^{L*} \rho_{ij}^{\kappa\lambda} \quad (2.110)$$

By analogy, the reduced two-electron transition density matrix π_{ijkl}^{KL} describing the two-electron transitions between the CI-states Ψ_K and Ψ_L can be obtained by the weighted sum of the appropriate reduced two-electron transition density matrix elements $\pi_{ijkl}^{\kappa\lambda}$.

$$\pi_{ijkl}^{KL} = \sum_{\kappa,\lambda} C_{\kappa}^K C_{\lambda}^{L*} \pi_{ijkl}^{\kappa\lambda} \quad (2.111)$$

The spinless forms of reduced (transition) density matrices can be obtained by replacing the basis of spin orbitals $\{\psi_i\}$ with a basis of spatial orbitals $\{\phi_i\}$.

2.3.7 Second quantization

In second quantization, the reduced (transition) density matrices can easily be expressed using the (singlet) excitation operator $a_j^\dagger a_i$ annihilating an electron in spin orbital i and recreating it in spin orbital j .

$$\rho_{ij}^{KL} = \langle \Psi_L | a_j^\dagger a_i | \Psi_K \rangle \quad (2.112)$$

$$\pi_{ijkl}^{KL} = \langle \Psi_L | a_j^\dagger a_l^\dagger a_k a_i | \Psi_K \rangle \quad (2.113)$$

If a basis of (orthonormal) spatial orbitals is used instead of spin orbitals, the excitation operator becomes

$$E_{ji} = \sum_{\sigma} a_{j\sigma}^\dagger a_{i\sigma} \quad (2.114)$$

where the index σ denotes the electron spin (α or β). The operator describes a transition of an electron from spatial orbital i to spatial orbital j and a conservation of the spin. In this case, the spin-free reduced one-electron transition density matrix is given by

$$P_{ij}^{KL} = \langle \Psi_L | \sum_{\sigma} a_{j\sigma}^\dagger a_{i\sigma} | \Psi_K \rangle \quad (2.115)$$

Analogously, this applies for the spin-free reduced two-electron transition density matrix.

$$e_{jilk} = \sum_{\sigma_1} \sum_{\sigma_2} a_{j\sigma_1}^\dagger a_{i\sigma_1} a_{l\sigma_2}^\dagger a_{k\sigma_2} = E_{ji} E_{lk} - \delta_{jk} E_{kj} \quad (2.116)$$

$$\Pi_{ijkl}^{KL} = \langle \Psi_L | e_{jilk} | \Psi_K \rangle \quad (2.117)$$

2.3.8 Extension to group-function theory: Molecular dimers

So far, only densities and transition densities of isolated molecules have been treated. The formalism can be extended to molecular aggregates in order to characterize the interaction between the individual subsystems, assuming that the interaction is weak such that the individuality of the subsystems will be preserved. The general idea is to expand the

supermolecular wave function in the basis of the subsystem wave functions in analogy to the expansion of a usual electronic wave function in the basis of spin orbitals. In the simplest case, one considers a molecular dimer composed of subsystems A and B. Here, the supermolecular wave function can be expressed as a simple product of the wave functions of the two subsystems each representing a group of electrons.

$$\Phi^{(HP)}(\vec{x}_1, \vec{x}_2, \dots, \vec{x}_{N_A+N_B}) = \Psi^{(A)}(\vec{x}_1, \vec{x}_2, \dots, \vec{x}_{N_A})\Psi^{(B)}(\vec{x}_{N_A+1}, \vec{x}_{N_A+2}, \dots, \vec{x}_{N_A+N_B}) \quad (2.118)$$

By this means, the total set of electrons is divided into two groups of electrons which either belong to subsystem A or subsystem B. Since the simple product does not fulfill the Pauli principle, the antisymmetry operator \mathcal{A} has to be introduced

$$\Phi(\vec{x}_1, \vec{x}_2, \dots, \vec{x}_{N_A+N_B}) = M \cdot \mathcal{A} \cdot \Phi^{(HP)}(\vec{x}_1, \vec{x}_2, \dots, \vec{x}_{N_A+N_B}) \quad (2.119)$$

where M is a normalization factor. It is obvious, that Eq. 2.119 represents a generalization of the formalism of a 1-determinantal wave function. Thus, the antisymmetrized product of group functions Φ is analogous to a Slater determinant which is defined as an antisymmetrized product of spin orbitals. This means that the representation of a supermolecular state as antisymmetrized product of the wavefunction of the individual molecules is analogous to a 1-determinantal description of a molecular electronic state.³ As we require orthogonality of the subsystem wave functions, the same definitions and calculation rules apply as in the case of Slater determinants. In particular, the definitions of the one- and two-electron (transition) density matrices are analogous.

As it is possible to represent the supermolecular ground-state wave function in terms of the ground-state wave functions of the monomers, the formalism can be extended to excited states by analogy. Here, the electronically excited states of the supermolecule are represented by antisymmetrized products of the subsystem wave functions in different electronic states which can either be the ground state or a certain excited state. These excited supermolecular wave functions behave analogously to singly (one monomer unit in an electronically excited state), doubly (two subsystems in an electronically excited state), ... excited Slater determinants. Restricting the considerations to a molecular dimer (RS), allowing only a single excited subsystem in the supermolecule and considering only a certain electronically excited state per subsystem (i.e. the S_1 state), we can formulate two supermolecular states Φ_κ and Φ_λ , respectively, in which either group R is in its electronic

³The subsystem-based description of the dimer can in principle be enhanced by a formalism similar to configuration interaction. Since this is usually not of interest in the framework of excitonic coupling, the formalism is not further considered in this work.

ground state r while group S is in its excited state s' or vice versa.

$$\Phi_\kappa = M \cdot \mathcal{A} \cdot (\Psi_r^{(R)} \Psi_{s'}^{(S)}) \quad (2.120)$$

$$\Phi_\lambda = N \cdot \mathcal{A} \cdot (\Psi_{r'}^{(R)} \Psi_s^{(S)}) \quad (2.121)$$

The expectation value of an arbitrary two-electron operator behaves in the same way as in the case of 1-determinantal wave functions. Considering the similarity of subsystem wave functions and spin orbitals with respect to Eqs. 2.100 and 2.100, respectively, Eq. 2.93 can be rewritten as

$$\langle \Psi_r^{(R)} \Psi_{s'}^{(S)} | \sum_{ij} \vec{r}_{ij} | \Psi_{r'}^{(R)} \Psi_s^{(S)} \rangle = \underbrace{\int \frac{P_R(rr'|\vec{r}_1) P_S(ss'|\vec{r}_2)}{\vec{r}_{12}} d\vec{r}_1 d\vec{r}_2}_{J^{RS}(rr',ss')} \quad (2.122)$$

$$- \underbrace{\frac{1}{2} \int \frac{P_R(rr'|\vec{r}_2; \vec{r}_1) P_S(ss'|\vec{r}_1; \vec{r}_2)}{\vec{r}_{12}} d\vec{r}_1 d\vec{r}_2}_{K^{RS}(rr',ss')} \quad (2.123)$$

where $P(rr'|\vec{r}_1, \vec{r}_1')$ is the **reduced one-electron transition density function** which refers to the transition from the electronic state r to state r' in group R . The matrix element $\langle \Psi_{r'}^{(R)} \Psi_{s'}^{(S)} | \sum_{ij} r_{ij}^{-1} | \Psi_r^{(R)} \Psi_s^{(S)} \rangle$ expresses the electrostatic interaction in terms of Coulomb and exchange contributions between an electronic transition in group R and a simultaneous transition in group S . If the overlap between the two electronic states is small, the exchange contribution becomes negligible and a simple product ansatz without antisymmetrization is sufficient. In this case, the exchange term vanishes and the matrix element reduces to the Coulomb contribution.

$$\langle \Psi_{r'}^{(R)} \Psi_{s'}^{(S)} | \sum_{ij} \vec{r}_{ij} | \Psi_r^{(R)} \Psi_s^{(S)} \rangle \approx \int \frac{P_R(rr'|\vec{r}_1) P_S(ss'|\vec{r}_2)}{\vec{r}_{12}} d\vec{r}_1 d\vec{r}_2 \quad (2.124)$$

2.3.9 Analysis of the excited-state wave functions

Here a method for the analysis of excited-state wave functions introduced by Plasser and Lischka [43] is reviewed which is based on the spin-free reduced one-electron transition density matrices $P_{qp}^{[\Phi\Psi_n]}$ between the electronic ground state Φ and an excited state Ψ_n .⁴ The method provides the percentage of local- and CT- transitions of an electronically excited state in terms of a CT matrix. The formalism holds true for all electronically excited states which are particularly dominated by one-electron contributions. Each supermolecular electronically excited state Ψ_n can be represented by a 2×2 CT matrix

⁴A very similar review has been given in ref. [63]

Ω^n

$$\Omega^n = \begin{pmatrix} \Omega_{AA}^n & \Omega_{AB}^n \\ \Omega_{BA}^n & \Omega_{BB}^n \end{pmatrix} \quad (2.125)$$

which recovers the extent of charge delocalization within the excited state and which can directly be computed from the transition density matrix in a subsystem-localized basis. [43] While the diagonal elements Ω_{AA}^n and Ω_{BB}^n represent the weight of local excitations on subsystems A and B, respectively, the off-diagonal elements Ω_{AB}^n and Ω_{BA}^n are known as CT numbers. They are defined as the percentage of electrons transferred from one subsystem to the other one during the excitation. Since the set of molecular orbitals (MO) $\{i\}$ generally is delocalized over the whole supermolecular system, the atomic orbital (AO) basis $\{\mu\}$ is used for the analysis. The one-electron transition density matrix $P'^{[\Phi\Psi_n]}$ in AO basis can be obtained by a transformation

$$P'^{[\Phi\Psi_n]}_{\mu\nu} = \sum_{pq} c_{\mu p}^* P^{[\Phi\Psi_n]}_{pq} c_{q\nu} \quad (2.126)$$

where $c_{q\nu}$ are the elements of the MO coefficient matrix. [64] Applying the AO overlap matrix S to ensure orthonormality, the elements of the CT matrix can be computed as given by

$$\Omega_{A \rightarrow B}^n = \frac{1}{2} \sum_{\mu \in A} \sum_{\nu \in B} (P'^{[\Phi\Psi_n]} S)_{\mu\nu} (S P'^{[\Phi\Psi_n]})_{\mu\nu} \quad (2.127)$$

where AOs μ are localized on subsystem A and AOs ν on subsystem B. Since contributions from all higher excitations are neglected within the one-electron density matrix, the CT matrix has to be normalized to 1.

$$\Omega^n = \sum_{A,B} \Omega_{AB} \stackrel{!}{=} 1 \quad (2.128)$$

The total percentage of one-electron excitations can be obtained from Eq. 2.128 before normalization. If the quantity is significantly smaller than 0.8 the method may be imprecise for the analysis of the appropriate excited state.

2.4 Excitonic coupling matrix element

2.4.1 The two-state system

An effective system of only two interacting states provides a sufficiently accurate model for the description of many processes in molecular systems as long as further states are not significantly involved. [6] The model provides analytically exact results such that further approximations are not necessary. Before applying the model to the process of EET, a

general review will be given in the following.

The Hamiltonian of a two-state quantum-mechanical system with eigenstates Ψ_{\pm} and eigenenergies E_{\pm} fulfilling the Schrödinger equation

$$\mathcal{H}\Psi = E\Psi \quad (2.129)$$

can be written as

$$\mathcal{H} = E_+ |\Psi_+\rangle \langle \Psi_+| + E_- |\Psi_-\rangle \langle \Psi_-| \quad (2.130)$$

The corresponding Hamiltonian matrix reads

$$H_a = \begin{pmatrix} E_+ & 0 \\ 0 & E_- \end{pmatrix} \quad (2.131)$$

To determine the unknown *adiabatic* eigenstates Ψ_{\pm} , one uses a basis of two first-order *diabatic* states $|\Phi_1\rangle$ and $|\Phi_2\rangle$ with energies ϵ_1 and ϵ_2 , respectively.

$$|\Psi\rangle = c_1 |\Phi_1\rangle + c_2 |\Phi_2\rangle \quad (2.132)$$

In the framework of a molecular dimer, the first-order diabatic states refer to the appropriate states of the isolated monomers. Using the diabatic states, the Hamiltonian of the two-state system given in Eq. 2.130 can be rewritten as

$$\mathcal{H} = \epsilon_1 |\Phi_1\rangle \langle \Phi_1| + \epsilon_2 |\Phi_2\rangle \langle \Phi_2| + V_{12} |\Phi_1\rangle \langle \Phi_2| + V_{21}^* |\Phi_2\rangle \langle \Phi_1| \quad (2.133)$$

The corresponding Hamilton matrix reads

$$H_d = \begin{pmatrix} \epsilon_1 & V_{12} \\ V_{21}^* & \epsilon_2 \end{pmatrix} \quad (2.134)$$

where $V_{12} = V_{21}^*$. The objective is to transform the Hamiltonian given in Eq. 2.133 to the form of Eq. 2.130 which is equivalent to a diagonalization of H_d yielding both, the adiabatic energies E_{\pm} and the expansion coefficients c_1 and c_2 .

$$C^\dagger H_d C = H_a \quad (2.135)$$

$$H_d C = C H_a \quad (2.136)$$

$$H_d C = H_a C \quad (2.137)$$

$$\begin{pmatrix} \epsilon_1 & V_{12} \\ V_{12} & \epsilon_2 \end{pmatrix} \cdot \begin{pmatrix} c_1 \\ c_2 \end{pmatrix} = E \cdot \begin{pmatrix} c_1 \\ c_2 \end{pmatrix} \quad (2.138)$$

In a two-state model, the adiabatic eigenvalues E_{\pm} can directly be determined by setting

the secular determinant to zero.

$$\begin{vmatrix} \epsilon_1 - E & V_{12} \\ V_{12} & \epsilon_2 - E \end{vmatrix} = 0 \quad (2.139)$$

$$E_{\pm} = \frac{1}{2} \left(\epsilon_1 + \epsilon_2 \pm \sqrt{(\epsilon_1 - \epsilon_2)^2 + 4|V_{12}|^2} \right) \quad (2.140)$$

In the special case where ϵ_1 equals ϵ_2 Eq. 2.140 simplifies to

$$E_{\pm} = \frac{1}{2} \left(2\epsilon \pm \sqrt{4|V_{12}|^2} \right) \quad (2.141)$$

$$= \epsilon \pm |V_{12}| \quad (2.142)$$

The energy difference between the two adiabatic states E_+ and E_- is symmetric

$$\Delta E = E_+ - E_- = (\epsilon + |V_{12}|) - (\epsilon - |V_{12}|) \quad (2.143)$$

$$= 2|V_{12}| \quad (2.144)$$

and is referred to as Davydov splitting. Therefore, $|V_{12}|$ can be computed from half of the Davydov splitting in the case of a molecular homodimer (section 2.4.3). However, the method only provides exact results if the simple two-state model really applies for the considered molecule.

2.4.2 Molecular heterodimer

The electronic Hamiltonian \mathcal{H} of a molecular aggregate consisting of M individual molecules can be expressed as the sum of the electronic Hamiltonians of the isolated molecules and the sum of the operators describing the interaction between each pair of molecules. [6, 52, 65]

$$\mathcal{H} = \sum_{m=1}^M \mathcal{H}_m + \frac{1}{2} \sum_{m=1}^M \sum_{n=1}^N \mathcal{V}_{mn} \quad (2.145)$$

$$= \sum_{m=1}^M \mathcal{H}_m + \sum_{m=1}^M \sum_{n>m}^N \mathcal{V}_{mn} \quad (2.146)$$

In a simple donor acceptor system the aggregate reduces to a molecular dimer which can be described by analogy.

$$\mathcal{H} = \mathcal{H}_D + \mathcal{H}_A + \mathcal{V}_{DA} \quad (2.147)$$

The ground and electronically excited states $\phi_D(\vec{r}_D)$, $\phi_{D^*}(\vec{r}_D)$, $\phi_A(\vec{r}_A)$ and $\phi_{A^*}(\vec{r}_A)$ of the isolated donor and acceptor are eigenstates of \mathcal{H}_D and \mathcal{H}_A , respectively, with eigenenergies ϵ_D , ϵ_{D^*} , ϵ_A and ϵ_{A^*} . If the electron overlap is small such that the electronic structure of the interacting monomers is largely preserved, the supermolecular ground state Ψ_G can

be written as product of the ground-state wave functions of the individual monomers.

$$|\Psi_G(\vec{r}_D, \vec{r}_A)\rangle = |\phi_D(\vec{r}_D)\rangle \cdot |\phi_A(\vec{r}_A)\rangle \quad (2.148)$$

$$= |D\rangle \cdot |A\rangle \quad (2.149)$$

$$= |DA\rangle \quad (2.150)$$

The Schrödinger equation of the supermolecular system with respect to the electronic ground state reads

$$\mathcal{H}|\Psi_G\rangle = E_G|\Psi_G\rangle \quad (2.151)$$

$$\mathcal{H}|DA\rangle = E_G|DA\rangle \quad (2.152)$$

Multiplication with $\langle DA|$ yields

$$\langle DA|\mathcal{H}|DA\rangle = E_G \cdot \underbrace{\langle DA|DA\rangle}_{=1} \quad (2.153)$$

Due to the definition of the supermolecular Hamiltonian, the supermolecular ground state energy can be expressed as sum of the ground state energies E_D and E_A of the isolated monomers and an additional term which is denoted as the van der Waals interaction energy V_{DA} by Kasha et al. [65]

$$E_G = \langle \Psi_G | \mathcal{H} | \Psi_G \rangle \quad (2.154)$$

$$= \langle DA | \mathcal{H} | DA \rangle \quad (2.155)$$

$$= \langle DA | (\mathcal{H}_D + \mathcal{H}_A + \mathcal{V}_{DA}) | DA \rangle \quad (2.156)$$

$$= \langle DA | \mathcal{H}_D | DA \rangle + \langle DA | \mathcal{H}_A | DA \rangle + \langle DA | \mathcal{V}_{DA} | DA \rangle \quad (2.157)$$

$$= \underbrace{\langle A | A \rangle}_{=1} \langle D | \mathcal{H}_D | D \rangle + \underbrace{\langle D | D \rangle}_{=1} \langle A | \mathcal{H}_A | A \rangle + \langle DA | \mathcal{V}_{DA} | DA \rangle \quad (2.158)$$

$$= E_D + E_A + V_{vdW} \quad (2.159)$$

The formalism can be extended to electronically excited states of the supermolecule and is analogous to the general case of a two-state model discussed in Sec. 2.4.1. In contrast to the electronic ground state, two limiting cases of perfectly locally excited states are conceivable. In D^*A the donor is in the electronically excited state and the acceptor remains in the electronic ground state while the acceptor is excited and the donor remains in the ground state in DA^* . Therefore, the supermolecular (adiabatic) excited states Ψ_E are expanded in the basis of the (diabatic) locally excited states

$$|\Psi_E\rangle = r|D^*A\rangle + s|DA^*\rangle \quad (2.160)$$

where r and s are expansion coefficients. As shown in Sec. 2.4.1 this leads to a linear system of equations which in matrix representation reads

$$\begin{pmatrix} \langle D^*A|\mathcal{H}|D^*A\rangle - E & \langle D^*A|\mathcal{H}|DA^*\rangle \\ \langle DA^*|\mathcal{H}|D^*A\rangle & \langle DA^*|\mathcal{H}|DA^*\rangle - E \end{pmatrix} \cdot \begin{pmatrix} r \\ s \end{pmatrix} = E \begin{pmatrix} r \\ s \end{pmatrix} \quad (2.161)$$

The energies E of the electronically excited states can be obtained by setting the secular determinant to zero.

$$\begin{vmatrix} \langle D^*A|\mathcal{H}|D^*A\rangle - E & \langle D^*A|\mathcal{H}|DA^*\rangle \\ \langle DA^*|\mathcal{H}|D^*A\rangle & \langle DA^*|\mathcal{H}|DA^*\rangle - E \end{vmatrix} = 0 \quad (2.162)$$

$$E_{\pm} = \frac{1}{2} \left\{ \langle D^*A|\mathcal{H}|D^*A\rangle + \langle DA^*|\mathcal{H}|DA^*\rangle \right. \quad (2.163) \\ \left. \pm \sqrt{\left(\langle D^*A|\mathcal{H}|D^*A\rangle - \langle DA^*|\mathcal{H}|DA^*\rangle \right)^2 + 4 \langle DA^*|\mathcal{H}|D^*A\rangle^2} \right\}$$

Eq. 2.163 exactly holds true for an arbitrary **heterodimer** in a 2-state model and is equivalent to Eq. 2.140. [6] Using the definition of the supermolecular Hamiltonian (Eq. 2.147) the matrix elements in Eq. 2.163 can further be simplified

$$\langle D^*A|\mathcal{H}|D^*A\rangle = \langle D^*A|(\mathcal{H}_D + \mathcal{H}_A + \mathcal{V}_{DA})|D^*A\rangle \quad (2.164)$$

$$= \underbrace{\langle D^*A|\mathcal{H}_D|D^*A\rangle}_{\langle A|A\rangle\langle D|\mathcal{H}_D|D^*\rangle} + \underbrace{\langle D^*A|\mathcal{H}_A|D^*A\rangle}_{\langle D^*|D^*\rangle\langle A|\mathcal{H}_A|A\rangle} + \langle D^*A|\mathcal{V}_{DA}|D^*A\rangle \quad (2.165)$$

$$= \langle D^*|\mathcal{H}_D|D^*\rangle + \langle A|\mathcal{H}_A|A\rangle + \langle D^*A|\mathcal{V}_{DA}|D^*A\rangle \quad (2.166)$$

$$= \epsilon_{D^*} + \epsilon_A + V_{vdW}^{(D^*A)} \quad (2.167)$$

$$\langle DA^*|\mathcal{H}|DA^*\rangle = \epsilon_D + \epsilon_{A^*} + V_{vdW}^{(DA^*)} \quad (2.168)$$

$$\langle DA^*|\mathcal{H}|D^*A\rangle = \langle DA^*|(\mathcal{H}_D + \mathcal{H}_A + \mathcal{V}_{DA})|D^*A\rangle \quad (2.169)$$

$$= \underbrace{\langle DA^*|\mathcal{H}_D|D^*A\rangle}_{\langle A^*|A\rangle\langle D|\mathcal{H}_D|D^*\rangle} + \underbrace{\langle DA^*|\mathcal{H}_A|D^*A\rangle}_{\langle D|D^*\rangle\langle A^*|\mathcal{H}_A|A\rangle} + \langle DA^*|\mathcal{V}_{DA}|D^*A\rangle \quad (2.170)$$

$$= \langle DA^*|\mathcal{V}_{DA}|D^*A\rangle \quad (2.171)$$

$$= V_{DA} \quad (2.172)$$

where $\langle DA^*|\mathcal{V}_{DA}|D^*A\rangle$ is defined as the ECME. Since V_{DA} is assumed to be the Coulomb operator, the matrix element is equivalent to Eq. 2.124 and can therefore be expressed in terms of the spin-free reduced one-electron transition densities P_A and P_D of the

monomers.

$$V_{DA} = \int \frac{P_D(\vec{r}_1)P_A(\vec{r}_2)}{\vec{r}_{12}} d\vec{r}_1 d\vec{r}_2 \quad (2.173)$$

2.4.3 Davydov splitting: The molecular homodimer

In honor of Soviet physicist Alexander Sergeevich Davydov, the splitting of excitonic energy levels in molecular crystals is termed Davydov splitting. [23] In the framework of EET, the term denotes the energy splitting ΔE between the coupled donor and acceptor localized states. In the special case of a **homodimer** where donor and acceptor are identical molecules, Eq. 2.163 simplifies to [6, 52]

$$E_{\pm} = \langle D^*A|\mathcal{H}|D^*A\rangle \pm \langle DA^*|\mathcal{V}_{DA}|D^*A\rangle \quad (2.174)$$

Thus, the two equivalent bright monomer states symmetrically split into an energetically stabilized and an energetically destabilized state. The distribution of the oscillator strength among the two states depends on the orientation of the transition dipoles. If the stabilized state is bright and the destabilized state is dark, the absorption spectrum is red shifted. If the destabilized state is bright while the stabilized state is dark, the absorption spectrum will be blue shifted. Geometrical donor acceptor arrangements leading to a red shift are termed J-aggregates while arrangements leading to a blue shift are termed H-aggregates. A splitting of the monomer absorption into two bands occurs if the oscillator strength is largely equally distributed among the two states and if the energetic splitting is large enough. In the case of a homodimer, the energy difference ΔE between the interacting states (Davydov splitting) is

$$\Delta E = E_- - E_+ = 2 \cdot V_{DA} \quad (2.175)$$

For this reason, the ECME in homodimeric systems can directly be calculated from half of the energy splitting of the interacting states (Fig. 2.3). However, even for small systems such as an ethylene dimer, the energy splitting may not be symmetric if the simple picture of the 2-state model does not fully apply. This can be traced back to the interaction of the considered Frenkel (local) excitonic states with energetically stabilized CT states. [63]

$$V_{DA} = \frac{\Delta E}{2} \quad (2.176)$$

For heterodimers the energetic splitting is not symmetric and the ECME has to be computed by diabatization schemes or monomer-based approaches which will be dealt with in the following.

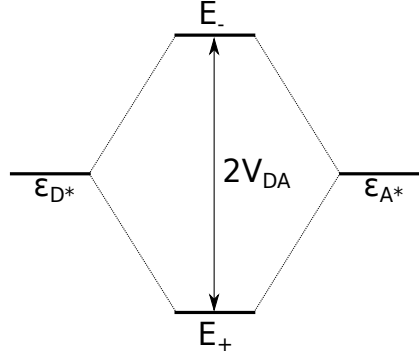


Figure 2.3: Energy splitting in a homodimeric system.

2.4.4 Ideal dipole approximation

If the spatial extensions of the transition densities of the coupled donor (D) and acceptor (A) localized transitions are small compared to the intermolecular distance, the ECME can be approximated as electrostatic interaction between the transition dipoles. [6] To this end, the interaction between the two transitions is written in terms of the distance vector \vec{r}_{mn} between the coordinates of the m-th electron of D and the n-th electron of A with respect to the intermolecular distance vector \vec{X} connecting the centers of mass of both chromophores.

$$V_{DA} = \sum_{m,n} \frac{e^2}{|\vec{X} + \vec{r}_{mn}|} \quad (2.177)$$

$$= e^2 \sum_{m,n} \frac{1}{|\vec{X} + \vec{r}_{mn}|} \quad (2.178)$$

To remove the negligible explicit short-range interaction between each electron on D and each electron on A, a multipole expansion in cartesian coordinates (three-dimensional Taylor expansion) is carried out

$$V_{DA} = e^2 \sum_{m,n} \frac{1}{|\vec{X} + \vec{r}_{mn}|} \quad (2.179)$$

$$= e^2 \sum_{m,n} \frac{1}{|\vec{X}|} + \vec{r}_{mn} \nabla_X \frac{1}{|\vec{X}|} + \frac{1}{2} (\vec{r}_{mn} \nabla_X) (\vec{r}_{mn} \nabla_X) \frac{1}{|\vec{X}|} + \dots \quad (2.180)$$

With

$$\vec{r}_{mn} \nabla_X \frac{1}{|\vec{X}|} = -\frac{\vec{r}_{mn} \vec{X}}{|\vec{X}|^3} \quad (2.181)$$

and

$$(\vec{r}_{mn} \nabla_X) (\vec{r}_{mn} \nabla_X) \frac{1}{|\vec{X}|} = -(\vec{r}_{mn} \nabla_X) \frac{\vec{r}_{mn} \vec{X}}{|\vec{X}|^3} \quad (2.182)$$

$$= -\vec{r}_{mn}^2 \nabla_X \left(\vec{X} \cdot \frac{1}{|\vec{X}|^3} \right) \quad (2.183)$$

$$= -\vec{r}_{mn}^2 \left(\vec{X} \cdot \nabla_X \frac{1}{|\vec{X}|^3} + \frac{1}{|\vec{X}|^3} \nabla_X \vec{X} \right) \quad (2.184)$$

$$= -\frac{\vec{r}_{mn}^2}{|\vec{X}|^3} + 3 \frac{(\vec{r}_{mn} \vec{X})^2}{|\vec{X}|^5} \quad (2.185)$$

Eq. 2.180 becomes

$$V_{DA} \approx e^2 \sum_{m,n} \frac{1}{|\vec{X}|} - \frac{\vec{r}_{mn} \vec{X}}{|\vec{X}|^3} + \frac{1}{2} \left(-\frac{\vec{r}_{mn}^2}{|\vec{X}|^3} + 3 \frac{(\vec{r}_{mn} \vec{X})^2}{|\vec{X}|^5} \right) \quad (2.186)$$

$$V_{DA} = e^2 \left(\sum_{m,n} \frac{1}{|\vec{X}|} - \frac{\vec{X} \vec{r}_m - \vec{X} \vec{r}_n}{|\vec{X}|^3} \right) - \frac{1}{2} \frac{\vec{r}_m^2 - 2\vec{r}_m \vec{r}_n + \vec{r}_n^2}{|\vec{X}|^3} \quad (2.187)$$

$$+ \frac{3}{2} \frac{\vec{X}^2 \vec{r}_m^2 - 2\vec{X} \vec{r}_m \vec{X} \vec{r}_n + \vec{X}^2 \vec{r}_n^2}{|\vec{X}|^5} \quad (2.188)$$

Since charge neutrality is assumed, the zeroth- and first-order terms of the multipole expansion as well as all terms comprising \vec{r}_m^2 and \vec{r}_n^2 vanish. With the definition of the transition dipole moment

$$\vec{\mu}_D = e \sum_m \vec{r}_m \quad (2.189)$$

$$\vec{\mu}_A = e \sum_n \vec{r}_n \quad (2.190)$$

one obtains

$$V_{DA} \approx \sum_{m,n} \frac{\vec{\mu}_m \vec{\mu}_n}{|\vec{X}|^3} - 3 \frac{\vec{X} \vec{\mu}_m \vec{X} \vec{\mu}_n}{|\vec{X}|^5} \quad (2.191)$$

Eq. 2.191 requires the knowledge of absolute value and direction of the transition dipole moments. In the framework of FRET experiments which are carried out in solution, the consideration of single ("frozen") donor acceptor orientations is not possible. Therefore the average relative orientation of the transition dipole moments has to be used, which results from a probability distribution. In this context, it would be comfortable to have an expression which only depends on the absolute value of the transition dipole moments

which can be multiplied by a statistical factor representing the average transition dipole moment orientation. Such an expression can be obtained by introducing unit vectors pointing in the direction of the transition dipole moments and a unit vector pointing in the direction of the intermolecular distance vector.

$$\vec{n}_D = \sum_m \frac{\vec{r}_m}{|\vec{r}_m|} \quad (2.192)$$

$$\vec{n}_A = \sum_n \frac{\vec{r}_n}{|\vec{r}_n|} \quad (2.193)$$

$$\vec{e}_{DA} = \frac{\vec{X}}{|\vec{X}|} \quad (2.194)$$

By this means, ECME becomes

$$V_{DA} = e^2 \sum_{m,n} \frac{\vec{r}_m \vec{r}_n}{|\vec{X}|^3} - 3 \frac{\vec{X} \vec{r}_m \vec{X} \vec{r}_n}{|\vec{X}|^5} \quad (2.195)$$

$$= e^2 \sum_{m,n} \frac{\frac{\vec{r}_m}{|\vec{r}_m|} |\vec{r}_m| \cdot \frac{\vec{r}_n}{|\vec{r}_n|} |\vec{r}_n|}{|\vec{X}|^3} - 3 \frac{\frac{\vec{X}}{|\vec{X}|} |\vec{X}| \cdot \frac{\vec{r}_m}{|\vec{r}_m|} |\vec{r}_m| \cdot \frac{\vec{X}}{|\vec{X}|} |\vec{X}| \cdot \frac{\vec{r}_n}{|\vec{r}_n|} |\vec{r}_n|}{|\vec{X}|^5} \quad (2.196)$$

$$= e^2 \sum_{m,n} \frac{\frac{\vec{r}_m}{|\vec{r}_m|} |\vec{r}_m| \cdot \frac{\vec{r}_n}{|\vec{r}_n|} |\vec{r}_n|}{|\vec{X}|^3} - 3 \frac{\frac{\vec{X}}{|\vec{X}|} \cdot \frac{\vec{r}_m}{|\vec{r}_m|} |\vec{r}_m| \cdot \frac{\vec{X}}{|\vec{X}|} \cdot \frac{\vec{r}_n}{|\vec{r}_n|} |\vec{r}_n|}{|\vec{X}|^3} \quad (2.197)$$

$$= \frac{\vec{n}_D |\vec{\mu}_m| \cdot \vec{n}_A |\vec{\mu}_n|}{|\vec{X}|^3} - 3 \frac{\vec{e}_{DA} \cdot \vec{n}_D |\vec{\mu}_m| \cdot \vec{e}_{DA} \cdot \vec{n}_A |\vec{\mu}_n|}{|\vec{X}|^3} \quad (2.198)$$

$$= \left\{ \vec{n}_D \cdot \vec{n}_A - 3 \left((\vec{e}_{DA} \cdot \vec{n}_D) \cdot (\vec{e}_{DA} \cdot \vec{n}_A) \right) \right\} \cdot \frac{|\vec{\mu}_m| \cdot |\vec{\mu}_n|}{|\vec{X}|^3} \quad (2.199)$$

$$= \kappa \cdot \frac{|\vec{\mu}_m| \cdot |\vec{\mu}_n|}{|\vec{X}|^3} \quad (2.200)$$

where κ is a scalar representing the relative transition dipole moment orientation. Since the EET rate depends on the absolute square of the ECME, the orientation factor is defined as κ^2 .

The orientation factor

The orientation factor κ^2 is a scalar describing the relative orientation of the two interacting transition dipole moments in the IDA. [6, 66] Since transition dipole moments are constant quantities of the regarded molecules, the orientation factor indirectly describes the relative orientation of the donor and the acceptor molecules. As shown in Eq. 2.200, unit vectors can be used for its calculation. In a more descriptive manner, the orientation factor κ^2 can be expressed in terms of the angles between the two interacting transition

dipole moment vectors (Fig. 2.4).

$$\kappa^2 = (\cos \theta_{DA} - 3 \cos \theta_D \cdot \cos \theta_A)^2 \quad (2.201)$$

κ^2 can adopt values between 0 and 4, where 0 describes the limiting case of a perfectly

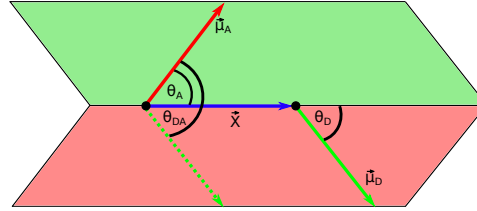


Figure 2.4: Illustration of the angles defining the relative orientation of the two interacting transition dipole moments according to the ideal dipole approximation (IDA). These angles can be used for the determination of the orientation factor κ^2 .

perpendicular orientation of the transition dipole moments while 4 describes the limiting case of the two vectors arranged in a row. [66] An orientation factor of 1 describes a coplanar orientation (Fig. 2.5). Nevertheless, it has to be stated that a certain value of

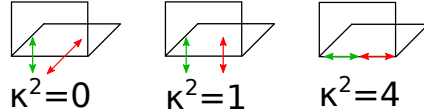


Figure 2.5: Limiting cases of the orientation factor κ^2 . $\kappa^2 = 0$ describes the limiting case of a perpendicular transition dipole moment orientation. $\kappa^2 = 1$ describes two transition dipole moment vectors which are arranged in a coplanar manner while an orientation factor of 4 describes an orientation of both vectors in a row.

κ^2 is not associated with only a single transition dipole moment orientation. Different relative orientations lead to the same orientation factor. This means that the actual relative transition dipole moment orientation cannot be traced back if the orientation factor is known (Fig. 2.6). Furthermore, only a coplanar orientation of the transition dipole moments leads to an orientation factor of 1 while all other parallel orientations lead to an orientation factor between 0 and 4.

In most experimental studies, a perfectly isotropic probability distribution of the transition dipoles of the interacting dyes is assumed. This is the case if both dyes are able to rotate freely in space. This approximation is justified if the interaction between the individual dye molecules is small. Nevertheless, the approximation is even fulfilled if the dye molecules are attached to a target molecule with largely flexible linkers. [67] A spherically isotropic

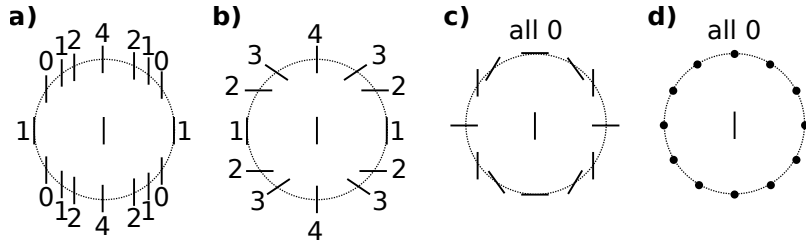


Figure 2.6: Examples of different arrangements of the donor and acceptor transition dipole moments. Points denote a perpendicular orientation of the appropriate transition dipole moments with respect to the plane defined by the intermolecular distance vector and the respective other transition dipole moment vector. Figure adapted from van der Meer et al. [66]

distribution of the transition dipoles results in a probability function of the orientation factor that can be described by an analytic discontinuous logarithmic function, which is highest for $\kappa^2 = 0$ and close to zero for $\kappa^2 = 4$ (Fig. 2.7). [68, 69, 70]

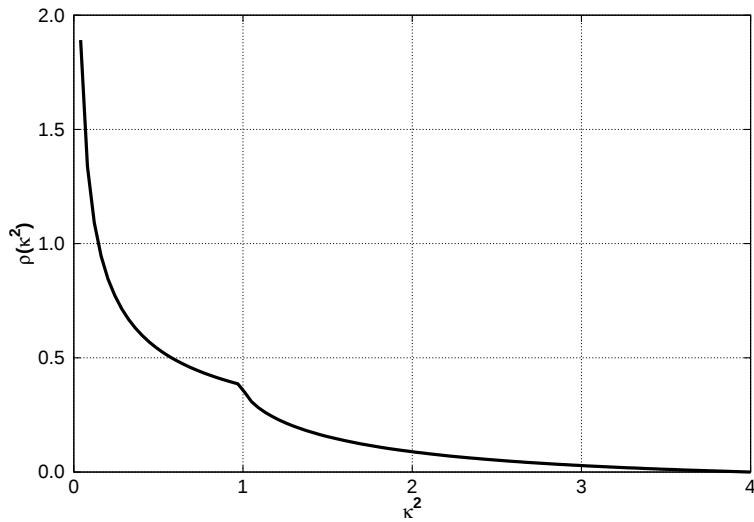


Figure 2.7: Isotropic transition dipole moment distribution. The orientation factor of $\frac{2}{3}$ usually used for freely rotation dyes can be obtained as the average of this distribution.

$$\rho(\kappa^2) = \begin{cases} \frac{1}{2\sqrt{3}\kappa^2} \ln(2 + \sqrt{3}) & 0 \leq \kappa^2 < 1 \\ \frac{1}{2\sqrt{3}\kappa^2} \ln\left(\frac{2+\sqrt{3}}{\sqrt{\kappa^2+\sqrt{\kappa^2-1}}}\right) & 1 \leq \kappa^2 \leq 4 \end{cases} \quad (2.202)$$

The average value $\langle \kappa^2 \rangle$ is calculated as the expectation value of the isotropic transition

dipole moment distribution

$$\langle \kappa^2 \rangle = \int_0^4 \kappa^2 \rho(\kappa^2) d\kappa^2 = \frac{2}{3} \quad (2.203)$$

2.4.5 Monomer transition density approach

The monomer transition density approach (MTD) is a method developed by Fink et al. [26, 27] for the computation of the ECME on the basis of spinless reduced one-electron transition density matrices of the exciton donor and the exciton acceptor. In contrast to the IDA, where the ECME is reduced to an interaction between two transition dipoles, the MTD is a more sophisticated method considering the whole transition densities. The method approximates the supermolecular wave function of the dimer as product of the monomer wave functions. Since antisymmetrization is neglected in the original version, the ECME reduces to the Coulomb contribution as given in Eq. 2.173.

$$V_{DA} \approx J_{DA} = \int \frac{P^{(D)}(\vec{r}_1) P^{(A)}(\vec{r}_2)}{\vec{r}_{12}} d\vec{r}_1 d\vec{r}_2 \quad (2.204)$$

Expanding the transition densities in terms of spatial MOs yields

$$J_{DA} = \int \frac{(\sum_{ij} P_{ij}^{(D)} \cdot \psi_i^*(\vec{r}_1) \psi_j(\vec{r}_1)) \cdot (\sum_{kl} P_{kl}^{(A)} \cdot \psi_k^*(\vec{r}_2) \psi_l(\vec{r}_2))}{\vec{r}_{12}} d\vec{r}_1 d\vec{r}_2 \quad (2.205)$$

$$= \sum_{ij} \sum_{kl} P_{ij}^{(D)} P_{kl}^{(A)} \int \psi_i^*(\vec{r}_1) \psi_j(\vec{r}_1) \cdot r_{12}^{-1} \cdot \psi_k^*(\vec{r}_2) \psi_l(\vec{r}_2) d\vec{r}_1 d\vec{r}_2 \quad (2.206)$$

where the indices i, j, k and l run over all donor and acceptor occupied and virtual orbitals. Using the definition of two-electron integrals in Mulliken notation,

$$(ij|kl) = \int \psi_i^*(\vec{r}_1) \psi_j(\vec{r}_1) \cdot r_{12}^{-1} \cdot \psi_k^*(\vec{r}_2) \psi_l(\vec{r}_2) d\vec{r}_1 d\vec{r}_2 \quad (2.207)$$

the ECME becomes

$$J_{DA} = \sum_{ijkl} P_{ij}^{(D)} P_{kl}^{(A)} (ij|kl) \quad (2.208)$$

The exchange contribution can be introduced by analogy to Eq. 2.123 [71, 34]

$$K_{DA} = -\frac{1}{2} \sum_{ijkl} P_{ij}^{(D)} P_{kl}^{(A)} (il|kj) \quad (2.209)$$

2.4.6 Supermolecular transition density approach: Consideration of CT contributions

At small intermolecular distances and in the presence of a molecular linker, the CT contributions to the ECME cannot be neglected. Unfortunately, the MTD approach only considers interactions between local transitions (direct contributions). The newly developed STD approach can be understood as extension of the MTD approach to CT transitions (indirect contributions) (Fig. 2.8). In the following, a novel method based on the supermolecular spin-free reduced one-electron matrices of the interacting electronically excited states is presented.⁵ Since the method does no longer require an artificial separation of donor and acceptor treated as isolated molecules, a further enhancement of the description of the direct contribution can be obtained at small intermolecular distances. The method is closely related to the TDFI-TI (transition-density-fragment interaction combined with transfer integral) method introduced by Fujimoto. [34, 35] In contrast to TDFI-TI, our method is not based on a subsystem formalism and is not restricted to a four-orbital–four-electron model considering the indirect contributions.

In a hypothetical biorthonormal subsystem-localized orbital basis, the wave functions of the initial and final states can be divided into two local and two CT contributions. This subdivision can be looked upon as a decomposition of the states into individual “substates”

$$|\Psi_I\rangle = |D^*A\rangle_I + |DA^*\rangle_I + |D^+A^-\rangle_I + |D^-A^+\rangle_I \quad (2.210)$$

$$\langle\Psi_F| = {}_F\langle DA^*| + {}_F\langle D^*A| + {}_F\langle D^+A^-| + {}_F\langle D^-A^+| \quad (2.211)$$

where the first term in expression (2.210), describing local excitations on D in the initial state $|\Psi_I\rangle$, and the first term in expression (2.211), describing local excitations on A in the final state $\langle\Psi_F|$ are expected to be dominant, respectively. To calculate the total ECME $\langle\Psi_F|\hat{\mathcal{V}}|\Psi_I\rangle$, all four “substates” of the final state have to be combined with all four “substates” of the initial state yielding 16 terms in total. ${}_F\langle D^*A|\hat{\mathcal{V}}|D^*A\rangle_I$ and ${}_F\langle DA^*|\hat{\mathcal{V}}|DA^*\rangle_I$ do not contribute to the ECME because they describe the interaction between two local excitons on the same subsystem, such that 14 coupling terms remain in

⁵The new method has already been presented in ref. [63]

total:

$$\langle \Psi_F | \hat{\mathcal{V}} | \Psi_I \rangle = \underbrace{{}_F \langle DA^* | \hat{\mathcal{V}} | D^* A \rangle_I + {}_F \langle D^* A | \hat{\mathcal{V}} | DA^* \rangle_I}_{V_{Dir}} \quad (2.212)$$

$$+ \underbrace{{}_F \langle D^+ A^- | \hat{\mathcal{V}} | D^- A^+ \rangle_I + {}_F \langle D^- A^+ | \hat{\mathcal{V}} | D^+ A^- \rangle_I}_{V_{CT}} \quad (2.213)$$

$$+ {}_F \langle D^+ A^- | \hat{\mathcal{V}} | D^* A \rangle_I + {}_F \langle D^- A^+ | \hat{\mathcal{V}} | D^* A \rangle_I \\ + {}_F \langle D^+ A^- | \hat{\mathcal{V}} | DA^* \rangle_I + {}_F \langle D^- A^+ | \hat{\mathcal{V}} | DA^* \rangle_I \\ + {}_F \langle D^* A | \hat{\mathcal{V}} | D^- A^+ \rangle_I + {}_F \langle DA^* | \hat{\mathcal{V}} | D^- A^+ \rangle_I \quad (2.214)$$

$$+ \underbrace{{}_F \langle D^* A | \hat{\mathcal{V}} | D^+ A^- \rangle_I + {}_F \langle DA^* | \hat{\mathcal{V}} | D^+ A^- \rangle_I}_{V_{Pol}} \\ + \underbrace{{}_F \langle D^+ A^- | \hat{\mathcal{V}} | D^+ A^- \rangle_I + {}_F \langle D^- A^+ | \hat{\mathcal{V}} | D^- A^+ \rangle_I}_{V_{Corr}} \quad (2.215)$$

The first two terms have been combined into V_{Dir} which describes the direct interactions between locally excited configurations. V_{CT} represents the interactions between two CT configurations that arise from an electron transfer from D to A and from A to D , respectively. The polarization term V_{Pol} is composed of eight mixed couplings between local and CT excitations. Finally, a correlation term V_{Corr} has been defined which represents the coupling between CT configurations of the same type. In a microscopic representation involving the reduced transition density matrices and two-electron integrals in the hypothetical biorthonormalized MO basis, the matrix element ${}_F \langle D^* A | \hat{\mathcal{V}} | DA^* \rangle_I$ reads

$${}_F \langle D^* A | \hat{\mathcal{V}} | DA^* \rangle_I = \sum_{i \in D} \sum_{a \in D} \sum_{j \in A} \sum_{b \in A} \rho_{ia}^{(F)} \rho_{jb}^{(I)} [(ai|jb) - \frac{1}{2}(ab|ji)] \quad (2.216)$$

corresponding to the well-known expression for the Förster and Dexter exchange contributions in the MTD approach [34, 26, 27].

The use of a biorthogonalized MO basis can be avoided if the AO basis is employed instead. In the following, greek letters label the AOs whereas roman letters denote the MOs which may be delocalized over the whole supermolecular system ($i, j, a, b \in DA$). Expressing the two-electron integrals in terms of the AO basis and the MO coefficients

$$(ai|jb) = \sum_{\mu} \sum_{\nu} \sum_{\lambda} \sum_{\sigma} c_{\mu i} c_{\lambda j} c_{\nu a} c_{\sigma b} (\nu \mu | \lambda \sigma) \quad (2.217)$$

Eq. (2.216) can be rewritten as [62]

$${}_F \langle D^* A | \hat{\mathcal{V}} | DA^* \rangle_I = \sum_{i \in DA} \sum_{a \in DA} \sum_{j \in DA} \sum_{b \in DA} \sum_{\mu \in D} \sum_{\nu \in D} \sum_{\lambda \in A} \sum_{\sigma \in A} \rho_{ia}^{(F)} \rho_{jb}^{(I)} c_{\mu i} c_{\lambda j} c_{\nu a} c_{\sigma b} [(\nu \mu | \lambda \sigma) - \frac{1}{2} (\nu \sigma | \lambda \mu)] \quad (2.218)$$

Transforming the reduced transition density matrices of the initial and the final state to the AO basis [62, 34, 64]

$$\rho_{\mu\nu}^{(F)} = \sum_{i \in DA} \sum_{a \in DA} c_{\mu i} c_{\nu a} \rho_{ia}^{(F)} \quad (2.219)$$

$$\rho_{\lambda\sigma}^{(I)} = \sum_{j \in DA} \sum_{b \in DA} c_{\lambda j} c_{\sigma b} \rho_{jb}^{(I)} \quad (2.220)$$

yields the final expression

$${}_F \langle D^* A | \hat{\mathcal{V}} | DA^* \rangle_I = \sum_{\mu \in D} \sum_{\nu \in D} \sum_{\lambda \in A} \sum_{\sigma \in A} \rho_{\mu\nu}^{(F)} \rho_{\lambda\sigma}^{(I)} [(\nu \mu | \lambda \sigma) - \frac{1}{2} (\nu \sigma | \lambda \mu)] \quad (2.221)$$

Similar formulae can be derived for the other 13 coupling matrix elements which only differ in the subsystems over which the indices μ , ν , λ and σ run.

2.5 Förster theory

The Förster theory is a formalism which allows the determination of the intermolecular distance X between the exciton donor and the exciton acceptor directly from the experimentally measured donor fluorescence intensity. [7, 8] In the framework of the Förster theory, EET is termed FRET (Fluorescence / Förster Resonant Energy Transfer). The FRET rate follows a Golden rule expression, where the ECME is given in Condon approximation (see Sec. 2.2.2)

$$k_{FRET} = \frac{2\pi}{\hbar} |V_{DA}|^2 \sum_{M,N} \sum_{K,L} f_{D^*N} f_{AK} \cdot |\langle \chi_{D^*N} | \chi_{DM} \rangle|^2 \cdot |\langle \chi_{AK} | \chi_{A^*L} \rangle|^2 \times \delta(E_{D^*N} + E_{AK} - E_{DM} - E_{A^*L}) \quad (2.222)$$

Using the IDA for expressing the ECME (see Sec. 2.4.4)

$$V_{DA} = \kappa \cdot \frac{|\vec{\mu}_D| \cdot |\vec{\mu}_A|}{|\vec{X}|^3} \quad (2.223)$$

the rate constant reads

$$k_{FRET} = \frac{2\pi\kappa^2 |\vec{\mu}_D|^2 |\vec{\mu}_A|^2}{\hbar |\vec{X}|^6} \sum_{M,N} \sum_{K,L} f_{D^*N} f_{AK} |\langle \chi_{D^*N} | \chi_{DM} \rangle|^2 |\langle \chi_{AK} | \chi_{A^*L} \rangle|^2 \times \delta(E_{D^*N} + E_{AK} - E_{DM} - E_{A^*L}) \quad (2.224)$$

Using

$$\begin{aligned} \int_{-\infty}^{\infty} \delta(E_{D^*N} - E_{DM} - \hbar\omega) &\times \delta(E_{AK} - E_{A^*L} + \hbar\omega) \, dE \\ &= \delta(E_{D^*N} + E_{AK} - E_{DM} - E_{A^*L}) \end{aligned} \quad (2.225)$$

and substituting the donor emission spectrum

$$I_D(\omega) = \frac{4\omega^3}{3c^3} |\vec{\mu}_D|^2 \sum_{M,N} f(E_{D^*N}) |\langle \chi_{D^*N} | \chi_{DM} \rangle|^2 \times \delta(E_{D^*N} + E_{DM} - \hbar\omega) \quad (2.226)$$

as well as the acceptor absorption coefficient

$$\alpha_A(\omega) = \frac{4\pi^2 \omega n_{mol}}{3\hbar c} |\vec{\mu}_A|^2 \sum_{K,L} f(E_{AK}) |\langle \chi_{AK} | \chi_{A^*L} \rangle|^2 \times \delta(E_{AK} + E_{A^*L} + \hbar\omega) \quad (2.227)$$

into Eq. 2.226, the EET rate becomes [72]

$$k_{FRET} = \frac{9c^4}{8\pi n_{agg}} \cdot \frac{\kappa^2}{|\vec{X}|^6} \cdot \int_0^{\infty} I_D(\omega) \cdot \alpha_A(\omega) \cdot \omega^{-4} \, d\omega \quad (2.228)$$

where n_{mol} and n_{agg} are the volume densities ($n = N/V$) of the absorbing and aggregate molecules, respectively. Note that the spectral overlap integral covers the absolute values of the interacting transition dipole moments which are parts of the ECME and therefore differs from the spectral overlap integral introduced in Sec. 2.2.3.⁶ It should clearly be stated that the spectral overlap integral is not the area enclosed by the two spectra and the coordinate system, but the integral over the product of the two spectra. [72]

Since free rotation of the dyes is assumed ($\kappa^2 = \frac{2}{3}$) and the spectral overlap integral is a constant for a given pair of dyes, Förster was able to provide an expression for the EET rate which solely depends on the length of the intermolecular distance vector.

$$k_{FRET} \propto X^{-6} \quad (2.229)$$

The FRET efficiency E is a value between 0 and 1 defined as the ratio of the FRET rate and all donor decay rates

$$E = \frac{k_{FRET}}{k_{FRET} + k_{fl} + k_{rl}} \quad (2.230)$$

where k_{fl} is the donor fluorescence rate and k_{rl} relates to the radiationless decay of the donor exciton. Neglecting radiationless processes, the FRET efficiency can be obtained

⁶To calculate the spectral overlap integral in practice, the acceptor absorption spectrum is normalized to the intensity of the absorption maximum and weighted by the molar absorption coefficient ($M^{-1}cm^{-1}$) while the donor fluorescence spectrum is normalized to unit area (dimensionless). Therefore, the quantity is given in units of $M^{-1}cm^{-1}nm^4$ if a nm energy scale is used.

from the ratio of the intensities of the donor fluorescence in the target donor acceptor system (I_{DA}) and the isolated donor (I_D).

$$E = 1 - \frac{I_{DA}}{I_D} \quad (2.231)$$

The Förster radius R_F is defined as the donor acceptor distance for which the FRET efficiency E reduces to 0.5. The quantity can be obtained from the spectral overlap integral and the donor fluorescence quantum yield and is listed for all typical pairs of FRET dyes. [73] Therefore, the donor acceptor distance can directly be calculated from the donor fluorescence intensity.

$$E = \frac{1}{1 + \frac{R_F^6}{X^6}} \quad (2.232)$$

$$X = R_F \cdot \left(E^{-1} - 1 \right)^{-\frac{1}{6}} \quad (2.233)$$

$$X = R_F \cdot \left\{ \left(1 - \frac{I_{DA}}{I_D} \right)^{-1} - 1 \right\}^{-\frac{1}{6}} \quad (2.234)$$

Since the Förster theory is based on the IDA, which does neither consider exchange nor CT contributions it is valid only for medium to large distances (30-80 Å) [9].

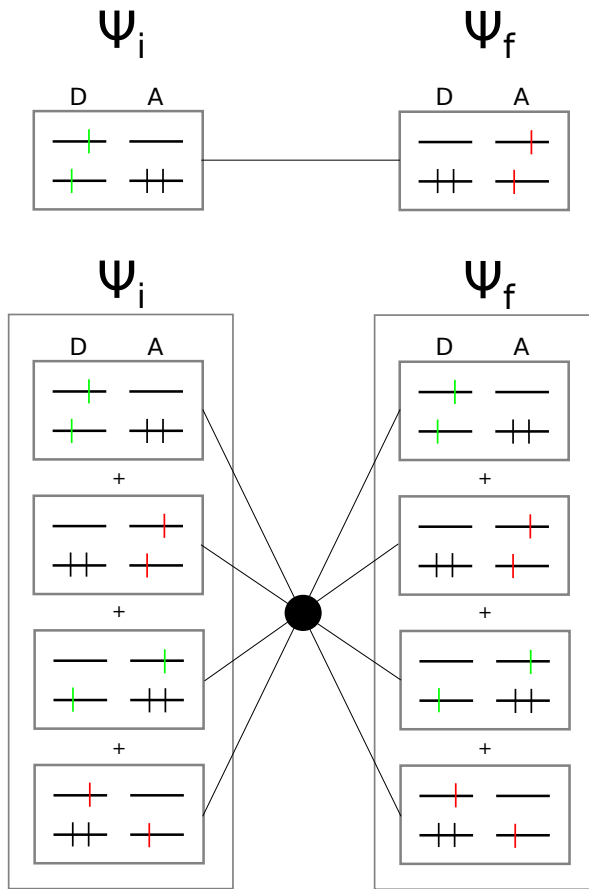


Figure 2.8: Schematic comparison of the MTD (top) and the STD approach (bottom) using a four-electron-four-orbital model. While in the MTD approach the interacting wave functions of the initial and final states are composed of local transitions on the donor (D) and the acceptor (A), respectively, the wave functions comprise CT transitions from D to A and vice versa in the STD approach. To obtain the total ECME each combination of transitions has to be considered.

Chapter 3

Implementations

All programs developed in the course of this work have been assembled in the Excitation Energy Transfer Kit (ExETraK) (Fig. 3.1). The code was specially devised for the theoretical study of heterodimeric molecular systems. At the moment the program suite provides routines for the computation of the singlet-singlet ECMEs and EET rates on the basis of monomer and supermolecule-based approaches. All implementations are adapted to the DFT/MRCI code developed by Grimme and Waletzke and extended by Lyskov et al. [46, 75]. The program package can be divided into six FORTRAN programs containing the main code and various BASH-scripts ensuring an automation of certain calculations. In the following, a brief overview of the major modules and their functionality will be given.

Foerster. Calculations of the ECME according to the IDA are carried out with the foerster program. The cartesian components of the transition dipole moment vectors of the two interacting excited states as well as the corresponding molecular geometries are required as input. Due to the general structure of the input, the program is not explicitly restricted to the DFT/MRCI program. The donor acceptor intermolecular distance is calculated as distance between the centers of mass according to the molecular geometries. The program is able to ignore atoms which are marked as dummy atoms in the coordinates file. In addition to the ECME the non-squared orientation factor κ is provided which is computed on the basis of the absolute values of the transition dipole moment vectors as well as the corresponding unit vectors defined in Eqs. 2.193-2.194.

Freck. This module is the core of the ExETraK package providing the ECME between two excited singlet states according to the MTD and the STD approaches. The program requires the spin-free reduced one-electron transition densities of the interacting states in the basis of spatial molecular orbitals as computed by the DFT/MRCI program. Further-

more, the program requires the two-electron integrals of the recomposed supermolecular system in the resolution of the identity (RI) approximation (see mergefrag) and the overlap matrix of the atomic orbital (AO) basis if a transformation from the MO to the AO basis is necessary. At the moment three calculation modes are offered: an MTD calculation in the MO basis, an MTD calculation in the AO basis (devised mainly for benchmark calculations) and an STD calculation in the AO basis.

MTD calculations: The freck program provides the possibility to carry out full MTD calculations according to Eqs. 2.208 and 2.209 including Coulomb and exchange contributions. Since the calculation time drastically increases with the number of basis functions, the code has been parallelized using the message passing interface (MPI). A further speed-up was obtained by freezing core and anti-core orbitals which are not considered in the MTD calculation. If the exchange contribution is neglected, the main loop running over the orbitals i , j , k and l can be reduced considering identical combinations. Nevertheless, due to the high computational cost, the method is still inefficient compared to the IDA. Therefore, an algorithm has been developed, which drastically reduces the calculation time from days to minutes. A plot of the transition density matrices reveals that most of the $N \times N$ matrix elements are zero or negligibly small (Fig. 3.2). The algorithm "pre-scans" both transition density matrices to ensure that only orbitals referring to matrix elements with an absolute value above a certain threshold are considered in the main loop. To carry out an MTD calculation with freck program, the supermolecular system has to be split into two individual subsystems that are treated in two individual quantum chemical calculations providing the transition densities. The two-electron integrals are obtained from an artificially recomposed system with the MOs of the subsystems. If the target system is composed of covalently linked donor and acceptor systems, a bond has to be split in a homolytical manner and has to be saturated with hydrogen atoms.

STD calculations: The newly developed STD approach according to Eqs. 2.212-2.215 has also been implemented to the freck program. At the moment the code is not optimized such that the calculations are very time consuming. A possibility to freeze core and anti-core orbitals and a "pre-scan" of the transition densities has not yet been implemented. In comparison to the MTD approach, the ECME calculation is directly based on a single quantum chemical calculation of the supermolecular arrangement of donor and acceptor. By this means, the problem of the artificially isolated subsystems in the MTD approach can be overcome since the interaction between the two subsystems is directly considered within the MOs and therefore within the transition densities. Since the calculation is performed in the AO basis, there is no need to split a covalent bond. The border between donor and acceptor moiety can simply be defined by an atom number.

Mergefrag. This program is responsible of creating the recomposed structure including the set of MOs in the case of an MTD calculation. In the MTD approach, the supermolecular system of donor and acceptor is artificially separated into an isolated donor and an isolated acceptor which are treated in individual quantum chemical calculations. In order to calculate the two-electron integrals ($ij|kl$) (Coulomb contribution) and ($il|kj$) (exchange contribution) connecting the two subsystems, the set of the supermolecular MOs is assumed to be composed of the sets of MOs of the isolated subsystems. Therefore, the monomer MOs are arranged in blocks with coefficients equal to zero on the other subsystem. To control the size of the integral file, the program takes care of orbital freezing and can be used for the "pre-scan" of the transition densities considering only orbitals that refer to non-zero matrix elements.

Aointprep. This tool is needed for the computation of two-electron integrals in the RI-approximation if the AO basis has to be used. A faked set of MOs each representing a single AO is created such that the integral calculation can be performed with the **ritraf** program which is part of the DFT/MRCI suite. The program ritraf is devised for the computation of two-electron integrals in the MO basis. Therefore, the orbitals have to pass an orthogonality check. This check is performed by calculating the number of electrons N from the trace of the product of the charge density matrix P and the overlap matrix S

$$N = \sum_i (PS)_{ii} \quad (3.1)$$

and compares it to the number of electrons deduced from the orbital occupation numbers as defined in the calculation settings. In the case of a deviation, the program aborts. The charge density matrix and the overlap matrix are defined as

$$P_{\mu\nu} = \sum_i^{N/2} c_{\mu i} \cdot c_{\nu i} \quad (3.2)$$

$$S_{\mu\nu} = \langle \mu | \nu \rangle \quad (3.3)$$

where $c_{\mu i}$ and $c_{\nu i}$ are expansion of the i -th MO in the AO basis $\{\mu\}$. The procedure provides a fast and efficient way for checking the orthogonality of a set of MOs. However, in the special case in which each MO is represented by a single AO

$$c_{\mu i} \begin{cases} 1 & \mu = i \\ 0 & \mu \neq i \end{cases} \quad (3.4)$$

the method fails and detects the correct number of electrons although the AO basis is not orthogonal. To explain the issue, the example of an arbitrary molecular system with 6 electrons is taken which is described in a basis of 5 AOs. Since each MO is doubly occupied in a closed-shell system, the number of occupied MOs is 3. According to Eq. 3.2 all diagonal elements of the charge density matrix for $\mu = \nu = i$ are equal to 2 while all other diagonal and off-diagonal elements are zero.

$$P = \begin{pmatrix} 2 & & & & \\ & 2 & 0 & & \\ & & 2 & & \\ & 0 & 0 & & \\ & & & & 0 \end{pmatrix} \quad (3.5)$$

The AO basis is non-orthogonal. Therefore, the off-diagonal elements of the overlap matrix are non-zero.

$$S = \begin{pmatrix} 1 & & & & \\ & 1 & & \neq 0 & \\ & & 1 & & \\ & \neq 0 & & 1 & \\ & & & & 1 \end{pmatrix} \quad (3.6)$$

Multiplication of both matrices yields a matrix with the first three diagonal elements equal to 2 and non-zero off-diagonal elements.

$$DS = \begin{pmatrix} 2 & & & & \\ & 2 & & \neq 0 & \\ & & 2 & & \\ & \neq 0 & & 0 & \\ & & & & 0 \end{pmatrix} \quad (3.7)$$

The trace of DS is 6 and therefore in compliance with the number of electrons of the molecule although the set of (fake) MOs is non-orthogonal. For this reason, the ritraf program can directly be used for the calculation of the two-electron integrals in the AO-basis without any modification.

Overlap. This program allows the computation of the spectral overlap integral defined in Eq. 2.61 on the basis of the vibrationally resolved donor emission and acceptor absorption spectra created with this VIBES program. The program takes care for a proper normalization of both spectra and calculates the product function which is numerically integrated using the trapezoidal rule to obtain the spectral overlap.

Align. The program is responsible for the alignment of molecular structures according to the minimum RMSD applying a quaternion-based algorithm developed by Coutsias et al. [76] The working principle of the algorithm has been revised in the supporting information of ref. [77] (see Sec. 4.2). The intention was to provide a tool which makes molecular structures obtained from molecular dynamics (MD) simulations accessible to a quantum chemical calculation of the ECME. An alignment of the MD-based structure with the relaxed ground state structures of the two dyes prevents a relaxation of the MD structure. Furthermore, the new MO coefficients, adapted to the new orientation of the molecule in the coordinate system, can simply be obtained by a rotation matrix. By this means, a recomputation of transition density matrices is circumvented, drastically reducing the computational cost.

Edbc. This program is a tool for the analysis of the transition densities in dimeric systems and uses a method developed by Lischka and Plasser which was reviewed in Sec. 2.3.9. The method provides a measure for contributions of local and CT transitions of an excited singlet state in terms of a 2×2 matrix. Before the STD approach is chosen for the calculation of the ECME, one has to define which supermolecular states correspond to the bright monomer states. The edbc program provides valuable information helping to identify CT states and states which are predominately centered on certain moieties of the supermolecule. At the moment, the program is restricted to molecular dimers but can in principle be extended to an arbitrary number of subsystems.

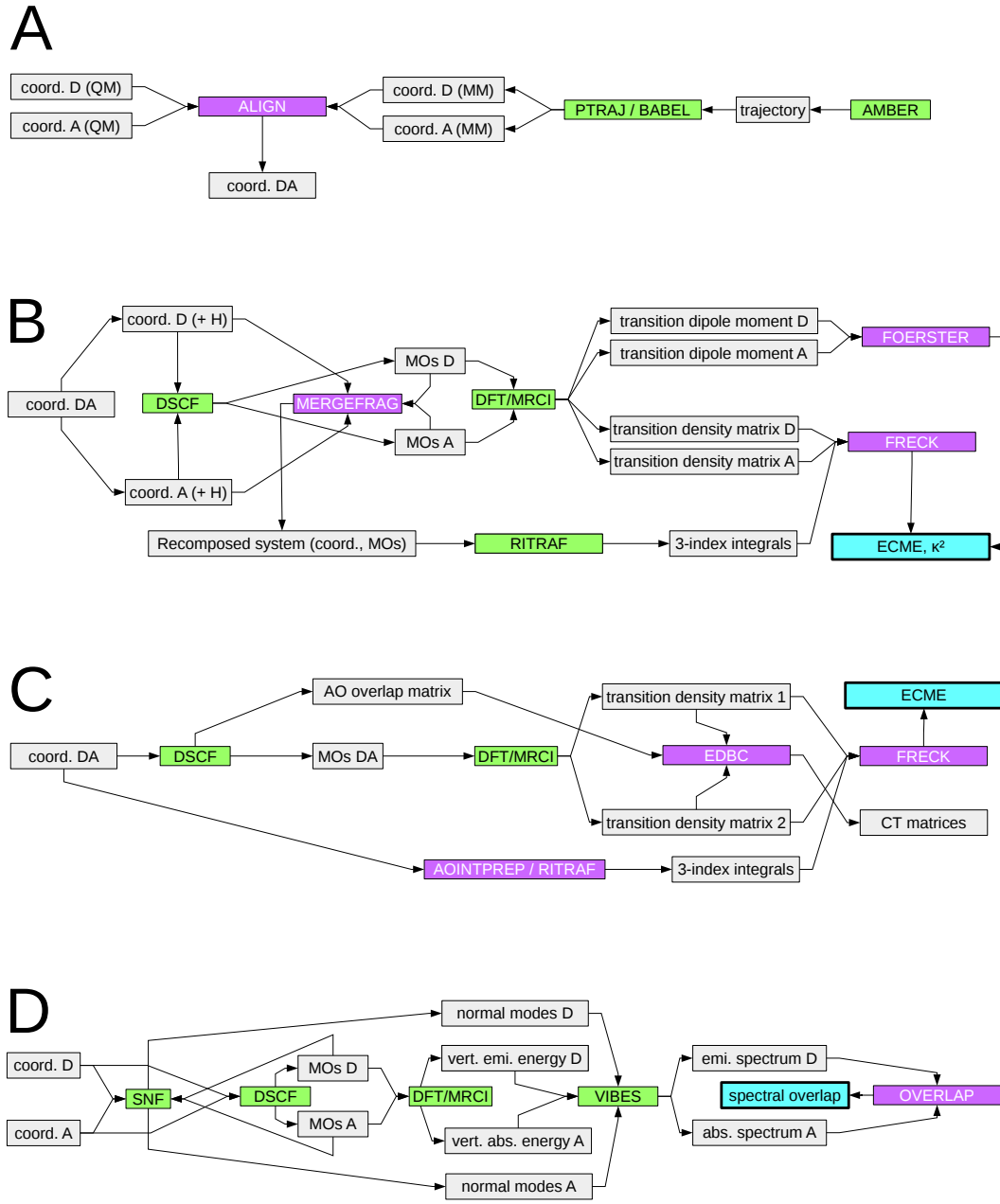


Figure 3.1: Implementation schemes of the main modules of the ExETraK program package. Newly devised programs are highlighted in purple. A: Connection of the AMBER suite [74], B: Implementation of the monomer-based IDA and MTD approaches, C: Implementation of the supermolecule-based STD approach, D: Calculation of the spectral overlap integral.

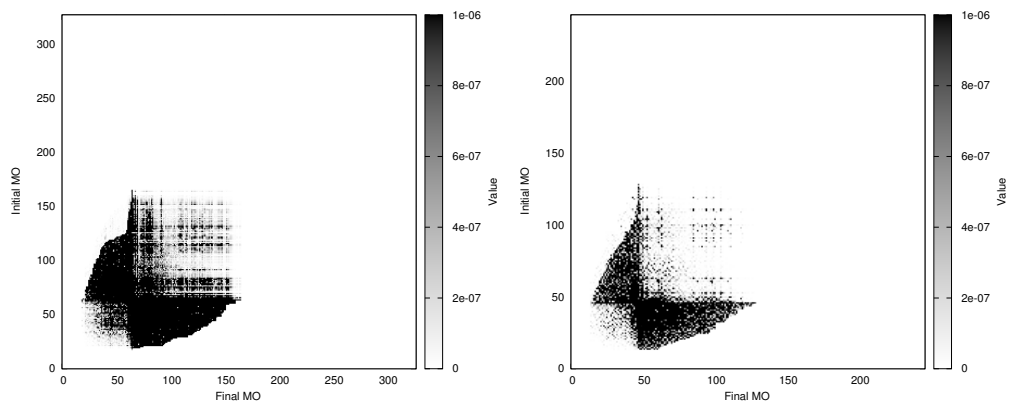


Figure 3.2: Graphical representation of the $S_0 \rightarrow S_1$ transition density matrices of BOD-IPY (l.h.s.) and anthracene (r.h.s.) using the absolute values of the matrix elements. The black areas represent the parts of the transition density matrices with absolute values larger than 2.0×10^{-7} a.u. All other matrix elements are negligibly small and therefore do not contribute to the ECME. Since less than one third of the total areas of the plots is black, the MTD calculation can be accelerated extremely by neglecting all matrix elements in the white areas.

Chapter 4

Results and discussion

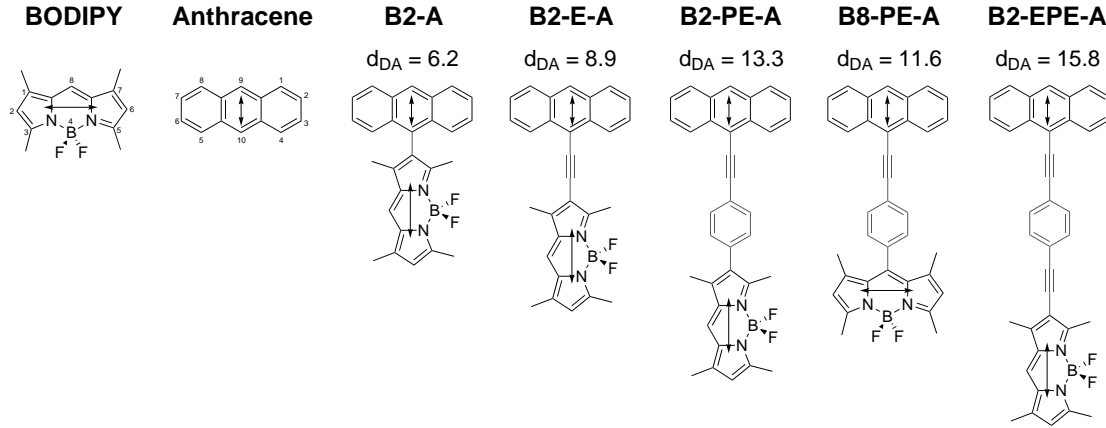
All results have already been published in different scientific journals (refs. [63, 77, 78]). In the following, the thematic connection including brief reviews of the major objectives and results will be presented.

4.1 BODIPY/anthracene-based EET cassettes

4.1.1 Direct contribution and the role of the molecular linker

In the first publication [78] the implementation of the ideal dipole approximation (IDA) and the monomer transition density (MTD) [26, 27] approach adapted to the DFT/MRCI code [46] was reported. The main objective was the investigation of five experimentally well studied EET cassettes [21, 22, 79] composed of anthracene as exciton donor and BODIPY as exciton acceptor (Fig. 4.1). The study particularly focuses on the role of the π -conjugated molecular linker differing in length and chemical structure. In order to distinguish between *through-space* and *through-bond* EET, two fragmentation models [38] were used completely neglecting or assigning the linker to the donor moiety of the system (Fig. 4.2). Since the methods are restricted to the direct contribution of the ECME, possible CT contributions could not be taken into account. The calculated ECMEs of the different EET cassettes and fragmentation models were used to compute the EET rates. The spectral overlap integral required for this purpose was obtained from the calculated vibrationally resolved donor fluorescence and acceptor absorption spectra which were considered either unshifted or shifted according to the location of the BODIPY and anthracene absorption maxima of appropriate supermolecular calculations (Fig. 4.3). Comparing the IDA to the more sophisticated MTD approach using an ethylene-dimer as benchmark model system, we find a better agreement of the MTD approach with the exact coupling obtained from the Davydov splitting at small intermolecular distances ($\leq 10 \text{ \AA}$). Disregarding the molecular linker in the EET cassettes leads to an underestimation of the

Figure 4.1: Nomenclature and chemical structure of studied EET cassettes. $S_0 \rightarrow S_1$ transition dipole moments of BODIPY and anthracene are indicated as arrows. Distances between the centers of mass are given in (Å).

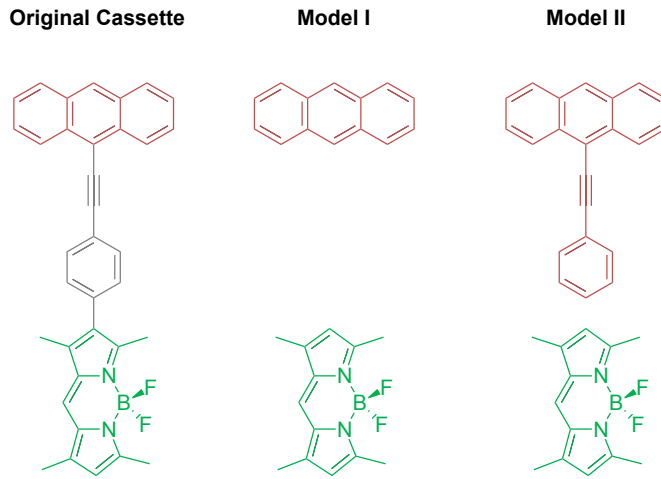


ECME and therefore of the EET rates. This effect gains in importance with increasing size of the linker. If the linker was assigned to the donor moiety of the cassettes, the experimentally observed EET rates of $\geq 5.0 \times 10^{-12} \text{ s}^{-1}$ [21] could fairly be reproduced. In one of the EET cassettes the transition dipole moments of donor and acceptor were perfectly perpendicularly oriented in the relaxed ground state geometry causing a vanishing EET rate although the experimentally observed EET rate is in the range of ps^{-1} . By the means of short *ab initio* molecular dynamics (MD) simulations it could be shown that a static description of the EET system is insufficient in this case. While the ECME almost does not change in the case of parallel transition dipole moments, only slight deviations from a perfectly perpendicular orientation cause a significantly non-zero ECME. An overview of the most important results is given in Tab. 4.1.

4.1.2 Charge transfer contributions

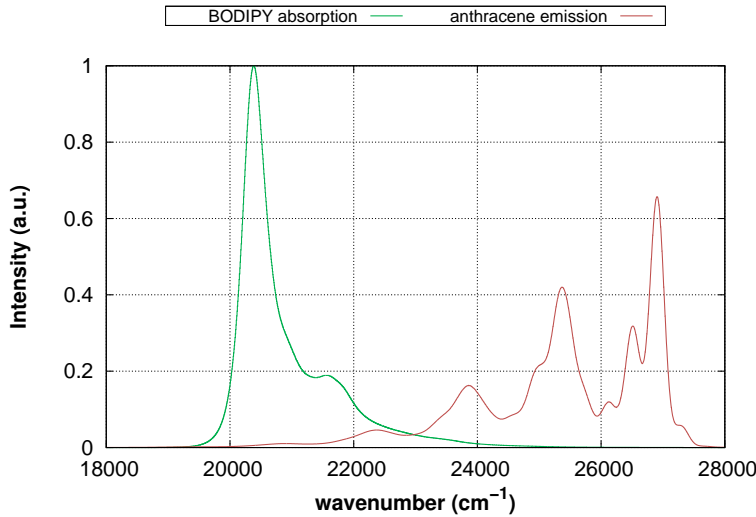
While the consideration of the ECME was restricted to direct contributions in the first publication, indirect contributions were the main focus of the second publication. [63] For this purpose, a new supermolecular transition density (STD) based method was developed which can be understood as an extension of the MTD method to CT excitations. In the STD approach, the transition densities of the interacting electronically excited states of the supermolecule are used instead of the transition densities of the isolated monomers. In the AO basis, this leads to block matrices where the diagonal blocks represent local excitations centered on the donor or the acceptor moiety, respectively, and the off-diagonal blocks represent CT excitations between the moieties. The total effective ECME is related

Figure 4.2: Fragmentation models developed to calculate the EC in the studied EET cassettes using the example of B2-PE-A. According to model I the linker is completely removed from the relaxed ground-state structure. Model II tries to approximate the influence of the molecular structure of the linker on the EC assigning the latter to the donor moiety. In both models the obtained fragments are saturated with hydrogen atoms and the newly created C-H bond were relaxed keeping the rest of the molecule fixed.



to the different combinations of transition density matrix blocks of the two interacting states yielding 14 coupling terms in total. The validity of the approach is assessed for a model system of two π -stacked ethylene molecules at varying intermolecular separation. Using a four-electron-four-orbital model and allowing only single excitations yields only four possible electronically excited states – two Frenkel and two CT excited states. It has to be mentioned that in the case of the ethylene dimer the electronic states are not localized. At large intermolecular separations, the two lowest-lying states correspond to positive and negative linear combinations of pure local excitations on monomer A and B, respectively, i.e. $A^*B \pm AB^*$ (Frenkel states). Likewise, the two higher-lying states are positive and negative linear combinations of the ionic terms A^+B^- and A^-B^+ , respectively, (CT states). The computed couplings were compared with the MTD approach and the energetic splitting between the appropriate adiabatic states. As may be seen in Fig. 4.4, STD and MTD results match nearly perfectly for intermolecular separations $> 5 \text{ \AA}$. The analysis of the transition density matrices using the method developed by Plasser and Lischka[43] shows that Frenkel and CT states start mixing at intermolecular separations smaller than approximately 5 \AA . For the upper Frenkel state (II), this is even the case for small intermolecular separations whereas (negative) CT contributions become more and more important for the lower Frenkel state (I) with decreasing intermolecular distance. When compared to the FullQM values, the STD and MTD approaches seemingly overshoot

Figure 4.3: Computed vibrationally resolved anthracene emission and BODIPY absorption spectrum.



at long intermolecular separations. This deviation is traced back to the scaling factor of 0.5682 with which the two-electron integral that couples the two Frenkel excitations is multiplied in the DFT/MRCI-R method [75], thus diminishing the Davydov splitting whereas the corresponding two-electron integrals remain unscaled in the STD and MTD approaches.

Finally, the method was applied to the five EET cassettes already considered in the first publication. For a proper quantum chemical description of the supermolecular systems required for the STD approach, the redesigned DFT/MRCI (DFT/MRCI-R) Hamiltonian developed by Lyskov et al. [75] was chosen. Using the original DFT/MRCI Hamiltonian [46], artificially low-lying excited states in ethylene-tetrafluoroethylene dimers were encountered. [75] This failure can be traced back to unphysically large contributions of four-open shell configurations in the CI expansion. The new Hamiltonian enables a physically reasonable description of molecules which are composed of more than one subsystem which is the case for the studied EET cassettes.

The STD approach overcomes the artificial separation of the subsystems into isolated monomers. At extremely small distances ($\leq 5 \text{ \AA}$) the MTD approach fails due to the missing indirect contributions which are perfectly covered in the STD approach. Irrespective of a systematic red shift, the calculated absorption spectra of the EET cassettes are in good agreement with the experiment if donor, bridge and acceptor are forced in a perfectly perpendicular orientation by symmetry constraints. This procedure is neces-

Table 4.1: Direct and exchange contributions to the EC matrix elements as well as EET rates of the studied EET cassettes calculated with different models.

Cassette		B2-A	B2-E-A	B2-PE-A	B2-EPE-A	B8-PE-A
S_0 geometry (fragmentation model I)						
Spectral overlap integral (cm)		1.06×10^{-5}				
IDA	$ J_{DA} $ (cm $^{-1}$)	983	350	109	63	0.0
	$ J_{DA} $ (cm $^{-1}$)	1141	423	119	67	0.0
MTD	$ K_{DA} $ (cm $^{-1}$)	30.0	3.5	0.0	0.0	0.0
	EET rate (s $^{-1}$)	2.3×10^{13}	3.2×10^{12}	2.6×10^{11}	8.3×10^{10}	4.3×10^0
Acceptor S_0, donor S_1 geometry (fragmentation model I)						
Spectral overlap integral (cm)		1.06×10^{-5}				
	$ J_{DA} $ (cm $^{-1}$)	1140	426	123	69	0.0
MTD	$ K_{DA} $ (cm $^{-1}$)	30.0	3.1	0.0	0.0	0.0
	EET rate (s $^{-1}$)	2.3×10^{13}	3.3×10^{12}	2.8×10^{11}	8.8×10^{10}	2.5×10^0
MD snapshots (fragmentation model I)						
Spectral overlap integral (cm)		1.06×10^{-5}				
MTD	$ J_{DA} $ (cm $^{-1}$)	951	377	114	62	6.9
	EET rate (s $^{-1}$)	2.1×10^{13}	2.8×10^{12}	2.7×10^{11}	7.1×10^{10}	1.62×10^9
S_0 geometry (fragmentation model II, spectral overlap of monomers)						
Spectral overlap integral (cm)		1.06×10^{-5}				
MTD	$ J_{DA} $ (cm $^{-1}$)		1013	766	678	0.0
	$ K_{DA} $ (cm $^{-1}$)		92	27	46	0.0
	EET rate (s $^{-1}$)		1.6×10^{13}	1.0×10^{13}	7.3×10^{12}	9.9×10^2
S_0 geometry (fragmentation model II, adapted spectral overlap)						
Spectral overlap integral (cm)			8.39×10^{-5}	2.46×10^{-4}	1.79×10^{-4}	2.46×10^{-4}
MTD	$ J_{DA} $ (cm $^{-1}$)		1013	766	678	0.0
	$ K_{DA} $ (cm $^{-1}$)		92	27	46	0.0
	EET rate (s $^{-1}$)		8.4×10^{13}	1.6×10^{14}	8.4×10^{13}	1.6×10^4
MD snapshots (frag. model II, adapted spectral overlap)						
Spectral overlap integral (cm)						
MTD	$ J_{DA} $ (cm $^{-1}$)					2.46×10^{-4}
	EET rate (s $^{-1}$)					18
	exp. EET rate[21] (s $^{-1}$)		$> 5.0 \times 10^{12}$			
						1.5×10^{11}
						2.5×10^{12}

sary due to the unsatisfactory description of CT states and long-range interactions by the BHLYP functional [80], for which the DFT/MRCI-R Hamiltonian is parameterized. In π -conjugated systems such as the studied EET cassettes, an almost coplanar orientation of donor, bridge and acceptor leads to an enhanced delocalization of certain frontier MOs throughout the whole system causing a strong mixture of local and CT states. While the vertical excitation energies of the lowest BODIPY-localized states of the almost perpendicular structures are in excellent agreement with the experiment, DFT/MRCI-R fails to properly describe the lowest BODIPY-localized states of the other systems. Here, substantial deviations from a perpendicular orientation lead to an energetic stabilization of the anthracene-to-BODIPY CT state which strongly mixes with the lowest BODIPY-centered state. The interaction of the two states leads to an energetic splitting resulting in a stabilized and a destabilized electronic state, both characterized by local and CT transitions in approximately equal parts and a non-zero oscillator strength. Therefore, the appro-

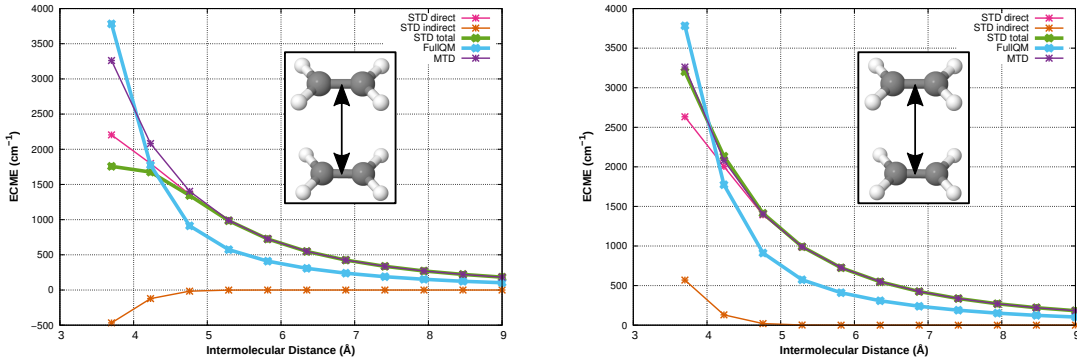


Figure 4.4: Benchmark calculations of the supermolecular transition density approach (STD) of the Frenkel states of the ethylene dimer (left: Frenkel state I, right Frenkel state II). The ECMEs are compared to the Davydov splitting of the coupled states (FullQM) and ECMEs of the monomer transition density approach (MTD). The curve labeled “STD direct” refers to the coupling between all local transitions on monomer A and all local transitions on monomer B while “STD indirect” includes all additional matrix elements.

priate experimental vertical excitation energy of the lowest BODIPY-localized state is significantly underestimated by the stabilized state and overestimated by the destabilized state. The use of symmetry restraints to overcome this problem can be justified by the extremely small rotational barriers suggesting a free rotation at room temperature. In agreement with the experiment [22], the absorption spectra of those compound with an intermediate link to an ethynyl group of the linker, were found to have a stronger red-shift and a broader spectral band shape due to the higher extent of electron delocalization. Neglecting the molecular linker, indirect contributions to the ECME become negligible even for small intermolecular distances such that the total ECME reduces to the direct contribution, which is in excellent agreement with the MTD approach. In the presence of the linker, substantial indirect contributions were found for all EET cassettes which either reinforce or diminish the direct contributions. The latter were generally found to be smaller than those computed with the MTD approach. In one of the EET cassettes, the transition dipole moments of donor and acceptor were perfectly perpendicularly oriented in the relaxed ground state geometry. The STD calculation of the ECME reveals that all direct and indirect coupling matrix elements are zero. This gives rise to the assumption presented in the previous publication that the non-zero EET rate in this cassette is solely caused by dynamic effects. A comparison of the ECME calculated with both MTD and STD is given in Tab. 4.2.

Table 4.2: Composition of the ECME of all P-systems computed using the supermolecular transition density approach (STD) in comparison with the monomer transition density approach (MTD).

Method	P_B2-A	P_B2-E-A	P_B2-PE-A	P_B2-EPE-A	P_B8-PE-A
STD	V _{dir}	944	942	408	216
	V _{CT}	54	109	-93	22
	V _{pol}	59	-62	-110	-23
	V _{corr}	-10	-15	2	-3
	V _{tot}	1047	974	207	212
MTD	V _{dir}	1264	1092	455	346
Method	P_B2(-E-)A	P_B2(-PE-)A	P_B2(-EPE-)A	P_B8(-PE-)A	
STD	V _{dir}		443	137	78
	V _{CT}		17	0	0
	V _{pol}		-1	0	0
	V _{corr}		-12	0	0
	V _{tot}		448	137	78
MTD	V _{dir}		467	134	76

4.2 Distance-dependent validity of IDA-based FRET model

So far, EET has particularly been investigated with respect to only a single geometry of the target system. This "static" consideration is mostly sufficient for rather rigid systems in which small deviations from the minimum geometry do not cause substantial deviations of the ECME. However, the larger a molecular system becomes, the more flexible the system may be. Thus, the importance of dynamic effects in the framework of EET increases. This is especially the case in the framework of FRET experiments aiming to provide information on the structure and dynamics of biophysical systems. In the third publication [77], a computationally efficient method is presented which makes a large number of snapshots obtained from molecular dynamics (MD) simulations accessible to a more sophisticated quantum chemical approach for the computation of the ECME than the IDA. To this end, the relaxed ground-state structures of the exciton donor and exciton acceptor are aligned to each snapshot of the MD trajectory (Fig. 4.5). The rotation matrix leading to the best-fit RMSD is used to transform the set of MOs according to their new orientation in space, which avoids the computationally costly recalculation of the transition densities for each configuration. By this means, the relative orientation can be well represented neglecting the only minor important intramolecular degrees of freedom. The procedure avoids the computationally costly relaxation of the geometry of each snapshot and the recomputation of molecular orbitals and the transition density matrices. Furthermore, a speed-up of the MTD approach could be achieved by considering only those orbitals that lead to non-zero transition density matrix elements. As the IDA is known to fail at small intermolecular distances, the presented study aims at a critical investigation of the IDA-based FRET model

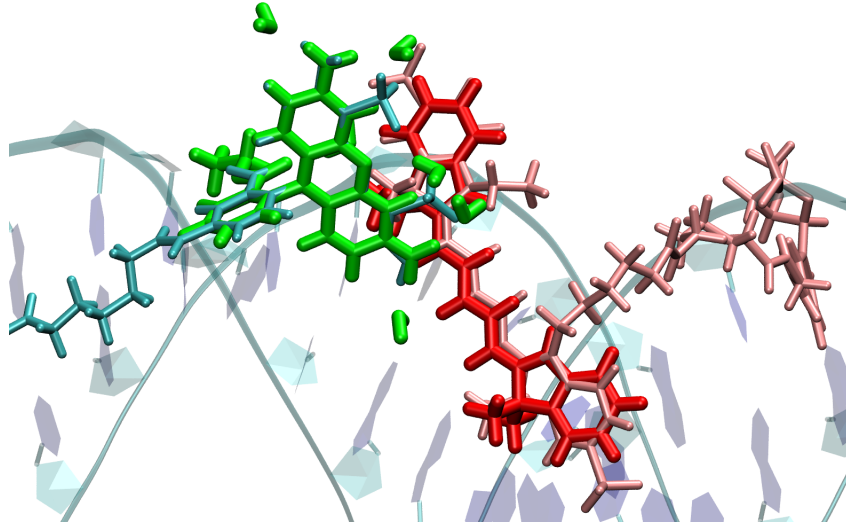


Figure 4.5: Overlay of the simplified and preoptimized structures of Alexa Fluor 488 (green) and Cy5 (red) to an MD snapshot according to the alignment procedure.

considering the deviation between IDA and the more sophisticated MTD approach. To this end, a rigid double-stranded RNA was chosen as model system which was labeled with a pair of FRET dyes at different positions using long and flexible molecular linkers (Fig. 4.6). In all setups, certain positions could be identified where the dyes are preferably located,

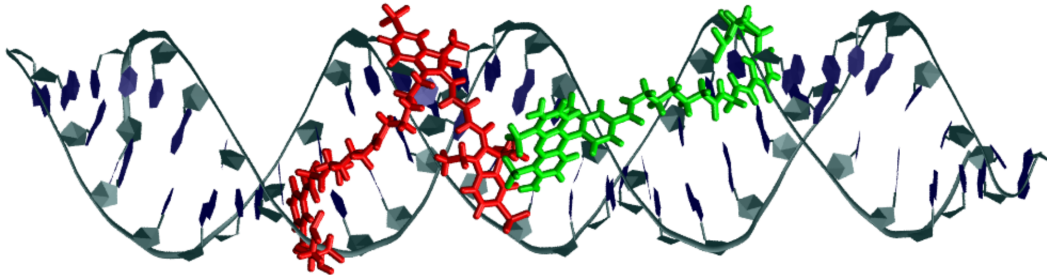


Figure 4.6: Illustration of the studied system composed of a rigid, double-stranded RNA which is labeled by a pair of FRET dyes using long and flexible linkers.

which causes a restriction of the free rotation in space. For two of three studied setups, certain arrangements could be identified in which the dyes stick close to each other at small distances in the range of 7 to 15 Å representing energetically favorable and stable states. For those setups, substantial deviations from a perfectly Gaussian distance distribution and a perfect isotropic distribution of the transition dipoles were found (Fig. 4.7). Within the periods in which the dyes come close to each other, substantial deviations between the

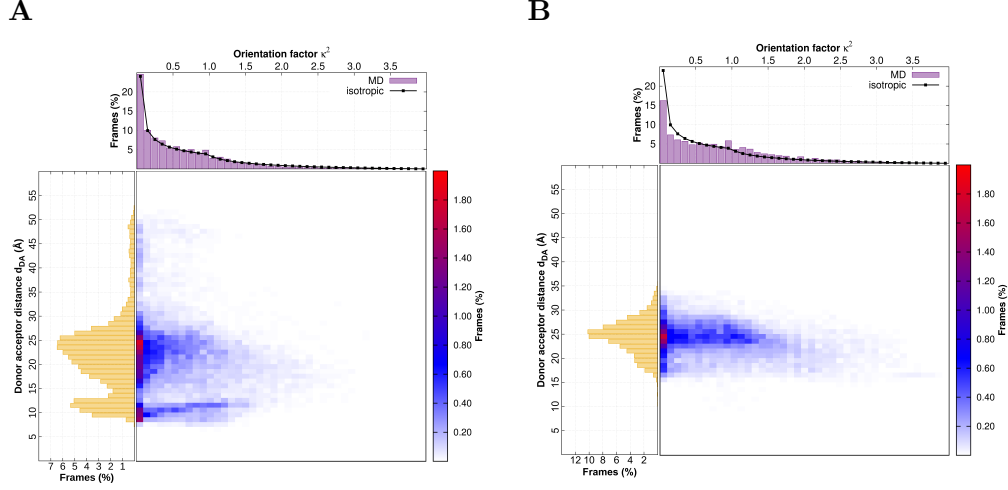


Figure 4.7: Distributions of the donor–acceptor distance and the orientation factor. In the two setups for which the dyes preferably are located in close distance, substantial deviation from a perfectly Gaussian distance distribution and a perfect isotropic distribution of the transition dipoles were found (A). In the third setup, the shapes of the distance and transition dipole distributions are largely preserved (B).

IDA and the MTD were found. Nevertheless, the number of snapshots affected by a large deviation of the IDA represents only a small part of the total trajectories. Thus, they only have a small statistical impact on the time-averaged EMCE and therefore on the EET rate. As a conclusion it is stated that the IDA is suited even for FRET experiments with small donor–acceptor distances as long as adherence of the dyes does not dominate the overall motion behavior.

Chapter 5

Outlook

The core of this work was the successful implementation of the MTD approach to the DFT/MRCI code. In a second step, the method was extended to exchange contributions and optimized to enhance the computational efficiency. Furthermore, a supermolecular transition density-based formalism was presented, which extends the MTD approach to indirect CT contributions. EET was studied both statically and dynamically applying the MTD approach to a set of EET cassettes as well as to a biomolecular system labeled with a pair of FRET dyes. In the course of the dynamics study, a fast and efficient alignment-based methodology was developed, which makes a large number of MD trajectories accessible to enhanced quantum chemical approaches for calculating the ECME. In the following, some propositions for a reasonable continuation of this work will be presented.

5.1 Extension of the MTD method to triplet-triplet couplings

So far, only singlet-singlet EET has been considered. However, for many applications such as triplet-triplet upconversion ECMEs between triplet states are an important issue as well. The MTD approach cannot consider triplet-triplet couplings because the method requires the monomer transition densities of the interacting excited states with respect to the electronic ground states. The transition densities with respect to the (singlet) electronic ground state are zero since transitions between singlet and triplet states are generally spin-forbidden unless spin orbital coupling is considered explicitly within the Hamiltonian. According to the Dexter model, the ECME is solely composed of the Dexter exchange term in the case of triplet-triplet couplings since the EET is based on a simultaneous migration of electrons from the donor to the acceptor and vice versa. For this reason, the IDA cannot be used to approximate triplet-triplet couplings which accounts for the Coulomb (Förster) contribution. A monomer-based approach for the computation of triplet-triplet excitonic

couplings may be provided by an extension of the MTD formalism. An expression for the spin-free reduced transition density matrix in second quantization has been given in Eq. 2.115. With this, the ECME between two excited singlet states expressed in terms of the spin-free reduced monomer transition densities reads

$$K_{DA}^{(SS)} = - \sum_{ijkl} (il|kj) \langle \Psi_D | E_{ij}^{(S)} | \Psi_{D^*} \rangle \times \langle \Psi_{A^*} | E_{kl}^{(S)} | \Psi_A \rangle \quad (5.1)$$

$$= - \sum_{ijkl} (il|kj) \langle \Psi_D | \frac{1}{\sqrt{2}} \sum_{\sigma} c_{i\sigma}^{\dagger} c_{j\sigma} | \Psi_{D^*} \rangle \times \langle \Psi_{A^*} | \frac{1}{\sqrt{2}} \sum_{\sigma} c_{k\sigma}^{\dagger} c_{l\sigma} | \Psi_A \rangle \quad (5.2)$$

$$= - \frac{1}{2} \sum_{ijkl} (il|kj) \underbrace{\langle \Psi_D | c_{i\alpha}^{\dagger} c_{j\alpha} + c_{i\beta}^{\dagger} c_{j\beta} | \Psi_{D^*} \rangle}_{P_{ij}^{(D)}} \times \underbrace{\langle \Psi_{A^*} | c_{k\alpha}^{\dagger} c_{l\alpha} + c_{k\beta}^{\dagger} c_{l\beta} | \Psi_A \rangle}_{P_{kl}^{(A)}} \quad (5.3)$$

Considering the electron spin, it has to be stated that electronic singlet states have only one component ($\alpha\beta - \beta\alpha$) while triplet states are composed of three components T_{+1} ($\alpha\alpha$), T_0 ($\alpha\beta + \beta\alpha$) and T_{-1} ($\beta\beta$) which are energetically degenerate in the non-relativistic case. Therefore, the triplet excitation operator $E_{ij}^{(T)}$ is composed of three components as well. [81]

$$\mathcal{T}_{ij}^{1,+1} = -a_{i\alpha}^{\dagger} a_{j\beta} \quad (5.4)$$

$$\mathcal{T}_{ij}^{1,0} = \frac{1}{\sqrt{2}} (a_{i\alpha}^{\dagger} a_{j\alpha} - a_{i\beta}^{\dagger} a_{j\beta}) \quad (5.5)$$

$$\mathcal{T}_{ij}^{1,-1} = a_{i\beta}^{\dagger} a_{j\alpha} \quad (5.6)$$

Following Nagae et al. [82], this definition of the triplet excitation operator can be used to deduce transition density matrix-like expressions for the triplet-triplet coupling case. In principle, these expressions are special cases transition density matrix explicitly accounting for the spin of the excited and deexcited electrons, respectively. Starting the derivation from an expression analogous to the singlet case

$$K_{DA}^{(TT)} = - \sum_{ijkl} (il|kj) \left(\langle \Psi_D | E_{ij}^{(T)} | \Psi_{D^*} \rangle \langle \Psi_{A^*} | E_{kl}^{(T)} | \Psi_A \rangle \right) \quad (5.7)$$

the transition density-like terms can be separated according to the three triplet components

$$\langle \Psi_D | E_{ij}^{(T)} | \Psi_{D^*} \rangle = \langle \Psi_D | \mathcal{T}_{ij}^{1,+1} + \mathcal{T}_{ij}^{1,0} + \mathcal{T}_{ij}^{1,-1} | \Psi_{D^*} \rangle \quad (5.8)$$

$$= \langle \Psi_D | \mathcal{T}_{ij}^{1,+1} | \Psi_{D^*} \rangle + \langle \Psi_D | \mathcal{T}_{ij}^{1,0} | \Psi_{D^*} \rangle + \langle \Psi_D | \mathcal{T}_{ij}^{1,-1} | \Psi_{D^*} \rangle \quad (5.9)$$

where

$$\langle \Psi_D | \mathcal{T}_{ij}^{1,+1} | \Psi_{D^*} \rangle = -\langle \Psi_D | a_{i\alpha}^\dagger a_{j\beta} | \Psi_{D^*} \rangle \quad (5.10)$$

$$\langle \Psi_D | \mathcal{T}_{ij}^{1,0} | \Psi_{D^*} \rangle = \frac{1}{\sqrt{2}} \langle \Psi_D | a_{i\alpha}^\dagger a_{j\alpha} - a_{i\beta}^\dagger a_{j\beta} | \Psi_{D^*} \rangle \quad (5.11)$$

$$= \frac{1}{\sqrt{2}} \langle \Psi_D | a_{i\alpha}^\dagger a_{j\alpha} | \Psi_{D^*} \rangle - \frac{1}{\sqrt{2}} \langle \Psi_D | a_{i\beta}^\dagger a_{j\beta} | \Psi_{D^*} \rangle$$

$$\langle \Psi_D | \mathcal{T}_{ij}^{1,-1} | \Psi_{D^*} \rangle = \langle \Psi_D | a_{i\beta}^\dagger a_{j\alpha} | \Psi_{D^*} \rangle \quad (5.12)$$

Similar matrix elements $\langle \Psi_{A^*} | E_{kl}^{(T)} | \Psi_A \rangle$ can be derived for the acceptor localized excitation.

$$\langle \Psi_{A^*} | \mathcal{T}_{kl}^{1,+1} | \Psi_A \rangle = -\langle \Psi_{A^*} | a_{k\alpha}^\dagger a_{l\beta} | \Psi_A \rangle \quad (5.13)$$

$$\langle \Psi_{A^*} | \mathcal{T}_{kl}^{1,0} | \Psi_A \rangle = \frac{1}{\sqrt{2}} \langle \Psi_{A^*} | a_{k\alpha}^\dagger a_{l\alpha} - a_{k\beta}^\dagger a_{l\beta} | \Psi_A \rangle \quad (5.14)$$

$$= \frac{1}{\sqrt{2}} \langle \Psi_{A^*} | a_{k\alpha}^\dagger a_{l\alpha} | \Psi_A \rangle - \frac{1}{\sqrt{2}} \langle \Psi_{A^*} | a_{k\beta}^\dagger a_{l\beta} | \Psi_A \rangle$$

$$\langle \Psi_{A^*} | \mathcal{T}_{kl}^{1,-1} | \Psi_A \rangle = \langle \Psi_{A^*} | a_{k\beta}^\dagger a_{l\alpha} | \Psi_A \rangle \quad (5.15)$$

In order obtain the ECME, one has to consider that T-operators are not self-adjoint. Therefore, one has to combine $\mathcal{T}_{ij}^{1,+1}$ with $\mathcal{T}_{kl}^{1,-1}$, $\mathcal{T}_{ij}^{1,-1}$ with $\mathcal{T}_{kl}^{1,+1}$ and $\mathcal{T}_{ij}^{1,0}$ with $\mathcal{T}_{kl}^{1,0}$ ($-\mathcal{T}_{ij}^{1,+1}\mathcal{T}_{kl}^{1,-1} - \mathcal{T}_{ij}^{1,-1}\mathcal{T}_{kl}^{1,+1} + \mathcal{T}_{ij}^{1,0}\mathcal{T}_{kl}^{1,0}$). By this means, the ECME for triplet-triplet couplings can be written as

$$\begin{aligned} K_{DA}^{(TT)} &= -\sum_{ijkl} (il|kj) \\ &\times \left\{ \begin{array}{l} -\langle \Psi_D | \mathcal{T}_{ij}^{1,+1} | \Psi_{D^*} \rangle \langle \Psi_{A^*} | \mathcal{T}_{kl}^{1,-1} | \Psi_A \rangle \\ -\langle \Psi_D | \mathcal{T}_{ij}^{1,-1} | \Psi_{D^*} \rangle \langle \Psi_{A^*} | \mathcal{T}_{kl}^{1,+1} | \Psi_A \rangle \\ +\langle \Psi_D | \mathcal{T}_{ij}^{1,0} | \Psi_{D^*} \rangle \langle \Psi_{A^*} | \mathcal{T}_{kl}^{1,0} | \Psi_A \rangle \end{array} \right\} \end{aligned} \quad (5.16)$$

Substituting the definitions of the matrix elements in Eqs. 5.10 - 5.15 into Eq. 5.16 the expression becomes

$$\begin{aligned}
 K_{DA}^{(TT)} = & - \sum_{ijkl} (il|kj) \\
 & \times \left\{ \begin{array}{l} \langle \Psi_D | a_{i\alpha}^\dagger a_{j\beta} | \Psi_{D*} \rangle \langle \Psi_{A*} | a_{k\beta}^\dagger a_{l\alpha} | \Psi_A \rangle \\ + \langle \Psi_D | a_{i\beta}^\dagger a_{j\alpha} | \Psi_{D*} \rangle \langle \Psi_{A*} | a_{k\alpha}^\dagger a_{l\beta} | \Psi_A \rangle \\ + \frac{1}{2} \langle \Psi_D | a_{i\alpha}^\dagger a_{j\alpha} | \Psi_{D*} \rangle \langle \Psi_{A*} | a_{k\alpha}^\dagger a_{l\alpha} | \Psi_A \rangle \\ + \frac{1}{2} \langle \Psi_D | a_{i\beta}^\dagger a_{j\beta} | \Psi_{D*} \rangle \langle \Psi_{A*} | a_{k\beta}^\dagger a_{l\beta} | \Psi_A \rangle \\ - \frac{1}{2} \langle \Psi_D | a_{i\alpha}^\dagger a_{j\alpha} | \Psi_{D*} \rangle \langle \Psi_{A*} | a_{k\beta}^\dagger a_{l\beta} | \Psi_A \rangle \\ - \frac{1}{2} \langle \Psi_D | a_{i\beta}^\dagger a_{j\beta} | \Psi_{D*} \rangle \langle \Psi_{A*} | a_{k\alpha}^\dagger a_{l\alpha} | \Psi_A \rangle \end{array} \right\} \quad (5.17)
 \end{aligned}$$

Introducing short notations for the transition density-like matrix elements the ECME can finally reads

$$\begin{aligned}
 K_{DA}^{(TT)} = & - \sum_{ijkl} (il|kj) \left\{ P_{i\alpha;j\beta}^{(D)} P_{k\beta;l\alpha}^{(A)} + P_{i\beta;j\alpha}^{(D)} P_{k\alpha;l\beta}^{(A)} \right. \\
 & \left. + \frac{1}{2} \left(P_{i\alpha;j\alpha}^{(D)} P_{k\alpha;l\alpha}^{(A)} + P_{i\beta;j\beta}^{(D)} P_{k\beta;l\beta}^{(A)} - P_{i\alpha;j\alpha}^{(D)} P_{k\beta;l\beta}^{(A)} - P_{i\beta;j\beta}^{(D)} P_{k\alpha;l\alpha}^{(A)} \right) \right\} \quad (5.18)
 \end{aligned}$$

The equation generally holds true as long as the electronic ground states have singlet multiplicity and the excited states have triplet multiplicity. [82] To implement the extension, mainly the DFT/MRCI code would have to be changed to generate the transition density matrix-like matrices. Some routines may be adopted from the SPOCK program suite [83, 84, 85] devised for the calculation of spin-orbit coupling matrix elements. Since CT contributions become important at distances where the Dexter exchange contributions are non-zero, it may also be valuable to extend the code in analogy to the STD method presented in this work.

5.2 Optimization of the STD code

In the current version, the STD is very inefficient and causes a much higher computational cost than the optimized version of the MTD approach. To be able to study larger systems or if the use of larger basis sets is necessary, freezing of core and anticore MOs below or above a certain energy threshold should be made possible. The computational time may be further decreased by applying a "pre-scan" similar to the MTD such that matrix elements below a certain threshold can be neglected. However, it will not be possible to achieve a similar speed-up since the transition densities are smeared out on most of

the AOs. Therefore, a pre-scan of the three-index integrals from which the two-electron integrals are recalculated according to the RI-approximation may be more promising.

5.3 Enhancement of the sampling procedure

Studying the dynamics of EET taking the example of a rigid-double stranded RNA, the focus was on an efficient interface to molecular mechanics (MM) based molecular dynamics simulations and a quantum chemical approach for computing the ECME. Therefore, the simplest possible sampling technique called independent snapshot method (ISM) was used. The ISM treats each snapshot as independent member of the population — or in other words — assumes that an EET between donor and acceptor occurs with the same probability for each snapshot. It has been stated by Speelman et al. [86] that the ISM provides improper results in the case of transiently occupied configurations. In future studies a more sophisticated sampling method such as a Markov chain model could be used. [86] For each snapshot the probabilities for the different decay events of the excited donor (fluorescence, EET or non-radiative decay) and the probability that the donor remains in the excited state are calculated. The probabilities depend on the rate constants of the appropriate events and the time between the trajectory points. According to the calculated probabilities a random number is generated deciding which of the events takes place. If the donor remains in the excited state, the next trajectory point is considered, otherwise the chain stops and the time between the first and last snapshot of the chain as well as the kind of the decay event are stored. The procedure is repeated several times for each snapshot as starting point of the chain. By this means, a distribution of the final decay events of each chain is obtained providing information on how likely the occurrence of an EET is for a certain geometry. This likelihood can be used as weighting factor when calculating the average EET rate from the ECMEs obtained for each snapshot.

5.4 Enhancement of the alignment procedure

To make a large number of MD-based snapshots accessible to an enhanced method for the quantum chemical calculation of the ECME, an approach was presented according to which preoptimized structures of the target molecules are aligned to the MD snapshots. At the moment, the preoptimized structures are the relaxed ground state geometries of the appropriate molecules. The procedure can be applied without any problems as long as the considered molecules are rather rigid, which means that molecular vibrations do not cause extreme deviations from the preoptimized structures. Otherwise the failure of the alignment becomes large such that any further analysis is questionable. To overcome this problem, the algorithm could be extended to more than only one preoptimized structure.

Considering for example a system which undergoes a *cis-trans*-isomerization during the MD simulation. A preoptimized *cis*-structure as well as a preoptimized *trans*-structure could be aligned to each snapshot discarding the worse of the two alignments. Since the computational cost for an alignment is low, the enhancement would provide an efficient way to treat more flexible systems with a high level of accuracy.

Bibliography

- [1] Peter W. Atkins. *Physikalische Chemie (German Edition)*. Wiley-VCH, 1996.
- [2] J. Frenkel. On the transformation of light into heat in solids. I. *Phys. Rev.*, 37(1):17–44, 1931.
- [3] Anthony Mark Fox. *Optical properties of solids*, volume 3. Oxford University Press, USA, 2001.
- [4] Gregory H. Wannier. The structure of electronic excitation levels in insulating crystals. *Phys. Rev.*, 52(3):191–197, 1937.
- [5] J. D. Wright. *Molecular Crystals*. Cambridge University Press, 1995.
- [6] Volkhard May and Oliver Kühn. *Charge and energy transfer dynamics in molecular systems*. Wiley-VCH, 2004.
- [7] Theodor Förster. Energiewanderung und Fluoreszenz. *Die Naturwissenschaften*, 6:166–175, 1946.
- [8] Theodor Förster. Zwischenmolekulare Energiewanderung und Fluoreszenz. *Ann. Phys. (Berlin)*, 437(1-2):55–75, 1948.
- [9] Mouldy Sioud, editor. *Ribozymes and siRNA protocols*. Springer Science + Business Media, 2004.
- [10] D. L. Dexter. A theory of sensitized luminescence in solids. *J. Chem. Phys.*, 21(5):836–850, 1953.
- [11] Nicholas D. Spencer and John H. Moore. *Encyclopedia of chemical physics and physical chemistry: Applications*, volume 3. Taylor & Francis, 2001.
- [12] Rudolph A. Marcus. On the theory of oxidation-reduction reactions involving electron transfer. Iwall. *J. Chem. Phys.*, 24(5):966–978, 1956.

- [13] H. Gaffron and K. Wohl. Zur Theorie der Assimilation. *Naturwissenschaften*, 24:81–90, 1936.
- [14] Harald Hoppe and Niyazi Serdar Sariciftci. Organic solar cells: An overview. *J. Mater. Res.*, 19(07):1924–1945, 2004.
- [15] Robert M. Clegg. Fluorescence resonance energy transfer and nucleic acids. *Methods Enzymol.*, pages 353–388, 1992.
- [16] Vladimir V. Didenko. DNA probes using fluorescence resonance energy transfer (FRET): designs and applications. *Biotechniques*, 31(5):1106, 2001.
- [17] Judith G. Voet and Donald Voet. *Biochemie*. Wiley-VCH, 1994.
- [18] Antonio Facchetti. π -conjugated polymers for organic electronics and photovoltaic cell applications. *Chem. Mater.*, 23(3):733–758, 2011.
- [19] Wallace C. H. Choy, editor. *Organic Solar Cells: Materials and Device Physics*. Springer London, 2013.
- [20] Chirlmin Joo, Hamza Balci, Yuji Ishitsuka, Chittanon Buranachai, and Taekjip Ha. Advances in single-molecule fluorescence methods for molecular biology. *Annu. Rev. Biochem.*, 77(1):51–76, 2008.
- [21] T. G. Kim, J. C. Castro, A. Loudet, J. G.-S. Jiao, R. M. Hochstrasser, K. Burgess, and M. R. Topp. Correlations of structure and rates of energy transfer for through-bond energy-transfer cassettes. *J. Phys. Chem. A*, 110(1):20–27, 2006.
- [22] Chi-Wai Wan, Armin Burghart, Jiong Chen, Fredrik Bergström, Lennart B.-Å. Johansson, Matthew F. Wolford, Taeg Gyum Kim, Michael R. Topp, Robin M. Hochstrasser, and Kevin Burgess. Anthracene–BODIPY Cassettes: Syntheses and Energy Transfer. *Chem. Eur. J.*, 9(18):4430–4441, 2003.
- [23] A. S. Davydov. The theory of molecular excitons. *Sov. Phys. Usp.*, 7(2):145–178, 1964.
- [24] Brent P. Krueger, Gregory D. Scholes, and Graham R. Fleming. Calculation of couplings and energy-transfer pathways between the pigments of LH2 by the ab initio transition density cube method. *J. Phys. Chem. B*, 102(27):5378–5386, 1998.
- [25] Cathy Y. Wong, Carles Curutchet, Sergei Tretiak, and Gregory D. Scholes. Ideal dipole approximation fails to predict electronic coupling and energy transfer between semiconducting single-wall carbon nanotubes. *J. Chem. Phys.*, 130(8):081104, 2009.

- [26] R. F. Fink, J. Pfister, A. Schneider, H. Zhao, and B. Engels. Ab initio configuration interaction description of excitation energy transfer between closely packed molecules. *Chem. Phys.*, 343(2-3):353–361, 2008.
- [27] Reinhold F. Fink, Johannes Pfister, Hong Mei Zhao, and Bernd Engels. Assessment of quantum chemical methods and basis sets for excitation energy transfer. *Chem. Phys.*, 346(1):275–285, 2008.
- [28] Carles Curutchet and Benedetta Mennucci. Toward a molecular scale interpretation of excitation energy transfer in solvated bichromophoric systems. *J. Am. Chem. Soc.*, 127(47):16733–16744, 2005.
- [29] Maria Francesca Iozzi, Benedetta Mennucci, Jacopo Tomasi, and Roberto Cammi. Excitation energy transfer (EET) between molecules in condensed matter: A novel application of the polarizable continuum model (PCM). *J. Chem. Phys.*, 120(15):7029–7040, 2004.
- [30] Richard D. Harcourt, Gregory D. Scholes, and Kenneth P. Ghiggino. Rate expressions for excitation transfer. II. Electronic considerations of direct and through-configuration exciton resonance interactions. *J. Chem. Phys.*, 101(12):10521, 1994.
- [31] Gregory D. Scholes, Richard D. Harcourt, and Kenneth P. Ghiggino. Rate expressions for excitation transfer. III. An ab initio study of electronic factors in excitation transfer and exciton resonance interactions. *J. Chem. Phys.*, 102(24):9574–9581, 1995.
- [32] Richard D. Harcourt, Kenneth P. Ghiggino, Gregory D. Scholes, and Shammai Speiser. On the origin of matrix elements for electronic excitation (energy) transfer. *J. Chem. Phys.*, 105(5):1897–1901, 1996.
- [33] Vincenzo Russo, Carles Curutchet, and Benedetta Mennucci. Towards a molecular scale interpretation of excitation energy transfer in solvated bichromophoric systems. II. the through-bond contribution. *J. Phys. Chem. B*, 111(4):853–863, 2007.
- [34] Kazuhiro J. Fujimoto. Transition-density-fragment interaction combined with transfer integral approach for excitation-energy transfer via charge-transfer states. *J. Chem. Phys.*, 137(3):034101, 2012.
- [35] Kazuhiro J. Fujimoto. *Chemical science of π -electron systems*, chapter Theoretical calculations of excitation energy transfer, pages 761–777. Springer, 2015.
- [36] Johannes Neugebauer. Couplings between electronic transitions in a subsystem formulation of time-dependent density functional theory. *J. Chem. Phys.*, 126(13):134116, 2007.

- [37] Johannes Neugebauer. Photophysical properties of natural light-harvesting complexes studied by subsystem density functional theory. *J. Phys. Chem. B*, 112(7):2207–2217, 2008.
- [38] Stefano Caprasecca and Benedetta Mennucci. Excitation energy transfer in donor-bridge- acceptor systems: A combined quantum-mechanical/classical analysis of the role of the bridge and the solvent. *J. Phys. Chem. A*, 118(33):6484–6491, 2014.
- [39] C.-P. Hsu, Z.-Q. You, and H.-C. Chen. Characterization of the short-range couplings in excitation energy transfer. *J. Phys. Chem. C*, 112:1204–1212, 2008.
- [40] Hung-Cheng Chen, Zhi-Qiang You, and Chao-Ping Hsu. The mediated excitation energy transfer: Effects of bridge polarizability. *J. Chem. Phys.*, 129(8):084708, 2008.
- [41] Chao-Ping Hsu. The electronic couplings in electron transfer and excitation energy transfer. *Acc. Chem. Res.*, 42(4):509–518, 2009.
- [42] Zhi-Qiang You and Chao-Ping Hsu. The fragment spin difference scheme for triplet-triplet energy transfer coupling. *J. Phys. Chem.*, 133(7):074105, 2010.
- [43] Felix Plasser and Hans Lischka. Analysis of excitonic and charge transfer interactions from quantum chemical calculations. *J. Chem. Theory Comput.*, 8(8):2777–2789, 2012.
- [44] Lluís Blancafort and Alexander A. Voityuk. Exciton delocalization, charge transfer, and electronic coupling for singlet excitation energy transfer between stacked nucleobases in DNA: An MS-CASpt2 study. *J. Chem. Phys.*, 140(9):095102, 2014.
- [45] Josh Vura-Weis, Marshall D Newton, Michael R Wasielewski, and Joseph E Subotnik. Characterizing the locality of diabatic states for electronic excitation transfer by decomposing the diabatic coupling. *J. Phys. Chem. C*, 114(48):20449–20460, 2010.
- [46] Stefan Grimme and Mirko Waletzke. A combination of Kohn–Sham density functional theory and multi-reference configuration interaction methods. *J. Chem. Phys.*, 111(13):5645–5655, 1999.
- [47] Kazuo Kitaura, Eiji Ikeo, Toshio Asada, Tatsuya Nakano, and Masami Uebayasi. Fragment molecular orbital method: an approximate computational method for large molecules. *Chem. Phys. Lett.*, 313(3):701–706, 1999.
- [48] Tatsuya Nakano, Tsuguchika Kaminuma, Toshiyuki Sato, Yutaka Akiyama, Masami Uebayasi, and Kazuo Kitaura. Fragment molecular orbital method: application to polypeptides. *Chem. Phys. Lett.*, 318(6):614–618, Mar 2000.

- [49] Michael W. Schmidt, Kim K. Baldridge, Jerry A. Boatz, Steven T. Elbert, Mark S. Gordon, Jan H. Jensen, Shiro Koseki, Nikita Matsunaga, Kiet A. Nguyen, Shujun Su, and et al. General atomic and molecular electronic structure system. *J. Comput. Chem.*, 14(11):1347–1363, Nov 1993.
- [50] Dmitri G. Fedorov and Kazuo Kitaura. Extending the power of quantum chemistry to large systems with the fragment molecular orbital method. *J. Phys. Chem. A*, 111(30):6904–6914, Aug 2007.
- [51] Dmitri G. Fedorov and Kazuo Kitaura. Multiconfiguration self-consistent-field theory based upon the fragment molecular orbital method. *J. Chem. Phys.*, 122(5):054108, 2005.
- [52] Volkhard May and Oliver Kühn. *Charge and energy transfer dynamics in molecular systems*. Wiley-Blackwell, 2011.
- [53] Roy McWeeny. *Methods of molecular quantum mechanics*. Academic Press Limited, London, 1989. p. 129.
- [54] James Franck and E. G. Dymond. Elementary processes of photochemical reactions. *Trans. Faraday Soc.*, 21:536–542, 1926.
- [55] Edward Condon. A theory of intensity distribution in band systems. *Phys. Rev.*, 28(6):1182, 1926.
- [56] Edward Condon. Nuclear motions associated with electron transitions in diatomic molecules. *Phys. Rev.*, 32(6):858, 1928.
- [57] M. Kasha. Characterization of electronic transitions in complex molecules. *Discuss. Faraday Soc.*, 9:14–19, 1950.
- [58] P. A. M. Dirac. The quantum theory of the emission and absorption of radiation. *Proc. Roy. Soc. A*, 114(767):243–265, 1927.
- [59] Enrico Fermi. *Nuclear physics*. University of Chicago Press, 1950. 9780226243658.
- [60] Leonard J. Brillson. *Surfaces and interfaces of electronic materials*. Wiley-Blackwell, 2010.
- [61] Roy F. Schwitters. Scattering and decays from Fermi’s golden rule including all the \hbar ’s and c’s. *University of Texas: PHY362L Supplementary Note*, 2004.
- [62] Emmanuelle Hennebicq, Geoffrey Pourtois, Gregory D. Scholes, Laura M. Herz, David M. Russell, Carlos Silva, Sepas Setayesh, Andrew C. Grimsdale, Klaus Müllen,

- and Jean-Luc Brédas et al. Exciton migration in rigid-rod conjugated polymers: An improved Förster model. *J. Am. Chem. Soc.*, 127(13):4744–4762, 2005.
- [63] J. Dominik Spiegel, Igor Lyskov, Martin Kleinschmidt, and Christel M. Marian. Charge-transfer contributions to the excitonic coupling matrix element in bodipy-based energy transfer cassettes. *Chem. Phys. (in press)*, 2016.
- [64] Trygve Helgaker, Helena Larsen, Jeppe Olsen, and Poul Jørgensen. Direct optimization of the AO density matrix in Hartree–Fock and Kohn–Sham theories. *Chem. Phys. Lett.*, 327(5-6):397–403, 2000.
- [65] M. Kasha, H. R. Rawls, and M. Ashraf El-Bayoumi. The exciton model in molecular spectroscopy. *Pure Appl. Chem.*, 11(3-4):371–392, 1965.
- [66] B. Wieb van der Meer, Daniel M. van der Meer, and Steven S. Vogel. Optimizing the orientation factor kappa-squared for more accurate FRET measurements. *FRET - Förster Resonance Energy Transfer*, page 63–104, 2013.
- [67] Stanislav Kalinin, Thomas Peulen, Simon Sindbert, Paul J. Rothwell, Sylvia Berger, Tobias Restle, Roger S. Goody, Holger Gohlke, and Claus A. M. Seidel. A toolkit and benchmark study for FRET-restrained high-precision structural modeling. *Nat. Methods*, 9(12):1218–1225, Nov 2012.
- [68] B. Wieb Van der Meer. Kappa-squared: from nuisance to new sense. *Rev. Mol. Biotechnol.*, 82(3):181–196, 2002.
- [69] Ben Corry and Dylan Jayatilaka. Simulation of structure, orientation, and energy transfer between AlexaFluor molecules attached to MscL. *Biophys. J.*, 95(6):2711–2721, 2008.
- [70] Luís Loura. Simple estimation of Förster resonance energy transfer (FRET) orientation factor distribution in membranes. *Int. J. Mol. Sci.*, 13(11):15252–15270, 2012.
- [71] Mathias Pabst and Andreas Köhn. Excited states of [3.3](4, 4) biphenylophane: The role of charge-transfer excitations in dimers with π - π interaction. *J. Phys. Chem. A*, 114(4):1639–1649, 2010.
- [72] Igor Medintz and Niko Hildebrandt, editors. *FRET - Förster Resonance Energy Transfer*. Wiley-Blackwell, 2013.
- [73] Roland Karl Hartmann, Albrecht Bindereif, Astrid Schon, and Eric Westhof. *Handbook of RNA biochemistry*. John Wiley & Sons, 2015.

- [74] David A. Case, Thomas E. Cheatham, Tom Darden, Holger Gohlke, Ray Luo, Kenneth M. Merz, Alexey Onufriev, Carlos Simmerling, Bing Wang, and Robert J. Woods. The Amber biomolecular simulation programs. *J. Comput. Chem.*, 26(16):1668–1688, 2005.
- [75] Igor Lyskov, Martin Kleinschmidt, and Christel M. Marian. Redesign of the DFT/MRCI hamiltonian. *J. Chem. Phys.*, 144:034104, 2016.
- [76] Evangelos A. Coutsias, Chaok Seok, and Ken A. Dill. Using quaternions to calculate RMSD. *J. Comput. Chem.*, 25(15):1849–1857, 2004.
- [77] J. Dominik Spiegel, Simone Fulle, Martin Kleinschmidt, Holger Gohlke, and Christel M. Marian. Failure of the IDA in FRET systems at close inter-dye distances is moderated by frequent low κ^2 values. *J. Phys. Chem. B*, 120:8845–8862, 2016.
- [78] J. Dominik Spiegel, Martin Kleinschmidt, Alexander Larbig, Jörg Tatchen, and Christel M. Marian. Quantum-chemical studies on excitation energy transfer processes in BODIPY-based donor–acceptor systems. *J. Chem. Theory Comput.*, 11(9):4316–4327, 2015.
- [79] Aurore Loudet and Kevin Burgess. BODIPY dyes and their derivatives: syntheses and spectroscopic properties. *Chem. Rev.*, 107(11):4891–4932, 2007.
- [80] Tanguy Van Regemorter, Maxime Guillaume, Gjergji Sini, John S. Sears, Victor Geskin, Jean-Luc Brédas, David Beljonne, and Jérôme Cornil. Density functional theory for the description of charge-transfer processes at ttf/tcnq interfaces. *Theor. Chem. Acc.*, 131(10), Sep 2012.
- [81] Trygve Helgaker, Poul Jorgensen, and Jeppe Olsen. *Molecular electronic-structure theory*. John Wiley & Sons, 2014.
- [82] Hiroyoshi Nagae, Toshiaki Kakitani, Tetsuya Katoh, and Mamoru Mimuro. Calculation of the excitation transfer matrix elements between the S_2 or S_1 state of carotenoid and the S_2 or S_1 state of bacteriochlorophyll. *J. Chem. Phys.*, 98(10):8012–8023, 1993.
- [83] Martin Kleinschmidt, Jörg Tatchen, and Christel M. Marian. Spin-orbit coupling of DFT/MRCI wavefunctions: Method, test calculations, and application to thiophene. *J. Comput. Chem.*, 23(8):824–833, 2002.
- [84] Martin Kleinschmidt and Christel M. Marian. Efficient generation of matrix elements for one-electron spin–orbit operators. *Chem. Phys.*, 311(1-2):71–79, 2005.

- [85] Martin Kleinschmidt, Jörg Tatchen, and Christel M. Marian. SPOCK.CI: A multireference spin-orbit configuration interaction method for large molecules. *J. Chem. Phys.*, 124(12):124101, 2006.
- [86] Amy L. Speelman, Aurora Muñoz-Losa, Katie L. Hinkle, Darren B. VanBeek, Benedetta Mennucci, and Brent P. Krueger. Using molecular dynamics and quantum mechanics calculations to model fluorescence observables. *J. Phys. Chem. A*, 115(16):3997–4008, 2011.

Acknowledgment

I thank my first rapporteur Prof. Dr. Christel M. Marian for her great support during the preparation of this thesis and always encouraging me to develop new ideas. I really enjoyed discussing with her also about non-scientific topics. I thank her for her willingness to take over my supervision especially under the given circumstances.

I thank Prof. Dr. Holger Gohlke for being my second rapporteur and Prof. Dr. Michael Schmitt for being my mentor according to the promotion regulation.

I wish to thank Dr. Martin Kleinschmidt for his kind, frequent and quick support helping me to put my ideas into practice - in particular for many constructive "only 5-minutes" discussions often lasting longer than one hour.

I thank Prof. Dr. Holger Gohlke and Dr. Simone Fulle for the great cooperation during the FRET project.

I like to thank the whole team of the Institute of Theoretical and Computational Chemistry for the nice and cooperative working atmosphere. In particular, I thank my office colleagues Nikolai Elfers and Adrian Heil for lively discussions (not always about chemistry ...) as well as Dr. Oliver Weingart, Dr. Vidisha Rai-Constapel, Irina Dokukina (Ambertools), Oliver Schillinger (MD) and Igor Lyskov (physics) for helping me in the case of special issues.

Finally, I wish to thank my lovely wife Maria Bous and my dear parents Ursula and Helmut Spiegel for believing in me in the last four years and encouraging me every time I was disappointed or frustrated. I thank my brother-in-law Edgar Bous for proof-reading this work.

It was certainly not always easy but it was a great time which I will miss for sure.

Funding by the Deutsche Forschungsgemeinschaft (DFG) through TA 725/1-1 is gratefully acknowledged.

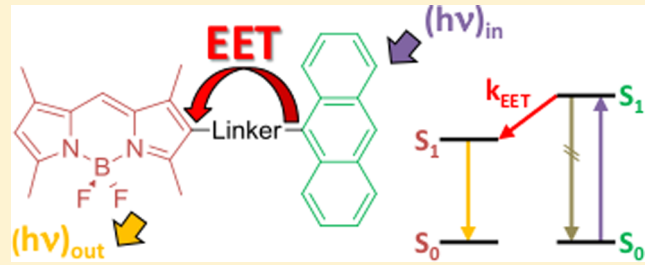
Quantum-Chemical Studies on Excitation Energy Transfer Processes in BODIPY-Based Donor–Acceptor Systems

J. Dominik Spiegel,[†] Martin Kleinschmidt,[†] Alexander Larbig,[†] Jörg Tatchen,[‡] and Christel M. Marian*,[†]

[†]Institute of Theoretical and Computational Chemistry, Heinrich Heine University Düsseldorf, Universitätsstr. 1, D-40225 Düsseldorf, Germany

[‡]Departamento de Química, Universidad de los Andes, Car. 1 No. 18A-12, Bogotá, Colombia

ABSTRACT: BODIPY-based excitation energy transfer (EET) cassettes are experimentally extensively studied and serve as excellent model systems for the investigation of photophysical processes, since they occur in any photosynthetic system and in organic photovoltaics. In the present work, the EET rates in five BODIPY-based EET cassettes in which anthracene serves as the donor have been determined, employing the monomer transition density approach (MTD) and the ideal dipole approximation (IDA). To this end, a new computer program has been devised that calculates the direct and exchange contributions to the excitonic coupling (EC) matrix element from transition density matrices generated by a combined density functional and multireference configuration interaction (DFT/MRCI) calculation for the monomers. EET rates have been calculated according to Fermi's Golden Rule from the EC and the spectral overlap, which was obtained from the calculated vibrationally resolved emission and absorption spectra of donor and acceptor, respectively. We find that the direct contribution to the EC matrix element is dominant in the studied EET cassettes. Furthermore, we show that the contribution of the molecular linker to the EET rate cannot be neglected. In our best fragment model, the molecular linker is attached to the donor moiety. For cassettes in which the transition dipole moments of donor and acceptor are oriented in parallel manner, our results confirm the experimental findings reported by Kim et al. [J. Phys. Chem. A 2006, 110, 20–27]. In cassettes with a perpendicular orientation of the donor and acceptor transition dipole moments, dynamic effects turn out to be important.



1. INTRODUCTION

Excitation energy transfer (EET) is one of the key issues in organic photovoltaics. In a system in which donor and acceptor molecules are covalently linked, EET can take place in two different ways. The limiting case of through-space excitation energy transfer (TSEET) is based on the interaction between a de-excitation process on the donor and a simultaneous excitation process on the acceptor. In 1948, Förster coined the term “direct coupling” for the coupling between a locally excited donor interacting with an acceptor through a Coulomb potential.¹ In 1953, Dexter showed that there is also an exchange contribution to the excitonic coupling (EC), which becomes more and more important as the donor–acceptor distance gets smaller.² Dexter explained this type of EET as a simultaneous exchange of electrons between donor and acceptor. In the limiting case of through-bond excitation energy transfer (TBEET), the excitation energy is directly transferred through the molecular bridge linking the donor and the acceptor. The superexchange mechanism proposed by McConnell in 1961^{3,4} describes the EET as a tunneling process where the EET rate decreases exponentially with the length of the linker. In a realistic EET system in which donor and acceptor are joined in a single molecule, both TSEET and TBEET coexist and contribute to the EET rate.

1.1. The Excitonic Coupling Matrix Element. The EC matrix element V_{DA} between an excitation on molecule A and a de-excitation on molecule D can be derived, considering the Hamiltonian of a bimolecular system AD.⁵ The Hamiltonian is given by the sum of the electronic Hamiltonian, the operator of the kinetic energy of the nuclei, and the operator of the internuclear repulsion:

$$\hat{H}(R) = \hat{H}_{\text{el}}(R) + \hat{T}_{\text{nuc}}(R) + \hat{V}_{(\text{nuc-nuc})}(R) \quad (1)$$

Herein, R is the set of coordinates of all nuclei. Assuming that the total system can be decomposed into two individual molecules A and D, intramolecular and intermolecular coordinates can be separated. In this case, the electronic Hamiltonian of the bimolecular system can be written as the sum of the electronic Hamiltonians of A and D and the interaction $\hat{V}_{DA}^{(\text{el-el})}$ between the electrons located at the two molecules consisting of a direct and an exchange term.

$$\hat{H}_{\text{el}}(R) = \hat{H}_D^{(\text{el})}(R) + \hat{H}_A^{(\text{el})}(R) + \frac{1}{2}\hat{V}_{DA}^{(\text{el-el})}(R) \quad (2)$$

The potential $\hat{V}_{DA}^{(\text{el-el})}$ is responsible for the EC. The electronic wave function of the total system $\phi_{a,d}$ is expanded

Received: May 27, 2015

Published: July 27, 2015



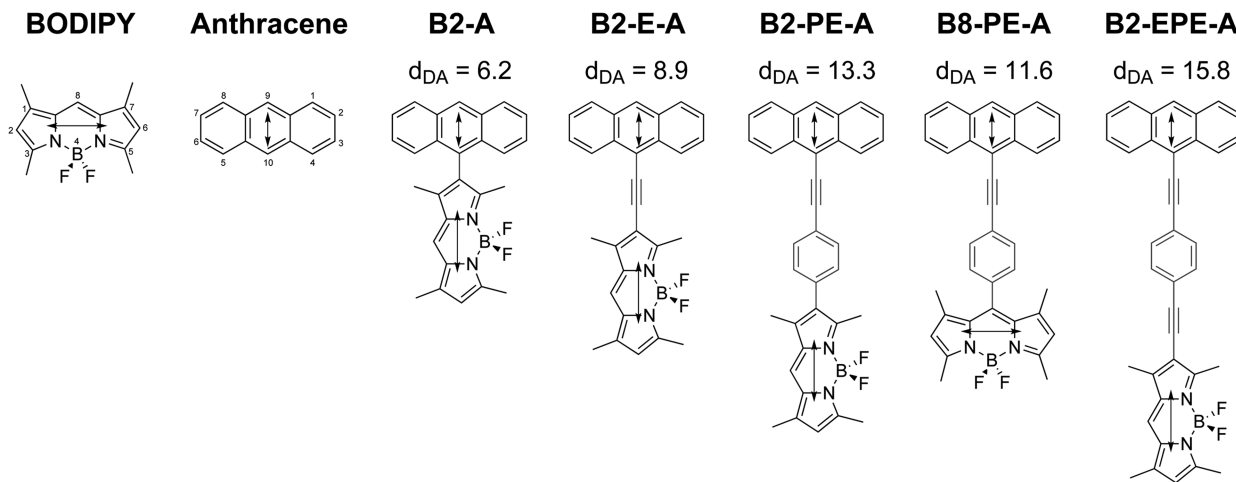


Figure 1. Nomenclature and chemical structure of studied EET cassettes. The $S_0 \rightarrow S_1$ transition dipole moments of BODIPY and anthracene are indicated as arrows. Distances between the centers of mass are given in Ångstroms.

as antisymmetrized product of the adiabatic electronic states of the individual systems

$$\phi_{a,d}(r_m, R) = \hat{\mathcal{A}}[\varphi_{Aa}(r_A, R)\varphi_{Dd}(r_d, R)] \quad (3)$$

where r_A and r_D denote the electronic coordinates of A and D, respectively, and “a” and “d” label the respective local electronic states. $\hat{\mathcal{A}}$ represents the antisymmetrization operator:

$$\hat{\mathcal{A}} = \frac{1}{\sqrt{N_p}} \sum_{\text{perm}} (-1)^p \hat{P} \quad (4)$$

where \hat{P} generates permutations of the electron coordinates of molecules A and D in the total system and p is the number of transpositions. The total number of permutations N_p is dependent on the number of electrons of the individual systems and is given by

$$N_p = \frac{(N_{el}^{(A)} + N_{el}^{(D)})!}{(N_{el}^{(A)}!N_{el}^{(D)}!)!} \quad (5)$$

Note that the resulting states of the total system are not orthonormal.

The EC matrix element between a local transition on molecule A from state a_1 to a_2 and a local transition on molecule D from state d_1 to d_2 is then given by

$$\begin{aligned} \langle \phi_{a_2 d_2} | \hat{V}_{DA}^{(el-el)} | \phi_{a_1 d_1} \rangle &= \int dr_A dr_D (\hat{\mathcal{A}}[\varphi_{a_2}(r_A, R)\varphi_{d_2}(r_D, R)] \cdot \hat{V}_{DA}^{(el-el)} \\ &\quad \cdot (\hat{\mathcal{A}}[\varphi_{a_1}(r_A, R)\varphi_{d_1}(r_D, R)]) \\ &\equiv J_{DA} + K_{DA} \end{aligned} \quad (6)$$

where J_{DA} is the direct contribution and K_{DA} is the exchange contribution. K_{DA} is dependent on the spatial overlap of molecular orbitals located at A and those located at D.

If the exchange contribution K_{DA} is neglected, the electronic state of the total system can be written as a Hartree product of the local electronic states:

$$\phi_{a,d}^{\text{HP}}(r_A, r_D, R) = \varphi_a(r_A, R)\varphi_d(r_D, R) \quad (7)$$

such that the right-hand side of eq 6 simplifies to the direct contribution term:

$$\langle \phi_{a_2 d_2} | \hat{V}_{DA}^{(el-el)} | \phi_{a_1 d_1} \rangle \approx \langle \varphi_{a_2} \varphi_{d_2} | \hat{V}_{DA}^{(el-el)} | \varphi_{a_1} \varphi_{d_1} \rangle = J_{DA} \quad (8)$$

1.2. The Energy Transfer Rate. The EET process is termed incoherent if it takes place on a much longer time scale than intermolecular and intramolecular relaxation ($\tau_{\text{trans}} \gg \tau_{\text{relax}}$). In this case, the EET rate can be described by a Golden Rule expression, which has already been applied successfully to such processes in the past.^{6–8}

$$\begin{aligned} k_{\text{EET}} = \frac{2\pi}{\hbar} \sum_{MN} \sum_{KL} f(E_{D^*M})f(E_{AL}) &| \langle \Psi_{DN} \Psi_{A^K} | \hat{V}_{DA}^{(el-el)} | \Psi_{D^*M} \Psi_{AL} \rangle |^2 \\ &\times \delta(E_{D^*M} + E_{AL} - E_{DN} - E_{A^K}) \end{aligned} \quad (9)$$

where $f(E_{D^*M})$ is the thermal occupation of the vibrational state M of the electronically excited donor molecule with vibronic wave function Ψ_{D^*M} and energy E_{D^*M} . Similarly, $f(E_{AL})$ denotes the thermal occupation of the vibrational state L of the acceptor molecule in the electronic ground state with vibronic wave function Ψ_{AL} and energy E_{AL} , etc. The delta distribution term (δ) ensures that only energy-conserving processes contribute to the EET rate. Assuming that the electronic part of the EC is not dependent on the nuclear coordinates (Condon approximation), the coupling matrix element becomes

$$\langle \Psi_{A^K} \Psi_{DN} | \hat{V}_{DA}^{(el-el)} | \Psi_{D^*M} \Psi_{AL} \rangle = V_{DA} \langle \chi_{AL} \chi_{A^K} \rangle \langle \chi_{D^*M} \chi_{DN} \rangle \quad (10)$$

where the χ denote purely vibrational wave functions of the donor and acceptor molecules in the electronic ground and excited states, respectively. The EET rate then reads as follows:

$$\begin{aligned} k_{\text{EET}} = \frac{2\pi}{\hbar} |V_{DA}|^2 \sum_{MN} \sum_{KL} f(E_{AL})f(E_{D^*M}) &| \langle \chi_{AL} \chi_{A^K} \rangle |^2 \langle \chi_{D^*M} \chi_{DN} \rangle \\ &\times \delta(E_{D^*M} + E_{AL} - E_{A^K} - E_{DN}) \end{aligned} \quad (11)$$

The Franck–Condon weighted density of states (FCWD)^{9,10} is typically approximated as the spectral overlap of the normalized donor emission $F_D(\omega)$ and the acceptor absorption spectrum $A_A(\omega)$. In this case, the EET rate is given by^{5,6}

$$k_{\text{EET}} = \frac{2\pi}{\hbar} |V_{DA}|^2 \int_0^\infty F_D(\omega) A_A(\omega) d\omega \quad (12)$$

1.3. Energy Transfer Cassettes. Because of their physical and chemical properties, donor–acceptor systems based on 4,4-difluoro-4a,4a-diaza-s-indacene (BODIPY) are eligible

candidates for use in organic photovoltaics.^{11–15} BODIPY dyes are characterized by strong absorption of UV light and sharp fluorescence with high quantum yields.¹⁶ The compounds are largely insensitive to the pH and polarity of the solvent. BODIPY itself is reported to be chemically unstable and therefore has not been synthesized until now.¹⁶ Within this article, we use BODIPY as an abbreviation for the 1,3,5,7-methylated derivate. Alkylated compounds barely differ in their absorption and emission spectra. Vertical absorption and emission energies of BODIPY have been calculated by Briggs et al. at the CAS-PT2 and Restricted Open-Shell Kohn-Sham levels, respectively.¹⁷

Cassettes in which BODIPY is covalently linked to a second chromophore are experimentally and extensively studied and serve as model systems for the description of EET processes. In this work, we present theoretical studies on the EET in five different BODIPY-based cassettes (see Figure 1). In all investigated systems, BODIPY serves as the acceptor while anthracene serves as the donor. Experimentally obtained fluorescence lifetimes and EET rates of these cassettes were reported by Kim and Wan.^{18,19} To the best of our knowledge, no theoretical studies of EET processes in the investigated BODIPY-based EET cassettes have been conducted so far. A theoretical study of the EET in another BODIPY-based dyad mainly concentrating on solvent screening effects was reported by Caprasecca et al.²⁰

In this work, we use a monomer-based approach to calculate the EC and determine the EET rate. The obtained results are compared to experimental data and confirm the assumption that the through-space contribution to the EC is dominant.

2. THEORETICAL METHODS

In practice, there are two main approaches to calculate the EC matrix element.²¹ In calculations that are based on a supermolecular description of the entire system, the full EC can directly be deduced from the energetic splitting of the involved excited states. In the case of unsymmetric systems, the eigenstates of the Hamiltonian must be transformed to a diabatic basis first.^{22,23} In monomer-based approaches, the individual contributions to the EC must be computed from physical quantities obtained from separate quantum-chemical calculations of the donor and acceptor parts of the total system. Within this paper, we employ the monomer transition density (MTD) approach,^{24–26} the ideal dipole approximation (IDA)^{1,27} as well as the symmetric energy splitting method (Davydov Splitting),^{28,29} which are outlined in the following. A detailed derivation of the EC has been given by May and Kühn.⁵

2.1. Exact Excitonic Coupling. The exact EC of homodimers, including direct and exchange contributions, can be calculated from the symmetric energetic splitting of the appropriate monomer excited states in a supermolecular calculation.

$$V_{AA} = \frac{E_2 - E_1}{2} \quad (13)$$

Since the method is not applicable to heterodimeric systems, approximate approaches based on monomer calculations are applied.

2.2. Monomer Transition Density Approach. Starting from eq 8, the EC matrix element can be regarded as an interaction between two transition densities located on monomers D and A.^{24,25} Within the MO basis, a transition

density is expressed in the form of a matrix. The spinless reduced one-particle transition density matrix connecting the electronic states Ψ_{a_1} and Ψ_{a_2} of an N -electron system A is defined as³⁰

$$\rho(a_1 a_2 | r_1; r_1') = N \int \int \cdots \int \Psi_{a_2}^*(x'_1, x_2, \dots, x_N) \times \Psi_{a_1}(x_1, x_2, \dots, x_N) \, dx_1 \, dx_2 \cdots dx_N \quad (14)$$

A similar expression is obtained for subsystem D. Let i and j be molecular orbitals (MOs) located on monomer A and k and l are MOs located on monomer D. Evaluating the transition density matrices in the MO basis yields

$$J_{DA} = \sum_{ijkl} \rho_{ij}^{(A)}(ijkl) \rho_{kl}^{(D)} \quad (15)$$

where we have used the Mulliken convention for denoting the electronic repulsion integral. Following Fujimoto,²⁶ the exchange contribution to the EC can be approximated in analogy to the direct contribution by

$$K_{DA} = -\frac{1}{2} \sum_{ijkl} \rho_{ij}^{(A)}(illkj) \rho_{kl}^{(D)} \quad (16)$$

The total coupling is the sum of direct and exchange contributions.

$$V_{DA} = J_{DA} + K_{DA} \quad (17)$$

2.3. Ideal Dipole Approximation. If the intermolecular distance X_{DA} is large compared to the intramolecular extensions of molecules A and D, the intermolecular Coulomb interaction can be subjected to a multipole expansion, which is truncated after the dipole–dipole contribution.

$$V_{DA} = \sum_{jk} \frac{e^2}{|\vec{X}_{DA} + \vec{r}_j^{(A)} - \vec{r}_k^{(D)}|} = \sum_{jk} \frac{e^2}{|\vec{X}_{DA} + \vec{r}_{jk}|} \quad (18)$$

$$\approx e^2 \sum_{jk} \frac{1}{|\vec{X}_{DA}|} + \vec{r}_{jk} \cdot \vec{\nabla} \frac{1}{|\vec{X}_{DA}|} - \frac{1}{2} (\vec{r}_{jk} \vec{r}_{jk} \cdot \vec{\nabla}) (\vec{r}_{jk} \cdot \vec{\nabla}) \frac{1}{|\vec{X}_{DA}|} \quad (19)$$

$$\approx e^2 \sum_{jk} \frac{1}{|\vec{X}_{DA}|} - \frac{\vec{r}_{jk} \cdot \vec{X}_{DA}}{|\vec{X}_{DA}|^3} - \frac{1}{2} \left(\frac{\vec{r}_{jk}^2}{|\vec{X}_{DA}|^3} - 3 \frac{(\vec{r}_{jk} \cdot \vec{X}_{DA})^2}{|\vec{X}_{DA}|^5} \right) \quad (20)$$

Herein, j denotes the j th electron of molecule A and k is the k th electron of molecule D. The first- and second-order terms, as well as parts of the third-order term, vanish because of the charge neutrality of the individual molecules. Employing the definition of the transition dipole moments,

$$\vec{\mu}_A = e \sum_j \vec{r}_j^{(A)} \quad \text{and} \quad \vec{\mu}_D = e \sum_k \vec{r}_k^{(D)} \quad (21)$$

of molecules A and D, respectively, the term finally reads

$$V_{DA} = \frac{\vec{\mu}_A \vec{\mu}_D}{|\vec{X}_{DA}|^3} - 3 \left[\frac{(\vec{\mu}_A \vec{X}_{DA})(\vec{\mu}_D \vec{X}_{DA})}{|\vec{X}_{DA}|^5} \right] \quad (22)$$

Introducing unit vectors pointing in the directions of the intermolecular distance vector \vec{e}_{DA} , which is defined as

$$\vec{e}_{\text{DA}} = \frac{\vec{X}_{\text{DA}}}{|\vec{X}_{\text{DA}}|}$$

and the directions of the transition dipole moments \vec{n}_D and \vec{n}_A , which are defined, respectively, as

$$\vec{n}_D = \frac{\vec{\mu}_D}{|\vec{\mu}_D|}$$

and

$$\vec{n}_A = \frac{\vec{\mu}_A}{|\vec{\mu}_A|}$$

the EC matrix element can be expressed in the familiar form

$$V_{\text{DA}} = \kappa_{\text{DA}} \frac{|\vec{\mu}_A| \cdot |\vec{\mu}_D|}{|\vec{X}_{\text{DA}}|^3} \quad (23)$$

where κ_{DA} is the so-called orientation factor,

$$\kappa_{\text{DA}} = \vec{n}_A \cdot \vec{n}_D - 3(\vec{e}_{\text{DA}} \cdot \vec{n}_A)(\vec{e}_{\text{DA}} \cdot \vec{n}_D) \quad (24)$$

2.4. Computational Details. The equilibrium geometries of the singlet ground states (S_0) of the EET cassettes and the individual monomers were optimized using density functional theory (DFT), in conjunction with the B3LYP hybrid functional.³¹ The molecular structures of the first excited singlet states (S_1) of both BODIPY and anthracene were optimized using time-dependent density functional theory (TDDFT). Unless otherwise stated, all calculations were performed with TURBOMOLE 6.5,³² employing a basis set of split valence quality with polarization functions on all atoms (SVP).³³ For the optimization of the minimum geometries of the EET cassettes and coordinate scans, the m5 integration grid was used. Frequency analyses at the S_0 and S_1 minimum geometries were carried out using the SNF program package.³⁴ Unrelaxed torsion angle scans of the EET cassettes were performed along selected internal coordinates starting from preoptimized C_s -symmetric structures in which the planes of BODIPY and anthracene are perpendicularly oriented.

The photophysical properties at the ground- and excited-state minima of the monomers (vertical transition energies, transition density matrices, and transition dipole moments) were calculated using the combined density functional and multireference configuration interaction (DFT/MRCI) program.³⁵ In these calculations, Kohn–Sham orbitals of a ground-state calculation employing the BHLYP functional³⁶ were utilized. The two-electron integrals used in the DFT/MRCI and MTD calculations were approximated with the resolution of the identity method, as given by

$$(ijkl) \approx \sum_{P,Q} (ij|P) \cdot (P|Q)^{-1} \cdot (Q|kl) \quad (25)$$

where P and Q are auxiliary basis sets.^{37,38}

In the DFT/MRCI method, dynamic correlation effects are considered by DFT, whereas static correlation effects are taken into account by a MRCI expansion. The configurations used in the MRCI are based on Kohn–Sham orbitals of a closed-shell electronic state. Double-counting of dynamic correlation is avoided by the use of an effective Hamiltonian comprising five empirical parameters that are independent from the target molecule. At present, parameter sets are only available for the BHLYP functional. The MRCI expansion is truncated by considering only orbitals below a certain energy cutoff. Within

this paper, we used the original set of parameters³⁵ and an orbital selection energy threshold of 1.0 E_H to compute the 10 lowest eigenvectors. The initial MRCI reference space was spanned by all single and double excitations from the four highest occupied MOs to the four lowest unoccupied MOs of the ground-state Kohn–Sham determinant. A second DFT/MRCI step was performed with a refined reference space comprising all configurations, which contribute to one of the 10 lowest-lying eigenvectors of the initial DFT/MRCI calculation with a squared coefficient of 0.003 and larger.

To calculate the EET between the donor and the acceptor in the EET cassettes, two fragmentation models were developed, which are based on the work of Caprasecca et al.³⁹ (Figure 2).

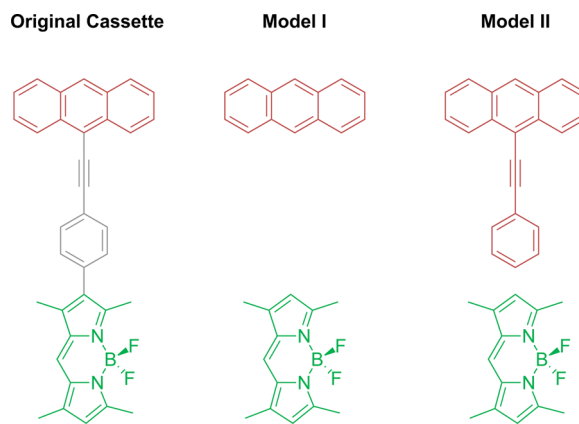


Figure 2. Fragmentation models developed to calculate the EC in the studied EET cassettes, using the example of B2-PE-A. According to fragmentation model I, the linker is completely removed from the relaxed ground-state structure. Fragmentation model II tries to approximate the influence of the molecular structure of the linker on the EC by assigning the latter to the donor moiety. In both models, the obtained fragments are saturated with hydrogen atoms and the newly created C–H bond were relaxed, keeping the rest of the molecule fixed.

According to fragmentation model I, only the distance between the donor and the acceptor was considered (TSEET). The molecular linker was removed from the optimized ground-state structure and the obtained monomers were saturated with hydrogen atoms. The newly created C–H bonds were relaxed keeping the rest of the molecules fixed. Fragmentation model II aims to take the influence of the molecular linker on the EC into account and, therefore, can also include the through-bond contribution. Based on the analysis of the MOs, the linker was assigned to the donor moiety. The obtained fragments were again saturated with hydrogen and relaxed.

EET rates were calculated from the spectral overlap and EC matrix element according to eq 12. The EC matrix elements were computed according to eqs 13, 17, and 23. To this end, a FORTRAN program (FRECK, which stands for Fragment Excitonic Coupling Kit) was newly devised that is adapted to the DFT/MRCI code. In the framework of IDA, the intermolecular distance r_{DA} serves as a measure for the distance between the coupled transition dipoles. As is common practice, we chose the barycenters of the respective monomers as reference.

Vibrationally resolved absorption and emission spectra of BODIPY and anthracene, respectively, were generated with the VIBES program,^{40,41} using a temperature of 298 K, an integration time interval of 3000 fs, and a Gaussian damping

of the correlation function of a width of 100 cm^{-1} . Both spectra were normalized to unit area and the spectral overlap was determined by numerical integration.

To approximate the influence of molecular vibrations on the EC matrix-element-free *ab initio* Born–Oppenheimer molecular dynamic (MD) simulations of all EET cassettes were performed on the ground-state potential energy surfaces (PES) using TURBOMOLE. The program employs the Leapfrog Verlet algorithm⁴² to integrate Newton's equation of motion. All simulations were performed in vacuum at a temperature of 298 K. The equilibrium geometries and random initial velocities corresponding to an initial temperature of 298 K were used as starting points for the MD simulations. The integration time step for the MD simulations was set to 1.94 fs. The MD simulations reached a length of 3.87 ps. Conformations saved at 97 fs intervals were used for analysis. The total EET rate was calculated by taking the average of the EET rates of each conformation, neglecting the exchange contribution to the EC and applying fragmentation model I. For B8-PE-A, we also used fragmentation model II for comparison.

3. RESULTS AND DISCUSSION

3.1. Benchmark Calculations. To validate the implementations of the IDA and MTD approaches, benchmark calculations were performed using a π -stacked ethylene dimer as the model system (Figure 3). For this system, literature data

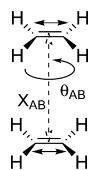


Figure 3. Chemical structure of the π -stacked ethylene dimer used for benchmark calculations. $S_0 \rightarrow S_1$ transition dipole moments are indicated as arrows. The distance X_{AB} between the two π -stacked monomers is indicated as a dashed arrow. θ_{AB} denotes the dihedral between the donor and the acceptor.

are available.²⁶ EC was calculated for varying intermolecular distances and torsion angles, while the intramolecular geometry parameters were kept fixed to their ground-state values. The exact EC referred to as "FullQM" obtained from half of the Davydov splitting was used as reference.

A DFT/MRCI calculation of an ethylene monomer using the TZVP (SVP) basis set⁴³ yields a vertical excitation energy of 8.03 eV (154 nm) (8.41 eV (147 nm)) at the ground-state geometry. The experimental absorption spectrum shows a very broad absorption band ranging from 140 nm (8.86 eV) to 172 nm (7.21 eV) with a maximum at ~ 161 nm (7.70 eV).⁴⁴ Taking into account that the S_1 state of ethylene exhibits a strongly displaced minimum geometry with orthogonally twisted CH₂ groups^{45,46} and considering a fidelity of the DFT/MRCI method of 0.2 eV, the agreement with the experiment is satisfactory. The wave function of the S_1 state is composed almost exclusively of the determinant describing the excitation from the highest occupied molecular orbital (HOMO) to the lowest unoccupied molecular orbital (LUMO). A total transition dipole moment of 4.27 D (4.24 D) was found pointing in the direction of the C=C bond.

EC matrix elements at various internuclear distances and orientations are displayed in Figures 4 and 5. When the intermolecular distance of the ethylene π -stack is increased at a

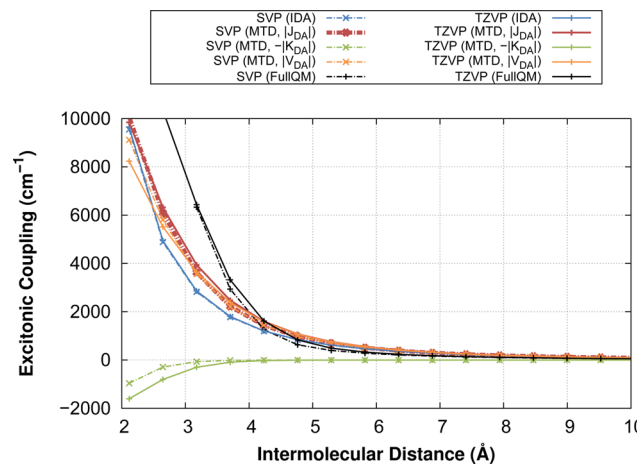


Figure 4. Distance and basis set dependency of IDA, MTD, and FullQM calculations on the ethylene π -stack. J_{DA} denotes the direct contribution to the EC, K_{DA} is the exchange contribution, and V_{DA} is the total through-space EC. "FullQM" denotes the exact EC derived from the Davydov splitting.

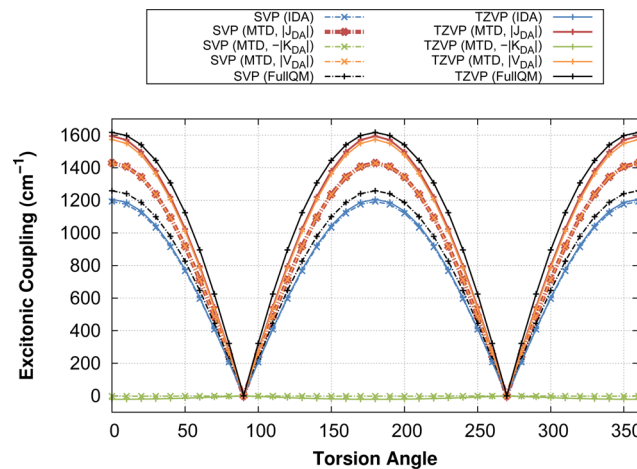


Figure 5. Basis set and torsional dependency of IDA, MTD, and FullQM calculations on the ethylene π -stack for an intermolecular distance of 8 \AA (4.23 Å). (For the denomination of terms, see Figure 4.)

fixed torsion angle of 0° , the direct contribution to the EC decreases as $|\vec{X}_{AB}|^{-3}$ (Figure 4). While the EC obtained from the IDA is almost independent of the basis set, MTD provides slightly higher direct contributions of the EC when the larger TZVP basis set is used. The exchange part of the EC only has an appreciable influence if the intermolecular distance is smaller than ~ 4.5 Å. The exchange contribution to the EC is dependent much stronger on the size of the basis set than the direct contribution. This behavior is to be expected, because the exchange interaction is dependent on the orbital overlap between the two molecules. At large intermolecular separations, the approximate methods are seen to perform quite well in comparison with the exact EC obtained from the Davydov splitting. Up to a distance of ~ 4.7 Å, the exact EC is somewhat smaller than the MTD and IDA values. When $|\vec{X}_{AB}|$ is decreased further, a crossover of the curves in Figure 4 is observed. Below the typical van der Waals distance, the Davydov splitting rises substantially steeper than $|\vec{X}_{AB}|^{-3}$. This behavior is attributed to the deformation of the π -orbital densities in the supermolecular calculation due to Pauli repulsion. In contrast, the shapes of the

corresponding monomer orbitals employed in the MTD and IDA approximations remain unchanged when the two ethylene molecules come closer.

Varying the torsion angle between the two monomers at a fixed distance of $8 a_0$ (4.24 Å), the modulus of the EC was found to reach the maximum value when the torsion angle amounts to 0° or 180° where the transition dipole moments are oriented in parallel manner (Figure 3). At the chosen intermolecular distance, the exchange contribution to the total EC is almost negligible. The EC is zero when the MTD moments are pointing in perpendicular directions. This is the case if the torsion angle is 90° or 270° . Between two minima, the EC is described by a reversed parabolically shaped function. These results are in accordance with what has been reported by Fujimoto.²⁶

In the SVP basis set, the exact EC obtained from the Davydov splitting has a maximum value of 1259 cm^{-1} , while the maximal exact EC amounts to 1617 cm^{-1} when using the larger TZVP basis set. The substantial deviation of 358 cm^{-1} can be traced back to the different representation of the outer parts of the $2p$ orbitals by the two basis sets. While the most diffuse p Gaussian function exhibits an exponent of 0.1527 in the SVP basis, this spatial region is covered by two freely varying Gaussian functions with exponents of 0.2889 and 0.1005 in the TZVP basis. The EC calculated at the DFT/MRCI level of theory, using the TZVP basis set is in good agreement with the results reported by Fujimoto for the same system using configuration interaction singles (CIS).

Calculating the EC with the MTD approach, we find only a small deviation from the exact EC when the TZVP basis set is used. If the SVP basis is employed instead, the MTD approximation overestimates the corresponding value derived from the Davydov splitting. These results suggest that the EC in an ethylene dimer can be determined without significant deviation if the MTD approach and at least the TZVP basis set is used.

The EC matrix elements computed using IDA significantly differ from the exact results obtained from the Davydov splitting when the TZVP basis set is used. Employing the smaller SVP basis set, the exact EC matrix elements are described with less accuracy, yielding much smaller results, similar to those obtained from IDA calculations with either the TZVP or SVP basis set. This result confirms the inferior performance of IDA at small distances previously reported by Wong et al.,²⁷ even if the larger TZVP basis set is used.

Summarizing, we find that the exact EC in a π -stacked ethylene dimer is strongly dependent on the size of the basis set. MTD is a good approximation as long as at least a basis set of TZVP quality is used. The exchange contribution to the EC coupling matrix element is negligible for intermolecular distances larger than 4.5 Å. The IDA description of the EC is not enhanced by the use of the larger TZVP basis instead of the SVP basis. The deviation between the monomer-based calculations and the exact EC is caused by the fact that the distortion of the electron density of one monomer by the other is not taken into account. Since donor and acceptor are well separated in the studied EET cassettes, the error is considered to be small. In principle, the influence of the electron density of the other monomer could, for example, be considered in a subsystem formalism.⁴⁷

3.2. Energy Transfer Cassettes. An overview over the calculated vertical absorption and emission energies of

anthracene and BODIPY and corresponding experimental results is given in Table 1.

Table 1. Calculated Vertical Absorption and Emission Energies, as Well as Corresponding Transition Dipole Moments (TDM) of BODIPY, Anthracene, and the Fragments Used in Fragmentation Model II^a

molecule/ fragment	$\Delta E_{S_0 \rightarrow S_1}$ (eV) [exp]	TDM (D)	$\Delta E_{S_0 \rightarrow S_1}$ (eV) [exp]	TDM (D)
BODIPY	2.64 [2.46] ^{16,54}	8.0	2.53 [2.40] ^{16,54}	3.2
anthracene	3.53 [3.60] ^{49–52}	3.1	3.13 [3.12] ^{52,53}	3.2
E-A	3.22	4.3		
PE-A	2.96	6.8		
EPE-A	2.83	8.2		

^aThe energies of the monomers (BODIPY and anthracene) are calculated with respect to their relaxed ground-state geometries. The excitation energies of the fragments are calculated with respect to the relaxed ground-state geometries of the preliminary cassettes after saturation with hydrogen and letting the newly created C–H bond relax.

3.2.1. Anthracene. In 2008, some of us already reported on the absorption spectrum of anthracene calculated at the DFT/MRCI level of theory.⁴⁸ The relevant results of that study will be reviewed here. We also comment on the calculation of the vibrationally resolved emission spectrum.

The ground and first excited states of anthracene can be classified according to the D_{2h} molecular point group. While the first excited singlet state belongs to the B_{2u} irreducible representation, the electronic ground state has A_g symmetry. The 1^1B_{2u} wave function is mainly composed of the HOMO \rightarrow LUMO excitation and to a minor extent of HOMO–1 \rightarrow LUMO+1. The involved frontier orbitals are shown in Figure 6. Using the SVP basis set, the vertical excitation energy at the ground-state equilibrium geometry is 3.52 eV (352 nm). When the larger TZVP basis set is employed, the vertical excitation energy does not change significantly. Comparison of these results to the experimental value of 3.60 eV (344 nm)^{49–52} suggests that the DFT/MRCI method using a SVP basis describes the $1^1A_g \rightarrow 1^1B_{2u}$ with a sufficient degree of precision. The calculated transition dipole moment has an absolute value of 3.10 D and points in the direction of the short molecular axis (Figure 1).

A DFT/MRCI calculation at the geometry of the optimized 1^1B_{2u} state yields a vertical emission energy of 3.13 eV (396 nm, $25\,245 \text{ cm}^{-1}$). The experimental fluorescence spectrum was measured in cyclohexane and is composed of five peaks at 375 nm (26667 cm^{-1}), 397 nm (25189 cm^{-1}), 421 nm (23753 cm^{-1}), 446 nm (22422 cm^{-1}), and 475 nm (21053 cm^{-1}).^{52,53} The calculated vertical transition with a wavelength of 396 nm corresponds to the experimental peak with the highest intensity at 397 nm. The vibrational frequencies of the S_0 and S_1 states and the adiabatic excitation energies were used for the calculation of a vibrationally resolved emission spectrum (see Figure 7). The computed emission spectrum has the same shape as the experimental fluorescence spectrum, with a peak at $26\,901 \text{ cm}^{-1}$ (372 nm) having a shoulder at $26\,512 \text{ cm}^{-1}$ (377 nm) and a peak at $25\,367 \text{ cm}^{-1}$ (394 nm) having a shoulder at $24\,976 \text{ cm}^{-1}$ (400 nm) as well as peaks at $23\,861 \text{ cm}^{-1}$ (419 nm) and $22\,365 \text{ cm}^{-1}$ (447 nm).

3.2.2. BODIPY. In this work, we used a C_{2v} symmetric BODIPY derivate, which carries four methyl substitutents at

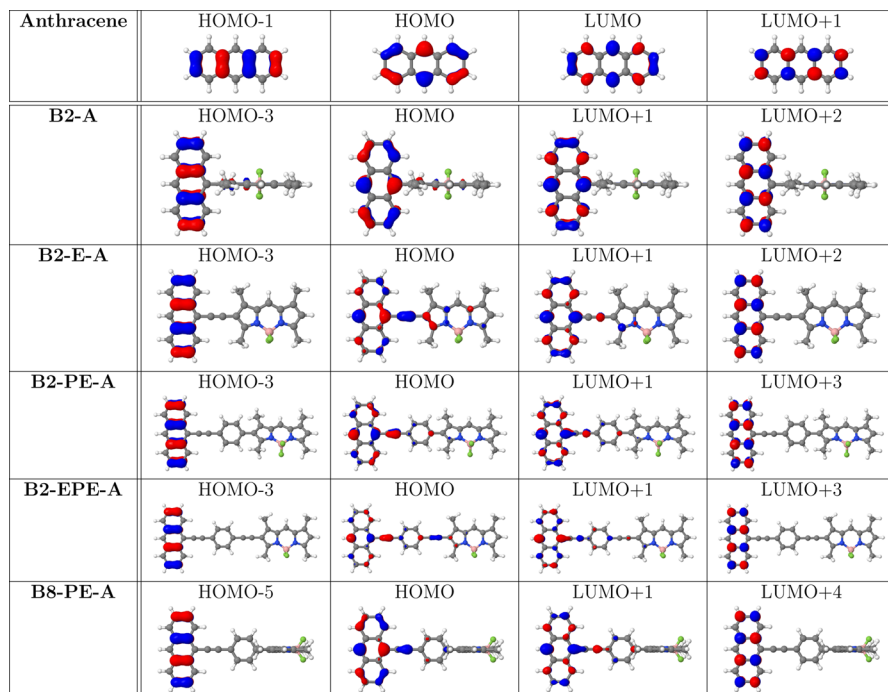


Figure 6. Frontier orbitals of anthracene involved in the $S_0 \rightarrow S_1$ transition and their corresponding orbitals computed for the EET cassettes.

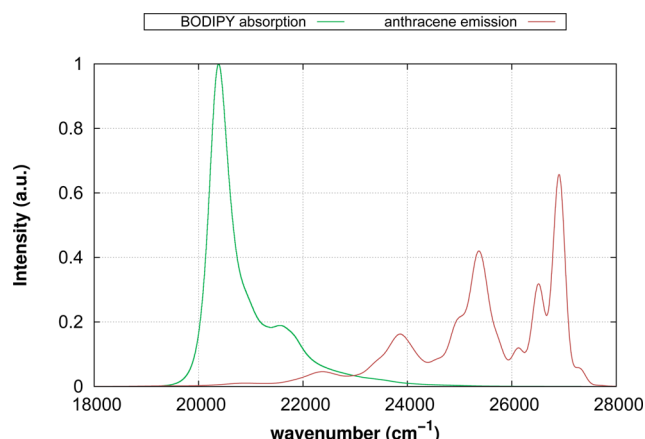


Figure 7. Computed vibrationally resolved anthracene emission and BODIPY absorption spectrum.

C1, C3, C5, and C7. Using either the SVP or the TZVP basis set, the first excited singlet state at DFT/MRCI level of theory is the 1^1B_2 state with a vertical transition energy of 2.63 eV (472 nm). This result agrees well with the experimental absorption maximum of 2.46 eV (505 nm),^{16,54} taking into account the precision of the theoretical method used and the fact that the experimental result was measured in ethanol. The S_1 state is dominated by the HOMO \rightarrow LUMO excitation but exhibits also contributions from the HOMO-1 \rightarrow LUMO excitation and the determinant describing the double excitation HOMO, HOMO-3 \rightarrow LUMO.² The MOs involved in the $S_0 \rightarrow S_1$ excitation are shown in Figure 8. The vibrationally resolved absorption spectrum (Figure 7) shows a sharp peak of high intensity at $\sim 20\,470\text{ cm}^{-1}$ (489 nm) with a smaller shoulder at $21\,571\text{ cm}^{-1}$ (464 nm).

The vertical emission energy, with respect to the optimized S_1 state, is 2.52 eV, corresponding to a wavelength of 492 nm, using either the SVP or the TZVP basis sets. This result again

agrees well to the experimental emission maximum of 2.40 eV (516 nm) measured in ethanol.^{16,54}

3.3. Orientation of the Donor and Acceptor Moieties.

To obtain an overview over the potential energy surfaces (PESs) of the EET cassettes, we performed unrelaxed scans along selected internal coordinates (Figure 9). In B8-PE-A, the linker was fixed in a perpendicular position, with respect to the BODIPY frame, because of the strong steric repulsion between the phenyl ring of the linker and the methyl groups located at C1 and C7 of the BODIPY moiety, even preventing a coplanar conformation. In B2-EPE-A and B2-PE-A, the linker was kept in plane with anthracene, since there is no obvious steric interaction between anthracene and the phenyl ring of the linker. The steric repulsion between the methyl groups located at C1 and C3 of the BODIPY moiety and the appropriate phenyl group is much weaker than in B8-PE-A. For that reason, the corresponding degree of freedom was scanned in these cases. The torsion angle of the minimum nuclear structure is dependent on the steric repulsion between the donor and the acceptor on the one hand and, as far as possible, the conservation of a planar π -conjugated system on the other hand. In case of B2-A, the donor and the acceptor come very close and torsion angles of 75° – 105° can be regarded as a compromise between conservation of the π -conjugated system and a strong steric repulsion. The methyl groups located at C1 and C3 of BODIPY even prevent a planar conformation. In contrast, in B2-E-A and B2-EPE-A, an almost planar conformation is preferred because the π -conjugated system can be conserved on the overall molecule. Assuming structures with an energy lower than $k_B T$ to be thermally occupied, the torsion angle may change up to 35° and 50° , respectively, around the global minimum. In B2-PE-A the steric interactions between the methyl groups of BODIPY and the adjacent phenyl ring of the linker determine the torsion angle. We find a global minimum at a torsion angle between the donor and acceptor frame of $\sim 62^\circ$. Because of the low rotational barrier,

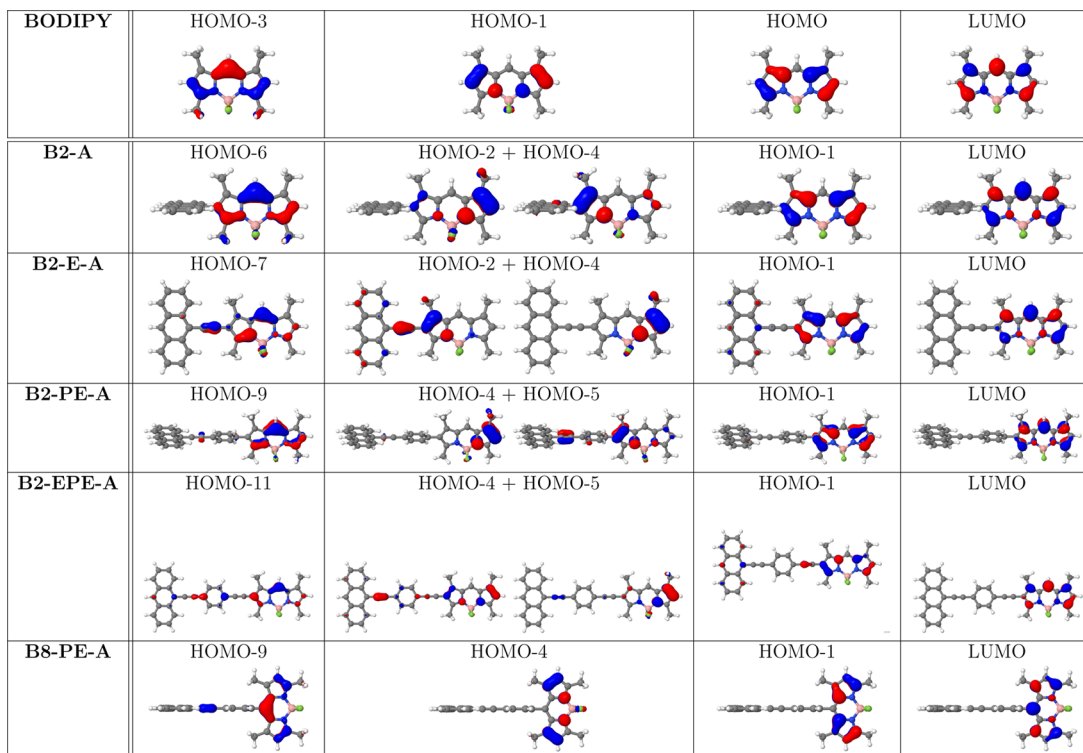


Figure 8. Frontier orbitals of BODIPY involved in the $S_0 \rightarrow S_1$ transition and their corresponding orbitals computed for the EET cassettes. For all EET cassettes except for B8-PE-A, HOMO-1 of BODIPY is recovered as a linear combination of two orbitals.

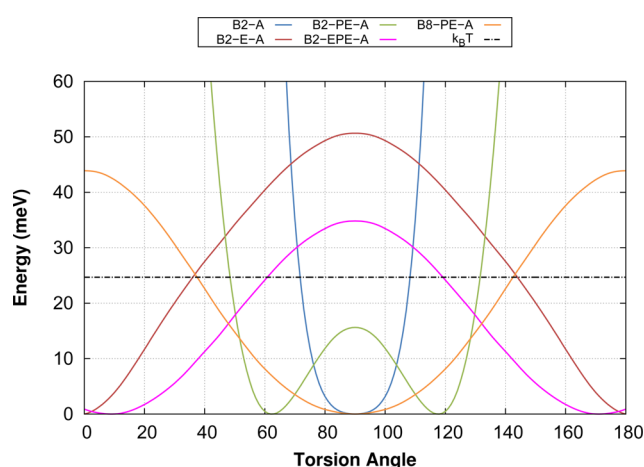


Figure 9. Unrelaxed electronic ground-state scans of the torsion angle between the planes of BODIPY and anthracene (B3LYP level of theory, steps of 1°). The linker was fixed perpendicular to the BODIPY frame in B8-PE-A. In B2-PE-A and B2-EPE-A, the linker was kept in plane with anthracene. All values are given with respect to the conformation that yields the lowest energy. Structures with an energy lower than $k_B T$ are assumed to be thermally occupied.

structures with dihedrals between 50° and 130° are assumed to be occupied. In B8-PE-A, a perpendicular orientation is preferred, because of the steric interaction between the methyl groups located at C1 and C7 of BODIPY and the adjacent phenyl ring of the linker. The torsion angle may change up to 55° around the global minimum. Nevertheless, the torsion angle does not significantly influence the EC coupling matrix element, since it does not change the relative orientation of the transition dipole moments. The dihedral angles between the donor and the acceptor moieties in the relaxed ground-state

geometries of the cassettes slightly deviate from those of the unrelaxed scans, particularly because of relaxation of the methyl groups and the phenyl rings.

3.4. Excitonic Coupling. In the framework of TSEET, the molecular linker is not directly involved in the EET but serves as a spacer conserving a certain distance and the relative orientation of the donor and the acceptor. This situation is described in our fragmentation model I. Our fragmentation model II takes also parts of TBEET into account while neglecting charge-transfer (CT) contributions. Excitonic couplings between BODIPY and anthracene calculated with the two different fragmentation models are shown in Table 2. Among the EET cassettes examined in this work, B2-A is the one with the smallest donor–acceptor distance. In this cassette, C2 of BODIPY is directly linked to C9 of anthracene. Using MTD and fragmentation model I, we find a value of 1141 cm^{-1} for the direct contribution and a value of 30.0 cm^{-1} for the exchange contribution. Because of the small intermolecular distance of only 6.3 \AA , the direct contribution is very high and the exchange contribution is not negligibly small. A substantially smaller value of 983 cm^{-1} for the direct contribution is obtained in the IDA. As already discussed for the ethylene dimer, IDA underestimates the exact EC at small distances, because of the limitations of the multipole expansion. With regard to the relative orientation of BODIPY and anthracene in this cassette, EC is maximal because the transition dipole moments are oriented in a parallel manner. In B2-E-A, B2-PE-A, and B2-EPE-A, the arrangement is essentially identical but the distance is successively increased. Concomitantly, direct contribution and exchange contributions successively become smaller. The exchange contribution decreases much faster than the direct contribution. It exhibits a value of 3.5 cm^{-1} for B2-E-A and is found to be zero in the case of all other EET cassettes. For a donor–acceptor distance

Table 2. Direct and Exchange Contributions to the EC Matrix Elements, as Well as EET Rates of the Studied EET Cassettes Calculated with Different Models

	B2-A	B2-E-A	B2-PE-A	B2-EPE-A	B8-PE-A
<i>S</i> ₀ Geometry (Fragmentation Model I)					
spectral overlap integral (cm)				1.06 × 10 ⁻⁵	
IDA					
J _{DA} (cm ⁻¹)	983	350	109	63	0.0
MTD					
J _{DA} (cm ⁻¹)	1141	423	119	67	0.0
K _{DA} (cm ⁻¹)	30.0	3.5	0.0	0.0	0.0
EET rate (s ⁻¹)	2.3 × 10 ¹³	3.2 × 10 ¹²	2.6 × 10 ¹¹	8.3 × 10 ¹⁰	4.3 × 10 ⁰
Acceptor <i>S</i> ₀ , Donor <i>S</i> ₁ Geometry (Fragmentation Model I)					
spectral overlap integral (cm)				1.06 × 10 ⁻⁵	
MTD					
J _{DA} (cm ⁻¹)	1140	426	123	69	0.0
K _{DA} (cm ⁻¹)	30.0	3.1	0.0	0.0	0.0
EET rate (s ⁻¹)	2.3 × 10 ¹³	3.3 × 10 ¹²	2.8 × 10 ¹¹	8.8 × 10 ¹⁰	2.5 × 10 ⁰
MD Snapshots (Fragmentation Model I)					
spectral overlap integral (cm)				1.06 × 10 ⁻⁵	
MTD					
J _{DA} (cm ⁻¹)	951	377	114	62	6.9
EET rate (s ⁻¹)	2.1 × 10 ¹³	2.8 × 10 ¹²	2.7 × 10 ¹¹	7.1 × 10 ¹⁰	1.62 × 10 ⁹
<i>S</i> ₀ Geometry (Fragmentation Model II, Spectral Overlap of Monomers)					
spectral overlap integral (cm)				1.06 × 10 ⁻⁵	
MTD					
J _{DA} (cm ⁻¹)		1013	766	678	0.0
K _{DA} (cm ⁻¹)		92	27	46	0.0
EET rate (s ⁻¹)		1.6 × 10 ¹³	1.0 × 10 ¹³	7.3 × 10 ¹²	9.9 × 10 ²
<i>S</i> ₀ Geometry (Fragmentation Model II, Adapted Spectral Overlap)					
spectral overlap integral (cm)		8.39 × 10 ⁻⁵	2.46 × 10 ⁻⁴	1.79 × 10 ⁻⁴	2.46 × 10 ⁻⁴
MTD					
J _{DA} (cm ⁻¹)		1013	766	678	0.0
K _{DA} (cm ⁻¹)		92	27	46	0.0
EET rate (s ⁻¹)		8.4 × 10 ¹³	1.6 × 10 ¹⁴	8.4 × 10 ¹³	1.6 × 10 ⁴
MD Snapshots (Fragmentation Model II, Adapted Spectral Overlap)					
spectral overlap integral (cm)					2.46 × 10 ⁻⁴
MTD					
J _{DA} (cm ⁻¹)					18
EET rate (s ⁻¹)					1.5 × 10 ¹¹
exp. EET rate ¹⁹ (s ⁻¹)	>5.0 × 10 ¹²	2.5 × 10 ¹²			

of more than 15 Å (**B2-EPE-A**), IDA and MTD almost provide the same result. Therefore, we strongly recommend that MTD be used for EET cassettes with small molecular linkers.

On the basis of fragmentation model I, we further examined how the relaxation of the anthracene scaffold to its *S*₁ state geometry affects the size of the EC matrix elements (Table 2). For **B2-E-A**, we find an increase of the direct contribution by only 3 cm⁻¹ out of 423 cm⁻¹ in the MTD approach, corresponding to a change by 0.7%. The exchange contribution differs by 0.4 cm⁻¹. On a relative scale, the latter change is larger (i.e., 11.4%). Nevertheless, we consider these changes to be negligible. The direct EC matrix elements of the larger cassettes increase slightly. From these results, we conclude that a possible relaxation of the donor to its *S*₁ state geometry has only a minor effect the EC matrix element. This justifies the use of donor and acceptor geometries directly derived from the electronic ground state of the EET cassette without any further optimization.

Furthermore, we tested the influence of the atomic orbital basis set on the size of the EC, taking the example of **B2-E-A**. Within the IDA, the EC increases by only 0.6% if the large

TZVP basis set is used instead of the SVP basis. The EC computed within the MTD approach is not affected much by an enhanced description of the EC in **B2-E-A** either. The direct contribution to EC decreases by 11 cm⁻¹, to a value of 421 cm⁻¹, if the TZVP basis set is used, while the exchange contribution increases by 0.4 cm⁻¹, to a value of 3.91 cm⁻¹.

Although the donor and acceptor moieties in BODIPY-based EET cassettes are connected covalently by a molecular bridge, there is no obvious way for TBEET.¹⁶ To get an estimate how strongly the linker affects the EC, we applied fragmentation model II. The MOs of the cassettes are largely localized on the donor and the acceptor parts of the system, respectively, and correspond quite well to the frontier orbitals computed for the monomers (see Figures 6 and 8). This holds true best for **B2-A**, since the donor and the acceptor are directly linked in a perpendicular orientation. In all other EET cassettes, we find a slight extension of some of the involved MOs to the linker moiety, indicating an additional contribution of the linker to the EC. Among the frontier orbitals, the HOMO of the donor and the LUMO of the acceptor may be assumed to be the two most important orbitals involved in the EC. As may be seen in

Figure 6, the electron density contribution of the HOMO of all investigated cassettes is mainly located on the donor but extends markedly to the linker atoms. In contrast, no linker contributions are observed for the LUMO (Figure 6), which appears to be an almost-pure acceptor MO. Hence, the molecular linker was assigned to the donor fragment. Using fragmentation model II, we find higher direct contributions of the EC, which decrease much more slowly as the size of the linker increases (see Table 2). The exchange contributions are still very small, compared to the direct contributions, but now are clearly different from zero. In B8-PE-A, the direct and exchange contributions are found to be extremely small in the minimum nuclear arrangement with both fragmentation models, because the transition dipole moments of BODIPY and anthracene are oriented in an almost-perpendicular manner. The influence of the EC on the EET rate will be discussed in the next section.

3.5. EET Rates. EET rates were calculated from the spectral overlap and the EC obtained with the MTD approach (Table 2). Since the spectral overlap of 1.06×10^5 cm is constant for a given donor–acceptor pair in fragmentation model I, the highest EET rate is observed for the EET cassette with the shortest linker. For B2-A, in which donor and acceptor are separated only by a single C–C bond, we obtain an EET rate of 2.3×10^{13} s⁻¹. Fragmentation models I and II do not differ for this cassette. Since the exchange contribution to the EC is extremely small, compared to the direct contribution, it has only a very slight influence on the total EET rate. For all other cassettes, in which the transition dipole moments of anthracene and BODIPY are oriented in a parallel manner, the calculated EET rates are smaller, ranging from 3.2×10^{12} s⁻¹ to 8.3×10^{10} s⁻¹, depending on the length of the molecular linker. Kim et al.¹⁹ found EET rates higher than the temporal resolution of their experiment (5.0×10^{12} s⁻¹) for all cassettes with a parallel orientation of the transition dipole moments. While B2-A and B2-E-A perfectly agree with the experimental evidence, the calculated EET rates of B2-PE-A and B2-EPE-A are smaller by 1 and 2 orders of magnitude, respectively, indicating an increasing influence of the linker. In B8-PE-A, in which the transition dipole moments of the donor and the acceptor are oriented in an almost-perpendicular manner, the calculated EET rate is extremely small (4.3×10^0 s⁻¹). Concomitantly, the calculated EET rate is significantly smaller than the experimental value of 2.5×10^{12} s⁻¹.

For that reason, we investigated the influence of dynamic effects with the help of short *ab initio* MD simulations. We found that the angle between the transition dipole moments of BODIPY and anthracene changes due to vibration. In B8-PE-A, the average displacement from the dihedral between the donor and acceptor moieties of the relaxed ground-state structure amounts to $\sim 5^\circ$ (Figure 10). Since the EC matrix element is minimal at 90° , sampling of the vibrational motion leads to an increased direct contribution and, hence, to an increased average EET rate (1.62×10^9 s⁻¹). Unfortunately, this rate is still smaller than the experimental value by ~ 3 orders of magnitude. In the other EET cassettes, vibrational averaging decreases the direct contribution to the EC between BODIPY and anthracene. Nevertheless, the effect is much weaker and the mean EET rates are only slightly smaller than those calculated for the static case. This behavior can be explained by considering the angular dependency of the EC. When the transition dipole moments of the donor and the acceptor are oriented in a parallel manner, the EC is large. At this point, the

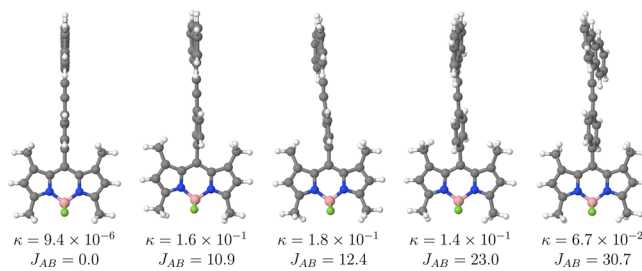


Figure 10. Selected snapshots of the MD simulation of B8-PE-A. J_{AB} denotes the direct coupling of the appropriate snapshot (given in units of cm⁻¹). Orientation factor κ indicates the relative orientation of the transition dipole moments.

slope which describes the change of the EC with the torsion angle is minimal. Thus, a small change of the torsion angle due to molecular vibrations causes only a small decrease of the EC. When the transition dipole moments are oriented in a perpendicular manner, as in the case of B8-E-A, the EC is zero but the slope is maximal. Thus, only small changes of the torsion angle cause a large change of the EC. Independent of the relative orientation of the transition dipole moments, the longer the molecular linker, the more significant the dynamic effects.

The influence of the structure of the molecular linker is estimated by fragmentation model II. Assuming an unchanged spectral overlap integral, we find EET rates ranging from 1.6×10^{13} s⁻¹ (B2-E-A) to 7.3×10^{12} s⁻¹ (B2-EPE-A) for all EET cassettes in which the transition dipole moments are oriented in a parallel manner. For B8-PE-A, we calculated an EET rate of 1.0×10^3 s⁻¹, which is still far from the experimentally predicted value. All calculated rates are higher by 1 to 2 orders of magnitude, compared to the results obtained with fragmentation model I but subsequently decrease with increasing length of the linker as well. Analyzing the $S_0 \rightarrow S_1$ transitions of the donor fragments, we find a decrease of the vertical excitation energy and an increase of the transition dipole moment with increasing size of the linker, when compared to the plain donor. The influence on the spectral overlap integral is crudely estimated by a red-shift of the emission spectrum of anthracene by the appropriate energy difference. Since the shifted donor emission spectrum and the unshifted acceptor absorption spectrum come closer, we find an increasing spectral overlap integral with increasing length of the linker. Taking both altered EC and spectral overlap integral into account, we find the highest EET rate of 1.6×10^{14} s⁻¹ for B2-PE-A. For B2-E-A and B2-EPE-A, we find very similar rates (8.4×10^{13} s⁻¹), which are in the range of the rate of B2-A, in which the donor and acceptor are directly linked via a single C–C bond. All calculated rates are in perfect agreement with experimental findings, predicting EET rates that are higher than the experimental lower limit of 5.0×10^{12} s⁻¹.¹⁹ Not unexpectedly, the rate calculated for B8-PE-A, using a static model (1.6×10^4 s⁻¹), is much smaller than the experimental value. Considering dynamic effects, the EET rate becomes 1.5×10^{11} s⁻¹, which is too small by only 1 order of magnitude.

4. CONCLUSIONS

The EET rate in five different BODIPY-based EET cassettes has been determined with quantum chemical methods. To this end, a computer program was devised that calculates the through-space contributions to the EET rates either in the IDA

or from monomer transition densities of DFT/MRCI wave functions. The correctness of the program was validated by benchmark calculations on a small homodimeric model system of two π -stacked ethylene molecules. Not unexpectedly, the IDA fails to describe the EC at small intermolecular distances. In contrast, the DFT/MRCI-based MTD is found to be a powerful method to approximate the EC and EET rates in EET cassettes with dominant through-space contributions.

Experimental absorption and emission spectra of the acceptor and donor units of the EET cassettes, BODIPY and anthracene, respectively, are reproduced well by vibrationally resolved computed spectra. In the cassettes with short to medium-long molecular linkers, we find that IDA produces significantly smaller EC matrix elements than MTD. Therefore, MTD was chosen for the calculation of the EET rates. For all EET cassettes in which the transition dipole moments of donor and acceptor are oriented in a parallel manner, we find EET rates in the order of the temporal resolution of the experiment¹⁹ when fragmentation model II is used, i.e., when contributions from the molecular linker are taken into account in an approximate manner. If the simpler fragmentation model I is applied to EET cassettes with a longer linker, the EET rates become significantly too small. For **B8-PE-A**, in which the transition dipole moments are oriented in a perpendicular manner, dynamic effects play an important role, increasing the computational EET rate by up to 10 orders of magnitude, compared to the static model.

One reason for the deviations of the calculated EET rate of **B8-PE-A** from the experimental values¹⁹ may be that charge-transfer (CT) contributions are not considered in our calculations. In π -stacked electronically excited perylenebisimide aggregates, such contributions have been shown to be important.⁵⁵ Furthermore, our consideration of the influence of the nuclear motion is only based on very short MD trajectories. More exact rates may be obtained either from longer force-field-based MD simulations or by including vibronic interactions through a Taylor expansion about the Franck–Condon point. Work along these lines is in progress.

AUTHOR INFORMATION

Corresponding Author

*Tel.: +49 211 81-13210. Fax: +49 211 81-13466. E-mail: Christel.Marian@uni-duesseldorf.de.

Notes

The authors declare no competing financial interest.

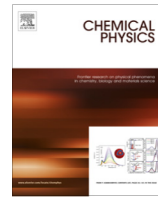
ACKNOWLEDGMENTS

Financial support by the Deutsche Forschungsgemeinschaft (through No. TA 725/1-1) is gratefully acknowledged.

REFERENCES

- (1) Förster, T. *Ann. Phys. (Berlin, Ger.)* **1948**, *437*, 55–75.
- (2) Dexter, D. L. *J. Chem. Phys.* **1953**, *21*, 836–850.
- (3) McConnell, H. M. *J. Chem. Phys.* **1961**, *35*, 508–515.
- (4) Pourtois, G.; Beljonne, D.; Cornil, J.; Ratner, M. A.; Brédas, J. L. *J. Am. Chem. Soc.* **2002**, *124*, 4436–4447.
- (5) May, V.; Kühn, O. *Charge and Energy Transfer Dynamics in Molecular Systems*; Wiley–VCH: Weinheim, Germany, 2004.
- (6) Hennebicq, E.; Pourtois, G.; Scholes, G. D.; Herz, L. M.; Russell, D. M.; Silva, C.; Setayesh, S.; Grimsdale, A. C.; Müllen, K.; Brédas, J.-L.; et al. *J. Am. Chem. Soc.* **2005**, *127*, 4744–4762.
- (7) Fückel, B.; Köhn, A.; Harding, M. E.; Diezemann, G.; Hinze, G.; Basché, T.; Gauss, J. *J. Chem. Phys.* **2008**, *128*, 074505.
- (8) Stehr, V.; Engels, B.; Deibel, C.; Fink, R. *J. Chem. Phys.* **2014**, *140*, 024503.
- (9) Dirac, P. A. M. *Proc. R. Soc. London, Ser. A* **1927**, *114*, 243–265.
- (10) Fermi, E. *Nuclear Physics: A Course Given by Enrico Fermi at the University of Chicago*; University of Chicago Press: Chicago, IL, 1950 (ISBN: 9780226243658).
- (11) Rousseau, T.; Cravino, A.; Bura, T.; Ulrich, G.; Ziessel, R.; Roncali, J. *J. Chem. Commun.* **2009**, 1673–1675.
- (12) Rousseau, T.; Cravino, A.; Ripaud, E.; Leriche, P.; Rihm, S.; de Nicola, A.; Ziessel, R.; Roncali, J. *J. Chem. Commun.* **2010**, *46*, 5082–5084.
- (13) Mueller, T.; Gresser, R.; Leo, K.; Riede, M. *Sol. Energy Mater. Sol. Cells* **2012**, *99*, 176–181.
- (14) Chen, J. J.; Conron, S. M.; Erwin, P.; Dimitriou, M.; McAlahney, K.; Thompson, M. E. *ACS Appl. Mater. Interfaces* **2015**, *7*, 662–669.
- (15) Bura, T.; Leclerc, N.; Fall, S.; Lévéque, P.; Heiser, T.; Retailleau, P.; Rihm, S.; Mirloup, A.; Ziessel, R. *J. Am. Chem. Soc.* **2012**, *134*, 17404–17407.
- (16) Loudet, A.; Burgess, K. *Chem. Rev.* **2007**, *107*, 4891–4932.
- (17) Briggs, E. A.; Besley, N. A.; Robinson, D. *J. Phys. Chem. A* **2013**, *117*, 2644–2650.
- (18) Wan, C.-W.; Burghart, A.; Chen, J.; Bergström, F.; Johansson, L. B.-Å.; Wolford, M. F.; Kim, T. G.; Topp, M. R.; Hochstrasser, R. M.; Burgess, K. *Chem.—Eur. J.* **2003**, *9*, 4430–4441.
- (19) Kim, T. G.; Castro, J. C.; Loudet, A.; Jiao, J. G.-S.; Hochstrasser, R. M.; Burgess, K.; Topp, M. R. *J. Phys. Chem. A* **2006**, *110*, 20–27.
- (20) Caprasecca, S.; Curutchet, C.; Mennucci, B. *Photochem. Photobiol. Sci.* **2011**, *10*, 1602–1609.
- (21) Hsu, C.-P. *Acc. Chem. Res.* **2009**, *42*, 509–518.
- (22) Hsu, C.-P.; You, Z.-Q.; Chen, H.-C. *J. Phys. Chem. C* **2008**, *112*, 1204–1212.
- (23) Blancafort, L.; Voityuk, A. A. *J. Chem. Phys.* **2014**, *140*, 095102.
- (24) Fink, R.; Pfister, J.; Schneider, A.; Zhao, H.; Engels, B. *Chem. Phys.* **2008**, *343*, 353–361.
- (25) Fink, R. F.; Pfister, J.; Zhao, H. M.; Engels, B. *Chem. Phys.* **2008**, *346*, 275–285.
- (26) Fujimoto, K. *J. J. Chem. Phys.* **2012**, *137*, 034101.
- (27) Wong, C. Y.; Curutchet, C.; Tretiak, S.; Scholes, G. D. *J. Chem. Phys.* **2009**, *130*, 081104.
- (28) Davydov, A. S. *Sov. Phys. Usp.* **1964**, *7*, 145–178.
- (29) Kasha, M.; Rawls, H. R.; Ashraf El-Bayoumi, M. *Pure Appl. Chem.* **1965**, *11*, 371–392.
- (30) McWeeny, R. *Methods of Molecular Quantum Mechanics*; Academic Press: London, 1989; p 129.
- (31) Stephens, P. J.; Devlin, F. J.; Chabalowski, C. F.; Frisch, M. J. *J. Phys. Chem.* **1994**, *98*, 11623–11627.
- (32) TURBOMOLE V6.5, 2013. A development of University of Karlsruhe and Forschungszentrum Karlsruhe GmbH (1989–2007), TURBOMOLE GmbH, since 2007; available via the Internet at: <http://www.turbomole.com>.
- (33) Schäfer, A.; Horn, H.; Ahlrichs, R. *J. Chem. Phys.* **1992**, *97*, 2571–2577.
- (34) Neugebauer, J.; Reiher, M.; Kind, C.; Hess, B. A. *J. Comput. Chem.* **2002**, *23*, 895–910.
- (35) Grimme, S.; Waletzke, M. *J. Chem. Phys.* **1999**, *111*, 5645–5655.
- (36) Becke, A. D. *J. Chem. Phys.* **1993**, *98*, 1372–1377.
- (37) Vahtras, O.; Almlöf, J.; Feyereisen, M. *Chem. Phys. Lett.* **1993**, *213*, 514–518.
- (38) Weigend, F.; Häser, M.; Patzelt, H.; Ahlrichs, R. *Chem. Phys. Lett.* **1998**, *294*, 143–152.
- (39) Caprasecca, S.; Mennucci, B. *J. Phys. Chem. A* **2014**, *118*, 6484–6491.
- (40) Etinski, M.; Tatchen, J.; Marian, C. M. *J. Chem. Phys.* **2011**, *134*, 154105.
- (41) Etinski, M.; Tatchen, J.; Marian, C. M. *Phys. Chem. Chem. Phys.* **2014**, *16*, 4740–4751.
- (42) Allen, M. P.; Tildesley, D. J. *Computer Simulation of Liquids*; Clarendon Press: Oxford, U.K., 1987.

- (43) Godbout, N.; Salahub, D. R.; Andzelm, J.; Wimmer, E. *Can. J. Chem.* **1992**, *70*, 560–571.
- (44) Platt, J. R.; Klevens, H. B.; Price, W. C. *J. Chem. Phys.* **1949**, *17*, 466–469.
- (45) Levine, B. G.; Ko, C.; Quenneville, J.; Martinez, T. J. *Mol. Phys.* **2006**, *104*, 1039–1051.
- (46) Filatov, M. *J. Chem. Theory Comput.* **2013**, *9*, 4526–4541.
- (47) König, C.; Schlüter, N.; Neugebauer, J. *J. Chem. Phys.* **2013**, *138*, 034104.
- (48) Marian, C. M.; Gilka, N. *J. Chem. Theory Comput.* **2008**, *4*, 1501–1515.
- (49) Biermann, D.; Schmidt, W. *J. Am. Chem. Soc.* **1980**, *102*, 3163–3173.
- (50) Parac, M.; Grimme, S. *Chem. Phys.* **2003**, *292*, 11–21.
- (51) Ferguson, J.; Reeves, L. W.; Schneider, W. G. *Can. J. Chem.* **1957**, *35*, 1117–1136.
- (52) Berlman, I. *Handbook of Fluorescence Spectra of Aromatic Molecules*; Academic Press: New York, 1971.
- (53) Dixon, J. M.; Taniguchi, M.; Lindsey, J. S. *Photochem. Photobiol.* **2005**, *81*, 212–213.
- (54) de Wael, E. V.; Padoen, J. A.; van Koeveringe, J. A.; Lugtenburg, J. *Recl. Trav. Chim. Pays-Bas* **1977**, *96*, 306–309.
- (55) Liu, W.; Settels, V.; Harbach, P. H.; Dreuw, A.; Fink, R. F.; Engels, B. *J. Comput. Chem.* **2011**, *32*, 1971–1981.



Charge-transfer contributions to the excitonic coupling matrix element in BODIPY-based energy transfer cassettes

J. Dominik Spiegel, Igor Lyskov, Martin Kleinschmidt, Christel M. Marian *

Institute of Theoretical and Computational Chemistry, Heinrich Heine University Düsseldorf, Universitätsstr. 1, D-40225 Düsseldorf, Germany

ARTICLE INFO

Article history:

Available online xxxx

ABSTRACT

BODIPY-based dyads serve as model systems for the investigation of excitation energy transfer (EET). Through-space EET is brought about by direct and exchange interactions between the transition densities of donor and acceptor localized states. The presence of a molecular linker gives rise to additional charge transfer (CT) contributions. Here, we present a novel approach for the calculation of the excitonic coupling matrix element (ECME) including CT contributions which is based on supermolecular one-electron transition density matrices (STD). The validity of the approach is assessed for a model system of two π -stacked ethylene molecules at varying intermolecular separation. Wave functions and electronic excitation energies of five EET cassettes comprising anthracene as exciton donor and BODIPY as exciton acceptor are obtained by the redesigned combined density functional theory and multireference configuration interaction (DFT/MRCI-R) method. CT contributions to the ECME are shown to be important in the covalently linked EET cassettes.

© 2016 Published by Elsevier B.V.

1. Introduction

The discovery of 4,4-difluoro-4-bora-3a,4a-diaza-s-indacene (BODIPY)-based compounds by Treibs and Kreuzer in 1968 [1] laid the foundation for a new class of fluorescence dyes characterized by high stability and high fluorescence quantum yields [2]. In the last decades, many applications of BODIPY derivatives ranging from biomolecular labels to sensitizers for solar cells have been reported [3,4]. Dyads in which BODIPY is covalently linked to anthracene as exciton donor serve as excellent model systems for the theoretical and experimental investigation of excitation energy transfer (EET) (Fig. 1). Whereas EET rates deduced from high-resolution spectroscopy measurements were interpreted assuming a through-space mechanism [2,5,6], quantum-chemical studies based on a monomer transition density approach [7,8] focused on through-space and through-bond mechanisms [9]. The contribution of charge transfer (CT) to the through-bond interactions is still an open question. A quantum-chemical study of the dyads may give insight into the relevant transitions. Recently, Liu et al. [10] presented a method with a similar objective as the here presented supermolecular approach. Dividing the target molecule into reasonable fragments, the set of canonical molecular orbitals (MOs) is localized using the Pipek-Mezey algorithm. The configuration interaction singles (CIS) wave functions of the electronically

excited states are transformed to the localized basis yielding local and CT configurations. Mixing of the electronically excited states such that the weight of a single configuration is maximized, quasi-diabatic states are produced which can be used for the calculation of excitonic coupling matrix elements (ECME) including local and CT contributions.

The fast and reliable prediction of excitation energies and excited states properties is one of the challenges in modern quantum chemistry. To this end, electron correlation methods are required treating ground and excited states at similar levels of accuracy. In the electronic ground state, a Kohn-Sham (KS) density functional theory (DFT) treatment is often sufficient. In contrast, multi-configuration approaches are required for a proper description of excited-state properties. For small molecules, *ab initio* complete active space second-order perturbation theory (CASPT2) or multi-reference configuration interaction (MRCI) are valuable methods for this purpose [11,12]. With increasing system size, the concept of active electrons in active orbitals quickly becomes a bottleneck, however. In 1999, Grimme and Waletzke introduced the semi-empirical combined density functional theory and multi-reference configuration interaction (DFT/MRCI) method [13]. Although the original parameterization was performed on a training set of small molecules, where the method reaches a general accuracy of ± 0.2 eV [14], a similar accuracy is observed for extended π -systems such as polyacenes and oligothiophenes [15,16]. This method was therefore employed in our first study of the EET transfer rates in anthracene-BODIPY cassettes based on a

* Corresponding author.

E-mail address: Christel.Marian@uni-duesseldorf.de (C.M. Marian).

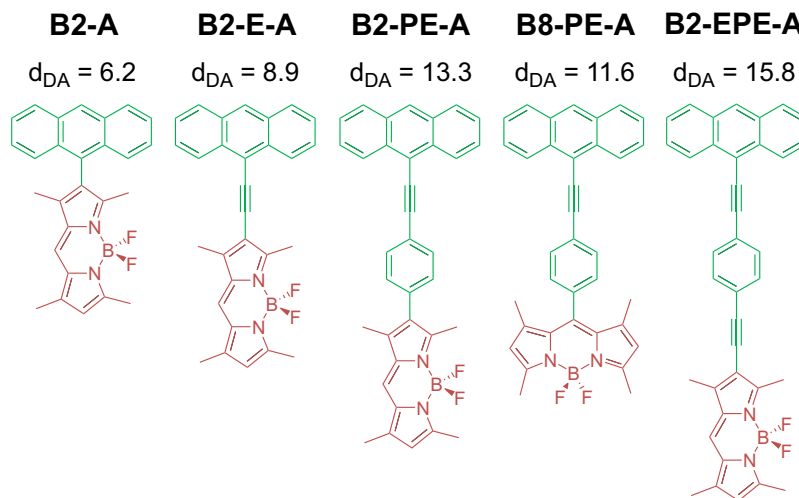


Fig. 1. Division of the studied EET cassettes into donor (green) and acceptor (red) moieties. The molecular linker is regarded as part of the donor fragment. Distances between the centers of mass of anthracene and BODIPY are given in Å. (For interpretation of the references to color in this figure legend, the reader is referred to the web version of this article.)

monomer transition density (MTD) approach [9]. However, in ethylene-tetrafluoroethylene dimers artificially low-lying excited states were encountered when using DFT/MRCI [17]. Most of these problems could be traced back to unphysically large contributions of four-open shell configurations. Recently, some of us presented a redesigned DFT/MRCI Hamiltonian (DFT/MRCI-R) which aims to properly treat supermolecules composed of more than one subsystem [17].

In this paper, we apply both, the original and redesigned DFT/MRCI Hamiltonians to a series of EET cassettes consisting of an anthracene subsystem as exciton donor and a BODIPY subsystem as exciton acceptor linked via a π -conjugated molecular bridge (Fig. 1). We compare the results to experimental absorption spectra of the studied EET cassettes and calculate the ECME between the two lowest donor- and acceptor-localized states using the newly developed supermolecular transition density (STD) approach. The CT contributions to the EET become apparent when comparing the ECMEs computed in the STD and MTD approaches, respectively.

2. Theoretical methods

2.1. Analysis of the excited-state wave functions

Let us start this section with a brief review of a method that is based on one-electron transition density matrices and was introduced by Plasser and Lischka [18] for the analysis of excited-state wave functions. The method provides the percentage of local- and CT-transitions of an electronically excited state in terms a CT matrix. Let A and B denote the subsystems of the supermolecule. According to Plasser and Lischka [18], the extent of charge delocalization within each supermolecular electronically excited state Ψ_n can be recovered from a 2×2 CT matrix Ω^n

$$\Omega^n = \begin{pmatrix} \Omega_{AA}^n & \Omega_{AB}^n \\ \Omega_{BA}^n & \Omega_{BB}^n \end{pmatrix} \quad (1)$$

which can directly be computed from the reduced transition density matrix in a subsystem-localized basis. While the diagonal elements Ω_{AA}^n and Ω_{BB}^n represent the weights of local excitations on subsystems A and B, respectively, the off-diagonal elements Ω_{AB}^n and Ω_{BA}^n are known as CT numbers. They are defined as the

percentage of charge density transferred from one subsystem to the other one during the excitation.

In this work, we employ the reduced transition density matrix in the atomic orbital (AO) basis $\rho^{[\Phi\Psi_n]}$ for constructing the CT matrix. The elements of $\rho^{[\Phi\Psi_n]}$ can be obtained from the reduced one-electron transition density matrix $\rho^{[\Phi\Psi_n]}$ between the electronic ground state Φ and an excited state Ψ_n in the MO basis with elements

$$\rho_{pq}^{[\Phi\Psi_n]} = \langle \Phi | \hat{E}_{pq} | \Psi_n \rangle \quad (2)$$

by the transformation [19]

$$\rho_{\mu\nu}^{[\Phi\Psi_n]} = \sum_{pq} c_{\mu p} \rho_{pq}^{[\Phi\Psi_n]} c_{\nu q} \quad (3)$$

where the $c_{\nu q}$ are elements of the MO coefficient matrix. Applying the AO overlap matrix S to ensure orthonormality, the elements of the CT matrix can be computed as given by

$$\Omega_{A-B}^n = \frac{1}{2} \sum_{\mu \in A} \sum_{\nu \in B} (\rho^{[\Phi\Psi_n]} S)_{\mu\nu} (S \rho^{[\Phi\Psi_n]})_{\mu\nu} \quad (4)$$

where AOs μ are localized on subsystem A and AOs ν on subsystem B. Because contributions from multiple excitations are neglected within the one-electron transition density matrix, the CT matrix has to be normalized to 1.

$$|\Omega^n| = \sum_{A,B} \Omega_{AB} \stackrel{!}{=} 1 \quad (5)$$

The total percentage of one-electron excitations can be obtained from Eq. 5 before normalization. If the quantity is significantly smaller than 0.8, the method may be inappropriate for the analysis of the excited state [18].

2.2. Excitonic coupling matrix element

In the weak coupling limit, the EET rate can be described by a Golden Rule expression comprising the square of the total ECME and the Franck-Condon weighted density (FCWD) of states [20–22]

$$k_{EET} = \frac{2\pi}{\hbar} |\langle \Psi_F | \hat{V} | \Psi_I \rangle|^2 \times FCWD \quad (6)$$

where the operator \hat{V} describes the interaction between the initial state Ψ_I and the final state Ψ_F with respect to the EET process. In case of a homodimeric system, the total ECME between two excited states Ψ_I and Ψ_F can directly be obtained from their energetic splitting (Davydov splitting).

$$\langle \Psi_F | \hat{V} | \Psi_I \rangle = \frac{E_F - E_I}{2} \quad (7)$$

In heterodimers, approximate methods have to be used to evaluate the ECME. To this end, the supermolecular system is divided into two subsystems. The division of the here investigated EET cassettes into a donor subsystem D and an acceptor subsystem A is based on a localization study of the involved frontier orbitals (Figs. 2 and 3). As indicated in Fig. 1, we decided to assign the molecular bridges between the two chromophores to the donor part of the system.

Accordingly, the supermolecular electronic Hamiltonian $\hat{\mathcal{H}}$ is expressed as the sum of the Hamiltonians of the individual subsystems D and A and the coupling term \hat{V} .

$$\hat{\mathcal{H}} = \hat{\mathcal{H}}_D + \hat{\mathcal{H}}_A + \hat{V} \quad (8)$$

2.2.1. Monomer transition density matrix approach

In fragment-based approaches, the coupling is described as the interaction between two excited states which are perfectly localized on two subsystems [23,24]. In this case, the ECME can be approximated by a monomer-based approach such as the MTD method [7–9] or the transition density cube method [25]. The MTD method approximates the ECME as sum of direct and exchange interactions between the spinless reduced one-electron transition density matrices $\rho^{(D)}$ and $\rho^{(A)}$ of the donor and the acceptor, respectively,

$$V_{DA} = \langle D^* A | \hat{V} | D A^* \rangle \approx \sum_{i,j \in D, k,l \in A} \rho_{ij}^{(D)} (ij|kl) \rho_{kl}^{(A)} - \frac{1}{2} \sum_{i,j \in D, k,l \in A} \rho_{ij}^{(D)} (il|kj) \rho_{kl}^{(A)} \quad (9)$$

where we have used the Mulliken convention for denoting the electronic repulsion integrals. Alternatively, frozen-density approaches may be used to determine the coupling between subsystem-localized electronic excitations [26–28].

2.2.2. Supermolecular transition density approach

At small intermolecular distances and in the presence of a molecular linker, the CT contributions to the ECME cannot be neglected. In the following, we present a novel method based on the STD matrices of the interacting electronically excited states. The method is closely related to the TDFI-TI (transition-density-fragment interaction combined with transfer integral) method introduced by Fujimoto [29,30]. In contrast to TDFI-TI, our method is not based on a subsystem formalism and is not restricted to a four-orbital–four-electron model considering the indirect contributions.

In a hypothetical biorthonormal subsystem-localized orbital basis, the wave functions of the initial and final states can be divided into two local and two CT contributions. This subdivision can be looked upon as a decomposition of the states into individual “substates”

$$|\Psi_I\rangle = |D^* A\rangle_I + |D A^*\rangle_I + |D^+ A^-\rangle_I + |D^- A^+\rangle_I \quad (10)$$

$$\langle \Psi_F | = {}_F\langle D A^* | + {}_F\langle D^* A | + {}_F\langle D^+ A^- | + {}_F\langle D^- A^+ | \quad (11)$$

where the first term in expression (10), describing local excitations on D in the initial state $|\Psi_I\rangle$, and the first term in expression (11), describing local excitations on A in the final state $\langle \Psi_F |$ are expected

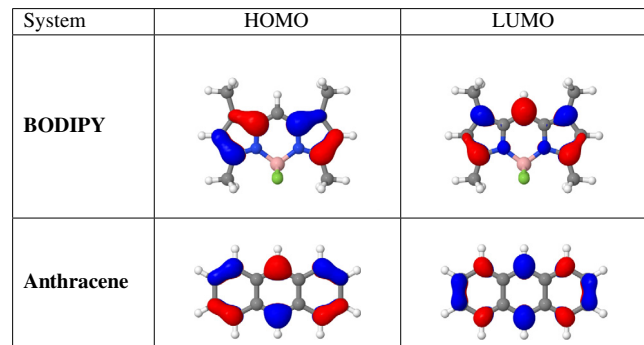


Fig. 2. Frontier orbitals involved in the first excited singlet states of the isolated monomers.

to be dominant, respectively. To calculate the total ECME $\langle \Psi_F | \hat{V} | \Psi_I \rangle$, all four “substates” of the final state have to be combined with all four “substates” of the initial state yielding 16 terms in total. ${}_F\langle D^* A | \hat{V} | D^* A \rangle_I$ and ${}_F\langle D A^* | \hat{V} | D A^* \rangle_I$ do not contribute to the ECME because they describe the interaction between two local excitons on the same subsystem, leaving us with 14 coupling terms in total:

$$\langle \Psi_F | \hat{V} | \Psi_I \rangle = \underbrace{{}_F\langle D A^* | \hat{V} | D^* A \rangle_I + {}_F\langle D^* A | \hat{V} | D A^* \rangle_I}_{V_{Dir}} \quad (12)$$

$$+ \underbrace{{}_F\langle D^+ A^- | \hat{V} | D^- A^+ \rangle_I + {}_F\langle D^- A^+ | \hat{V} | D^+ A^- \rangle_I}_{V_{CT}} \quad (13)$$

$$+ {}_F\langle D^+ A^- | \hat{V} | D^* A \rangle_I + {}_F\langle D^- A^+ | \hat{V} | D^* A \rangle_I \\ + {}_F\langle D^+ A^- | \hat{V} | D A^* \rangle_I + {}_F\langle D^- A^+ | \hat{V} | D A^* \rangle_I \\ + {}_F\langle D^* A | \hat{V} | D^- A^+ \rangle_I + {}_F\langle D A^* | \hat{V} | D^- A^+ \rangle_I \quad (14)$$

$$+ \underbrace{{}_F\langle D^* A | \hat{V} | D^+ A^- \rangle_I + {}_F\langle D A^* | \hat{V} | D^+ A^- \rangle_I}_{V_{Pol}} \\ + \underbrace{{}_F\langle D^+ A^- | \hat{V} | D^+ A^- \rangle_I + {}_F\langle D^- A^+ | \hat{V} | D^- A^+ \rangle_I}_{V_{Corr}} \quad (15)$$

The first two terms have been combined into V_{Dir} which describes the direct interactions between locally excited configurations. V_{CT} represents the interactions between two CT configurations that arise from an electron transfer from D to A and from A to D, respectively. The polarization term V_{Pol} is composed of eight mixed couplings between local and CT excitations. Finally, we define a correlation term V_{Corr} which represents the coupling between CT configurations of the same type. In a microscopic representation involving the reduced transition density matrices and two-electron integrals in the hypothetical biorthonormalized MO basis, the matrix element ${}_F\langle D^* A | \hat{V} | D A^* \rangle_I$ reads

$${}_F\langle D^* A | \hat{V} | D A^* \rangle_I = \sum_{i \in D} \sum_{j \in A} \sum_{a \in D} \sum_{b \in A} \rho_{ia}^{(F)} \rho_{jb}^{(I)} \left[(ai|jb) - \frac{1}{2} (ab|ji) \right] \quad (16)$$

corresponding to the well-known expression for the Förster and Dexter exchange contributions in the MTD approach [7,8,29].

The use of a biorthogonalized MO basis can be avoided if the AO basis is employed instead. In the following, greek letters label the AOs whereas roman letters denote the MOs which may be delocalized over the whole supermolecular system ($i, j, a, b \in DA$). Expressing the two-electron integrals in terms of the AO basis and the MO coefficients

$$(ai|jb) = \sum_{\mu} \sum_{\nu} \sum_{\lambda} \sum_{\sigma} c_{\mu i} c_{\nu j} c_{\lambda a} c_{\sigma b} (\nu\mu|\lambda\sigma) \quad (17)$$

Eq. (16) can be rewritten as [20]

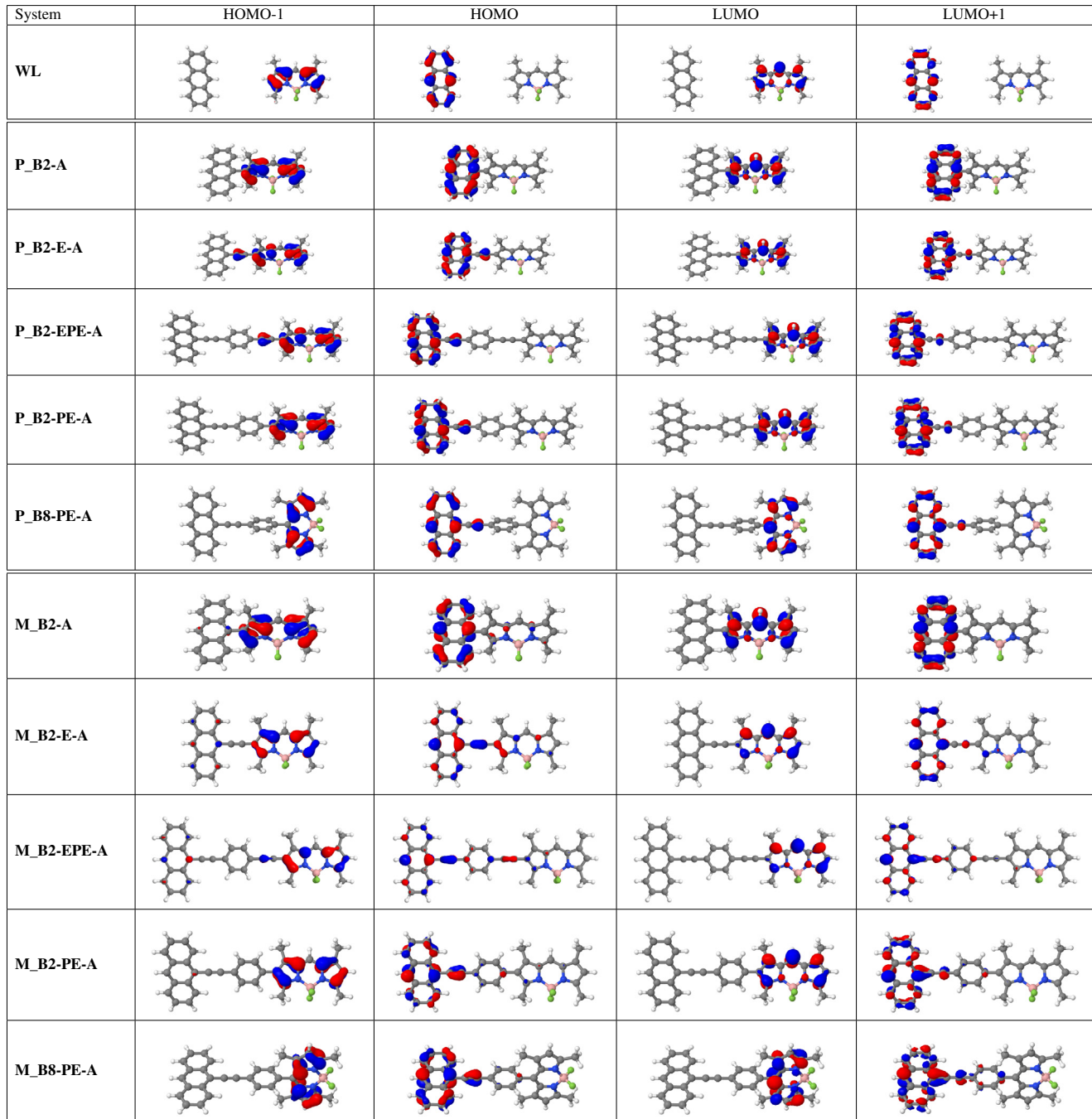


Fig. 3. Frontier molecular orbitals of the monomers and EET cassettes involved in the dominant transitions of the coupled electronically excited states in the studied EET cassettes. WL = all structures without linker.

$${}_F\langle D^*A|\hat{\mathcal{V}}|DA^*\rangle_I = \sum_{i \in DA} \sum_{a \in DA} \sum_{j \in DA} \sum_{b \in DA} \sum_{\mu \in D} \sum_{v \in D} \sum_{\lambda \in A} \sum_{\sigma \in A} \rho_{ia}^{(F)} \rho_{jb}^{(I)} c_{\mu i} c_{\lambda j} c_{va} c_{\sigma b} \times \left[(v\mu|\lambda\sigma) - \frac{1}{2}(v\sigma|\lambda\mu) \right] \quad (18)$$

Transforming the reduced transition density matrices of the initial and the final state to the AO basis [19,20,29]

$$\rho_{\mu v}^{(F)} = \sum_{i \in DA} \sum_{a \in DA} c_{\mu i} c_{va} \rho_{ia}^{(F)} \quad (19)$$

$$\rho_{\lambda\sigma}^{(I)} = \sum_{j \in DA} \sum_{b \in DA} c_{\lambda j} c_{\sigma b} \rho_{jb}^{(I)} \quad (20)$$

yields our final expression

$${}_F\langle D^*A|\hat{\mathcal{V}}|DA^*\rangle_I = \sum_{\mu \in D} \sum_{v \in D} \sum_{\lambda \in A} \sum_{\sigma \in A} \rho_{\mu v}^{(F)} \rho_{\lambda\sigma}^{(I)} \left[(v\mu|\lambda\sigma) - \frac{1}{2}(v\sigma|\lambda\mu) \right] \quad (21)$$

Similar formulae can be derived for the other 13 coupling matrix elements which only differ in the subsystems over which the indices μ , v , λ and σ run.

2.3. Computational details

2.3.1. Setup of the studied EET cassettes

The EET cassettes studied in this work are composed of an anthracene exciton donor which is linked to a BODIPY exciton acceptor by a π -conjugated molecular bridge. In a recent study

[9], we presented the minimum ground state geometries, referred to as **M_B2-A**, **M_B2-E-A**, **M_B2-EPE-A**, **M_B2-PE-A** and **M_B8-PE-A** (M-structures) in the following (Table 1). While the overall relative orientation of the donor and acceptor moieties is almost coplanar in **M_B2-E-A** and **M_B2-EPE-A**, the orientation is close to a perfectly perpendicular arrangement in **M_B2-A** and **M_B8-PE-A**. In **M_B2-PE-A**, donor and linker adopt a torsion angle of about 62° with respect to the acceptor. However, in those cassettes in which an ethynyl linker is attached to BODIPY, the rotational barriers are extremely low (< 50 meV) such that a nearly free rotation can be assumed in B2-E-A and B2-EPE-A [9]. To sample also these conformations, we introduced **P_B2-A**, **P_B2-E-A**, **P_B2-EPE-A**, **P_B2-PE-A** and **P_B8-PE-A** (P-structures) enforcing a perfectly perpendicular orientation of donor, phenyl bridge, and acceptor molecular planes by symmetry constraints (Table 1). The difference between the equilibrium ground state energies of the corresponding M- and P-structures is small (Table 1) which suggests that the P-structures are thermally accessible. To study the influence of the molecular linkers, all calculations were repeated after removal of the molecular linker from the optimized ground-state structure and saturation of the obtained monomers with hydrogen atoms. The newly created C-H bonds were relaxed keeping the rest of the molecules fixed. The corresponding structures are referred to as **M_B2(-E-) A**, etc.

2.3.2. Geometry optimizations

The equilibrium geometries of the singlet ground states (S_0) of the dyads and the individual monomers were taken from a previous study [9]. While the M-structures had been optimized without symmetry constraints, C_s or C_{2v} symmetry was employed for the P-structures. To this end, KS DFT in conjunction with the B3-LYP hybrid density functional [31] was used. All calculations were per-

formed with TURBOMOLE [32] employing a basis set of split valence quality with polarization functions on all atoms (SVP) [33].

2.3.3. Excitation energies and excited-state properties

The excited-state properties (vertical excitation energies, transition density matrices, static dipole moments, transition dipole moments and oscillator strengths) of the monomers and the EET cassettes were calculated using a locally modified version of the DFT/MRCI program [13,17,34]. In the semi-empirical DFT/MRCI method, dynamic correlation effects are considered by DFT whereas static correlation effects are taken into account by a MRCI expansion. The configurations in the MRCI are built up from KS orbitals of a closed-shell determinant employing the BH-LYP functional [35]. Double-counting of dynamic correlation is avoided by damping the off-diagonal matrix elements by a rapidly decreasing function that depends on the energy difference of the configurations and two parameters. All calculations were carried out employing the original (DFT/MRCI) [13] as well as the recently redesigned and reparameterized Hamiltonians (DFT/MRCI-R) [17]. The two-electron integrals were approximated with the resolution of the identity method [36,37]. Only orbitals that refer to configurations below a certain energy cut-off are considered in the CI-expansion. Within this paper we used an energy selection threshold of 1.0 E_H to compute the lowest 10 eigenvectors. The initial MRCI reference space was spanned by all single and double excitations from the four highest occupied MOs to the four lowest unoccupied MOs of the ground state KS determinant. A second DFT/MRCI(-R) step was performed with a refined reference space comprising all configurations which contribute to one of the 10 lowest-lying eigenvectors of the initial run with a squared coefficient of 0.003 and larger. In a few cases, the number of roots had to be increased to 15 or 20, respectively. A detailed description of DFT/MRCI and DFT/MRCI-R has been given elsewhere [13,17].

Table 1

Molecular structures of the studied monomers and EET cassettes. Relative orientation of the donor, linker and acceptor indicated by colored planes. In the P-structures, a strong delocalization of the molecular orbitals is avoided by symmetry constraints enforcing a perfectly perpendicular orientation of the donor and the acceptor planes (P_B2-A, P_B2-E-A) or a perfectly perpendicular orientation of the linker plane with respect to donor and acceptor planes (P_B2-PE-A, P_B2-EPE-A, P_B8-PE-A). The M-structures represent the absolute minimum geometries obtained by geometry optimization without symmetry constraints. ΔE_{PM} refers to the difference between the DFT/MRCI-R ground state energies of the corresponding P- and M-structures.

BODIPY	Anthracene	ΔE_{PM} (meV)
		M_B2-A $d_{DA} = 6.2\text{ \AA}$ C_1
		M_B2-E-A $d_{DA} = 8.9\text{ \AA}$ C_1
		M_B2-EPE-A $d_{DA} = 15.8\text{ \AA}$ C_1
		M_B2-PE-A $d_{DA} = 13.3\text{ \AA}$ C_1
		M_B8-PE-A $d_{DA} = 11.6\text{ \AA}$ C_1

2.3.4. Excitonic coupling matrix elements

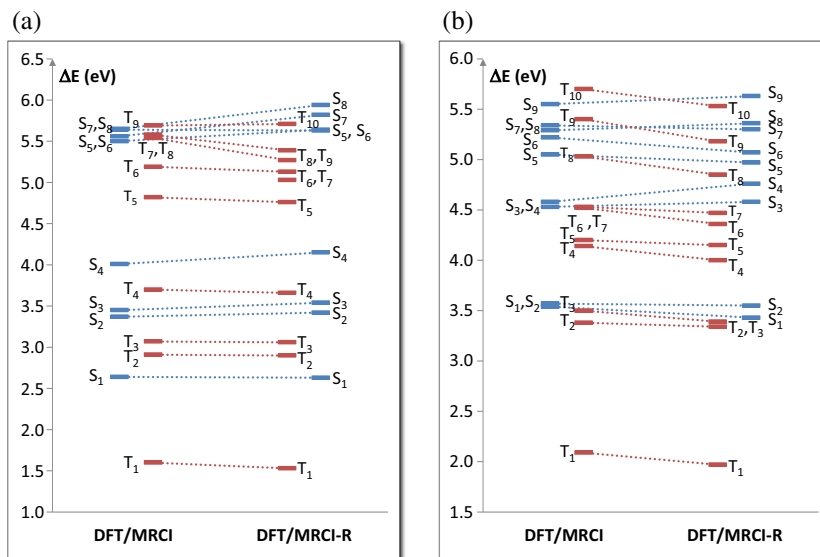
The ECME was computed using the newly developed STD approach (Eqs. (12)–(15)) and the established MTD approach (Eq. (9)) for comparison. In STD, the ECME calculations were based on supermolecular DFT/MRCI-R wave functions of the EET cassettes. The MTD calculations of the ECME were based on the S_1 transition density matrices obtained by individual DFT/MRCI-R calculations of the fragments. To accelerate the calculations, only transition density matrix elements with an absolute value higher than 10^{-6} were considered.

3. Results and discussion

3.1. Comparison of DFT/MRCI and DFT/MRCI-R

3.1.1. Monomers

DFT/MRCI and DFT/MRCI-R find the same energetic order of the BODIPY excited states and very similar compositions of the wave functions (Fig. 4, Table 2). Correspondingly, the transition densities are very similar. While all triplet states are slightly stabilized in DFT/MRCI-R, most singlet energies are weakly blue-shifted in



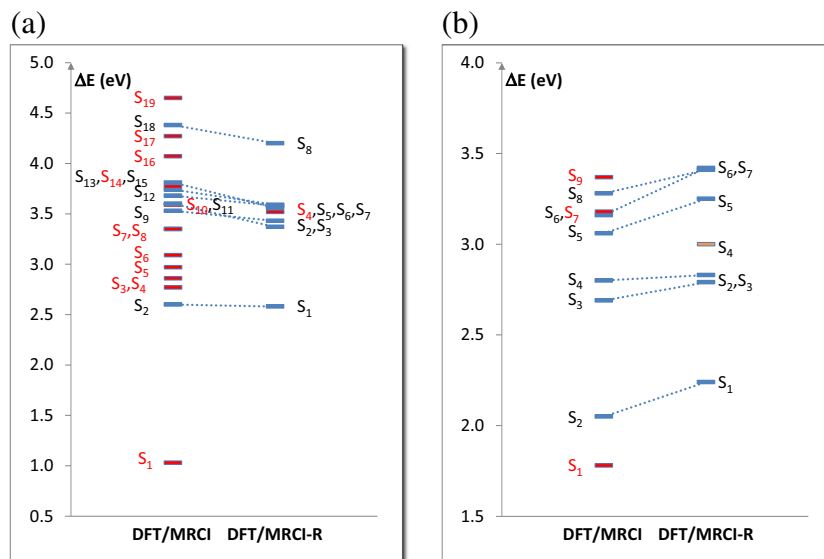


Fig. 5. Vertical excitation energies with respect to the relaxed ground state geometries of (a) M_B2(-PE-)A and (b) M_B2-PE-A calculated using DFT/MRCI and DFT/MRCI-R. Corresponding states are connected by dashed lines. States dominated by four-open-shell configurations are shown in red. (For interpretation of the references to color in this figure legend, the reader is referred to the web version of this article.)

comparison to DFT/MRCI, but the deviations lie within the confidence interval of the method (± 0.2 eV). In particular, the first bright singlet state, which is dominated by a HOMO–LUMO excitation, is found to have almost the same energy of 2.63 eV (DFT/MRCI) and 2.64 eV (DFT/MRCI-R). Hence, we conclude that the absorption behavior of BODIPY can be described by DFT/MRCI and DFT/MRCI-R with the same level of accuracy when compared to an experimental absorption maximum of 2.46 eV measured in ethanol [38]. The first excited triplet state is located at 1.60 eV (DFT/MRCI) or 1.53 eV (DFT/MRCI-R) which is in good agreement with the experimental value of 1.59 eV in phosphorescent BODIPY derivatives [39].

The energetic order of the states is also preserved for anthracene using both Hamiltonians (Fig. 4b, Table 2). We find that the energetic separation between the S_1 and the S_2 states increases from 0.03 eV in DFT/MRCI to 0.12 eV in DFT/MRCI-R. A qualitatively similar behavior is observed for the S_3 and the S_4 states. The experimental absorption maximum of 3.60 eV [40–42] is well reproduced with both DFT/MRCI (3.54 eV) and DFT/MRCI-R (3.43 eV). The first excited triplet state is located at 2.09 eV (DFT/MRCI) or 1.97 eV (DFT/MRCI-R) which is in fair agreement with an experimental 0–0 transition energy of 1.87 eV in the gas phase [43].

3.1.2. Dimers

While the description of the isolated monomers is more or less identical using the original and the redesigned Hamiltonians, respectively, substantial differences are found for the supermolecular arrangements. Let us start by analyzing the excitation energies of the non-linked supermolecular arrangements of BODIPY and anthracene. **M_B2(-PE-) A**, for example, is characterized by an intermolecular separation of 13.3 Å between the centers of mass of the BODIPY and the anthracene moieties. With both Hamiltonians we find a perfectly BODIPY locally excited (LE) state (S_2 at 2.60 eV in DFT/MRCI, S_1 at 2.58 eV in DFT/MRCI-R), a perfectly anthracene LE state (S_{11} at 3.60 eV in DFT/MRCI, S_2 at 3.37 eV in DFT/MRCI-R) and an almost pure anthracene to BODIPY CT state which corresponds to the HOMO–LUMO transition (S_{13} at 3.74 eV in DFT/MRCI, S_7 at 3.59 eV in DFT/MRCI-R) (Figs. 4 and 5). Nevertheless, using the original DFT/MRCI Hamiltonian,

approximately half of the excited states are dominated by four-open-shell configurations. In particular, the first excited singlet state exhibits a double excitation with four open shells as the leading term of the MRCI expansion. At infinite separation, the first supermolecular four-open-shell singlet state can be regarded as coupled pair of the lowest monomer triplet states. Thus, the energy can be approximated as the sum of the T_1 energies of the monomers.

$$E_{1(T_1(A) \otimes T_1(B))} \approx E_{T_1(A)} + E_{T_1(B)} \quad (22)$$

At the DFT/MRCI level, the energy of the first singlet-coupled triplet-pair state (S_1 , 1.03 eV) is less than one third of the sum of the T_1 energies of the monomers (3.69 eV). Using DFT/MRCI-R, we find the lowest four-open-shell dominated state (S_4) located at an energy of 3.46 eV, in excellent agreement with the expected value of 3.50 eV in this case. Owing to the wrong asymptotic behavior of the underlying BH-LYP density functional, both variants of the DFT/MRCI method underestimate the energy of the CT state, which is expected to appear at ≈ 4.6 eV.¹ by about 1 eV. Qualitatively similar results are obtained for the other unlinked structures. Summarizing, we conclude that the redesigned DFT/MRCI-R Hamiltonian is better suited for the calculation of supermolecular arrangements with more than one subsystem than the original DFT/MRCI Hamiltonian. In the following, therefore only the results of the latter method will be discussed.

3.1.3. Absorption spectra of the EET cassettes

In all P-structures, a perfectly perpendicular orientation of the donor, phenyl bridge and acceptor has been enforced. The vertical excitation energies of their BODIPY LE states are systematically blue shifted with respect to the corresponding experimental peak maxima by 0.12–0.24 eV (Fig. 6 and Table 2). A similar behavior is found for the anthracene LE state with a systematic overestimation of the experimental value by 0.16–0.19 eV except

¹ The experimental ionization potential (IP) of anthracene is 7.44 eV [44]. No experimental data was found for the electron affinity (EA) of BODIPY. In this case, we use a value of 1.67 eV reported for CCSD(T) calculations [45]. The difference between the IP and the EA has to be corrected by the Coulomb interaction energy of the cation and anion at finite intermolecular separation which amounts to ≈ -1 eV in a point-charge model.

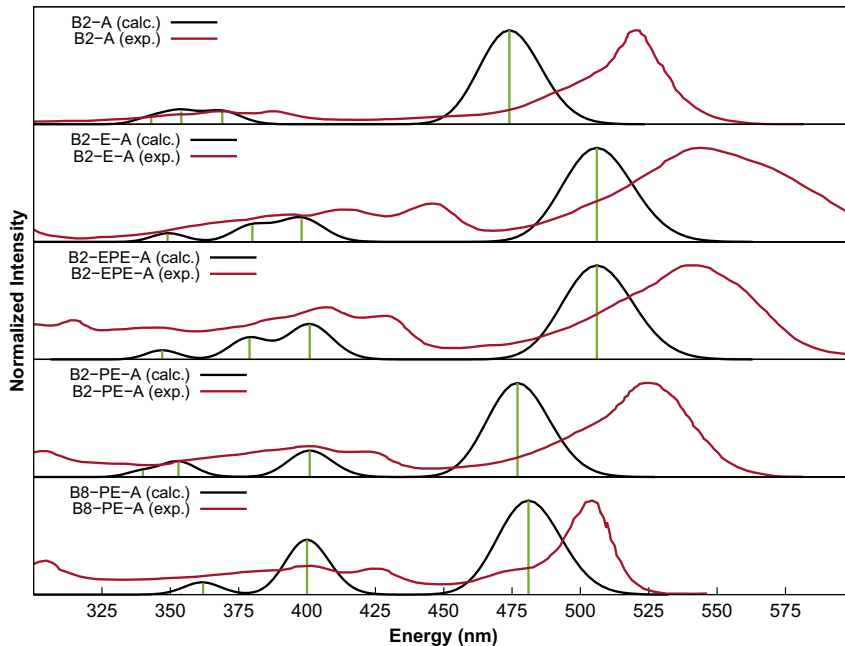


Fig. 6. Gaussian-broadened vertical DFT/MRCI-R absorption spectra of the studied EET cassettes (P-structures) assuming a full width at half maximum of 500 cm^{-1} . Digitalized experimental spectral spectra (red) were read from Ref. [6]. (For interpretation of the references to color in this figure legend, the reader is referred to the web version of this article.)

for **P_B2-E-A** where a larger deviation of 0.34 eV is observed. Owing to the systematic blue shift of the vertical excitation energies, the relative positions and intensities of the absorption maxima are qualitatively well reproduced. Solvent effects on the absorption energies were found to be small, in agreement with experimental observations [6]. Recalculation of **P_B2-A** using the implicit solvent model COSMO [46] to mimic an ethanol environment ($\epsilon = 24.5$) did not lead to a significant change of the vertical excitation energies.

For the majority of the M-structures, representing the global minimum geometries of the EET cassettes, we find very good agreement between the calculated vertical excitation energies of the anthracene LE state and the experimental peak positions. Note that experimental peak maximum of the anthracene absorption in **B2-E-A** is substantially red shifted with regard to the other cassettes [6] possibly a consequence of the low torsional barrier and the enhanced π -conjugation that sets in when the π systems of anthracene and BODIPY are not perfectly perpendicular (Fig. 7)). Likewise, the almost coplanar orientation of donor, bridge and acceptor in **M_B2-EPE-A** leads to a significant delocalization of HOMO and LUMO+1 densities which in turn causes a strong energetic stabilization of the transition. Comparison of the vertical excitation energies of the M- and P-structures with the position of the experimental band maximum suggests that the bridging phenyl ring has an orientation intermediate between a perpendicular and coplanar arrangement on the average.

The proper description of the BODIPY absorption appears to be more critical. While the vertical excitation energies of the lowest BODIPY LE states of the nearly perpendicular structures **M_B2-A**, **M_B2-PE-A**, and **M_B8-PE-A** are in good agreement with the experimental values, this is not the case for **M_B2-E-A** and **M_B2-EPE-A**. The almost coplanar orientations of donor, phenyl bridge, and acceptor moieties of the latter structures cause a marked delocalization of the frontier MOs (Fig. 3) and an energetic stabilization of the anthracene-to-BODIPY CT state (HOMO \rightarrow LUMO) which in turn strongly mixes with the lowest BODIPY LE state (HOMO-1 \rightarrow LUMO). Energy profiles for a scan along the

twisting angle between anthracene and BODIPY in **B2-E-A** are displayed in Fig. 7. The excitation energy of the lowest optically bright BODIPY state is seen to depend markedly on this coordinate. At a torsion angle of 90° , the oscillator strength of the local BODIPY transition is largely concentrated in $S_1 \leftarrow S_0$. At the nearly coplanar minimum geometry, the S_1 and S_2 states are characterized by local and CT transitions in approximately equal parts and both exhibit substantial oscillator strengths. For **B2-E-A** and **B2-EPE-A**, Wan et al. [6] notice a stronger red shift and a broader spectral band shape of the acceptor absorption which they interpret as being caused by the immediate linkage of BODIPY to an ethynyl group. The increasing red shift and broadening of the lowest absorption maximum can be regarded as a measure for the extent of electron delocalization. The red shift can also be interpreted as measure of the coplanarity of the entire system. Comparison with experiment therefore suggests a relative orientation of the dyes and the bridge in between the P- and M-structure on the average.

3.2. CT contributions to the ECME

3.2.1. STD benchmark calculations

The performance of the newly developed STD approach was tested using a π -stacked ethylene dimer varying the intermolecular distance between approximately 3.5 and 9 Å. Supermolecular MOs were obtained from closed-shell KS calculations using the BH-LYP functional [35] and an SVP basis set [33]. The MOs are completely delocalized over the supermolecule. For the sake of clarity, DFT/MRCI-R single excitation calculations were carried out for four electrons in four orbitals yielding four electronically excited states. At large intermolecular separations, the two lowest-lying states correspond to positive and negative linear combinations of pure local excitations on monomer A and B, respectively, i.e. $A^*B \pm AB^*$ (Frenkel states). Likewise, the two higher-lying states are positive and negative linear combinations of the ionic terms A^+B^- and A^-B^+ , respectively, (CT states). The CT matrix formalism developed by Plasser and Lischka [18], (see Section 2.1), provides a valuable tool for the quantification of the

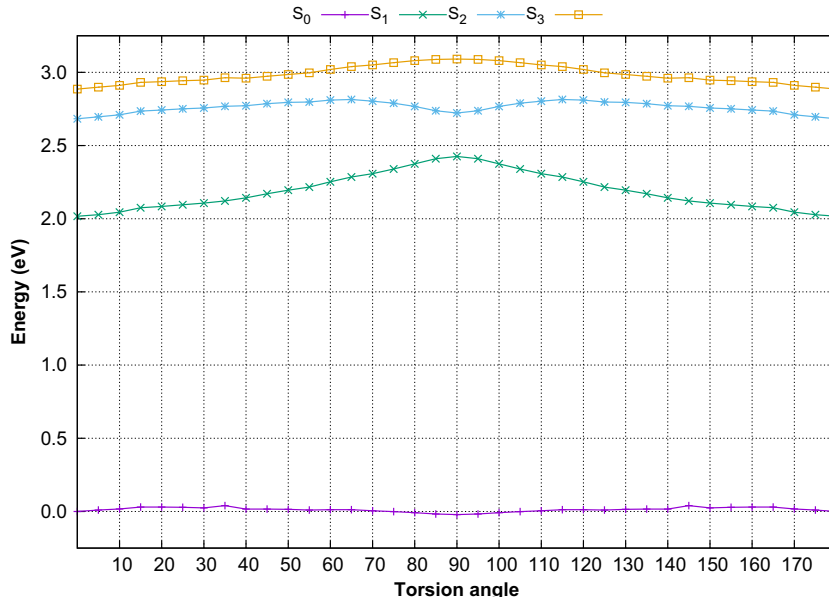


Fig. 7. DFT/MRCI-R energy profiles of the lowest-lying states along the twisting angle between the anthracene and BODIPY molecular plane of P_B2-E-A.

percentage of the LE and the CT character of an electronically excited state. The analysis shows that Frenkel and CT states start mixing at intermolecular separations smaller than approximately 5 Å (for details see [supplementary information \(SI\)](#)).

In the adiabatic supermolecular representation, all off-diagonal coupling terms vanish. The ECMEs are instead computed as expectation values of the operator \hat{V} in STD. In contrast, MTD requires the computation of off-diagonal matrix elements of LE states, i.e., $\langle A^*B|\hat{V}|AB^* \rangle$. The total ECMEs of the two Frenkel states, calculated with the STD approach, were compared to the coupling obtained from their Davydov splitting at the DFT/MRCI-R level (FullQM) and the couplings evaluated with the MTD approach. To get more insight, we further split up the STD ECMEs into a direct term (Eq. (12)) and the sum of all indirect terms (Eqs. (13)–(15)). As may be seen in Fig. 8, STD and MTD results match nearly perfectly for intermolecular separations >5 Å. For the upper Frenkel state (II), this is even the case for small intermolecular separations whereas (negative) CT contributions become more and more important for the lower Frenkel state (I) with decreasing intermolecular distance. Similar conclusions were also drawn from the results of test calculations using the recently developed wave function frozen-density embedding approach [28]. In purely monomer-based approaches, these CT contributions to the ECME are not taken into account. When compared to the FullQM values, the STD and MTD approaches seemingly overshoot at long intermolecular separations. This deviation is traced back to the scaling factor of 0.5682 with which the two-electron integral that couples the two Frenkel excitations is multiplied in the DFT/MRCI-R method [17], thus diminishing the Davydov splitting whereas the corresponding two-electron integrals remain unscaled in the STD and MTD approaches.

3.2.2. LE and CT character of the supermolecular states of the anthracene-BODIPY EET cassettes

In the anthracene–BODIPY EET cassettes, the CT matrix analysis tool was applied to the excited states which correlate with the lowest optically bright states of the isolated monomers. Because both states may comprise a certain amount of CT contributions in both directions, we have to identify four excited states in total which result from the excitonic interaction. In all P- and M-structures

without linker, the picture is quite clear ([Tables 3 and 4](#)). The S_1 states (dominant contribution: HOMO-1 → LUMO) is always almost completely localized on the BODIPY moiety while the S_2 state (dominant contribution: HOMO → LUMO + 1) is almost completely localized the anthracene moiety. The corresponding anthracene-to-BODIPY CT state (dominant contribution: HOMO → LUMO) is destabilized with increasing intermolecular distance. Accordingly, it can be identified as the S_3 state in **P_B2(-E-)A** and as the S_7 state in **P_B2(-EPE-)A**. The BODIPY-to-anthracene CT states are (dominant contribution: HOMO-1 → LUMO + 1) are again higher in energy which also depends on the intermolecular distance.

The clear picture of perfectly LE and pure CT states in a well-defined energetic order becomes blurred when the molecular linker is taken into account ([Table 3](#)). In **P_B2-A**, the perpendicularly oriented anthracene and BODIPY moieties are connected by a single C–C bond only. Nevertheless, the BODIPY-centered S_1 state covers 2% of local transitions on anthracene and 2% of CT transitions. A similar composition was found for the anthracene-centered S_3 state. The anthracene-to-BODIPY CT state is energetically stabilized by the covalent linkage and can be assigned to the S_2 state. In **P_B2-E-A** we find a similar order of the electronic states but slightly increased CT contributions to the LE states owing to the ethynyl linker. In **P_B2-EPE-A** and **P_B8-PE-A** the energetic order is similar to the structures without linker because the anthracene-to-BODIPY CT state is stabilized to a minor extent only. Despite the enforced perpendicular orientation of donor, phenyl linker, and acceptor and a nearly perfect localization of the frontier MOs ([Fig. 3](#)), CT contributions are not negligible in **P_B2-PE-A**. While the BODIPY-centered S_1 state comprises 8% of CT contributions, the S_2 state is composed of only 50% local contributions on the anthracene-moiety, 39% CT transitions and 11% local transitions on the BODIPY-moiety. The net CT is almost zero in this state, however, which is also reflected in the nearly unchanged permanent dipole moment of the S_2 state with respect to the electronic ground state.

The qualitative picture, based on the analysis of the wave functions of the M-structures, is corroborated by the elements of the CT matrices ([Table 4](#)). While LE and CT states can be told apart for **M_B2-A** and **M_B8-PE-A**, a strong mixture of LE and CT character can be made out for **M_B2-E-A**, **M_B2-EPE-A** and **M_B2-PE-A**.

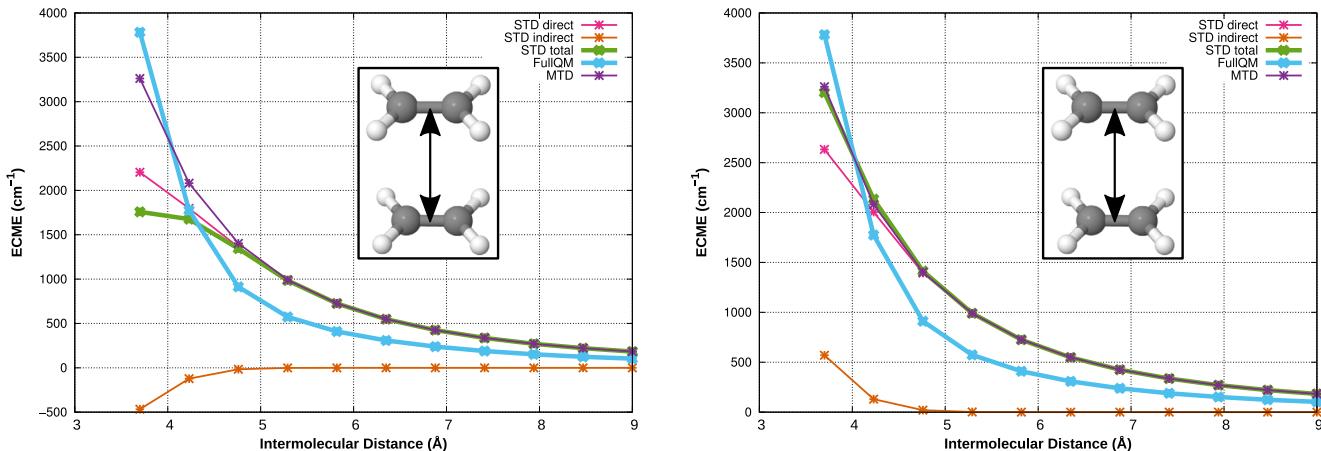


Fig. 8. Benchmark calculations of the supermolecular transition density approach (STD) of the Frenkel states of the ethylene dimer (left: Frenkel state I, right Frenkel state II). The ECMEs are compared to the Davydov splitting of the coupled states (FullQM) and ECMEs of the monomer transition density approach (MTD). The curve labeled "STD direct" refers to the coupling between all local transitions on monomer A and all local transitions on monomer B while "STD indirect" includes all additional matrix elements.

Table 3
Vertical excitation energies, oscillator strengths f, static dipole moments (SDM), transition dipole moments (TDM), percentage of one-electron contributions and CT matrices of the studied P-structures with respect to their relaxed ground state geometries.

System	State	E (eV) (nm)	f	SDM (D)	TDM (D)	1e⁻ contr. (%)	Ω _{D→D} (%)	Ω _{A→A} (%)	Ω _{A→D} (%)	Ω _{D→A} (%)
P_B2(-E-)A	S ₁	2.65 (468)	0.84254	2.95	9.15	89	0	100	0	0
	S ₂	3.38 (367)	0.14602	3.81	3.37	91	100	0	0	0
	S ₃	3.39 (366)	0.00000	40.24	0.01	86	0	0	0	100
	S ₈	4.19 (296)	0.00000	40.26	0.01	86	0	0	100	0
P_B2(-EPE-)A	S ₁	2.63 (471)	0.75359	2.97	8.69	89	0	100	0	0
	S ₂	3.37 (368)	0.14331	3.78	3.35	91	100	0	0	0
	S ₇	3.77 (329)	0.00000	75.29	0.00	86	0	0	0	100
	S ₉	4.62 (268)	0.00000	75.21	0.00	86	0	0	100	0
P_B2(-PE-)A	S ₁	2.64 (470)	0.77963	2.98	8.82	89	0	100	0	0
	S ₂	3.36 (369)	0.14331	3.77	3.35	91	100	0	0	0
	S ₇	3.67 (338)	0.00000	62.66	0.00	86	0	0	0	100
	S ₉	4.52 (274)	0.00000	62.57	0.00	86	0	0	100	0
P_B8(-PE-)A	S ₁	2.53 (490)	0.67929	3.20	8.41	89	0	100	0	0
	S ₂	3.36 (369)	0.15264	4.05	3.46	91	100	0	0	0
	S ₆	3.53 (351)	0.00000	56.12	0.00	86	0	0	0	100
	S ₉	4.40 (282)	0.00000	49.57	0.00	86	0	0	100	0
P_B2-A	S ₁	2.61 (474)	0.97981	2.96	9.94	89	2	96	1	1
	S ₂	2.91 (427)	0.00038	25.01	0.19	85	1	3	0	96
	S ₃	3.36 (369)	0.13500	3.83	3.26	91	93	5	1	1
	S ₇	3.64 (341)	0.00007	23.69	0.07	86	5	2	93	0
P_B2-E-A	S ₁	2.45 (506)	1.04627	3.82	10.61	87	3	84	2	11
	S ₂	2.75 (451)	0.00000	31.13	0.02	83	4	2	0	94
	S ₃	3.12 (398)	0.26320	3.82	4.72	91	93	4	1	2
	S ₆	3.34 (372)	0.00000	25.09	0.02	85	35	2	63	0
P_B2-EPE-A	S ₁	2.45 (506)	1.07564	3.73	10.76	88	0	99	0	1
	S ₂	3.09 (401)	0.46270	3.82	5.86	92	84	2	9	6
	S ₄	3.32 (374)	0.00739	61.95	0.77	83	0	17	0	83
P_B2-PE-A	S ₁	2.60 (477)	1.05301	2.94	10.33	90	1	91	4	4
	S ₂	3.09 (401)	0.29518	3.77	5.02	92	50	11	19	20
	S ₃	3.36 (369)	0.00329	53.91	0.51	83	4	26	1	69
	S ₁₁	4.06 (306)	0.00046	55.73	0.17	84	4	26	68	2
P_B8-PE-A	S ₁	2.58 (481)	0.67300	3.72	8.30	90	0	98	2	0
	S ₂	3.10 (400)	0.39285	5.21	5.78	92	99	0	0	1
	S ₃	3.36 (369)	0.00043	49.06	0.18	84	3	0	0	97
	S ₇	3.83 (323)	0.00000	42.07	0.00	84	0	0	100	0

3.2.3. Composition of the total ECMEs

As we have analyzed the supermolecular states of all studied systems, we were able to calculate the ECME between the lowest BODIPY- and anthracene-centered states (Table 5). In the P-structures without linker, the total ECME is almost exclusively com-

posed of the direct contributions (V_{Dir}) because CT transitions are high lying in well-separated donor–acceptor systems. For this reason, STD and MTD provide identical results. Only in **P_B2(-E-) A** in which the intermolecular distance between BODIPY and anthracene is rather short (8.9 Å), we find small indirect contributions

Table 4

Vertical excitation energies, oscillator strengths f, static dipole moments (SDM), transition dipole moments (TDM), percentage of one-electron contributions and CT matrices of the studied M-structures with respect to their relaxed ground-state geometries.

System	State	E (eV) (nm)	f	SDM (D)	TDM (D)	1e ⁻ contr. (%)	$\Omega_{D \rightarrow D}$ (%)	$\Omega_{A \rightarrow A}$ (%)	$\Omega_{A \rightarrow D}$ (%)	$\Omega_{D \rightarrow A}$ (%)
M_B2(-E-)A	S ₁	2.60 (478)	0.78664	2.98	8.94	89	0	100	0	0
	S ₂	3.30 (376)	0.00109	40.05	0.29	86	0	0	0	100
	S ₃	3.37 (367)	0.17518	3.61	3.70	91	97	3	0	0
	S ₈	4.20 (296)	0.00010	39.98	0.08	86	0	0	100	0
M_B2(-EPE-)A	S ₁	2.58 (481)	0.70734	3.03	8.50	89	0	100	0	0
	S ₂	3.37 (368)	0.15718	3.81	3.51	91	100	0	0	0
	S ₇	3.68 (337)	0.00000	75.26	0.00	86	0	0	0	100
	S ₉	4.64 (267)	0.00000	75.05	0.00	86	0	0	100	0
M_B2(-PE-)A	S ₁	2.56 (485)	0.73601	3.04	8.67	89	0	100	0	0
	S ₂	3.35 (370)	0.14975	3.84	3.42	91	100	0	0	0
	S ₇	3.58 (347)	0.00000	62.65	0.00	86	0	0	0	100
	S ₉	4.53 (274)	0.00000	62.56	0.00	86	0	0	100	0
M_B8(-PE-)A	S ₁	2.54 (488)	0.70469	3.20	8.55	89	0	100	0	0
	S ₂	3.36 (369)	0.15373	4.06	3.47	91	100	0	0	0
	S ₅	3.52 (352)	0.00000	56.15	0.00	86	0	0	0	100
	S ₉	4.41 (281)	0.00000	49.56	0.00	86	0	0	100	0
M_B2-A	S ₁	2.47 (503)	0.83059	3.95	9.42	89	2	88	1	9
	S ₂	2.85 (435)	0.07221	21.98	2.58	84	1	14	0	85
	S ₃	3.31 (374)	0.15745	3.83	3.54	91	90	7	2	1
	S ₈	3.71 (334)	0.00032	22.60	0.15	80	4	3	93	0
M_B2-E-A	S ₁	1.94 (638)	0.68295	11.63	9.63	80	6	50	2	42
	S ₂	2.64 (469)	0.59529	5.46	7.71	69	11	53	10	26
	S ₃	2.88 (430)	0.05041	4.44	2.15	90	64	22	9	5
	S ₈	3.58 (347)	0.00815	6.57	0.78	79	2	93	2	3
M_B2-EPE-A	S ₁	1.98 (628)	1.05630	11.77	11.88	82	7	58	3	32
	S ₂	2.63 (471)	0.37516	14.50	6.13	57	6	48	6	40
	S ₃	2.67 (464)	0.59822	3.69	7.69	90	87	6	3	4
	S ₆	3.22 (385)	0.08782	6.19	2.68	76	50	11	21	18
M_B2-PE-A	S ₁	2.24 (552)	1.05376	8.55	11.13	86	6	72	2	20
	S ₂	2.79 (445)	0.01956	16.29	1.36	70	22	40	0	38
	S ₃	2.83 (438)	0.52841	3.82	7.02	80	85	4	3	8
	S ₈	3.50 (354)	0.03283	17.99	1.57	76	47	9	40	4
M_B8-PE-A	S ₁	2.58 (480)	0.69475	3.92	8.42	90	0	98	2	0
	S ₂	2.86 (433)	0.68676	6.20	7.95	91	99	0	0	1
	S ₃	3.06 (405)	0.00000	42.70	0.00	84	2	1	0	97
	S ₅	3.39 (366)	0.00000	31.16	0.01	84	0	2	98	0

Table 5

Composition of the ECME of all P-systems computed using the supermolecular transition density approach (STD) in comparison with the monomer transition density approach (MTD).

Method	P_B2-A	P_B2-E-A	P_B2-PE-A	P_B2-EPE-A	P_B8-PE-A
STD	V _{dir}	944	942	408	216
	V _{CT}	54	109	-93	22
	V _{pol}	59	-62	-110	-23
	V _{corr}	-10	-15	2	-3
	V _{tot}	1047	974	207	212
MTD	V _{dir}	1264	1092	455	346
	P_B2(-E-)A				
	V _{dir}	443	137	78	0
	V _{CT}	17	0	0	0
	V _{pol}	-1	0	0	0
STD	V _{corr}	-12	0	0	0
	V _{tot}	448	137	78	0
	V _{dir}	467	134	76	0
	P_B2(-EPE-)A				
	V _{dir}	443	137	78	0
MTD	V _{CT}	17	0	0	0
	V _{pol}	-1	0	0	0
	V _{corr}	-12	0	0	0
	V _{tot}	448	137	78	0
	V _{dir}	467	134	76	0

and therefore a slightly higher total ECME in the STD approach in comparison to MTD. Individual contributions of all coupling terms to the ECMEs may be found in the SI.

The presence of a molecular linker gives rise to additional indirect contributions to the total ECME. For all systems, we find increased total ECMEs with both STD and MTD indicating an enhancement of the EET process. However, the results obtained

using the MTD approach are substantially larger than the appropriate STD couplings which can be traced back to the fact that indirect contributions are not explicitly taken into account in the MTD model and the total coupling therefore is overestimated. For **P_B2-A** we find a direct contribution of 944 cm⁻¹ in the STD approach compared to 1263 cm⁻¹ in the MTD approach. The deviation of more than 200 cm⁻¹ indicates that the decomposition of

the molecular dimer into two isolated monomers fails at very close separations of the interacting molecules. STD yields additional positive indirect contributions (V_{CT} and V_{Pol}) of 113cm^{-1} in total and negative indirect contributions (V_{Corr}) of 10cm^{-1} leading to a total ECME of 1047 cm^{-1} . In **P_B2-E-A** and **P_B2-EPE-A**, the CT contributions (V_{CT}) are positive while the polarization and correlation contributions are negative. As V_{CT} and V_{Pol} almost cancel each other out, the total ECME is in the range of the direct contribution. In **P_B2-PE-A**, we find a smaller total ECME than in **P_B2-EPE-A** although the linker is shorter. This can be explained by the CT and polarization terms which are both negative, thus drastically reducing the direct contribution.

In **P_B8-PE-A** the direct coupling matrix element is zero due to the perpendicular orientation of the transition dipole moments of the interacting electronic states. Owing to the fact that all indirect coupling matrix elements are zero as well, the high experimentally obtained EET rate of $2.5 \times 10^{12}\text{ s}^{-1}$ [5] can only be explained by vibrational effects causing slight deviations from the perfectly perpendicular orientation of the transition dipole moments [9].

For the M-structures, the STD approach provides similar results compared to the corresponding P-structures in case of **M_B2-A** and **M_B8-PE-A**. Because DFT/MRCI-R yields strongly mixed wave functions for the excited states of the residual three non-orthogonally oriented EET cassettes, a proper determination of the ECME using the STD approach is not possible in this case.

4. Conclusions

The redesigned DFT/MRCI-R Hamiltonian enables the calculation of excited state energies and properties for donor–acceptor molecular systems. While the DFT/MRCI expansions of these systems suffer from physically inappropriate contributions of configurations with four open shells, DFT/MRCI-R provides a proper description of the lowest-lying electronically excited states. Vertical excitation energies could be obtained in good agreement with the experiment except for cassettes in which an ethynyl linker is directly coupled to the acceptor. In the latter cassettes, the shifts of the optically bright transitions with respect to the corresponding monomer transitions depend markedly on the relative orientation of the donor, bridge, and acceptor π systems. As the torsional barriers are very small (<50 meV), broad absorption bands result, in agreement with experimental observations [6]. With regard to CT transitions, DFT/MRCI-R reveals a similar long-range behavior as the underlying BH-LYP density functional for which it was parameterized. It may thus be worthwhile to reparameterize the Hamiltonian in conjunction with long-range corrected functionals.

The newly introduced STD approach was shown to be a valuable tool for the calculation of the electronic coupling matrix elements including CT contributions. In case of non-linked donor–acceptor systems, we generally recommend the use of the much faster MTD approach since CT contributions play a negligible role. The presence of a molecular linker gives rise to additional indirect contributions reinforcing or reducing the direct coupling matrix element.

Acknowledgements

Financial support by the Deutsche Forschungsgemeinschaft through projects TA 725/1-1 and MA 1051/14-1 and funds (INST 208/704-1 FUGG) to purchase the hybrid compute cluster used in this study is gratefully acknowledged.

Appendix A. Supplementary data

Supplementary data associated with this article can be found, in the online version, at <http://dx.doi.org/10.1016/j.chemphys.2016.10.004>.

References

- [1] A. Treibs, F.-H. Kreuzer, *Justus Liebigs Ann. Chem.* 718 (1968) 208–223.
- [2] A. Loudet, K. Burgess, *Chem. Rev.* 107 (2007) 4891–4932.
- [3] L.J. Jones, R.H. Upson, R.P. Haugland, N. Panchuk-Voloshina, M. Zhou, R.P. Haugland, *Anal. Biochem.* 251 (1997) 144–152.
- [4] S. Hattori, K. Ohkubo, Y. Urano, H. Sunahara, T. Nagano, Y. Wada, N.V. Tkachenko, H. Lemmetyinen, S. Fukuzumi, *J. Phys. Chem. B* 109 (2005) 15368–15375.
- [5] T.G. Kim, J.C. Castro, A. Loudet, J.G.-S. Jiao, R.M. Hochstrasser, K. Burgess, M.R. Topp, *J. Phys. Chem. A* 110 (2006) 20–27.
- [6] C.-W. Wan, A. Burghart, J. Chen, F. Bergström, L.B.-Å. Johansson, M.F. Wolford, T.G. Kim, M.R. Topp, R.M. Hochstrasser, K. Burgess, *Chem. Eur. J.* 9 (2003) 4430–4441.
- [7] R. Fink, J. Pfister, A. Schneider, H. Zhao, B. Engels, *Chem. Phys.* 343 (2008) 353–361.
- [8] R.F. Fink, J. Pfister, H.M. Zhao, B. Engels, *Chem. Phys.* 346 (2008) 275–285.
- [9] J.D. Spiegel, M. Kleinschmidt, A. Larbig, J. Tatchen, C.M. Marian, *J. Chem. Theory Comput.* 11 (2015) 4316–4327.
- [10] W. Liu, B. Lunkenheimer, V. Settels, B. Engels, R.F. Fink, A. Köhn, *J. Chem. Phys.* 143 (2015) 084106.
- [11] K. Andersson, P.Å. Malmqvist, B.O. Roos, A.J. Sadlej, K. Wolinski, *J. Phys. Chem.* 94 (1990) 5483–5488.
- [12] P.G. Szalay, T. Müller, G. Gidofalvi, H. Lischka, R. Shepard, *Chem. Rev.* 112 (2011) 108–181.
- [13] S. Grimme, M. Waletzke, *J. Chem. Phys.* 111 (1999) 5645–5655.
- [14] M.R. Silva-Junior, M. Schreiber, S.P.A. Sauer, W. Thiel, *J. Chem. Phys.* 129 (2008) 104103.
- [15] C.M. Marian, N. Gilka, *J. Chem. Theory Comput.* 4 (2008) 1501–1515.
- [16] S. Siegert, F. Vogeler, C. Marian, R. Weinkauf, *Phys. Chem. Chem. Phys.* 13 (2011) 10350–10363.
- [17] I. Lyskov, M. Kleinschmidt, C.M. Marian, *J. Chem. Phys.* 144 (2016) 034104.
- [18] F. Plasser, H. Lischka, *J. Chem. Theory Comput.* 8 (2012) 2777–2789.
- [19] T. Helgaker, H. Larsen, J. Olsen, P. Jørgensen, *Chem. Phys. Lett.* 327 (2000) 397–403.
- [20] E. Hennebicq, G. Pourtois, G.D. Scholes, L.M. Herz, D.M. Russell, C. Silva, S. Setayesh, A.C. Grimsdale, K. Müllen, J.-L. Brédas, et al., *J. Am. Chem. Soc.* 127 (2005) 4744–4762.
- [21] B. Fückel, A. Köhn, M.E. Harding, G. Diezemann, G. Hinze, T. Basché, J. Gauss, *J. Chem. Phys.* 128 (2008) 074505.
- [22] V. Stehr, B. Engels, C. Deibel, R. Fink, *J. Chem. Phys.* 140 (2014) 024503.
- [23] V. May, O. Kühn, *Charge and Energy Transfer Dynamics in Molecular Systems*, Wiley-VCH, 2004.
- [24] T. Förster, *Ann. Phys. (Berlin)* 437 (1948) 55–75.
- [25] B.P. Krueger, G.D. Scholes, G.R. Fleming, *J. Phys. Chem. B* 102 (1998) 5378–5386.
- [26] J. Neugebauer, *J. Chem. Phys.* 126 (2007) 134116.
- [27] C. König, N. Schlüter, J. Neugebauer, *J. Chem. Phys.* 138 (2013) 034104.
- [28] S. Höfener, L. Visscher, *J. Chem. Theory Comput.* 12 (2016) 549–557.
- [29] K.J. Fujimoto, *J. Chem. Phys.* 137 (2012) 034101.
- [30] K.J. Fujimoto, in: T. Akasaka (Ed.), *Chemical Science of π -Electron Systems*, Springer, 2015, pp. 761–777.
- [31] P.J. Stephens, F.J. Devlin, C.F. Chabalowski, M.J. Frisch, *J. Phys. Chem.* 98 (1994) 11623–11627.
- [32] TURBOMOLE V6.5 2013. A development of University of Karlsruhe and Forschungszentrum Karlsruhe GmbH (1989–2007), TURBOMOLE GmbH, since 2007, available from <http://www.turbomole.com>.
- [33] A. Schäfer, H. Horn, R. Ahlrichs, *J. Chem. Phys.* 97 (1992) 2571–2577.
- [34] M. Kleinschmidt, C.M. Marian, M. Waletzke, S. Grimme, *J. Chem. Phys.* 130 (2009) 044708.
- [35] A.D. Becke, *J. Chem. Phys.* 98 (1993) 1372–1377.
- [36] O. Vahteras, J. Almlöf, M. Feyereisen, *Chem. Phys. Lett.* 213 (1993) 514–518.
- [37] F. Weigend, M. Häser, H. Patzelt, R. Ahlrichs, *Chem. Phys. Lett.* 294 (1998) 143–152.
- [38] E.V. de Wael, J.A. Pardo, J.A. van Koeveringe, J. Lugtenburg, *Recl. Trav. Chim. Pays-Bas* 96 (1977) 306–309.
- [39] A.C. Benniston, G. Copley, *Phys. Chem. Chem. Phys.* 11 (2009) 4124–4131.
- [40] D. Biermann, W. Schmidt, *J. Am. Chem. Soc.* 102 (1980) 3163–3173.
- [41] J. Ferguson, L.W. Reeves, W.G. Schneider, *Can. J. Chem.* 35 (1957) 1117–1136.
- [42] I. Berlman, *Handbook of Fluorescence Spectra of Aromatic Molecules*, Academic Press, N.Y., 1971.
- [43] J. Schiedt, R. Weinkauf, *Chem. Phys. Lett.* 266 (1997) 201–205.
- [44] <http://www.nist.gov>.
- [45] J.W. Knight, X. Wang, L. Gallandi, O. Dolgounitcheva, X. Ren, J.V. Ortiz, P. Rinke, T. Körzdörfer, N. Marom, *J. Chem. Theory Comput.* 12 (2016) 615–626.
- [46] A. Klamt, G. Schürmann, *J. Chem. Soc., Perkin Trans. 2* (1993) 799–805.

**Supporting information for:
Charge-transfer contributions to the excitonic coupling
matrix element in BODIPY-based energy transfer cassettes**

J. Dominik Spiegel, Igor Lyskov, Martin Kleinschmidt, Christel M. Marian*

Institute of Theoretical and Computational Chemistry, Heinrich Heine University
Düsseldorf, Universitätsstr. 1, D-40225 Düsseldorf, Germany

*E-mail: Christel.Marian@uni-duesseldorf.de
Phone: +49 211 81-13210. Fax: +49 211 81-13466

Table S1 Composition of the excitonic coupling matrix elements calculated for the P-structures. The exchange terms have already been multiplied by a factor of $\frac{1}{2}$.

Method and contribution		ECME	With bridge														
			P_B2-A			P_B2-E-A			P_B2-PE-A			P_B2-EPE-A					
			Coulomb	Exchange	Total	Coulomb	Exchange	Total	Coulomb	Exchange	Total	Coulomb	Exchange	Total			
STD	V_{Dir}	$\langle D'A V D'A \rangle$	941.3	-11.0	952.3	-629.8	7.7	-637.5	-343.7	-5.8	-337.9	213.4	-0.1	213.5	0.0	0.0	0.0
		$\langle D'A V DA \rangle$	-9.0	-0.9	-8.1	-4.6	-0.2	-4.5	-79.9	-10.2	-69.8	1.8	-0.4	2.2	0.0	0.0	0.0
	V_{CT}	$\langle D'A V D'A \rangle$	1.8	-39.4	41.1	-7.8	81.5	-89.3	-3.1	-71.8	68.7	2.3	-19.0	21.3	0.0	0.0	0.0
		$\langle D'A V DA \rangle$	-0.2	-13.5	13.3	-6.6	12.6	-19.2	-5.6	-30.0	24.4	0.2	-0.4	0.6	0.0	0.0	0.0
	V_{pol}	$\langle D'A V D'A \rangle$	-20.8	-10.4	-19.0	29.5	-48.5	63.1	13.1	50.0	30.4	0.8	29.6	0.0	0.0	0.0	0.0
		$\langle D'A V D'A \rangle$	-56.9	22.3	-79.2	89.2	2.3	86.9	12.2	2.6	9.6	-25.8	-0.7	-25.1	0.0	0.0	0.0
		$\langle D'A V DA \rangle$	1.1	9.5	-8.3	3.1	3.8	-0.7	-30.6	-44.2	13.6	7.3	3.9	3.4	0.0	0.0	0.0
		$\langle D'A V DA \rangle$	19.4	12.7	6.8	-7.3	-10.3	3.0	10.7	54.6	-44.0	-5.4	1.9	-7.3	0.0	0.0	0.0
		$\langle D'A V D'A \rangle$	-0.3	10.0	-10.4	15.9	-9.3	25.3	77.1	30.0	47.2	0.1	2.6	-2.5	0.0	0.0	0.0
		$\langle D'A V D+A \rangle$	-31.5	8.5	-40.0	80.2	-3.0	83.2	6.9	-19.7	26.6	-26.3	0.5	-26.8	0.0	0.0	0.0
	V_{corr}	$\langle D'A V D'A \rangle$	11.4	0.7	10.7	-16.5	-11.5	-5.0	10.6	-7.5	18.0	-0.5	0.5	-1.0	0.0	0.0	0.0
		$\langle D'A V DA \rangle$	205.0	15.3	189.7	-90.5	-8.4	-82.1	9.8	20.7	-11.0	-3.6	-10.6	7.1	0.0	0.0	0.0
	Direct	$\langle D'A V D'A \rangle$	-0.4	-0.2	-0.2	5.9	0.4	5.5	-0.6	4.3	-4.9	-3.5	-0.9	-2.6	0.0	0.0	0.0
		$\langle D'A V DA \rangle$	-12.2	2.3	9.9	12.3	2.9	9.4	4.4	2.0	2.5	-0.3	0.2	-0.5	0.0	0.0	0.0
		CT	941.1	-24.5	965.6	-636.4	20.3	-656.7	-349.2	-35.8	-313.4	213.6	-0.5	214.1	0.0	0.0	0.0
		Polarization	-31.9	8.3	-40.2	86.2	-2.6	88.8	6.3	-15.4	21.7	-29.7	-0.4	-29.3	0.0	0.0	0.0
		Correlation	152.0	9.8	142.2	-53.4	86.8	-140.2	-7.4	-42.6	35.2	6.6	-23.6	30.1	0.0	0.0	0.0
		Indirect	-12.6	7.7	-20.3	28.2	-6.5	34.7	81.6	31.9	49.6	-0.2	2.8	-2.9	0.0	0.0	0.0
		Total	1048.6	1.3	1047.2	-575.4	98.1	-673.5	-268.7	-61.8	-206.9	190.3	-21.7	212.0	0.0	0.0	0.0
		MTD	1287.1	23.6	1263.5	1104.1	12.6	1091.5	460.6	5.8	454.7	-350.6	-4.8	-345.8	0.0	0.0	0.0

Method and contribution		ECME	Without bridge														
			P_B2-A			P_B2(-E)-A			P_B2(-PE)-A			P_B2(-EPE)-A			P_B8(-PE)-A		
			Coulomb	Exchange	Total	Coulomb	Exchange	Total	Coulomb	Exchange	Total	Coulomb	Exchange	Total	Coulomb	Exchange	Total
STD	V_{Dir}	$\langle D'A V D'A \rangle$				-443.4	-0.5	-442.9	-137.0	0.0	-137.0	78.0	0.0	78.0	0.0	0.0	0.0
		$\langle D'A V DA \rangle$				-0.9	-0.3	-0.6	0.0	0.0	0.0	0.0	0.0	0.0	0.0	0.0	0.0
	V_{CT}	$\langle D'A V D'A \rangle$				-0.1	0.5	-0.7	0.0	0.0	0.0	0.0	0.0	0.0	0.0	0.0	0.0
		$\langle D'A V DA \rangle$				-0.9	0.9	-1.8	0.0	0.0	0.0	0.0	0.0	0.0	0.0	0.0	0.0
	V_{pol}	$\langle D'A V D'A \rangle$				-19.8	0.1	-19.9	0.0	0.0	0.0	0.0	0.0	0.0	0.0	0.0	0.0
		$\langle D'A V D'A \rangle$				16.5	0.3	16.2	0.0	0.0	0.0	0.0	0.0	0.0	0.0	0.0	0.0
		$\langle D'A V DA \rangle$				3.2	0.3	3.0	0.0	0.0	0.0	0.0	0.0	0.0	0.0	0.0	0.0
		$\langle D'A V DA \rangle$				-1.0	0.0	-1.1	0.0	0.0	0.0	0.0	0.0	0.0	0.0	0.0	0.0
		$\langle D'A V D'A \rangle$				-0.2	0.4	-0.6	0.0	0.0	0.0	0.0	0.0	0.0	0.0	0.0	0.0
		$\langle D'A V DA \rangle$				14.5	0.2	14.3	0.0	0.0	0.0	0.0	0.0	0.0	0.0	0.0	0.0
	V_{corr}	$\langle D'A V D'A \rangle$				0.2	-0.1	0.3	0.0	0.0	0.0	0.0	0.0	0.0	0.0	0.0	0.0
		$\langle D'A V DA \rangle$				-14.7	0.5	-15.1	0.0	0.0	0.0	0.0	0.0	0.0	0.0	0.0	0.0
	Direct	$\langle D'A V D'A \rangle$				0.6	0.3	0.2	0.0	0.0	0.0	0.0	0.0	0.0	0.0	0.0	0.0
		$\langle D'A V DA \rangle$				0.7	0.3	0.4	0.0	0.0	0.0	0.0	0.0	0.0	0.0	0.0	0.0
		CT				-444.2	0.4	-444.6	-137.0	0.0	-137.0	78.0	0.0	78.0	0.0	0.0	0.0
		Polarization				-20.7	-0.2	-20.5	0.0	0.0	0.0	0.0	0.0	0.0	0.0	0.0	0.0
		Correlation				0.8	0.2	0.6	0.0	0.0	0.0	0.0	0.0	0.0	0.0	0.0	0.0
		Indirect				-429.7	0.6	-430.3	-137.0	0.0	-137.0	78.0	0.0	78.0	0.0	0.0	0.0
		Total				-445.4	2.9	-448.3	-137.0	0.0	-137.0	78.0	0.0	78.0	0.0	0.0	0.0
		MTD				-468.6	-2.0	-466.6	133.5	0.0	133.5	75.9	0.0	75.9	0.0	0.0	0.0

Table S2 CT matrices of the ethylene dimer.

Distance (a_0)	2a (Frenkel I)				3a (Frenkel II)			
	BA	AB	AA	BB	BA	AB	AA	BB
7	0.147	0.147	0.353	0.353	0.067	0.067	0.433	0.433
8	0.063	0.063	0.437	0.437	0.013	0.013	0.487	0.487
9	0.014	0.014	0.486	0.486	0.002	0.002	0.498	0.498
10	0.002	0.002	0.498	0.498	0.000	0.000	0.500	0.500
11	0.000	0.000	0.500	0.500	0.000	0.000	0.500	0.500
12	0.000	0.000	0.500	0.500	0.000	0.000	0.500	0.500
13	0.000	0.000	0.500	0.500	0.000	0.000	0.500	0.500
14	0.000	0.000	0.500	0.500	0.000	0.000	0.500	0.500
15	0.000	0.000	0.500	0.500	0.000	0.000	0.500	0.500
16	0.000	0.000	0.500	0.500	0.000	0.000	0.500	0.500
17	0.000	0.000	0.500	0.500	0.000	0.000	0.500	0.500
18	0.000	0.000	0.500	0.500	0.000	0.000	0.500	0.500
<hr/>								
Distance (a_0)	4a (CT I)				5a (CT II)			
	BA	AB	AA	BB	BA	AB	AA	BB
7	0.433	0.433	0.067	0.067	0.353	0.353	0.147	0.147
8	0.487	0.487	0.013	0.013	0.437	0.437	0.063	0.063
9	0.498	0.498	0.002	0.002	0.486	0.486	0.014	0.014
10	0.500	0.500	0.000	0.000	0.498	0.498	0.002	0.002
11	0.500	0.500	0.000	0.000	0.500	0.500	0.000	0.000
12	0.500	0.500	0.000	0.000	0.500	0.500	0.000	0.000
13	0.500	0.500	0.000	0.000	0.500	0.500	0.000	0.000
14	0.500	0.500	0.000	0.000	0.500	0.500	0.000	0.000
15	0.500	0.500	0.000	0.000	0.500	0.500	0.000	0.000
16	0.500	0.500	0.000	0.000	0.500	0.500	0.000	0.000
17	0.500	0.500	0.000	0.000	0.500	0.500	0.000	0.000
18	0.500	0.500	0.000	0.000	0.500	0.500	0.000	0.000

Table S3 Energies of the Frenkel and CT states of the ethylene dimer.

State	Absolute Energies (H)					Relative Energies (cm ⁻¹)					Splitting (cm ⁻¹)	
	1a	2a	3a	4a	5a	1a	2a	3a	4a	5a	2a - 3a	4a - 5a
Distance (a ₀)	Ground State	Frenkel I	Frenkel II	CT I	CT II	Ground State	Frenkel I	Frenkel II	CT I	CT II		
7	-156.9465	-156.6781	-156.6436	-156.6286	-156.6110	400.8	59322.9	66887.5	70175.5	74047.7	-7564.6	-3872.2
8	-156.9479	-156.6633	-156.6471	-156.6212	-156.6159	113.2	62561.7	66111.0	71797.6	72978.2	-3549.3	-1180.6
9	-156.9481	-156.6573	-156.6490	-156.6136	-156.6125	68.7	63870.8	65694.5	73463.0	73713.4	-1823.6	-250.4
10	-156.9481	-156.6557	-156.6504	-156.6075	-156.6073	52.0	64242.2	65389.0	74815.0	74860.2	-1146.8	-45.2
11	-156.9482	-156.6552	-156.6515	-156.6026	-156.6025	34.5	64336.6	65155.2	75896.5	75909.0	-818.6	-12.5
12	-156.9483	-156.6551	-156.6523	-156.5985	-156.5985	21.9	64365.1	64981.2	76789.8	76797.0	-616.1	-7.2
13	-156.9483	-156.6551	-156.6529	-156.5950	-156.5950	15.1	64374.3	64851.7	77545.7	77551.1	-477.4	-5.5
14	-156.9483	-156.6551	-156.6533	-156.5921	-156.5921	10.5	64373.9	64751.2	78192.9	78197.3	-377.3	-4.4
15	-156.9483	-156.6551	-156.6537	-156.5895	-156.5895	7.7	64367.7	64671.5	78753.4	78756.9	-303.8	-3.5
16	-156.9483	-156.6551	-156.6540	-156.5873	-156.5873	5.7	64358.5	64606.7	79243.5	79246.4	-248.2	-2.9
17	-156.9483	-156.6552	-156.6542	-156.5853	-156.5853	4.2	64347.3	64553.0	79675.4	79677.9	-205.6	-2.4
100	-156.9484	-156.6430	-156.6430	-156.5729	-156.5729	0.0	67012.4	67013.3	82405.0	82405.0	-0.9	0.0

Figure S1 Energies of the Frenkel and CT states of the ethylene dimer

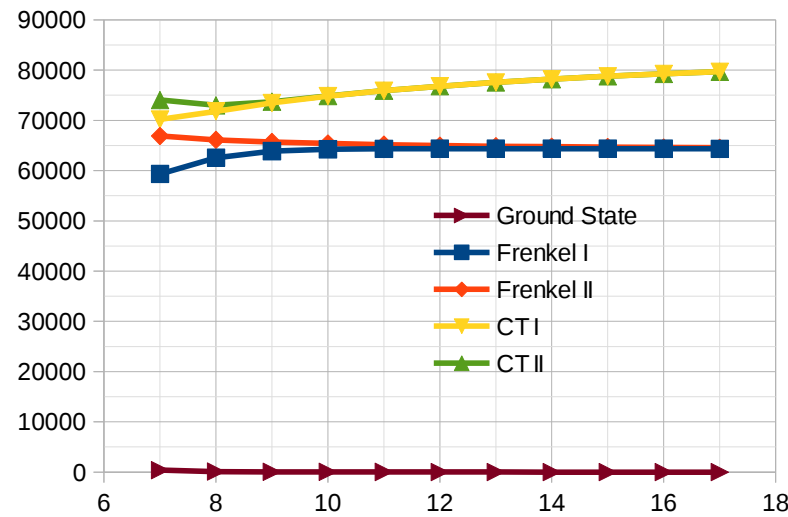


Table S4 Couplings of the Frenkel excitonic states of the ethylene dimer.

Distance (a_0)	<2a V 2a>						<3a V 3a>				
	V_{dir}	V_{CT}	V_{pol}	V_{corr}	V_{tot}		V_{dir}	V_{CT}	V_{pol}	V_{corr}	V_{tot}
7	-2204.46	420.68	26.41	20.12	-1757.38		2632.58	-136.56	697.49	8.56	3202.07
8	-1797.04	123.63	-2.55	1.41	-1675.97		2004.80	-18.53	148.00	0.44	2134.71
9	-1360.27	18.17	-1.75	0.04	-1343.85		1393.47	-2.41	22.37	0.01	1413.45
10	-985.80	1.64	-0.25	0.00	-984.40		988.96	-0.23	2.32	0.00	991.04
11	-725.35	0.11	-0.02	0.00	-725.27		725.57	-0.02	0.17	0.00	725.72
12	-548.37	0.01	0.00	0.00	-548.37		548.38	0.00	0.01	0.00	548.39
13	-424.83	0.00	0.00	0.00	-424.83		424.83	0.00	0.00	0.00	424.83
14	-336.01	0.00	0.00	0.00	-336.01		336.01	0.00	0.00	0.00	336.01
15	-270.47	0.00	0.00	0.00	-270.47		270.47	0.00	0.00	0.00	270.47
16	-221.03	0.00	0.00	0.00	-221.03		221.03	0.00	0.00	0.00	221.03
17	-183.01	0.00	0.00	0.00	-183.01		183.01	0.00	0.00	0.00	183.01

Figure S2 Couplings of the Frenkel excitonic states of the ethylene dimer. <2a|V|2a> (l.h.s.), <3a|V|3a> (r.h.s.)

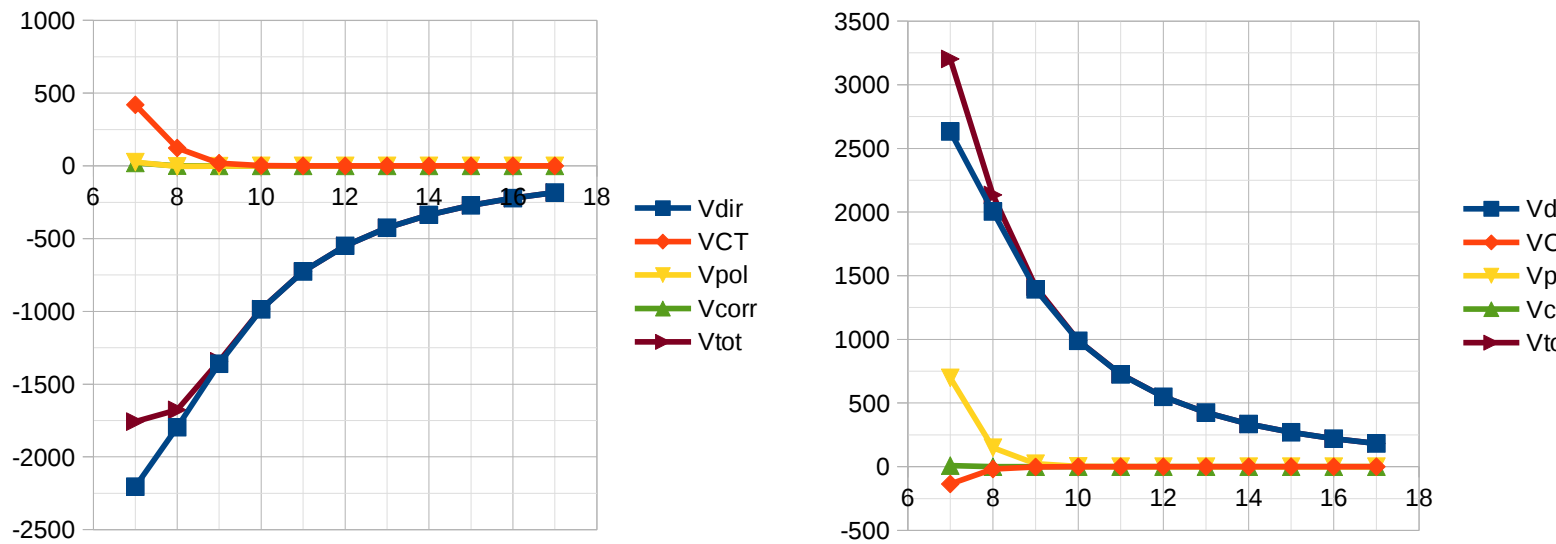
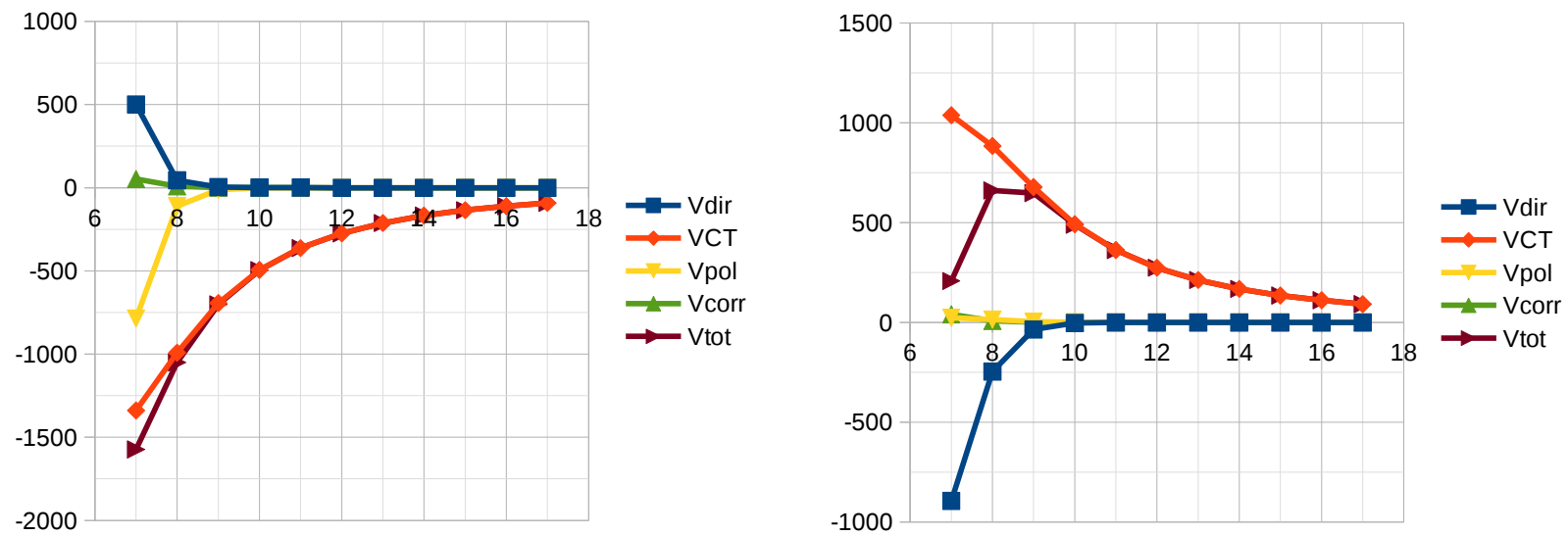


Table S5 Coupling of CT state of the ethylene dimer.

Distance (a_0)	<4a V 4a>					V_{tot}	<5a V 5a>				
	V_{dir}	V_{CT}	V_{pol}	V_{corr}	V_{tot}		V_{dir}	V_{CT}	V_{pol}	V_{corr}	V_{tot}
7	499.74	-1338.86	-786.47	51.97	-1573.62		-894.03	1037.63	23.23	40.60	207.435
8	45.18	-992.56	-111.27	8.84	-1049.80		-246.11	884.16	14.74	7.79	660.574
9	3.67	-694.74	-11.96	0.94	-702.09		-35.34	678.22	3.65	0.91	647.436
10	0.24	-494.27	-0.97	0.06	-494.93		-3.18	492.75	0.46	0.06	490.097
11	0.01	-362.77	-0.06	0.00	-362.81		-0.20	362.67	0.04	0.00	362.504
12	0.00	-274.19	0.00	0.00	-274.19		-0.01	274.18	0.00	0.00	274.177
13	0.00	-212.42	0.00	0.00	-212.42		0.00	212.42	0.00	0.00	212.416
14	0.00	-168.01	0.00	0.00	-168.01		0.00	168.01	0.00	0.00	168.006
15	0.00	-135.24	0.00	0.00	-135.24		0.00	135.24	0.00	0.00	135.237
16	0.00	-110.52	0.00	0.00	-110.52		0.00	110.52	0.00	0.00	110.515
17	0.00	-91.50	0.00	0.00	-91.50		0.00	91.50	0.00	0.00	91.502

Figure S3 Couplings of the CT states of the ethylene dimer. $\langle 4a|V|4a\rangle$ (l.h.s.), $\langle 5a|V|5a\rangle$ (r.h.s.).



Failure of the IDA in FRET Systems at Close Inter-Dye Distances Is Moderated by Frequent Low κ^2 Values

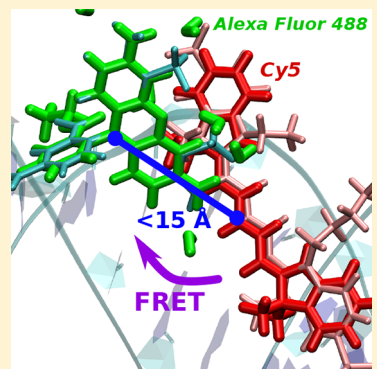
J. Dominik Spiegel,[†] Simone Fulle,[§] Martin Kleinschmidt,[†] Holger Gohlke,[‡] and Christel M. Marian*,[†]

[†]Institute of Theoretical and Computational Chemistry and [‡]Institute of Pharmaceutical and Medicinal Chemistry, Heinrich Heine University Düsseldorf, Universitätsstr. 1, D-40225 Düsseldorf, Germany

[§]BioMed X Innovation Center, Im Neuenheimer Feld 515, 69120 Heidelberg, Germany

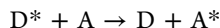
Supporting Information

ABSTRACT: Förster resonance energy transfer (FRET) is analyzed in terms of distance- and orientation-dependent interactions between the transition dipole moments of the involved donor and acceptor molecules. However, the ideal dipole approximation (IDA) is known to fail at short donor–acceptor distances. In this work, we model FRET in a Cy5- and Alexa Fluor 488-labeled double-stranded RNA by means of combined molecular dynamics (MD) simulations and quantum-chemical calculations involving the IDA as well as the more sophisticated monomer transition density (MTD) approach. To this end, the relaxed ground-state geometries of the dyes were fitted to the MD-based structures. Although substantial deviations between IDA and MTD results can be observed for individual snapshots, the statistical impact of the failure on the FRET rates is negligible in the chosen examples. Our results clearly demonstrate that the IDA-based Förster model can still be applied to systems with small donor–acceptor distances, provided that the dyes are not trapped in arrangements with a high IDA failure and that the distribution of the relative transition dipole orientations is fairly isotropic.



INTRODUCTION

Förster resonance energy transfer (FRET)¹ is a powerful method applied in biophysics for the analysis of the structure and dynamics of biomolecular systems such as proteins or nucleic acids.^{2–4} Labeling the target system with a suitable pair of fluorescent dyes, excitation energy can be transferred from an electronically excited singlet state of the donor to the acceptor.



Whereas the excited donor D^* returns to its singlet ground state in a nonradiative process, the acceptor A is excited to its first excited singlet state and relaxes to its electronic ground state by fluorescence. As the efficiency of the process depends on the distance and the relative orientation of the two fluorophores, structural information of the target system can be deduced from the excitation energy transfer (EET) rate.⁵ The experimental determination of intermolecular distances is directly based on the FRET efficiency E , which is defined as the ratio of the EET rate and the sum of all rates describing the decay of the excited donor (EET, fluorescence, and non-radiative processes).⁶

$$E = \frac{k_{\text{EET}}}{k_{\text{EET}} + k_{\text{fl}} + k_{\text{nr}}} \quad (1)$$

The FRET efficiency can, for instance, be obtained from the donor fluorescence intensity in the presence and absence of the acceptor. The donor–acceptor distance r for which the FRET efficiency reduces to 50% is defined as the Förster radius R_F .

$$E = \frac{1}{1 + \left(\frac{r}{R_F}\right)^6} \quad (2)$$

The exponent of six in the denominator of eq 2 can be traced back to the fact that the Förster model is based on the ideal dipole approximation (IDA) describing the excitonic coupling of the interacting dyes as the interaction between two transition dipole moments. The EET rate is proportional to the square of this coupling, which decreases with the third power of the donor–acceptor distance. The Förster radius is a constant parameter for a given pair of dyes, which depends on the fluorescence quantum yield of the donor, Q_D , and the spectral overlap integral of the donor emission and acceptor absorption spectra. [The acceptor absorption spectrum, $\alpha_A(\lambda)$, is normalized to the intensity of the absorption maximum and weighted by the molar absorption coefficient ($M^{-1} \text{ cm}^{-1}$) whereas the donor fluorescence spectrum, $F_D(\lambda)$, is normalized to unit area (dimensionless). Therefore, the quantity is given in units of $M^{-1} \text{ cm}^{-1} \text{ nm}^4$ if a nm energy scale is used.]

$$R_F = \sqrt[6]{\frac{9 \ln 10 \cdot \kappa^2 \cdot Q_D}{128 \pi^5 \cdot n^4 \cdot N_A} \cdot \int F_D(\lambda) \cdot \alpha_A(\lambda) \cdot \lambda^{-4} d\lambda} \quad (3)$$

Received: June 7, 2016

Revised: August 4, 2016

Published: August 4, 2016

where n is the refractive index of the solvent and κ^2 is the orientation factor. FRET provides accurate results on the scale of the target system, typically in the range of 30–80 Å.⁷ A similar distance range is covered by EPR spectroscopy, with continuous-wave EPR providing distance information up to ~25 Å,⁸ and advanced pulse EPR methods, such as pulsed electron double resonance (PELDOR),^{9,10} up to ~60 Å. Complementary structural information for lower distances down to 5 Å can be obtained by nuclear magnetic resonance spectroscopy.^{7,11}

The first biophysical application of FRET started in 1970.¹² Whereas the early research was focused on proteins, applications to nucleic acids have become more important since the 1980s. In biomedical research, FRET is used as a reporter method for monitoring different reactions of the DNA.¹² In 1985, Heller and Morrison¹³ presented a FRET-based method permitting a real-time observation of the hybridization process of oligonucleotides to a DNA sequence. A method for monitoring DNA amplification by the polymerase chain reaction was developed by Livak et al.^{14,15} Furthermore, the cleavage of a DNA by restriction enzymes can be verified due to separation of donor and acceptor moieties in space if the DNA is labeled with a pair of FRET dyes at suitable positions.¹⁶ In bioanalytics, FRET-based biosensors are used for the detection of heavy metals.¹⁷ A comprehensive review on DNA-based FRET applications in vitro and in vivo has been given by Didenko.¹² In the recent past, important RNA-based FRET applications have also been reported. Berman et al. could show by means of single molecule FRET (sm-FRET) that the RNA-subunit of the ribonucleoprotein telomerase contributes to the template positioning within the active site.¹⁸ In 2014, Keller et al. presented a study on the folding kinetics of the Diels–Alderase ribozyme, which is based on a newly devised hidden Markov model for the evaluation of sm-FRET measurements.¹⁹ An experimental study on the Mg²⁺-facilitated conformational change of an RNA three-helix junction was reported by Kim et al.²⁰

Typically, large molecular linkers are used to couple the dyes to the target system. By this means, a largely free rotation of the dyes in space is achieved, such that the mean relative donor–acceptor orientation follows the well-known isotropic probability distribution.^{21–23} Because classical FRET theory is based on the IDA,^{1,24} a reasonable structure prediction is possible only if the assumption of the IDA is widely valid.

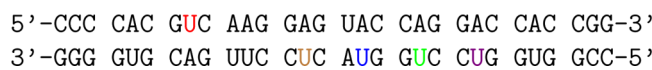
As the IDA is known to fail at small donor–acceptor distances,²⁵ the question arises as to how strongly this failure affects the conclusions drawn for a realistic system. To this end, we studied the dynamics of a double-stranded RNA (dsRNA) tagged with Alexa Fluor 488 as the exciton donor and Cy5 as the acceptor at different positions. Both dyes as well as the dsRNA are known to be largely rigid such that the flexibility of the whole system is mainly based on the degrees of freedom of the linkers.^{2,26,27} Similar model systems with larger donor–acceptor distances have been extensively studied by Seidel, Gohlke, and co-workers using both experimental and theoretical methods.^{2–4,28} Widengren and Schwille stated that approximately 50% of Cy5 undergoes a photoisomerization to the nonfluorescent cis-conformer, which is not able to transfer the excitation energy to the acceptor dye.²⁸ In this work, we neglect isomerization processes and concentrate on the fluorescent trans-conformer of Cy5. In 2002, Dietrich et al. presented an anisotropy-measurement-based study on the impact of the distance between different rhodamine and

cyanine dyes on the FRET efficiency.²⁹ Using C₆-aminolinkers to attach the dyes to a rigid oligonucleotide, they found that in none of their model systems did the dyes rotate freely in space, resulting in a dynamic inhomogeneous distribution of the donor–acceptor distance and orientation. The FRET efficiency was found to be strongly correlated with the donor–acceptor distance, depending on whether fluorescence quenching or electron transfer was promoted. In 2010, Di Fiori and Meller reported a sm-FRET study on the effect of dye–dye interactions in double-stranded DNA molecules labeled with different rhodamine and cyanine dyes.³⁰ The authors state that sm-FRET can be used for the accurate determination of inter-dye distances even at small distances down to 3 nm. A time-dependent density functional theory (TD-DFT) and configuration interaction singles-based study on critical FRET distances between cyanine and rhodamine dyes was presented by Muñoz-Losa et al.³¹ The IDA was found to perform well down to inter-dye distances of about 20 Å in the case of an isotropic transition dipole distribution and down to about 50 Å if the molecular motions of the dyes are restricted. In 2011, Speelman et al.³² presented a theoretical study on the sampling methods of donor–acceptor excitonic couplings obtained from molecular dynamics (MD) simulations, focusing on the problem of transiently occupied states. The couplings were calculated using either the IDA, which was found to significantly overestimate the couplings at close distances, or a more sophisticated approach based on the full donor and acceptor transition densities. The authors state that a Markov chain-based sampling model, accounting for fluctuations in the EET rate, provides physically better results in comparison with an independent sampling of equally weighted trajectory points.

In this work, we aimed at providing a fast and efficient method for making a large number of donor acceptor configurations, obtained from MD simulations, accessible to a quantum-chemical approach beyond the IDA to investigate the impact of a possible failure of IDA on FRET rates. Simplified DFT-optimized relaxed ground-state structures of Alexa Fluor 488 and Cy5 were fitted to frames of the MD trajectories, minimizing the root-mean-square deviation (RMSD). Using the transformation matrix for rotating the molecular orbitals (MOs), a computationally costly recalculation of the transition density matrices of the dyes can be avoided.

THEORETICAL METHODS

MD Simulations. Starting Structure Generation. Canonical A-form dsRNA structures were generated using the nucgen module of the Amber10 package.³³ The linker and dye residues of Cy5 were attached to a modified uracil base of the 8th nucleotide from the 5'-end of one RNA strand, whereas different positions were tested for attaching the linker carrying the Alexa Fluor 488 dye to sample small distances between the two dyes. The initially tested sequence and dye positions are given below, where the colored nucleotides refer to the labeling positions with dyes Cy5 (red) and Alexa Fluor 488 (brown, blue, green, and purple).



The smallest distances (≤ 8 Å) between the dyes were sampled by attaching the linker carrying the Alexa Fluor 488 dye to a modified uracil base at position 23nt (23rd nucleotide in the 3' → 5' direction) (purple) followed by a few snapshots

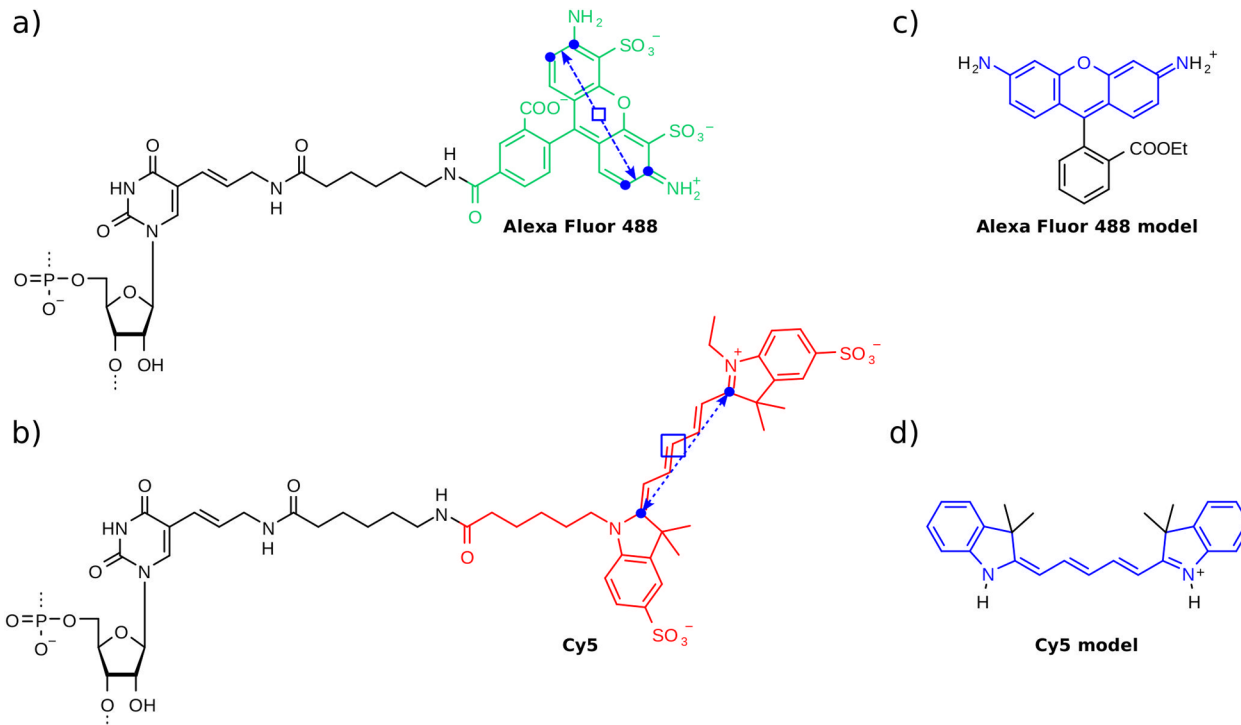


Figure 1. Structures of (a) Alexa Fluor 488 and (b) Cy5 bound to a uridine unit of the dsRNA as well as simplified structures (c) and (d) used for QM calculations. Location of the mass-weighted average positions (blue boxes) and transition dipoles (dashed blue arrows) used to calculate distances and angles between the dyes within the MD part of this article. Parts of the model structures considered for the fit to the MD snapshots are highlighted in blue.

with distances about 10 Å by attaching Alexa Fluor 488 at position 14nt (brown) and 20nt (green).

Further dye positions of Alexa Fluor 488 (blue and green) were tested around position 23nt using the sequence and dye positions given below.

5'-CCC CAC GUC AAG GAG UAC AAA AAA CAC CGG-3'
3'-GGG GUG CAG UUC CUC AUG UUU UUU GUG GCC-5'
In doing so, several snapshots with small distances between the dyes (≤ 8 Å) were sampled by attaching Alexa Fluor 488 to a modified uracil base at position 22nt (green).

The trajectories with Alexa Fluor 488 attached to positions 22nt and 23nt thus formed the basis for the main analysis and are named **dsRNA_8nt_22nt** and **dsRNA_8nt_23nt**. For comparison, we also analyzed the trajectories with Alexa Fluor 488 attached to position 14nt (**dsRNA_8nt_14nt**), as this position is very close to the anchor point of Alexa Fluor 488 but nevertheless results only in distances of about 10 Å. In addition, the simulation of **dsRNA_8nt_23nt** was repeated to enhance the sampling of snapshots with small distances between the dyes (named **dsRNA_8nt_23ntII**).

Setup of MD Simulations and Production Runs. All MD simulations were performed with the AMBER14 suite of programs³³ together with the ff99SB force field.^{34,35} Charges of the dyes, the 6-aminohexanal part of the linker, and the remaining part of the modified nucleotide (prop-2-en-1-amine group) were determined separately using the RESP procedure,³⁶ which involves restrained fitting to an electrostatic potential derived at the HF/6-31G* level. Other force-field parameters were assigned using the generalized Amber force field (GAFF),³⁷ which is appropriate given that the linker consists of ω -amino acids and that the dyes are largely rigid. To prevent large internal motions of the RNA, harmonic positional

restraints with force constants of 1 kcal/(mol × Å²) were applied to all phosphorus atoms. That way, the main results of our simulations should not be sensitive to the Amber force field used for the dsRNA. For explicit solvent MD simulations, Mg²⁺ ions were added at a concentration of 0.02 M. Nonbonded parameters for Mg²⁺ were taken from Åqvist.³⁸ The system was neutralized by adding sodium counter ions and solvated in a box of TIP3P water molecules,³⁹ forming a solvent shell of at least 11 Å around the solute. The system was thermalized (see below) and then simulated in the canonical ensemble (constant number of particles, temperature, and volume; NVT) using the particle mesh Ewald method⁴⁰ to treat long-range electrostatic interactions; bonds involving hydrogen atoms were constrained by the SHAKE algorithm.⁴¹ The integration time step for the MD simulations in explicit water was 2 fs, with a direct-space, nonbonded cutoff of 9 Å. Conformations saved at 20 ps intervals were used for analysis. The analyzed MD trajectories had a length of 300 ns for **dsRNA_8nt_14nt** and 400 ns for **dsRNA_8nt_22nt**, **dsRNA_8nt_23nt**, and **dsRNA_8nt_23ntII**, respectively.

Thermalization Protocol for MD Simulations. Initially, the energy of the system was minimized by 250 steps of a steepest descent minimization followed by 250 steps of a conjugate gradient minimization. Afterward, MD simulations in the canonical ensemble were carried out for 50 ps during which the system was heated from 100 to 295 K. Subsequently, MD simulations in the isothermal-isobaric ensemble (NPT) were performed for 50 ps to adjust the solvent density. Harmonic restraints with force constants of 5 kcal/(mol × Å²) were applied to all solute atoms during these steps. Finally, the harmonic constraints were removed from the dyes, and those applied to the RNA nucleotides were gradually reduced to 1 kcal/(mol × Å²) during 250 ps of NVT-MD.

Analysis of MD Trajectories. Within the MD part of this work, distances between the dyes were calculated between the centers of mass defined by the mass-weighted average positions of C9 and O10 in the xanthene ring of Alexa Fluor 488 and C3 of the pentyl chain of Cy5 (Figure 1; blue boxes). The angles between the orientations were calculated on the basis of the transition dipoles, defined by the vector between the average positions of C2 and C3, and C6 and C7, in the xanthene ring in Alexa Fluor 488 and the vector between the C2 atoms of the two 2,3-dihydro-1H-indole rings in Cy5 (Figure 1; dashed blue arrows). In this work, we consider only the trajectories in which Cy5 is all-trans configured in the electronic ground state. In all QM-based calculations, the centers of mass were calculated from the positions and masses of all atoms of the appropriate dye. The distance refers to the length of the vector connecting the centers of mass of the two dyes. The transition dipole moments were obtained from DFT-optimized structures (see below), which were adapted by rotation to the MD orientation of the appropriate dye.

Quantum-Chemical Calculations. Simplified Structures of the Dyes. Within the QM part of our calculations, we used simplified structures of Alexa Fluor 488 and Cy5 (Figure 1). To avoid handling of the strongly negatively charged systems, which are poorly described by usual density functionals, the sulfonate groups were removed. Alexa Fluor 488 is a sulfonate derivative of a rhodamine precursor. Sulfonation aims to achieve a better water solubility and to prevent quenching effects due to sticking to nucleic acids.⁴² However, the dye is reported to have absorption and emission maxima close to its precursor.⁴² The same holds true for Cy5 compared to its nonsulfonated precursor Quasar 670.⁴³ Therefore, we assume the simplifications to be justified for our purposes. Furthermore, we performed test calculations on Alexa Fluor 488 and Cy5 including the sulfonate substituents with and without explicit solvation. Although the absorption behavior can be excellently reproduced, the description of the emission behavior fails when sulfonate groups are present. In these cases, TD-DFT, used for the geometry optimization of excited states, yields electronic structures that are dominated by charge-transfer (CT) instead of local excitations. A further simplification was introduced by substitution of the carboxylate group located at the phenyl ring of Alexa Fluor 488 by an ethyl ester to prevent cyclization of the structure during the geometry optimization of the S_1 state.

As previously reported, we used a solvation model including six explicit water molecules for the calculation of the vertical excitation energies and the excited-state properties of the rhodamine dye.⁴⁴ Two water molecules each were placed on the two amino groups and the other two close to the central oxygen atom of the xanthenyl moiety. The microhydration model correctly describes hydrogen bonding effects between solvents and solutes, which turned out to be essential for reproducing the solvent shift of rhodamines in polar protic solvents.^{44,45} To obtain a perfectly C_s symmetric structure, better suited for a fit to the MD structures, the methyl groups located at the nitrogen atoms of Cy5 were substituted by hydrogen. In the rest of the text, we do not distinguish between the original and simplified structures of the dyes.

Geometry Optimization. The equilibrium geometries of the singlet ground states (S_0) of both (simplified) Alexa Fluor 488 and Cy5 were optimized using DFT in conjunction with the BHLYP hybrid functional.⁴⁶ The molecular structures of the first excited singlet states (S_1) of both dyes were optimized

using TD-DFT. All calculations were performed with TURBOMOLE 6.5,⁴⁷ employing a basis set of split valence quality with polarization functions on all atoms (SVP).⁴⁸ Frequency analyses at the S_0 and S_1 minimum geometries were carried out using the SNF program package.⁴⁹

Excitation Energies and Transition Densities. The photochemical properties at the ground- and excited-state minima of the dyes (vertical transition energies, transition density matrices, and transition dipole moments) were calculated using the combined DFT and multi-reference configuration interaction (MRCI) program.⁵⁰ In these calculations, Kohn–Sham orbitals of a ground-state calculation employing the BHLYP functional⁴⁶ were used. In the semiempirical DFT/MRCI method, dynamic correlation effects are considered by DFT, whereas static correlation effects are taken into account by a MRCI expansion. The configurations used in the MRCI are based on the Kohn–Sham orbitals of a closed-shell electronic state. At present, parameter sets are available for the BHLYP functional.^{50,51} Double counting of dynamic correlation is avoided by damping the off-diagonal matrix elements by a rapidly decreasing function that depends on the energy difference of the configurations and a cutoff parameter. Within this article, we used the original set of parameters⁵⁰ and an orbital selection energy threshold of 1.0 E_H to compute the lowest 12 eigenvectors in the case of Cy5 and the lowest 30 eigenvalues in the case of Alexa Fluor 488. The initial MRCI reference space was spanned by all single and double excitations from the six highest occupied MOs to the six lowest unoccupied MOs of the ground-state Kohn–Sham determinant. A second DFT/MRCI step was performed, with a refined reference space comprising all configurations that contribute to one of the 12 (30) lowest-lying eigenvectors of the initial DFT/MRCI calculation, with a squared coefficient of 0.003 or larger.

Vibrationally Resolved Spectra. vibrationally resolved absorption and emission spectra of both Alexa Fluor 488 and Cy5 were generated with the VIBES program^{52,53} using a temperature of 298 K, an integration time interval of 3000 fs, and a Gaussian damping of the correlation function of width 100 cm⁻¹. To avoid large displacements of the normal coordinates due to explicit solvent molecules, we used the normal modes and geometries of the relaxed S_0 and the S_1 states in vacuum. The obtained vibrationally resolved spectrum was shifted by the adiabatic energy difference of the relaxed S_0 and S_1 states in the presence of an aqueous environment.

EMCE, EET Rates, Spectral Overlap, and EET Efficiencies. According to Fermi's golden rule, the EET rate can be calculated in Condon approximation from the excitonic coupling matrix element (ECME) and the Franck–Condon weighted density (FCWD) of the involved excited states²⁴

$$k_{\text{EET}} = \frac{2\pi}{\hbar} |V_{\text{DA}}|^2 \sum_{\text{MN}} \sum_{\text{KL}} f(E_{\text{D}^*\text{M}}) f(E_{\text{AL}}) |\langle \chi_{\text{D}^*\text{M}} | \chi_{\text{DN}} \rangle \\ \langle \chi_{\text{AL}} | \chi_{\text{A}^*\text{K}} \rangle|^2 \times \delta(E_{\text{D}^*\text{M}} + E_{\text{AL}} - E_{\text{A}^*\text{K}} - E_{\text{DN}}) \quad (4)$$

where $f(E_{\text{D}^*\text{M}})$ is the thermal occupation of the vibrational state M of the electronically excited donor molecule with energy $E_{\text{D}^*\text{M}}$. Likewise, $f(E_{\text{AL}})$ denotes the thermal occupation of the vibrational state L of the acceptor molecule in the electronic ground state with energy E_{AL} , and so forth. The delta distribution term ensures that only energy-conserving processes contribute to the EET rate. χ denote purely vibrational wavefunctions of the donor and acceptor molecules in the

electronic ground and excited states, respectively. The FCWD can be easily approximated as an overlap integral of the vibrationally resolved donor emission $I_D(E)$ and the acceptor absorption $A_A(E)$ spectra, both normalized to unit area on an energy scale.⁵⁴ It should be mentioned that this definition of the spectral overlap integral, which is based only on the line shapes of the spectra, is different from the definition in eq 3. The integral in the theoretical expression (eq 5) accounts for only the FCWD, whereas the integrated experimental intensities in eq 3 also cover the absolute values of the transition dipole moments, which are part of the ECME.

$$k_{\text{EET}} = \frac{2\pi}{\hbar} |V_{\text{DA}}|^2 \int_0^\infty A_A(E) I_D(E) dE \quad (5)$$

If d_{DA} is large compared to the intramolecular extensions of molecules D and A, the ECME is well described by the IDA^{1,25} as the dipole–dipole interaction between the transition dipole moments $\vec{\mu}_D$ and $\vec{\mu}_A$ of the donor and acceptor localized states. Furthermore, if Dexter⁵⁵ and CT contributions can be neglected, the ECME in IDA is given by

$$V_{\text{DA}} = \kappa \frac{|\vec{\mu}_A| \cdot |\vec{\mu}_D|}{|d_{\text{DA}}|^3} \quad (6)$$

The orientation factor κ^2 depends on the relative orientation of the interacting transition dipole moments⁵⁶

$$\kappa^2 = (\vec{n}_A \vec{n}_D - 3(\vec{e}_{\text{DA}} \vec{n}_A)(\vec{e}_{\text{DA}} \vec{n}_D))^2 \quad (7)$$

where \vec{e}_{DA} , \vec{n}_D , and \vec{n}_A are unit vectors pointing in the directions of the intermolecular distance vector and the transition dipole moments, respectively.²⁴

At small donor–acceptor distances, the Dexter EET cannot be neglected. Moreover, when the intermolecular separation is of the same size as the intramolecular extension, the expression for the dipole–dipole contribution in eq 6 becomes questionable. In these cases, the monomer transition density (MTD) approach was shown to provide better results than the IDA.^{57–59} The method approximates the ECME as the sum of direct and exchange interactions between the spinless reduced one-electron transition density matrices ρ_D and ρ_A of the donor and acceptor, respectively,

$$V_{\text{DA}} = \langle D^* A! \hat{V} | D A^* \rangle \approx \sum_{i,j \in D} \sum_{k,l \in A} \rho_{ij}^{(D)}(ijkl) \rho_{kl}^{(A)} - \frac{1}{2} \sum_{i,j \in D} \sum_{k,l \in A} \rho_{ij}^{(D)}(illkj) \rho_{kl}^{(A)} \quad (8)$$

where we have used the Mulliken convention for denoting the electronic repulsion integrals.

For each considered MD snapshot, the optimal overlay of the quantum mechanically and classically determined structures was computed and the ECMEs were calculated with IDA (eq 6) and MTD (eq 8). To speed up the calculation, we neglected all transition density matrix elements with an absolute value below $1.0 \times 10^{-7} a_0$. EET rates were calculated from the spectral overlap integral and ECMEs according to eq 5. The EET efficiency was computed according to eq 1 from the calculated EET rate and the calculated fluorescence rate of Alexa Fluor 488, neglecting nonradiative transitions.

Structure Superposition. To find the optimal overlay of the simplified DFT-optimized structures of Alexa Fluor 488 and Cy5 and those obtained from MD trajectory snapshots, we implemented a quaternion-based algorithm developed by

Coutsias et al.⁶⁰ In contrast to the Euler transformation, this approach does not suffer from coordinate singularities. In the Supporting Information (SI), we give a brief summary of the working principle. To represent the MD-based configuration of the dyes as best as possible, we neglected extremely flexible, freely rotating groups and hydrogen atoms in the fitting procedure (Figure 1). The calculated RMSD values serve as a measure of quality and refer to those parts of the dyes that have actually been aligned.

Rotation of MOs. To avoid a recalculation of the transition density matrix of the DFT-optimized structures fitted to the MD-based structures by translation and rotation, the MOs of each dye have to be rotated as well. Mathematically, the rotation of MOs is treated as a basis set transformation. MOs ψ_i can be expressed as linear combinations of a set of atom-centered basis functions φ_j ,

$$\psi_i = \sum_{j=1}^N c_{ij} \varphi_j \quad (9)$$

where c_{ij} are the expansion coefficients. Herein, the basis functions are Cartesian Gaussians that can be divided into s -, p -, d -, ...-type functions. On changing the orientation of the molecule in space leaving the coordinate system unchanged, the atom-centered basis functions are shifted to new positions, whereas their orientation with respect to the coordinate axes remains unaffected. Instead of rotating the molecule within the coordinate system, the latter can be rotated while keeping the molecule fixed. From this point of view, the positions of the basis functions remain unaffected but their orientation coupled to the orientation of the coordinate axes changes. Because the MOs are completely independent of the location of the molecule within the coordinate system, the expansion coefficients change when the orientation of the atomic orbital (AO) basis is altered. The transformation matrix T between the old and new AO basis can be used to obtain the new expansion coefficients $C^{(\text{new})}$.

$$C^{(\text{new})} = T^{-1} C \quad (10)$$

The transformation is applied in blocks of basis functions with the same angular momentum. Whereas s -functions are independent of the rotation of the coordinate system due to their spherical symmetry, the transformation matrices of higher angular momentum functions can be expressed by Euler angles. In this work, we use Euler transformations directly deduced from the quaternion corresponding to the best-fit superposition of model and target structures for the rotation of the MOs. Transformation matrices for p - and d -functions as well as information on the conversion of quaternions to Euler angles are given in the SI.

RESULTS AND DISCUSSION

Quantum-Chemical Description of the Dyes. Alexa Fluor 488. In 2014, some of us already reported on the absorption and emission spectra of rhodamine A (RhA) calculated at the DFT/MRCI level of theory.⁴⁴ Because RhA is used here as a model system to mimic the spectral properties of Alexa Fluor 488, the relevant results of that study will be briefly reviewed in the following. We also comment on the calculation of the vibrationally resolved emission spectrum.

To calculate the vertical excitation energies with respect to the relaxed S_0 and S_1 geometries, an explicit solvation model comprising six water molecules was used to take account of

hydrogen bonding effects.⁴⁴ Further tests showed that an implicit solvent model produced almost no solvent shift, in contrast to experimental evidence. The S_1 wave function is mainly composed of the HOMO \rightarrow LUMO excitation. The involved frontier orbitals are predominantly localized on the xanthene moiety of the molecule (Figure 2). Because of its high

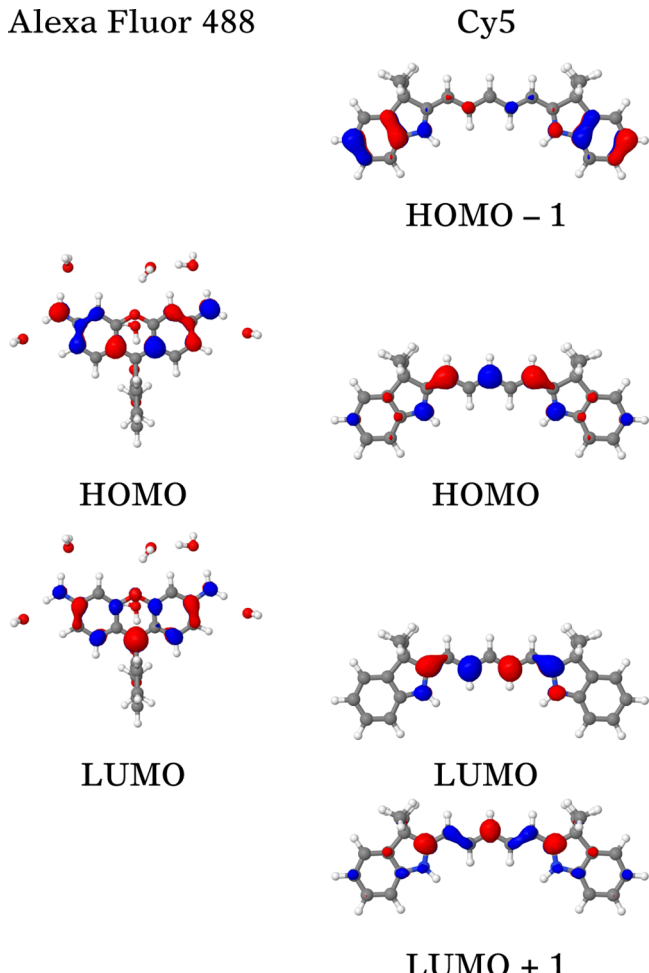


Figure 2. Frontier MOs involved in the $S_0 \rightarrow S_1$ transitions of the model structures of Alexa Fluor 488 and Cy5.

oscillator strength of 0.98, the $S_0 \rightarrow S_1$ transition dominates the spectrum. The vertical excitation energy at the ground-state equilibrium geometry is 2.51 eV (493 nm, 20 276 cm⁻¹). This value is in excellent agreement with the experimental absorption maximum of 2.48 eV (500 nm, 20 000 cm⁻¹) of RhA⁶¹ and with the absorption maximum of Alexa Fluor 488 (2.50 eV, 495 nm, 20 202 cm⁻¹)⁶² measured in aqueous solution. This confirms that the introduced structure simplifications have a minor effect on the spectral properties. The calculated transition dipole moment of the $S_0 \rightarrow S_1$ transition has an absolute value of 10.1 D and points in the direction of the long molecular axis of the xanthene molecular frame (Figure 1).

A DFT/MRCI calculation at the geometry of the optimized S_1 state yields a vertical emission energy of 2.39 eV (520 nm, 19 244 cm⁻¹) with a transition dipole moment of 10.1 D. The calculated emission energy is in excellent agreement with the experimental fluorescence maximum of rhodamine 123 at 2.36 eV (524 nm, 19 084 cm⁻¹)^{61,63} and the experimental

fluorescence maximum of Alexa Fluor 488 measured in aqueous solution (2.39 eV, 519 nm, 19 268 cm⁻¹).⁶² (In rhodamine 123, the ethyl ester of RhA has been exchanged for a methyl ester.) For the calculation of the band shape of the emission spectrum (Figure 3), we used the normal modes of the relaxed S_0 and S_1 geometries in vacuum, respectively. The calculated spectrum is in excellent agreement with the experimental spectrum^{64,65} and has a maximum at 18 789 cm⁻¹ and a shoulder at approximately 17 300 cm⁻¹.

Cy5. The electronic ground state and the first excited state of our Cy5 model can be classified according to the C_{2v} molecular point group. The S_1 wave function is mainly composed of the HOMO \rightarrow LUMO excitation and, to a minor extent, of HOMO – 1, HOMO \rightarrow LUMO², and HOMO – 1 \rightarrow LUMO + 1. Except for HOMO – 1, the involved frontier orbitals are mainly localized on the polyene backbone of the molecule (Figure 2). The calculated vertical excitation energy at the ground-state equilibrium geometry is 1.99 eV (622 nm, 16 067 cm⁻¹). Comparison of these results to the experimental value of 1.92 eV (646 nm, 15 480 cm⁻¹)⁶² measured in water suggests that the DFT/MRCI method describes the $S_0 \rightarrow S_1$ transition with a sufficient degree of accuracy. The calculated transition dipole moment has an absolute value of 15.9 D and points in the direction of the polyene bridge (Figure 1). A DFT/MRCI calculation at the geometry of the relaxed S_1 state yields a vertical emission energy of 1.82 eV (679 nm, 14 730 cm⁻¹) with a transition dipole moment of 16.4 D, in very good agreement with the experimental value of 1.87 eV (662 nm, 15 106 cm⁻¹).⁶²

The vibrationally resolved absorption spectrum (Figure 3) shows a maximum at 15 520 cm⁻¹ and a smaller shoulder at approximately 16 700 cm⁻¹. Although the shape and spectral shift are in perfect agreement with the experiment, the relative intensity of the absorption maximum is slightly underestimated in the calculation.

The spectral overlap integral obtained from the normalized fluorescence spectrum of the exciton donor Alexa Fluor 488 and the normalized absorption spectrum of exciton acceptor Cy5 according to eq 5 is 1.23×10^{-4} cm when a wavenumber scale is used.

ECME Benchmark Calculations. To get a first impression of the donor–acceptor distance critical for a proper description by the IDA, we performed a distance scan of the ECME calculated with both IDA and MTD, taking the example of a π -stacked arrangement of Alexa Fluor 488 and Cy5 (Figure 4a) in which the transition dipoles are oriented in a parallel manner ($\kappa^2 = 1$). For this orientation, we find pronounced deviations between IDA and MTD for distances approximately ≤ 15 Å. In contrast, for larger distances in the typical FRET range of > 30 Å, IDA and MTD are in perfect agreement. The case of perpendicular orientation ($\kappa^2 = 0$) was not considered because the ECME is 0 by definition.

In the framework of FRET, the donor–acceptor distance is defined as the length of the intermolecular distance vector between the barycenters of the interacting dyes. Although the quantity is well defined for the molecular π -stack, it overestimates the real distance in a collinear arrangement ($\kappa^2 = 4$). For the closest possible collinear arrangement of the Alexa Fluor 488 and Cy5 model systems, the length of the distance vector is 17 Å. For such an arrangement, we find pronounced deviations between IDA and MTD for distances ≤ 20 Å (Figure 4a). To account for the problem concerning the definition of the distance vector, we performed a further benchmark

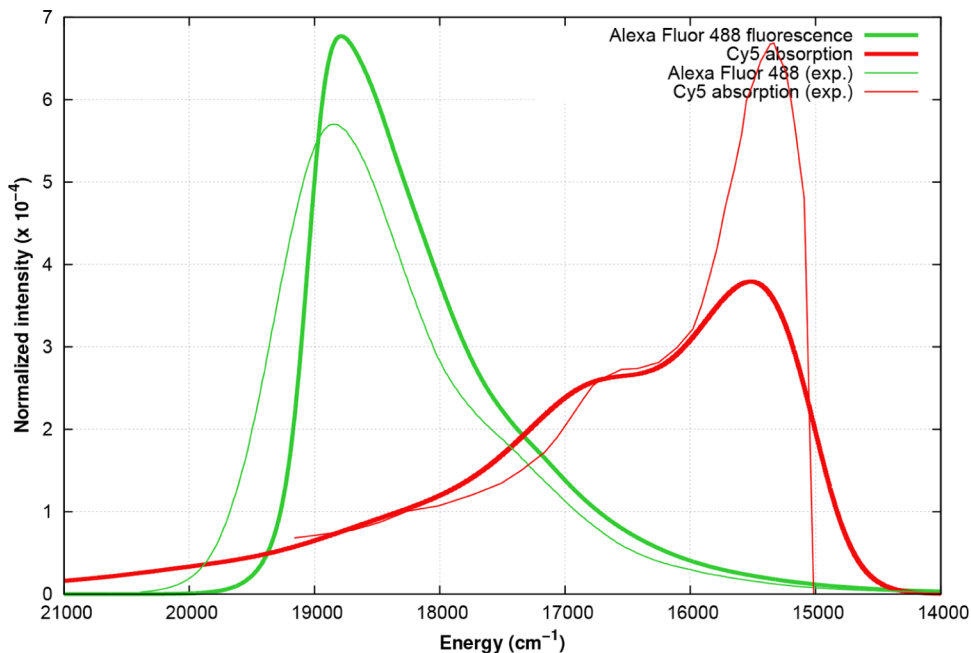


Figure 3. Computed vibrationally resolved fluorescence spectrum of Alexa Fluor 488 (green) and absorption spectrum of Cy5 (red) as used for the calculation of the spectral overlap integral. Simplified structures were used for the calculations (see Figure 1). The experimental spectra are given for comparison.^{62,64,65}

calculation starting from a π -stacked arrangement with a fixed distance of 4.23 Å (Figure 4b). Shifting Cy5 along the long axis of the xanthene frame of Alexa Fluor 488, the orientation factor first steeply decreases from 1 to 0 and then gradually increases to 4 until an almost collinear arrangement is reached. Whereas a coplanar orientation of the transition dipole moments always leads to an orientation factor of 1, κ^2 varies between 0 and 4 for other parallel arrangements. A detailed explanation of this behavior has been given by van der Meer.⁵⁶ In our calculations, we find a small but pronounced underestimation of the ECME by the IDA from 20 Å down to 12 Å where the orientation factor is in the range of 2.5–3.5. For a donor–acceptor distance below 10 Å, where $\kappa^2 < 2$, the IDA strongly overestimates the ECME.

As high orientation factors indicating an almost collinear orientation of the dyes are statistically of small importance according to an isotropic dipole distribution (Figure 5), we refer to the value of ≤ 15 Å obtained from the first benchmark calculation and consider donor–acceptor distances below this threshold to be critical.

Analysis of the MD Trajectories. Quality of the Fit. To check whether the calculated trajectories are suitable for our purpose of studying EET at small distances, we analyzed the donor–acceptor distance as well as the angle between the transition dipole moments. Indeed, we could identify a sufficient number of snapshots below the critical distance of 15 Å and transition dipole orientations different from 90° (Figure 6). For each snapshot of the MD trajectories, the dyes were replaced with their simplified DFT-optimized counterparts by a fitting procedure (Figure 7). For Alexa Fluor 488, we find a largely constant RMSD in the range of 0.2 Å, which is considered satisfactory. For Cy5, the RMSD mainly varies in an interval between 0.7 and 1.0 Å. This high RMSD relates to the fact that the polyene system of Cy5 is much more flexible and therefore more difficult to fit than the largely rigid xanthene moiety of Alexa Fluor 488.

Arrangement of the Dyes within the Different Setups. Our investigations are based on three different setups differing in the position at which Alexa Fluor 488 is linked to the dsRNA, whereas the position of Cy5 remains unchanged (Figures 8). By choosing different anchor positions, the relative arrangement of the dyes can be controlled. In all setups, the dyes are linked to complementary strands of the dsRNA and differ in the number of nucleotides in between. Generally, we find that Cy5 preferably tends to stick to the RNA backbone, whereas Alexa Fluor 488, in contrast, moves largely freely in space.

In the **dsRNA_8nt_23nt** and **dsRNA_8nt_22nt** configurations (Figure 8b,c), where the anchor points of the dyes are separated by one turn of the double helix, both linker–dye combinations sample stable configurations in which the dyes come very close (<12 Å) although both Alexa Fluor 488 and Cy5 are negatively charged. For this, the peptide linkers of Alexa Fluor 488 and Cy5 need to be in a linear conformation. This occurs, for example, in the **dsRNA_8nt_23nt** trajectory between 180 and 210 ns as well as between 300 and 350 ns (Figures 6 and 9). A visual inspection of these trajectory sections combined with a hydrogen bond analysis indicated that the Alexa Fluor 488 configuration is stabilized by weak hydrogen bonds between the amide group of its linker and phosphate groups of the RNA backbone (i.e., nucleotides 17 and 18 from the 5'-end of the RNA strand where Cy5 is attached to; Table 1, Figure 10) as well as by more stable hydrogen bonds between the carboxylic group of Alexa Fluor 488 and 2'OH groups of the RNA backbone (i.e., nucleotides 16 and 17; Table 1). Similarly, the Cy5 configuration is stabilized by strong hydrogen bonds between the amide group of its linker and a phosphate group of the RNA backbone (i.e., nucleotide 13 from the 3'-end of the RNA strand where Alexa Fluor 488 is attached to; Table 1), assisted by weaker hydrogen bonds between the sulfonate group of the dye and 2'OH groups of the RNA backbone (i.e., nucleotides 13 and 15; Table 1). Alexa Fluor 488 tries to escape the repulsive steric and

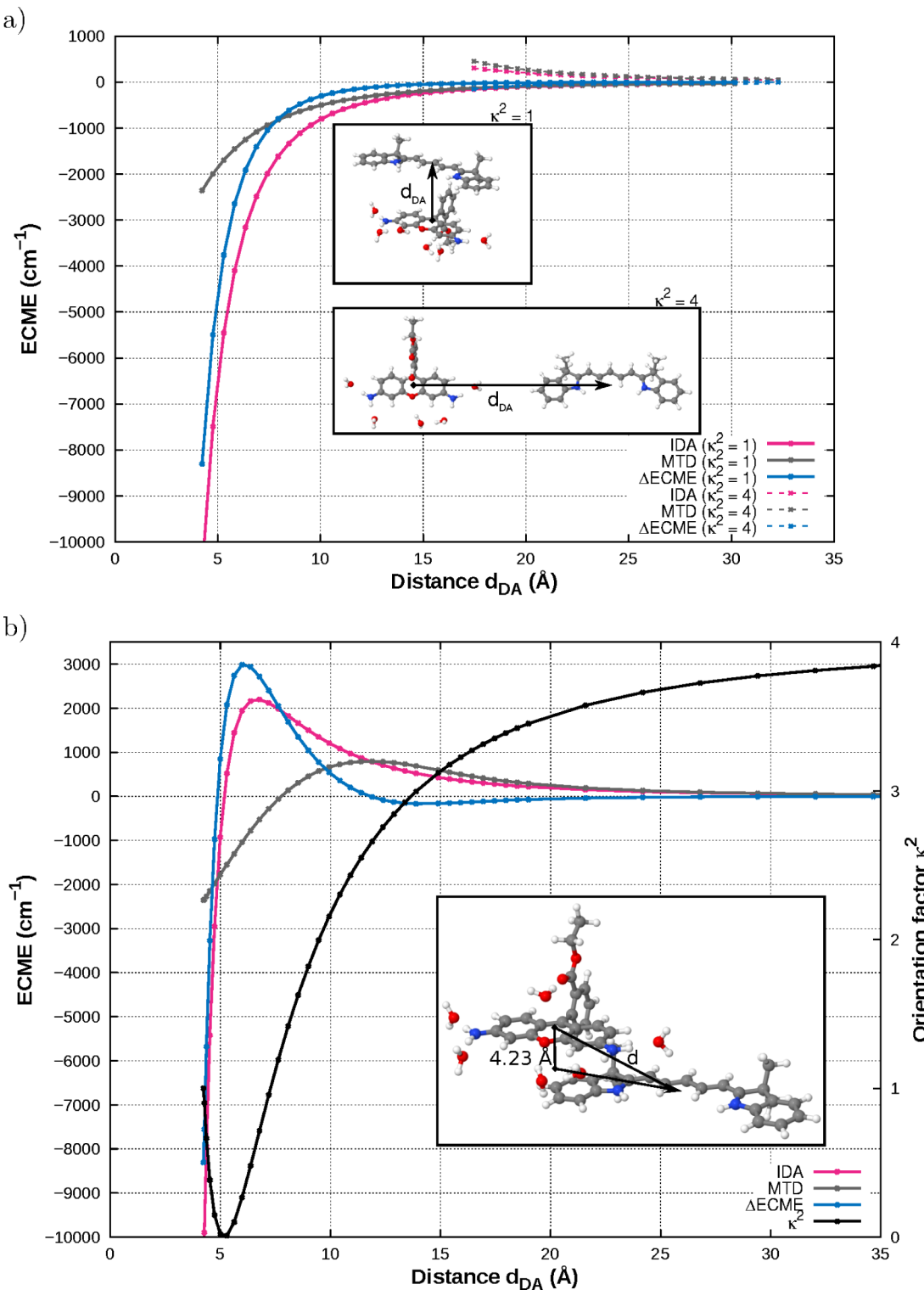


Figure 4. Distance dependency of the ECME calculated using both IDA and MTD (a) taking the examples of a π -stack of Alexa Fluor 488 and Cy5 with an orientation factor of $\kappa^2 = 1$ and a collinear arrangement of both dyes with an orientation factor of $\kappa^2 = 4$ as well as (b) shifting Cy5 along the axis of the xanthene frame of Alexa Fluor 488. The deviation between the two methods was used for a crude approximation of the critical donor–acceptor distance.

electrostatic interactions by slight variation of the torsion angles within the linker and by changes in the torsion angle between the phenyl and the xanthene moieties as observed by visual inspection of the MD trajectory. Similar results are found in the **dsRNA_8nt_23ntII** trajectory for the section 180–240 ns (Figure 6b). Also in the **dsRNA_8nt_22nt** trajectory, quite

stable hydrogen bonds are formed between the amide group of the linkers of Alexa Fluor 488 or Cy5, respectively, with phosphate groups of the RNA backbone, respectively (Table 1). However, no strong hydrogen bonds between the dye and the RNA backbone were formed. Overall, these analyses

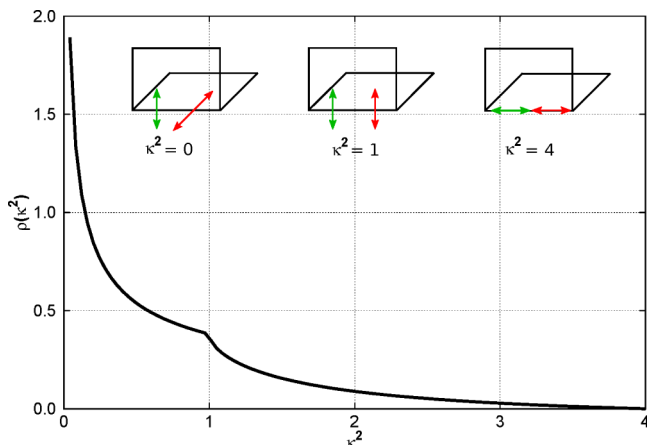


Figure 5. Analytic function describing the probability distribution of two isotropic transition dipoles using the orientation factor κ^2 . The relative arrangements of the transition dipoles for the limiting cases $\kappa^2 = 0$ (perpendicular), $\kappa^2 = 1$ (coplanar), and $\kappa^2 = 4$ (collinear) are indicated by arrows.

suggest that the close distances between the two dyes are fostered by their favorable interactions with the RNA backbone.

Although dsRNA_8nt_14nt is the setup with the shortest distance between the two anchor points (Figure 8a), only a few snapshots with distances of about 10 Å between the dyes were

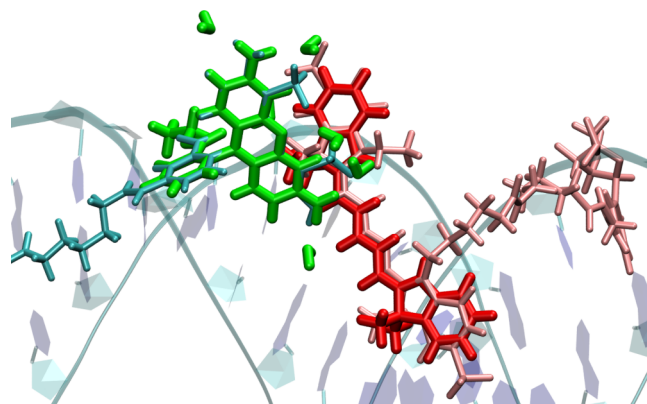


Figure 7. Overlay of the simplified and preoptimized structures of Alexa Fluor 488 (green) and Cy5 (red) to an MD snapshot. The water molecules are part of the explicit solvent model used for the calculation of RhA mimicking Alexa Fluor 488.

sampled, whereas the majority had distances above 20 Å (Figure 6d). One reason for this is that the Cy5 dye has to sample the other helix groove to come into short distance with Alexa Fluor 488, which is only possible when the Cy5 linker adopts a twisted, energetically rather unfavorable conformation. During the course of the simulation, the Cy5 dye mainly samples two orientations where it either sticks to the RNA

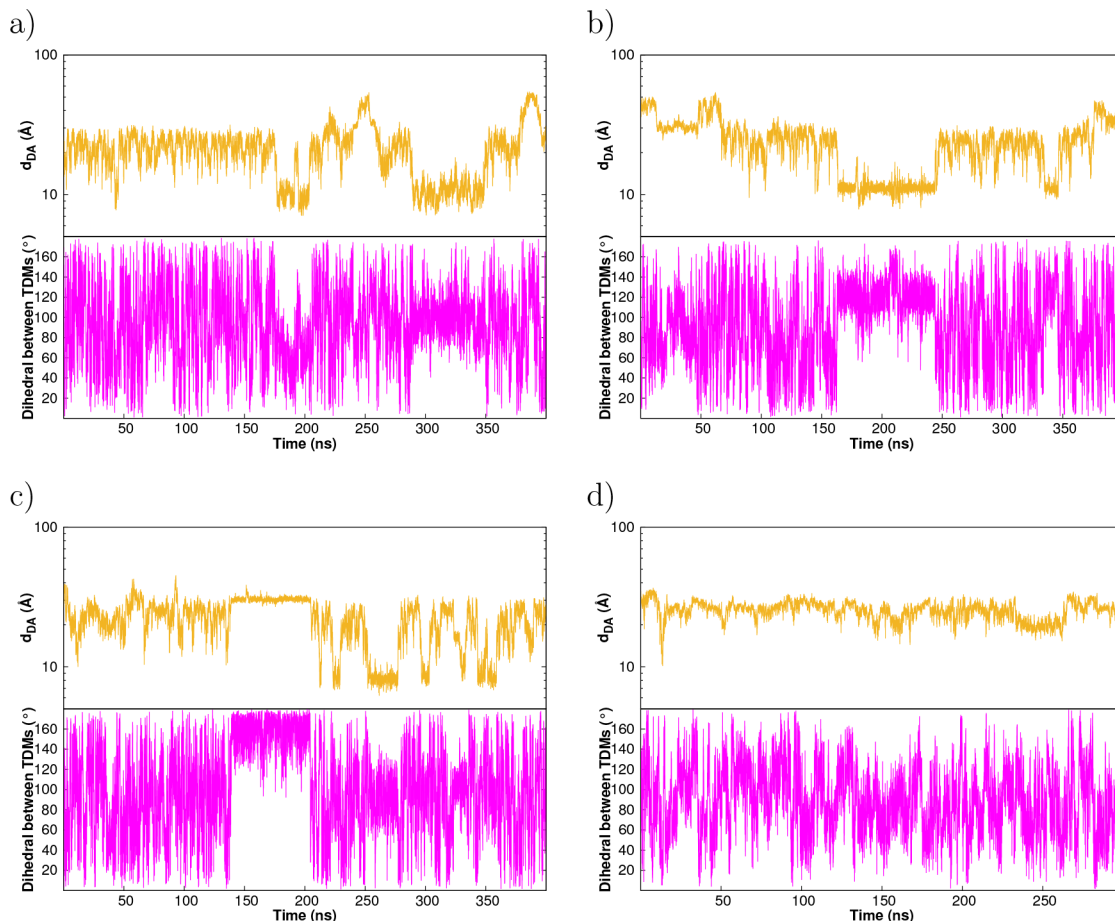


Figure 6. Distances between the exciton donor Alexa Fluor 488 and the exciton acceptor Cy5 (orange) as well as the angles between their transition dipole moment vectors (magenta) determined directly from the MD trajectories, as indicated in Figure 1. (a) dsRNA_8nt_23nt, (b) dsRNA_8nt_23ntII, (c) dsRNA_8nt_22nt, and (d) dsRNA_8nt_14nt.

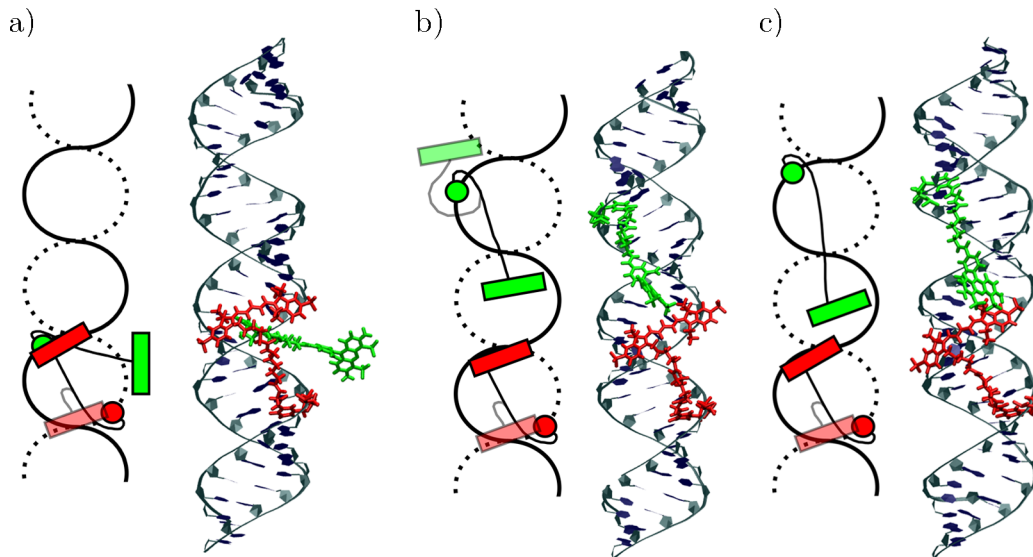


Figure 8. Schematic representation of the three different setups: (a) dsRNA_8nt_14nt, (b) dsRNA_8nt_22nt, and (c) dsRNA_8nt_23nt. Anchor points of Alexa Fluor 488 (green) and Cy5 (red) at the dsRNA are indicated by circles, and the dyes are represented by rectangles. Cy5 predominately sticks to the RNA backbone at two different positions, whereas Alexa Fluor 488 largely moves freely in space.

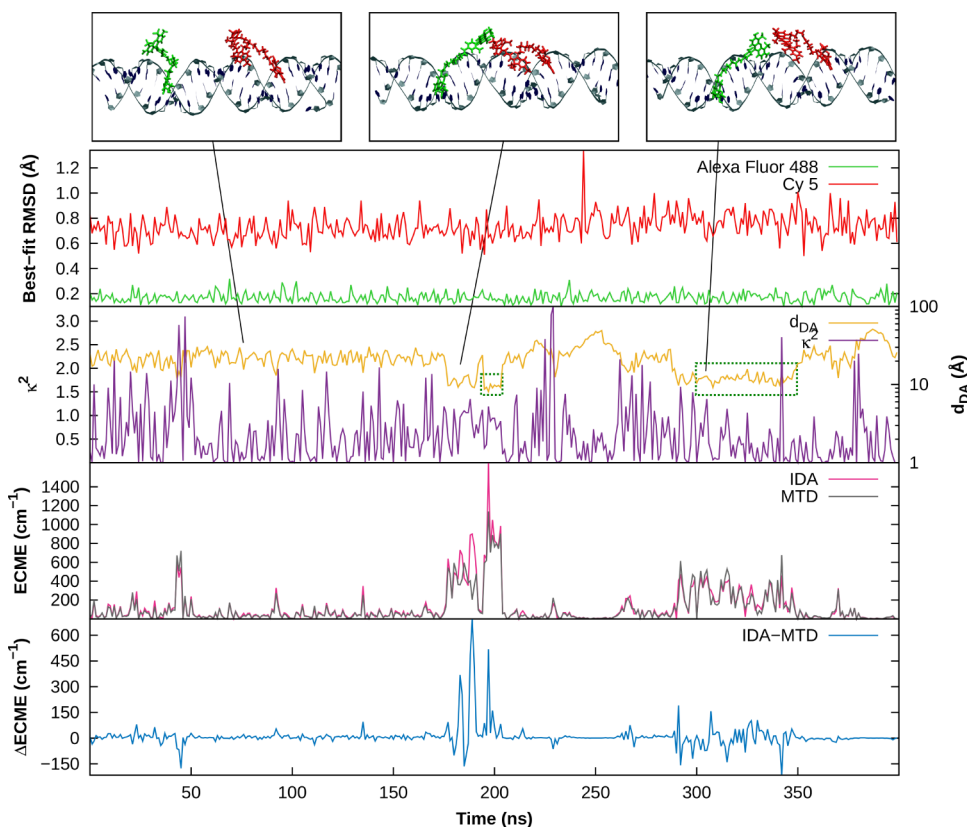


Figure 9. Processed trajectory dsRNA_8nt_23nt in which Alexa Fluor 488 and Cy5 were replaced by their preoptimized simplified structures. Snapshots saved at 1 ns intervals (every 50th snapshot) were used for the analysis. The quality of the fit of the preoptimized dyes to the MD structure is indicated by the best-fit RMSD. Distances d_{DA} and orientation factors κ^2 were computed between the centers of mass of the dyes and the rotated transition dipole moments, respectively. The EMCE was calculated for each considered snapshot using both IDA and MTD approach. Ranges for which H-bonds were analyzed are marked by green boxes (Table 1).

backbone close to the anchor point of Alexa Fluor 488 or to its own anchor point. In contrast, Alexa Fluor 488 is much more mobile and does not form stable interactions with the RNA helix.

Distance Distribution and Orientation Factor Distribution.

In most FRET experiments, a perfectly isotropic probability distribution of the transition dipoles of the interacting dyes is assumed. This is indeed the case if both dyes are able to rotate freely in space or if only one dye is able to rotate freely in space,

Table 1. Hydrogen Bond Formation for Trajectory Sections with Small Dye Distances^a

dye	trajectory	section (ns)	acceptor	donor	% occupied
Cy5	dsRNA_8nt_22nt	260–280	nt13@O1P dye	:linker@NH ^b	64 ^b
	dsRNA_8nt_23nt	180–210	nt13@O1P dye@SO3	:linker@NH nt13@2'OH	61 23
	dsRNA_8nt_23nt	300–350	^b	:linker@NH	^b
	dsRNA_8nt_23ntII	180–240	dye@SO3 nt13@O1P	nt15@2'OH :linker@NH	10 54
Alexa Fluor 488	dsRNA_8nt_22nt	260–280	dye@SO3 nt17@O1P dye	nt13@2'OH :linker@NH ^b	11 31 ^b
	dsRNA_8nt_23nt	180–210	nt17@O1P dye@COO ⁻	:linker@NH nt16@2'OH	10 10
	dsRNA_8nt_23nt	300–350	dye@COO ⁻ nt18@O1P	nt17@2'OH :linker@NH	20 23
	dsRNA_8nt_23ntII	180–240	nt18@O1P dye@COO ⁻	nt17@2'OH nt18@O1P dye@COO ⁻	49 27 35

^aThe dsRNA_8nt_22nt trajectory is analyzed in the trajectory section 260–280 ns, dsRNA_8nt_23nt in the sections 180–210 ns and 300–350 ns, and dsRNA_8nt_23ntII in the section 180–240 ns, where inter-dye distances are approximately 10 Å (Figures 6 and 9). Hydrogen bonds were defined by a distance cutoff of 3.2 Å and an angle cutoff of 120° and were only considered if their occupancies attained >10% (percent of simulation time in which the hydrogen bond is formed). The analysis was performed using the “ptraj” module of Amber10.³³ Nucleotide positions of interaction partners are given for Cy5 from the 3'-end of the RNA strand where Alexa Fluor 488 is attached to and for Alexa Fluor 488 from the 5'-end of the RNA strand where Cy5 is attached to. ^bNo stable hydrogen bonds (occupancies <10%) were formed.

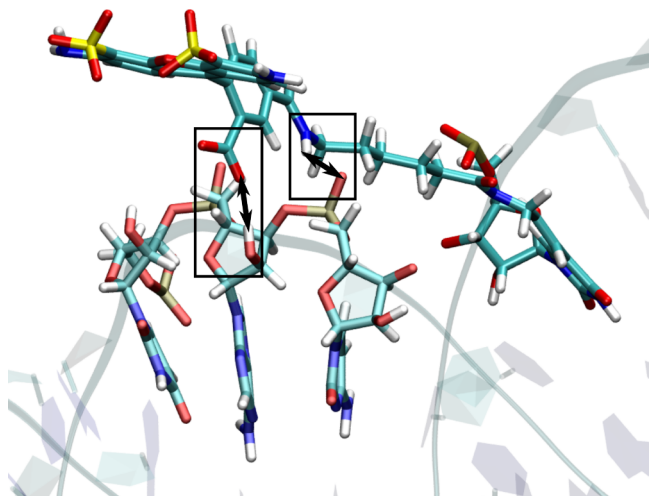


Figure 10. Hydrogen bonds (black two-pointed arrows) between Alexa Fluor 488 and the RNA backbone when the dye is located close to Cy5.

whereas the other one is retained in a fixed position. For large donor–acceptor separations (>30 Å), Kalinin et al.² showed that this assumption is largely fulfilled and that the dyes move freely within their accessible volumes. A spherically isotropic distribution of the transition dipoles results in a probability function of the orientation factor that can be described by an analytic discontinuous logarithmic function, which is highest for $\kappa^2 = 0$ and close to zero for $\kappa^2 = 4$ (Figure 5).^{21–23}

$$\rho(\kappa^2) = \begin{cases} \frac{1}{2\sqrt{3}\kappa^2} \ln(2 + \sqrt{3}) & 0 \leq \kappa^2 < 1 \\ \frac{1}{2\sqrt{3}\kappa^2} \ln\left(\frac{2 + \sqrt{3}}{\sqrt{\kappa^2} + \sqrt{\kappa^2 - 1}}\right) & 1 \leq \kappa^2 \leq 4 \end{cases} \quad (11)$$

The average value $\langle \kappa^2 \rangle$ is calculated as the expectation value of the isotropic transition dipole moment distribution

$$\langle \kappa^2 \rangle = \int_0^4 \kappa^2 \rho(\kappa^2) d\kappa^2 = \frac{2}{3} \quad (12)$$

Following Lakowicz and Periasamy,^{66,67} a Gaussian distribution of the donor–acceptor distance may be expected in an ideal FRET system. Because of restrictions caused by the length and flexibility of the molecular linker as well as due to attractive and repulsive interactions between the dyes and between the dyes and the target system, deviations from the model κ^2 and distance distributions may occur in a realistic system (see also Conclusion section). In the following, we discuss our results obtained for small donor–acceptor distances below the typical FRET range of 30 Å.

For dsRNA_8nt_14nt (Figures 11 and S4), we find a quite narrow distribution of the donor–acceptor distance between 10 and 36 Å with a maximum at 25 Å and a small shoulder at about 20 Å. The shape of the distribution function closely corresponds to a Gaussian distribution. Distances in the critical range <15 Å are extremely rare in this setup (0.32% of all snapshots). The κ^2 distribution primarily follows the isotropic model. Small orientation factors are found frequently, whereas high orientation factors rarely occur.

The close similarity to a perfectly Gaussian distance distribution and a near-perfectly isotropic κ^2 distribution, respectively, can be explained by the choice of the anchor positions of the dyes. These are located very close to each other such that the length of the molecular linkers prevents a large

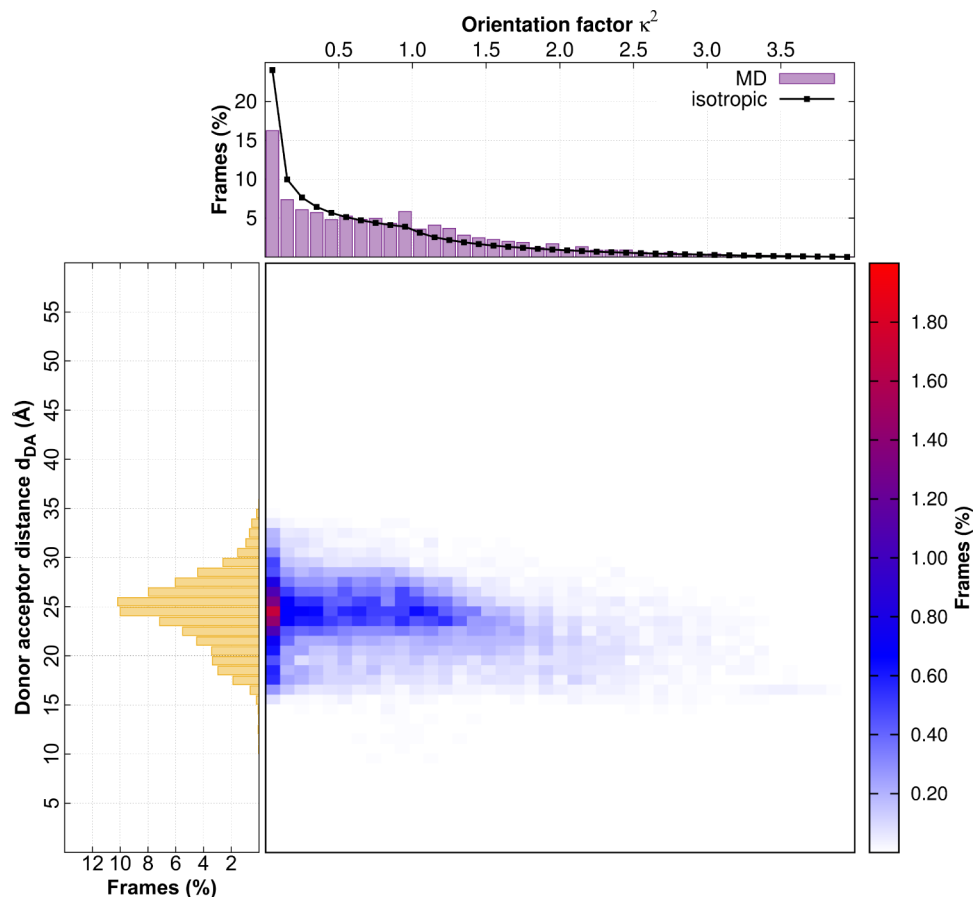


Figure 11. Distributions of the donor–acceptor distance and the orientation factor for **dsRNA_8nt_14nt**. The analysis is based on averaging all snapshots within distance intervals of 1 Å and intervals of 0.1 concerning the orientation factor.

overlap of the accessible volumes: To achieve a small distance between the dyes, the linkers would have to adopt a folded, energetically unfavorable structure. Because Cy5 predominantly sticks to the RNA backbone, relative orientations between the dyes are mainly determined by the freely moving Alexa Fluor 488. Cy5 sticks to two different positions of the RNA backbone with different probabilities, producing two superimposed distributions. The minor one results in the small shoulder of the distance distribution.

In **dsRNA_8nt_23nt**, the situation is completely different (Figure 12). We find a very broad distribution of the donor–acceptor distance between 7 and 54 Å, which is composed of more than one superimposed Gaussian distribution. The dominant and broadest one ($\text{FWHM} \approx 12 \text{ \AA}$) has a maximum at 25 Å and describes the free rotation of Alexa Fluor 488 relative to Cy5 sticking to the complementary RNA strand directly opposite to its anchor point. Analogous to **dsRNA_8nt_14nt**, the shoulder at about 20 Å can be explained by the fact that Cy5 sticks to the RNA backbone at two different positions with different probabilities.

The second distribution is significantly narrower ($\text{FWHM} \approx 4 \text{ \AA}$) and has a maximum at about 12 Å. It represents 23% of all snapshots and can be traced back to those periods in which the two dyes stick close to each other. As the adherence of the dyes is caused by an interaction of the linker of Alexa Fluor 488 and the RNA backbone (Figure 10), the dye itself is not completely fixed in space, changing between a perpendicular and a parallel orientation with respect to Cy5. During this motion, the intermolecular distance vector remains almost unchanged

causing the distribution of small distances, whereas the orientation factor changes between 0 and 2.

Larger distances between 35 and 54 Å were found to be extremely rare and are represented by a further distribution. They occur in those arrangements in which the linker of Alexa Fluor 488 is completely unfolded and points in a direction opposite to the location of Cy5.

The overall κ^2 distribution almost perfectly resembles the isotropic model. Nevertheless, orientation factors >2.5 are underrepresented due to the restriction of the accessible volumes of the dyes by their molecular linkers. For donor–acceptor distances below 10 Å, we do not find a single snapshot with an orientation factor >2 . We emphasize that this range is not underrepresented in our simulation. Because of the definition of the intermolecular distance vector as the distance between the centers of mass of the interacting dyes, large orientation factors cannot be obtained in combination with small donor–acceptor distances.

With one exception, redundant results were obtained in a second, independent MD simulation based on the same setup (**dsRNA_8nt_23ntII**, Figure S5). Here, we find a slight overestimation of the orientation factor between 0.5 and 1.0, which can be traced back to the periods in which the dyes stick close to each other. In these periods, parallel orientations of Alexa Fluor 488 and Cy5 are preferred over a perpendicular one. The deviations between the two trajectories indicate a lack of convergence, which may be solved by longer simulation times.

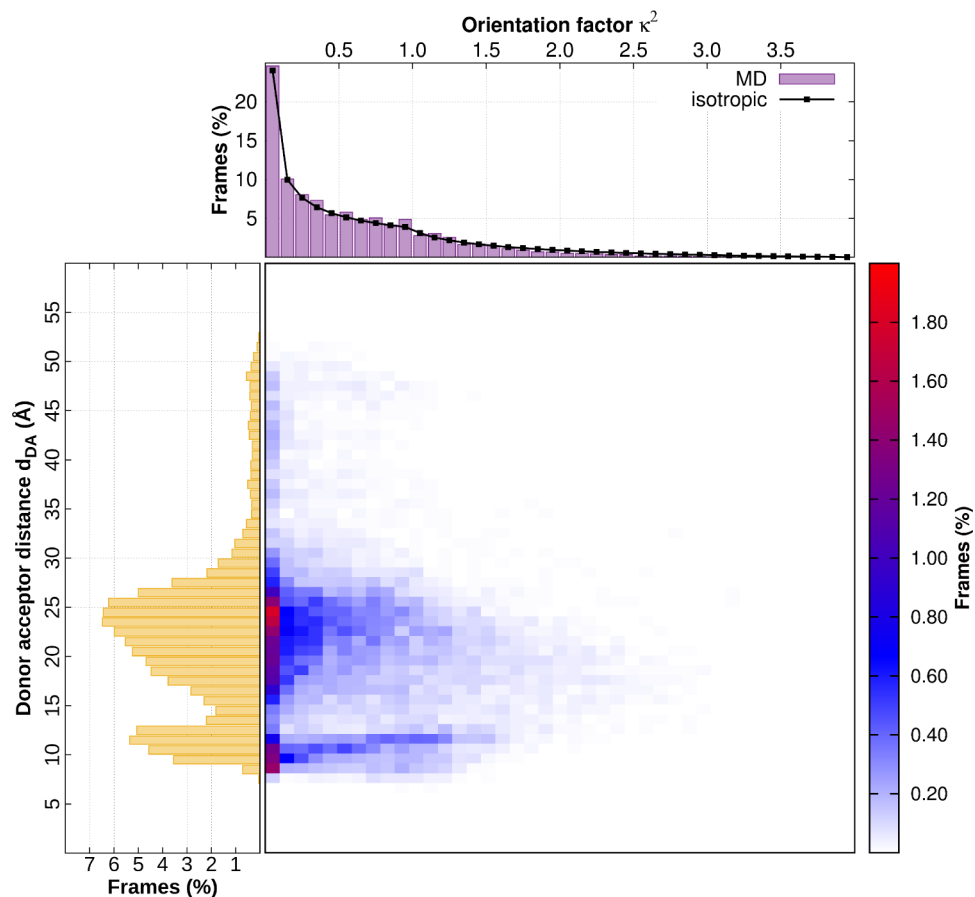


Figure 12. Distributions of the donor–acceptor distance and the orientation factor for **dsRNA_8nt_23nt**. The analysis is based on averaging all snapshots within distance intervals of 1 Å and intervals of 0.1 concerning the orientation factor.

In **dsRNA_8nt_22nt**, we find a broad distance distribution between 7 and 46 Å, which is composed of three superimposed Gaussian distributions (Figure S6). The two distributions with maxima at 25 and 10 Å can be interpreted analogous to **dsRNA_8nt_23nt**. We find a third extremely narrow distribution with a maximum at about 30 Å, which can be traced back to the periods in which Alexa Fluor 488 sticks to the RNA at a position near its own anchor point. In this case, Cy5 as well as Alexa Fluor 488 are fixed in space and therefore in a fixed arrangement relative to each other. This arrangement is characterized by an orientation factor between 0.7 and 1.0, causing a deviation of the overall κ^2 distribution compared to the isotropic model. Generally, orientation factors >1.5 are underrepresented in this setup due to the restriction of the accessible volumes of the dyes by their molecular linkers.

In summary, dye configurations with donor–acceptor distances below the critical value of 15 Å constitute a marked proportion of the overall distance distribution (23% for **dsRNA_8nt_23nt**, 19% for **dsRNA_8nt_22nt**, and <1% for **dsRNA_8nt_14nt**). Thereby, close inter-dye distances can be the result of dye or linker interactions with the RNA.

Deviation of IDA and MTD. To study the quality of the IDA in our model systems, we recomputed the ECME using the MTD approach. As the EET rate is proportional to the square of the ECME, it is reasonable to consider the absolute value of the quantity, which will just be termed ECME in the following. Here, we discuss the question whether the IDA overestimates or underestimates the ECME depending on the donor–acceptor distance on the one hand and the orientation factor on

the other hand. To this end, for every 50th snapshot of the appropriate trajectory, the ECMEs were computed using both IDA (IDA50) and MTD (MTD50). The analysis is based on averaging the deviations of all snapshots within intervals of 1 Å with regard to the intermolecular distance vector and intervals of 0.1 with regard to the orientation factor.

In **dsRNA_8nt_23nt**, we find deviations between IDA50 and MTD50 in the range of -300 and 600 cm^{-1} (Figure 13a). The maximum underestimation is hence only half the size of the maximum overestimation. This can be explained by the fact that underestimates are generally found at larger distances (12–15 Å) when compared with overestimates (7–11 Å). The ECME decreases with increasing distance and therefore also the absolute deviation between the two methods. For donor–acceptor distances >15 Å, the deviation is small ($<100\text{ cm}^{-1}$). This confirms our approximation of the critical distance of about 15 Å obtained by benchmark calculations of a π -stacked and a collinear arrangement of Alexa Fluor 488 and Cy5.

For a closer examination of the critical range, we recomputed the ECME for every single snapshot with a donor–acceptor separation below the threshold of ≤ 15 Å using both IDA (IDAfull) and MTD (MTDfull) (Figure 13b). Here, we find a deviation of the two methods between -300 and 1200 cm^{-1} . The higher maximum overestimation of the ECME obtained from IDAfull and MTDfull in comparison with IDA50 and MTD50 is based on the fact that single snapshots with a high deviation were, by chance, not considered in our first analysis.

Analyzing the distance dependency of the deviation between IDA and MTD first, two distinct distance ranges are revealed.

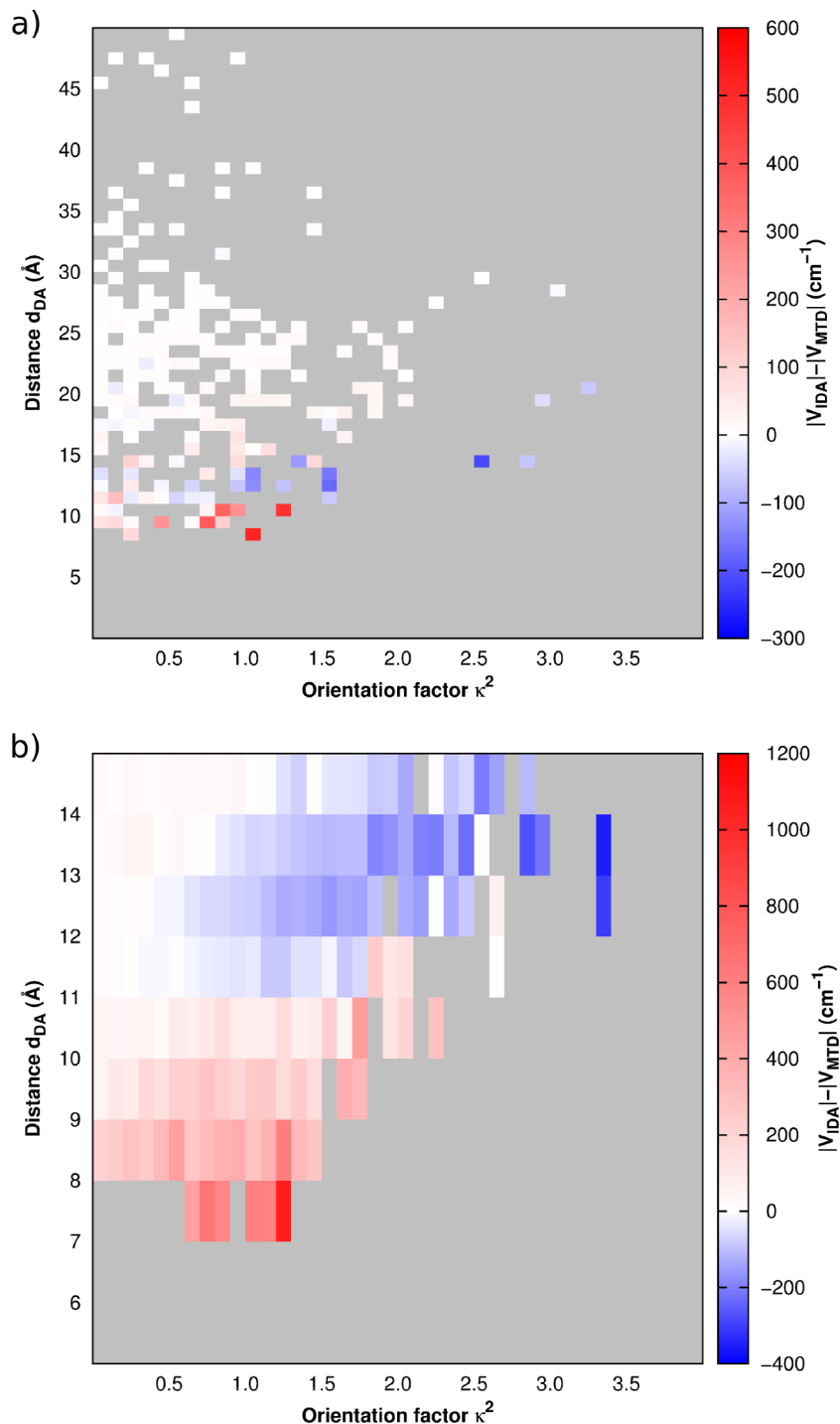


Figure 13. Deviation of the ECME calculated with IDA and MTD in dsRNA_8nt_23nt considering (a) every 50th snapshot and (b) every single snapshot with a donor–acceptor distance below 15 Å. The analysis is based on averaging all snapshots within distance intervals of 1 Å and intervals of 0.1 with regard to the orientation factor. Gray-colored areas denote combinations of the donor–acceptor distance and the orientation factor for which no data points exist.

For distances between 7 and 11 Å, we find an overestimation of the ECME by the IDA, whereas the range from 11 to 15 Å is characterized by an underestimation. This change of sign can be explained by considering IDA and MTD as two functions decreasing with the donor–acceptor distance (d_{DA}^{-3}). Because the two functions are similar but not identical, an intersection of both functions can be found. Here, this intersection is located at approximately 11 Å for almost all orientation factors.

As the ECME increases with the orientation factor, as given by eq 6, an increasing deviation between IDA and MTD is to be expected as well. Indeed, such a behavior was found in our analysis. Consequently, the orientation factor needs to be high to produce a significant failure of the IDA, if the donor–acceptor distance is close to the critical value. In the distance interval between 14 and 15 Å, for example, significant deviations between IDA and MTD are observed only for orientation factors $\gg 1.0$ (Figure 13).

Table 2. Time-Averaged ECMEs and EET Rates Calculated with Both IDA and MTD^a

setup	IDAfull	IDA50	MTD50	combined MTD/IDA
$\langle V_{DA} \rangle$ (cm ⁻¹)				
dsRNA_8nt_23nt	127	123	113	122
dsRNA_8nt_23ntII	130	134	128	
dsRNA_8nt_22nt	105	105	99	
dsRNA_8nt_14nt	54	55	49	
EET rate (s ⁻¹)				
dsRNA_8nt_23nt	7.9×10^{12}	7.5×10^{12}	6.1×10^{12}	6.9×10^{12}
dsRNA_8nt_23ntII	6.9×10^{12}	7.3×10^{12}	6.9×10^{12}	
dsRNA_8nt_22nt	5.6×10^{12}	5.6×10^{12}	4.6×10^{12}	
dsRNA_8nt_14nt	8.1×10^{11}	7.7×10^{11}	7.1×10^{11}	

^aIDAfull is based on every single snapshot of the appropriate trajectory, whereas the number of considered data points is limited to every 50th snapshot in IDA50 and MTD50. In dsRNA_8nt_23nt, an additional analysis was carried out considering every snapshot with a donor–acceptor distance ≤ 15 Å with the MTD approach (combined MTD/IDA).

dsRNA_8nt_22nt essentially shows the same behavior as dsRNA_8nt_23nt (Figures S7 and S8). Here, we could identify a maximum underestimation of the ECME by the IDA of -200 cm⁻¹ and a maximum overestimation of 1200 cm⁻¹. Significant deviations were not observed for distances > 15 Å.

In dsRNA_8nt_14nt, we find deviations in the range of -100 to 100 cm⁻¹, which are small compared to the other two setups (Figure S9). This can be explained by the fact that the critical distance of 15 Å is reached only in very few snapshots. Extremely low distances (10 Å) causing high deviations do not occur.

Averaged ECME and EET Rates. For all setups, we calculated the averaged ECMEs and the averaged EET rates according to IDAfull, IDA50, and MTD50 (Table 2). In dsRNA_8nt_23ntI/II, we find averaged ECME values (IDAfull) of 127 and 130 cm⁻¹, respectively, which are the highest values among all setups. This can be explained by the long periods in which the dyes stick close to each other at a quite small distance. In dsRNA_8nt_22nt, which is very similar to the latter setup, the ECME is slightly smaller by about 25 cm⁻¹. The smaller value results from the periods in which Alexa Fluor 488 sticks to the RNA backbone at a position far away from Cy5. In dsRNA_8nt_14nt, we find an ECME of only 54 cm⁻¹, which can be traced back to the fact that the dyes do not come as close to each other as in the other two setups.

Generally, we find that IDAfull and IDA50 provide almost identical results with a maximum deviation of 3.1% . This confirms that our approximation of considering only every 50th snapshot is justified.

For dsRNA_8nt_23nt and dsRNA_8nt_22nt, we find EET rates in the range of 10^{12} s⁻¹. The values obtained at the IDAfull, IDA50, and MTD50 levels vary only slightly (Table 2), with MTD50 providing the smallest results. Nevertheless, the calculated EET rates may be considered identical within the error bounds of the applied methods. Generally, a significant change in the mean EET rate by a factor of 10 can only be achieved if the ECME values are increased by a factor of 3.16 on average.

$$k_{EET} = \text{const.} \times V_{DA}^2$$

$$10 \times k_{EET} = \text{const.} \times (\sqrt{10} V_{DA})^2$$

$$10 \times k_{EET} \approx \text{const.} \times (3.16 V_{DA})^2 \quad (13)$$

Small differences in ECME values calculated by different methods thereby do not have a huge impact on the EET rates. For dsRNA_8nt_14nt, we find an EET rate in the range of 10^{11} s⁻¹, which can be traced back to the larger mean donor–acceptor distance compared to the other two setups.

EET and donor fluorescence are two directly competing processes. The spontaneous fluorescence rate k_f of the donor can be calculated from the vertical energy difference $\Delta E_{S_0 \leftarrow S_1}$ with respect to the relaxed geometry of the S_1 state and the electronic transition dipole moment μ_{el} between the fluorescent state and the electronic ground state.

$$k_f = \frac{4e^2}{3c_0^3 \hbar^4} \Delta E_{S_0 \leftarrow S_1}^3 \times \mu_{el}^2 \quad (14)$$

For all setups, we find a FRET efficiency $> 95\%$ due to large EET rates compared to the fluorescence rate of the donor, which was computed as 0.23×10^9 s⁻¹ for (simplified) Alexa Fluor 488. A FRET efficiency in this range was to be expected because the average distance between the dyes of about 25 Å is only half the size of the Förster radius of Alexa Fluor 488 and Cy5 of 49 Å.⁶⁸

To validate our approach, we exploit the definition of the Förster radius as the donor–acceptor distance at which the FRET efficiency is reduced to one half. Consequently, an arbitrary snapshot with a donor–acceptor separation in the range of 49 Å and an orientation factor of 0.66 should provide an EET rate in the range of the donor fluorescence rate. Indeed, for such a snapshot, we find a rate of 4.10×10^9 s⁻¹, which is in approximate agreement with the donor fluorescence rate, considering the accuracy of the computational approach and that nonradiative decay of the donor fluorescent state has been neglected.

CONCLUSIONS

In this work, we investigated how the failure of the IDA affects the analysis of FRET experiments at small donor–acceptor distances taking the example of Alexa Fluor 488 and Cy5 attached to different positions of a dsRNA. For this purpose, QM-optimized model structures of the dyes were overlayed to snapshots of trajectories from all-atom MD simulations at the classical level. The ECME was calculated using both IDA and MTD to analyze the deviation between the two methods depending on the distance and relative orientation of the transition dipoles.

The vibrationally resolved absorption spectrum of the acceptor and the emission spectrum of the donor were described exactly with the chosen QM model. The calculated spectra were successfully used for the calculation of the spectral overlap integral needed for the calculation of the FRET rate. Taking the example of a π -stacked and a collinear arrangement of Alexa Fluor 488 and Cy5, we identified a distance threshold of 15 Å, below which the IDA significantly deviates from the MTD approach. This finding was confirmed by further calculations based on the MD trajectories.

In all setups, we could identify certain positions where the dyes are preferably located. This causes a restriction of the free rotation in space and leads to deviations from a perfectly Gaussian distance distribution and a perfect isotropic distribution of the transition dipoles. For two of three studied setups, we could identify certain arrangements in which the dyes stick close to each other at small distances in the range of 7–15 Å. We emphasize that the distance between the anchor points of the dyes does not directly imply how close the dyes can really come to each other. To obtain a better estimate, the flexibility and length of the molecular linker has to be taken into account as well, as have to be potential interactions between linker or dye and the biomolecular target. Dyes in close distance represent energetically favorable states, which can be stable for tens to hundreds of nanoseconds. Within these periods, we could identify significant deviations between the IDA and the MTD. Nevertheless, the number of snapshots affected by a large deviation of the IDA represents only a small part of the total trajectories. Thus, they have only a small statistical impact on the time-averaged EMCE and therefore on the EET rate. We therefore conclude that the IDA is suited even for FRET experiments with small donor–acceptor distances as long as adherence of the dyes does not dominate the overall motion behavior. Nevertheless, we strongly recommend to study the target FRET system by means of MD simulations to ensure that the assumption of an isotropic dipole distribution is still justified and that the number of snapshots affected by the failure of the IDA is small.

In addition, it needs to be considered that energy transfer in realistic systems at finite temperature is only one of many dynamic molecular processes, which relates to the question which averaging regime applies for κ^2 .^{69,70} In case the transfer time $\tau_{\text{EET}} = 1/k_{\text{EET}}$ is much shorter than characteristic relaxation times of dynamic molecular processes, the assumption of a static κ^2 -distribution is valid. In our case of short distances, the transfer time is at least one order of magnitude shorter (Table 2) than the fastest rotational correlation times measured for Cy5 and Alexa488 in donor-only and acceptor-only samples when attached to DNA or RNA.³ In this regime, time-independent orientation factor distributions $\rho(\kappa^2)$, rather than $\langle \kappa^2 \rangle = 2/3$, need to be considered to experimentally recover donor–acceptor distances.

ASSOCIATED CONTENT

Supporting Information

The Supporting Information is available free of charge on the ACS Publications website at DOI: [10.1021/acs.jpcb.6b05754](https://doi.org/10.1021/acs.jpcb.6b05754).

Detailed information on the mathematical algorithm used for the structure superposition; four figures showing RMSD, κ^2 , and ECME of the processed trajectories; two figures illustrating the distribution of the donor–acceptor

distance and the orientation factor; three figures showing the deviation of the ECME calculated with IDA and MTD (PDF).

AUTHOR INFORMATION

Corresponding Author

*E-mail: christel.marian@uni-duesseldorf.de. Phone: +49 211 81-13210. Fax: +49 211 81-13466.

Notes

The authors declare no competing financial interest.

ACKNOWLEDGMENTS

We are grateful to Dr. Thomas Peulen and Mykola Dimura for fruitful discussions. Financial support by Deutsche Forschungsgemeinschaft (DFG) through TA 725/1-1 and funds (INST 208/704-1 FUGG) to purchase the hybrid computer cluster used in this study is gratefully acknowledged.

REFERENCES

- (1) Förster, T. Zwischenmolekulare Energiewanderung und Fluoreszenz. *Ann. Phys. (Berlin, Ger.)* **1948**, *437*, 55–75.
- (2) Kalinin, S.; Peulen, T.; Sindbert, S.; Rothwell, P. J.; Berger, S.; Restle, T.; Goody, R. S.; Gohlke, H.; Seidel, C. A. M. A Toolkit and Benchmark Study for FRET-Restrained High-Precision Structural Modeling. *Nat. Methods* **2012**, *9*, 1218–1225.
- (3) Sindbert, S.; Kalinin, S.; Nguyen, H.; Kienzler, A.; Clima, L.; Bannwarth, W.; Appel, B.; Müller, S.; Seidel, C. A. M. Accurate Distance Determination of Nucleic Acids via Förster Resonance Energy Transfer: Implications of Dye Linker Length and Rigidity. *J. Am. Chem. Soc.* **2011**, *133*, 2463–2480.
- (4) Widengren, J.; Schweinberger, E.; Berger, S.; Seidel, C. A. Two New Concepts to Measure Fluorescence Resonance Energy Transfer via Fluorescence Correlation Spectroscopy: Theory and Experimental Realizations. *J. Phys. Chem. A* **2001**, *105*, 6851–6866.
- (5) Clegg, R. M. Fluorescence Resonance Energy Transfer and Nucleic Acids. *Methods Enzymol.* **1992**, *211*, 353–388.
- (6) Stryer, L.; Haugland, R. P. Energy Transfer: A Spectroscopic Ruler. *Proc. Natl. Acad. Sci. U.S.A.* **1967**, *58*, 719–726.
- (7) Sioud, M., Ed. *Ribozymes and siRNA Protocols*; Springer Science + Business Media, 2004.
- (8) Kim, N.-K.; Murali, A.; DeRose, V. J. A Distance Ruler for RNA Using EPR and Site-Directed Spin Labeling. *Chem. Biol.* **2004**, *11*, 939–948.
- (9) Schiemann, O.; Weber, A.; Edwards, T. E.; Prisner, T. F.; Sigurdsson, S. T. Nanometer Distance Measurements on RNA Using PELDOR. *J. Am. Chem. Soc.* **2003**, *125*, 3434–3435.
- (10) Schiemann, O.; Piton, N.; Mu, Y.; Stock, G.; Engels, J. W.; Prisner, T. F. A PELDOR-Based Nanometer Distance Ruler for Oligonucleotides. *J. Am. Chem. Soc.* **2004**, *126*, 5722–5729.
- (11) Galas, D. J.; McCormack, S. J. *Genomic Technologies: Present and Future*; Horizon Scientific Press, 2002; Vol. 1.
- (12) Didenko, V. V. DNA Probes Using Fluorescence Resonance Energy Transfer (FRET): Designs and Applications. *Biotechniques* **2001**, *31*, 1106.
- (13) Heller, M. J.; Morrison, L. E. *Chemiluminescent and Fluorescent Probes for DNA Hybridization Systems*; New York: Academic Press, 1985; pp 245–256.
- (14) Livak, K. J.; Flood, S.; Marmaro, J.; Giusti, W.; Deetz, K. Oligonucleotides with Fluorescent Dyes at Opposite Ends Provide a Quenched Probe System Useful for Detecting PCR Product and Nucleic Acid Hybridization. *Genome Res.* **1995**, *4*, 357–362.
- (15) Livak, K.; Marmaro, J.; Flood, S. *Guidelines for Designing TaqMan Fluorogenic Probes for 5' Nuclease Assays*; PE Applied Biosystems, 1995.
- (16) Ghosh, S. S.; Eis, P. S.; Blumeyer, K.; Fearon, K.; Millar, D. P. Real Time Kinetics of Restriction Endonuclease Cleavage Monitored

- by Fluorescence Resonance Energy Transfer. *Nucleic Acids Res.* **1994**, *22*, 3155–3159.
- (17) Li, J.; Lu, Y. A Highly Sensitive and Selective Catalytic DNA Biosensor for Lead Ions. *J. Am. Chem. Soc.* **2000**, *122*, 10466–10467.
 - (18) Berman, A. J.; Akiyama, B. M.; Stone, M. D.; Cech, T. R. The RNA Accordion Model for Template Positioning by Telomerase RNA During Telomeric DNA Synthesis. *Nat. Struct. Mol. Biol.* **2011**, *18*, 1371–1375.
 - (19) Keller, B. G.; Kobitski, A.; Jäschke, A.; Nienhaus, G. U.; Noé, F. Complex RNA Folding Kinetics Revealed by Single-Molecule FRET and Hidden Markov Models. *J. Am. Chem. Soc.* **2014**, *136*, 4534–4543.
 - (20) Kim, H. D.; Nienhaus, G. U.; Ha, T.; Orr, J. W.; Williamson, J. R.; Chu, S. Mg²⁺-Dependent Conformational Change of RNA Studied by Fluorescence Correlation and FRET on Immobilized Single Molecules. *Proc. Natl. Acad. Sci. U.S.A.* **2002**, *99*, 4284–4289.
 - (21) Van der Meer, B. W. Kappa-Squared: From Nuisance to New Sense. *Rev. Mol. Biotechnol.* **2002**, *82*, 181–196.
 - (22) Corry, B.; Jayatilaka, D. Simulation of Structure, Orientation, and Energy Transfer between AlexaFluor Molecules Attached to MscL. *Biophys. J.* **2008**, *95*, 2711–2721.
 - (23) Loura, L. Simple Estimation of Förster Resonance Energy Transfer (FRET) Orientation Factor Distribution in Membranes. *Int. J. Mol. Sci.* **2012**, *13*, 15252–15270.
 - (24) May, V.; Kühn, O. *Charge and Energy Transfer Dynamics in Molecular Systems*; Wiley-VCH, 2004.
 - (25) Wong, C. Y.; Curutchet, C.; Tretiak, S.; Scholes, G. D. Ideal Dipole Approximation Fails to Predict Electronic Coupling and Energy Transfer between Semiconducting Single-Wall Carbon Nanotubes. *J. Chem. Phys.* **2009**, *130*, No. 081104.
 - (26) Noy, A.; Pérez, A.; Lankas, F.; Javier Luque, F.; Orozco, M. Relative Flexibility of DNA and RNA: A Molecular Dynamics Study. *J. Mol. Biol.* **2004**, *343*, 627–638.
 - (27) Perez, A. The Relative Flexibility of B-DNA and A-RNA Duplexes: Database Analysis. *Nucleic Acids Res.* **2004**, *32*, 6144–6151.
 - (28) Widengren, J.; Schwille, P. Characterization of Photoinduced Isomerization and Back-Isomerization of the Cyanine Dye Cy5 by Fluorescence Correlation Spectroscopy. *J. Phys. Chem. A* **2000**, *104*, 6416–6428.
 - (29) Dietrich, A.; Buschmann, V.; Müller, C.; Sauer, M. Fluorescence Resonance Energy Transfer (FRET) and Competing Processes in Donor-Acceptor Substituted DNA Strands: A Comparative Study of Ensemble and Single-Molecule Data. *Rev. Mol. Biotechnol.* **2002**, *82*, 211–231.
 - (30) Di Fiori, N.; Meller, A. The Effect of Dye-Dye Interactions on the Spatial Resolution of Single-Molecule FRET Measurements in Nucleic Acids. *Biophys. J.* **2010**, *98*, 2265–2272.
 - (31) Muñoz-Losa, A.; Curutchet, C.; Krueger, B. P.; Hartsell, L. R.; Mennucci, B. Fretting About FRET: Failure of the Ideal Dipole Approximation. *Biophys. J.* **2009**, *96*, 4779–4788.
 - (32) Speelman, A. L.; Muñoz-Losa, A.; Hinkle, K. L.; VanBeek, D. B.; Mennucci, B.; Krueger, B. P. Using Molecular Dynamics and Quantum Mechanics Calculations to Model Fluorescence Observables. *J. Phys. Chem. A* **2011**, *115*, 3997–4008.
 - (33) Case, D. A.; Cheatham, T. E.; Darden, T.; Gohlke, H.; Luo, R.; Merz, K. M.; Onufriev, A.; Simmerling, C.; Wang, B.; Woods, R. J. The Amber Biomolecular Simulation Programs. *J. Comput. Chem.* **2005**, *26*, 1668–1688.
 - (34) Hornak, V.; Abel, R.; Okur, A.; Strockbine, B.; Roitberg, A.; Simmerling, C. Comparison of Multiple Amber Force Fields and Development of Improved Protein Backbone Parameters. *Proteins: Struct., Funct., Bioinf.* **2006**, *65*, 712–725.
 - (35) Wang, J.; Cieplak, P.; Kollman, P. A. How Well Does a Restrained Electrostatic Potential (RESP) Model Perform in Calculating Conformational Energies of Organic and Biological Molecules? *J. Comput. Chem.* **2000**, *21*, 1049–1074.
 - (36) Bayly, C. I.; Cieplak, P.; Cornell, W.; Kollman, P. A. A Well-Behaved Electrostatic Potential Based Method Using Charge Restraints for Deriving Atomic Charges: The RESP Model. *J. Phys. Chem.* **1993**, *97*, 10269–10280.
 - (37) Wang, J.; Wolf, R. M.; Caldwell, J. W.; Kollman, P. A.; Case, D. A. Development and Testing of a General Amber Force Field. *J. Comput. Chem.* **2004**, *25*, 1157–1174.
 - (38) Åqvist, J. Modelling of Ion-Ligand Interactions in Solutions and Biomolecules. *J. Mol. Struc.: THEOCHEM* **1992**, *256*, 135–152.
 - (39) Jorgensen, W. L.; Chandrasekhar, J.; Madura, J. D.; Impey, R. W.; Klein, M. L. Comparison of Simple Potential Functions for Simulating Liquid Water. *J. Chem. Phys.* **1983**, *79*, 926.
 - (40) Cheatham, T. E. I.; Miller, J. L.; Fox, T.; Darden, T. A.; Kollman, P. A. Molecular Dynamics Simulations on Solvated Biomolecular Systems: The Particle Mesh Ewald Method Leads to Stable Trajectories of DNA, RNA, and Proteins. *J. Am. Chem. Soc.* **1995**, *117*, 4193–4194.
 - (41) Ryckaert, J. P.; Ciccotti, G.; Berendsen, H. J. C. Numerical Integration of the Cartesian Equations of Motion of a System with Constraints: Molecular Dynamics of n-Alkanes. *J. Comput. Phys.* **1977**, *23*, 327–341.
 - (42) Panchuk-Voloshina, N.; Haugland, R. P.; Bishop-Stewart, J.; Bhagat, M. K.; Millard, P. J.; Mao, F.; Leung, W.-Y.; Haugland, R. P. Alexa Dyes, a Series of New Fluorescent Dyes that Yield Exceptionally Bright, Photostable Conjugates. *J. Histochem. Cytochem.* **1999**, *47*, 1179–1188.
 - (43) Huang, S. Real-Time Detection of Amplification Products Through Fluorescence Quenching or Energy Transfer. In *Advanced Techniques in Diagnostic Microbiology*; Tang, Y.-W., Stratton, C. W., Eds.; Springer Science + Business Media, 2013; p 420, Tab. 24.1.
 - (44) Marian, C. M.; Etinski, M.; Rai-Constatel, V. Reverse Intersystem Crossing in Rhodamines by Near-Infrared Laser Excitation. *J. Phys. Chem. A* **2014**, *118*, 6985–6990.
 - (45) Pfiffi, D.; Bier, B. A.; Marian, C. M.; Schaper, K.; Seidel, C. A. M. Diphenylhexatrienes as Photoprotective Agents for Ultrasensitive Fluorescence Detection. *J. Phys. Chem. A* **2010**, *114*, 4099–4108.
 - (46) Becke, A. D. A New Mixing of Hartree-Fock and Local Density-Functional Theories. *J. Chem. Phys.* **1993**, *98*, 1372–1377.
 - (47) TURBOMOLE, V6.5; TURBOMOLE GmbH, 2013. <http://www.turbomole.com>.
 - (48) Schäfer, A.; Horn, H.; Ahlrichs, R. Fully Optimized Contracted Gaussian Basis Sets for Atoms Li to Kr. *J. Chem. Phys.* **1992**, *97*, 2571–2577.
 - (49) Neugebauer, J.; Reiher, M.; Kind, C.; Hess, B. A. Quantum Chemical Calculation of Vibrational Spectra of Large Molecules. Raman and IR Spectra for Buckminsterfullerene. *J. Comput. Chem.* **2002**, *23*, 895–910.
 - (50) Grimme, S.; Waletzke, M. A Combination of Kohn-Sham Density Functional Theory and Multi-Reference Configuration Interaction Methods. *J. Chem. Phys.* **1999**, *111*, 5645–5655.
 - (51) Lyskov, I.; Kleinschmidt, M.; Marian, C. M. Redesign of the DFT/MRCI Hamiltonian. *J. Chem. Phys.* **2016**, *144*, No. 034104.
 - (52) Etinski, M.; Tatchen, J.; Marian, C. M. Time-Dependent Approaches for the Calculation of Intersystem Crossing Rates. *J. Chem. Phys.* **2011**, *134*, No. 154105.
 - (53) Etinski, M.; Tatchen, J.; Marian, C. M. Thermal and Solvent Effects on the Triplet Formation in Cinnoline. *Phys. Chem. Chem. Phys.* **2014**, *16*, 4740–4751.
 - (54) Hennebicq, E.; Pourtois, G.; Scholes, G. D.; Herz, L. M.; Russell, D. M.; Silva, C.; Setayesh, S.; Grimsdale, A. C.; Müllen, K.; Brédas, J.-L.; et al. Exciton Migration in Rigid-Rod Conjugated Polymers: An Improved Förster Model. *J. Am. Chem. Soc.* **2005**, *127*, 4744–4762.
 - (55) Dexter, D. L. A Theory of Sensitized Luminescence in Solids. *J. Chem. Phys.* **1953**, *21*, 836–850.
 - (56) van der Meer, B. W.; van der Meer, D. M.; Vogel, S. S. Optimizing the Orientation Factor Kappa-Squared for More Accurate FRET Measurements. In *FRET – Förster Resonance Energy Transfer: From Theory to Applications*; Medintz, I., Hildebrandt, N.; Wiley-VCH Verlag GmbH & Co. KGaA: Weinheim, Germany, 2013; pp 63–104.
 - (57) Fink, R.; Pfister, J.; Schneider, A.; Zhao, H.; Engels, B. Ab Initio Configuration Interaction Description of Excitation Energy Transfer between Closely Packed Molecules. *Chem. Phys.* **2008**, *343*, 353–361.

- (58) Fink, R. F.; Pfister, J.; Zhao, H. M.; Engels, B. Assessment of Quantum Chemical Methods and Basis Sets for Excitation Energy Transfer. *Chem. Phys.* **2008**, *346*, 275–285.
- (59) Fujimoto, K. J. Transition-Density-Fragment Interaction Combined with Transfer Integral Approach for Excitation-Energy Transfer via Charge-Transfer States. *J. Chem. Phys.* **2012**, *137*, No. 034101.
- (60) Coutsias, E. A.; Seok, C.; Dill, K. A. Using Quaternions to Calculate RMSD. *J. Comput. Chem.* **2004**, *25*, 1849–1857.
- (61) Pakalnis, S.; Sitas, V.; Schneckenburger, H.; Rotomskis, R. Picosecond Absorption Spectroscopy of Biologically Active Pigments NADH, FMN and Fluorescence Marker Rhodamine-123. *The Third Internet Photochemistry and Photobiology Conference in association with J. Photochem. Photobiol. B*, 2000; http://www.photobiology.com/photobiology2000/VSitas/ps_abs_sp_index.htm.
- (62) Hörner, A.; Hagendorn, T.; Schepers, U.; Bräse, S. Photophysical Properties and Synthesis of New Dye-Cyclooctyne Conjugates for Multicolor and Advanced Microscopy. *Bioconjugate Chem.* **2015**, *26*, 718–724.
- (63) Pal, P.; Zeng, H.; Durocher, G.; Girard, D.; Li, T.; Gupta, A. K.; Giasson, R.; Blanchard, L.; Gaboury, L.; Balassy, A. Phototoxicity of Some Bromine-Substituted Rhodamine Dyes: Synthesis, Photophysical Properties and Application as Photosensitizers. *Photochem. Photobiol.* **1996**, *63*, 161–168.
- (64) Dixon, J. M.; Taniguchi, M.; Lindsey, J. S. PhotochemCAD 2: A Refined Program with Accompanying Spectral Databases for Photochemical Calculations. *Photochem. Photobiol.* **2005**, *81*, 212–213.
- (65) Du, H.; Fuh, R.-C. A.; Li, J.; Corkan, L. A.; Lindsey, J. S. PhotochemCAD: A Computer-Aided Design and Research Tool in Photochemistry. *Photochem. Photobiol.* **1998**, *68*, 141–142.
- (66) Lakowicz, J. R.; Gryczynski, I.; Wiczk, W.; Laczko, G.; Prendergast, F. C.; Johnson, M. L. Conformational Distributions of Melittin in Water/Methanol Mixtures from Frequency-Domain Measurements of Nonradiative Energy Transfer. *Biophys. Chem.* **1990**, *36*, 99–115.
- (67) Periasamy, A., Day, R. N., Eds. *Molecular Imaging – FRET Microscopy and Spectroscopy*; Oxford University Press, 2005.
- (68) Rothwell, P. J.; Berger, S.; Kensch, O.; Felekyan, S.; Antonik, M.; Wohrl, B. M.; Restle, T.; Goody, R. S.; Seidel, C. A. M. Multiparameter Single-Molecule Fluorescence Spectroscopy Reveals Heterogeneity of HIV-1 Reverse Transcriptase: Primer/Template Complexes. *Proc. Natl. Acad. Sci. U.S.A.* **2003**, *100*, 1655–1660.
- (69) Westlund, P.-O.; Wennerström, H. Electronic Energy Transfer in Liquids. The Effect of Molecular Dynamics. *J. Chem. Phys.* **1993**, *99*, 6583.
- (70) Opanasyuk, O.; Johansson, L. B.-Å. Extended Förster Theory: A Quantitative Approach to the Determination of Inter-Chromophore Distances in Biomacromolecules. *Phys. Chem. Chem. Phys.* **2010**, *12*, 7758.

Supporting information for:

Failure of the IDA in FRET Systems at Close Inter-Dye Distances is Moderated by Frequent Low κ^2 Values

J. Dominik Spiegel,[†] Simone Fulle,[‡] Martin Kleinschmidt,[†] Holger Gohlke,[¶] and
Christel M. Marian^{*,†}

*Institute of Theoretical and Computational Chemistry, Heinrich Heine University
Düsseldorf, Universitätssstr. 1, D-40225 Düsseldorf, Germany, BioMed X Innovation
Center, Im Neuenheimer Feld 515, 69120 Heidelberg, Germany, and Institute of
Pharmaceutical and Medicinal Chemistry, Heinrich Heine University Düsseldorf,
Universitätsstr. 1, D-40225 Düsseldorf, Germany*

E-mail: Christel.Marian@uni-duesseldorf.de

Phone: +49 211 81-13210. Fax: +49 211 81-13466

*To whom correspondence should be addressed

[†]Heinrich Heine University, Düsseldorf, Germany

[‡]BioMed X Innovation Center, Heidelberg, Germany

[¶]Heinrich Heine University, Düsseldorf, Germany

Structure superposition

To find the optimal overlay of a model structure an a target structure, we search for an orthogonal transformation U and a translation r which minimizes the residual distance d

$$d = \frac{1}{N} \sum_{k=1}^N |U\vec{x}_k + \vec{r} - \vec{y}_k|^2 \quad (1)$$

for a given set of model coordinates $\{\vec{x}_k\}$ (DFT-optimized structures) and target coordinates $\{\vec{y}_k\}$ (MD structures) in real space where N is the total number of atoms of the respective molecule. As a first step, the position vectors of the structures are expressed with respect to an origin located at the respective center of mass, i.e., \bar{x} and \bar{y} .

$$\tilde{\vec{x}}_k = \vec{x}_k - \bar{x} \quad (2)$$

$$\tilde{\vec{y}}_k = \vec{y}_k - \bar{y} \quad (3)$$

The quaternion q corresponding to the best-fit orthogonal transformation is the eigenvector L_{max} of the auxiliary matrix F with the largest eigenvalue λ_{max}

$$F = \begin{pmatrix} R_{11} + R_{22} + R_{33} & R_{23} - R_{32} & R_{31} - R_{13} & R_{12} - R_{21} \\ R_{23} - R_{32} & R_{11} - R_{22} - R_{33} & R_{12} + R_{21} & R_{13} + R_{31} \\ R_{31} - R_{13} & R_{12} + R_{21} & -R_{11} + R_{22} - R_{33} & R_{23} + R_{32} \\ R_{12} - R_{21} & R_{13} + R_{31} & R_{23} + R_{32} & -R_{11} - R_{22} + R_{33} \end{pmatrix} \quad (4)$$

with matrix elements

$$R_{ij} = \sum_{k=1}^N \tilde{x}_{ik} \tilde{y}_{jk}, \quad (5)$$

where k labels the atoms and i and j denote the components of the position vectors in real space. The corresponding best-fit RMSD is then given by

$$RMSD = \sqrt{\frac{1}{N} \sum_{k=1}^N (\tilde{x}_k^2 + \tilde{y}_k^2) - 2\lambda_{max}}. \quad (6)$$

The rotation matrix U in real space can directly be computed from the components of q .

$$U = \begin{pmatrix} q_0^2 + q_1^2 - q_2^2 - q_3^2 & 2(q_1 q_2 - q_0 q_3) & 2(q_1 q_3 + q_0 q_2) \\ 2(q_1 q_2 + q_0 q_3) & q_0^2 - q_1^2 + q_2^2 - q_3^2 & 2(q_2 q_3 - q_0 q_1) \\ 2(q_1 q_3 - q_0 q_2) & 2(q_2 q_3 + q_0 q_1) & q_0^2 - q_1^2 - q_2^2 + q_3^2 \end{pmatrix} \quad (7)$$

To obtain the position vectors $\tilde{\vec{x}}'$ of the rotated model structure, the mass-centered position vectors $\tilde{\vec{x}}_k$ have to be multiplied by the rotation matrix.

$$\tilde{\vec{x}}' = U \tilde{\vec{x}} \quad (8)$$

Finally, the molecule-fixed coordinate system of the rotated model structure $\{\tilde{\vec{x}}'\}$ has to be shifted to the center of mass \bar{y} of the target structure. The final set of coordinates $\{\vec{x}'\}$ of the fitted model structure then is given by

$$\vec{x}' = U(\vec{x} - \bar{x}) + \bar{y}. \quad (9)$$

Rotation of molecular orbitals

A set of p-functions p_x , p_y and p_z transforms according to rotation matrix $T^{(p)S1}$

$$T^{(p)} = \begin{pmatrix} \cos(\gamma) & \sin(\gamma) & 0 \\ -\sin(\gamma) & \cos(\gamma) & 0 \\ 0 & 0 & 1 \end{pmatrix} \begin{pmatrix} \cos(\beta) & 0 & -\sin(\beta) \\ 0 & 1 & 0 \\ \sin(\beta) & 0 & \cos(\beta) \end{pmatrix} \begin{pmatrix} \cos(\alpha) & \sin(\alpha) & 0 \\ -\sin(\alpha) & \cos(\alpha) & 0 \\ 0 & 0 & 1 \end{pmatrix} \quad (10)$$

where α , β and γ are Euler angles in ZY'Z" convention. The rotation matrix $T^{(d)}$ of a set of d -orbitals $d_{2z^2-x^2-y^2}$, d_{xz} , d_{yz} , d_{xz} and $d_{x^2-y^2}$ reads^{S1}

$$T^{(d)} = \begin{pmatrix} 1 & 0 & 0 & 0 & 0 \\ 0 & \cos(\gamma) & \sin(\gamma) & 0 & 0 \\ 0 & -\sin(\gamma) & \cos(\gamma) & 0 & 0 \\ 0 & 0 & 0 & \cos(2\gamma) & -\sin(2\gamma) \\ 0 & 0 & 0 & \sin(2\gamma) & \cos(2\gamma) \end{pmatrix} \begin{pmatrix} \frac{1}{4}(1 + 3\cos(2\beta)) & \frac{1}{2}\sqrt{3}\sin(2\beta) & 0 & \frac{1}{4}\sqrt{3}(1 - \cos(2\beta)) \\ -\frac{1}{2}\sqrt{3}\sin(2\beta) & \cos(2\beta) & 0 & \frac{1}{2}\sin(2\beta) \\ 0 & 0 & \cos(\beta) & 0 \\ 0 & 0 & -\sin(\beta) & 0 \\ \frac{1}{4}\sqrt{3}(1 - \cos(2\beta)) & -\frac{1}{2}\sin(2\beta) & 0 & \frac{1}{4}(3 + \cos(2\beta)) \end{pmatrix} \begin{pmatrix} 1 & 0 & 0 & 0 & 0 \\ 0 & \cos(\alpha) & \sin(\alpha) & 0 & 0 \\ 0 & -\sin(\alpha) & \cos(\alpha) & 0 & 0 \\ 0 & 0 & 0 & \cos(2\alpha) & -\sin(2\alpha) \\ 0 & 0 & 0 & \sin(2\alpha) & \cos(2\alpha) \end{pmatrix} \quad (11)$$

Herein, α , β and γ are Euler angles in ZY'Z" convention. The Euler angles corresponding to the best-fit superposition of model and target structures can directly be obtained from the corresponding quaternion q as given by^{S2}

$$\begin{aligned} \alpha &= \text{atan2}(2(q_2q_3 + q_0q_1), 2(q_1q_3 - q_0q_2)) \\ \beta &= \arccos(q_0^2 - q_1^2 - q_2^2 + q_3^2) \\ \gamma &= \text{atan2}(2(q_2q_3 - q_0q_1), -2(q_1q_3 + q_0q_2)) \end{aligned} \quad (12)$$

where atan2 is defined as

$$\text{atan2}(x, y) := \begin{cases} \arctan \frac{y}{x} & \text{if } x > 0 \\ \arctan \frac{y}{x} + \pi & \text{if } x < 0, y \geq 0 \\ \arctan \frac{y}{x} - \pi & \text{if } x < 0, y < 0 \\ +\frac{\pi}{2} & \text{if } x = 0, y > 0 \\ -\frac{\pi}{2} & \text{if } x = 0, y < 0 \\ 0 & \text{if } x = 0, y = 0 \end{cases} \quad (13)$$

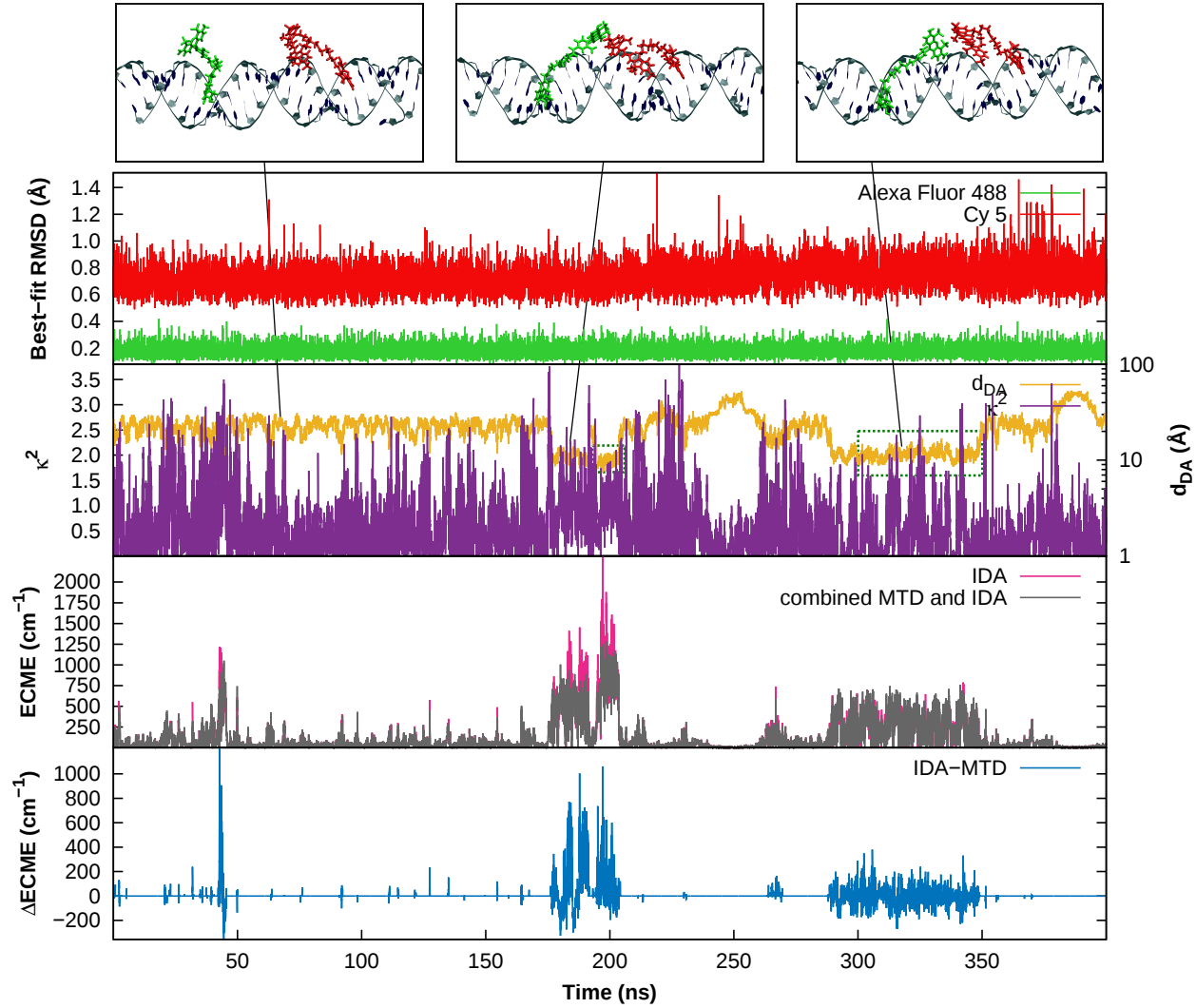


Figure S1: Processed trajectory dsRNA-8nt_nt23 in which Alexa Fluor 488 and Cy5 were replaced by their preoptimized simplified structures. Every single snapshot was used for the analysis. MTD was used for every snapshot with a donor–acceptor distance $\leq 15 \text{ \AA}$. The quality of the fit of the preoptimized dyes to the MD structure is indicated by the best-fit RMSD. Distances d_{DA} and orientation factors κ^2 were computed between the barycenters of the dyes and the rotated transition dipole moments, respectively. Ranges for which H-bonds were analyzed are marked by green boxes.

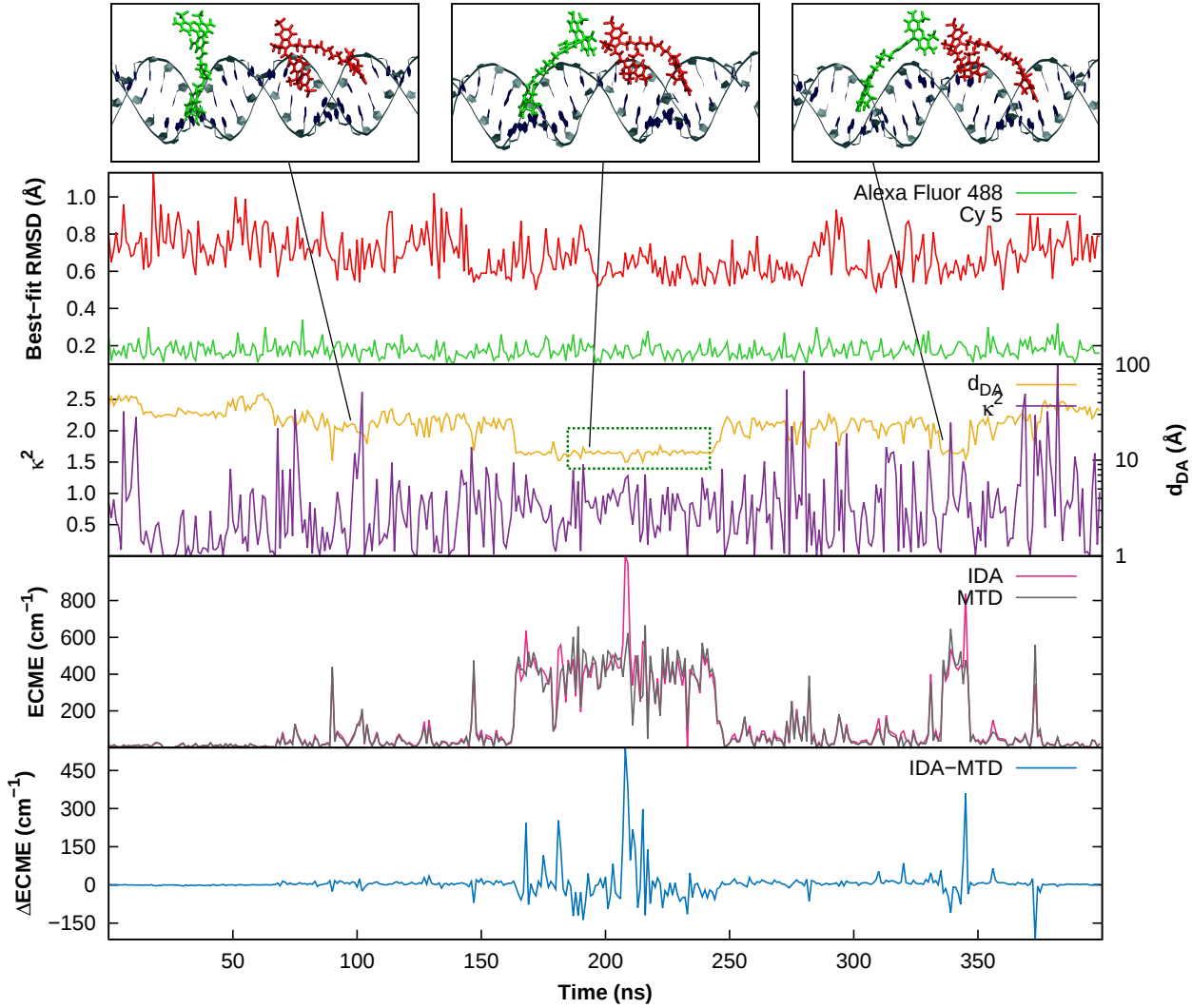


Figure S2: Processed trajectory dsRNA-8nt_nt23II in which Alexa Fluor 488 and Cy5 were replaced by their preoptimized simplified structures. Every 50th snapshot was used for the analysis. The quality of the fit of the preoptimized dyes to the MD structure is indicated by the best-fit RMSD. Distances d_{DA} and orientation factors κ^2 were computed between the barycenters of the dyes and the rotated transition dipole moments, respectively. The EMCE was calculated for each considered snapshot using both IDA and MTD. Ranges for which H-bonds were analyzed are marked by green boxes.

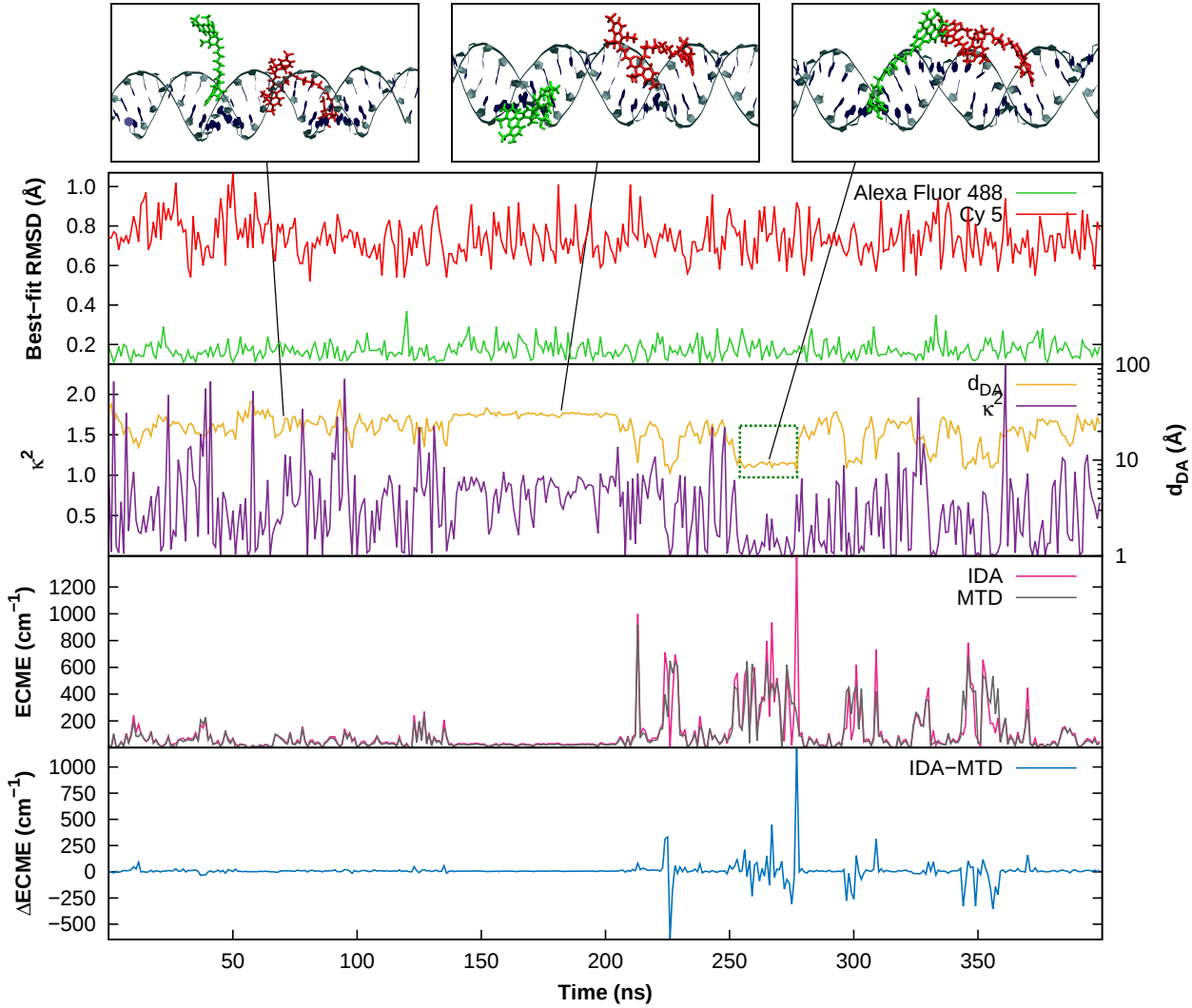


Figure S3: Processed trajectory dsRNA-8nt_nt22 in which Alexa Fluor 488 and Cy5 were replaced by their preoptimized simplified structures. Every 50th snapshot was used for the analysis. The quality of the fit of the preoptimized dyes to the MD structure is indicated by the best-fit RMSD. Distances d_{DA} and orientation factors κ^2 were computed between the barycenters of the dyes and the rotated transition dipole moments, respectively. The EMCE was calculated for each considered snapshot using both IDA and MTD. Ranges for which H-bonds were analyzed are marked by green boxes.

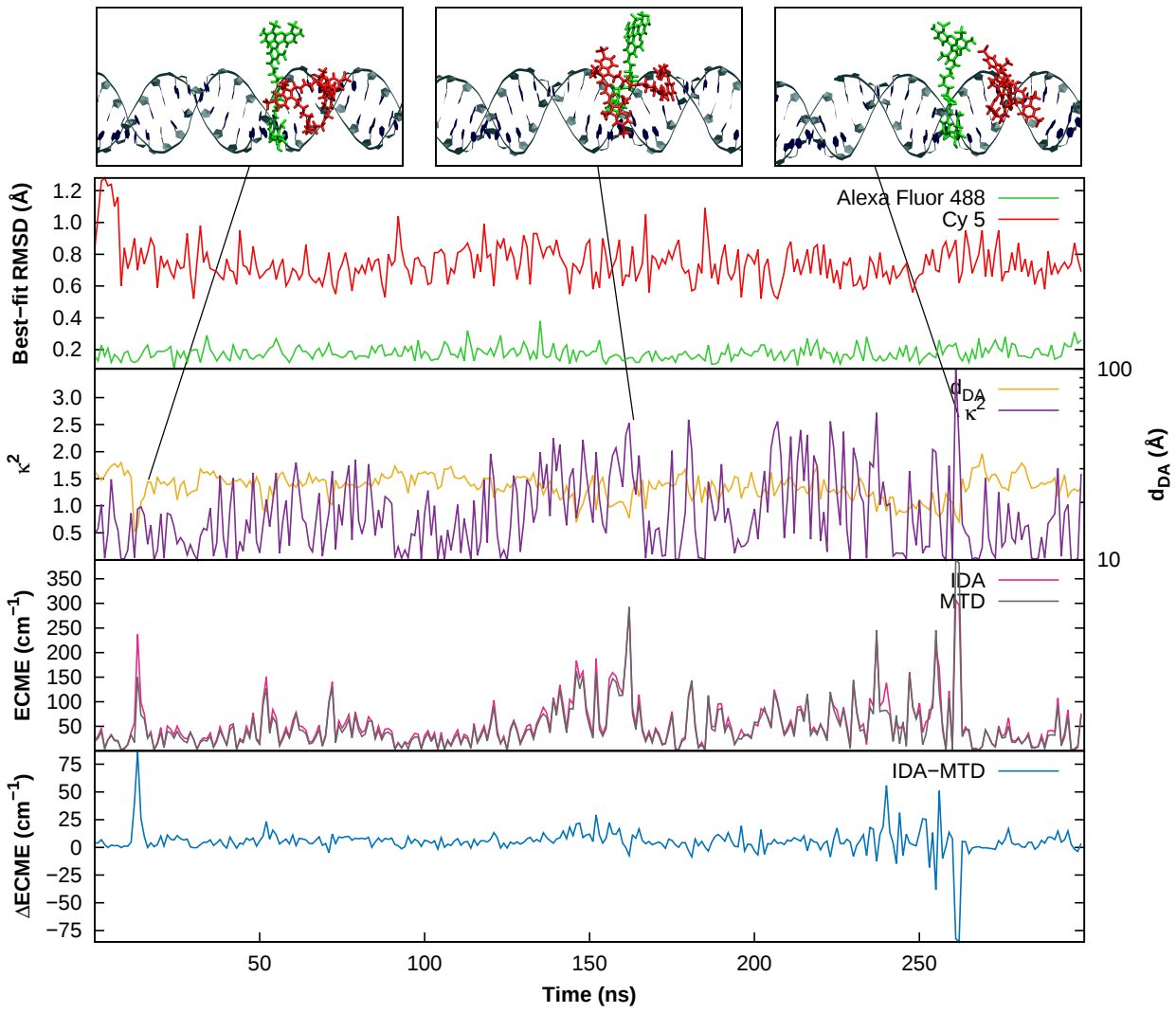


Figure S4: Processed trajectory dsRNA-8nt_nt14 in which Alexa Fluor 488 and Cy5 were replaced by their preoptimized simplified structures. Every 50th snapshot was used for the analysis. The quality of the fit of the preoptimized dyes to the MD structure is indicated by the best-fit RMSD. Distances d_{DA} and orientation factors κ^2 were computed between the barycenters of the dyes and the rotated transition dipole moments, respectively. The EMCE was calculated for each considered snapshot using both IDA and MTD.

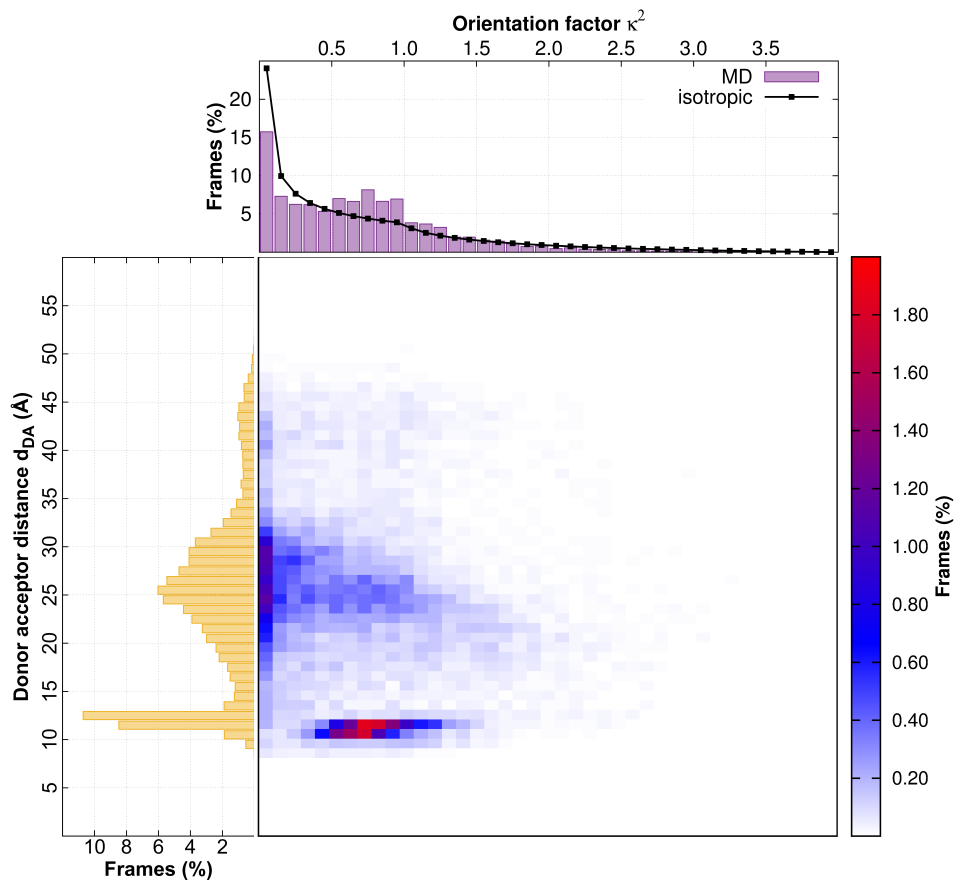


Figure S5: Distributions of the donor–acceptor distance and the orientation factor for dsRNA-8nt_nt23II. The analysis is based on averaging all snapshots within distance intervals of 1 Å and intervals of 0.1 with regard to the orientation factor.

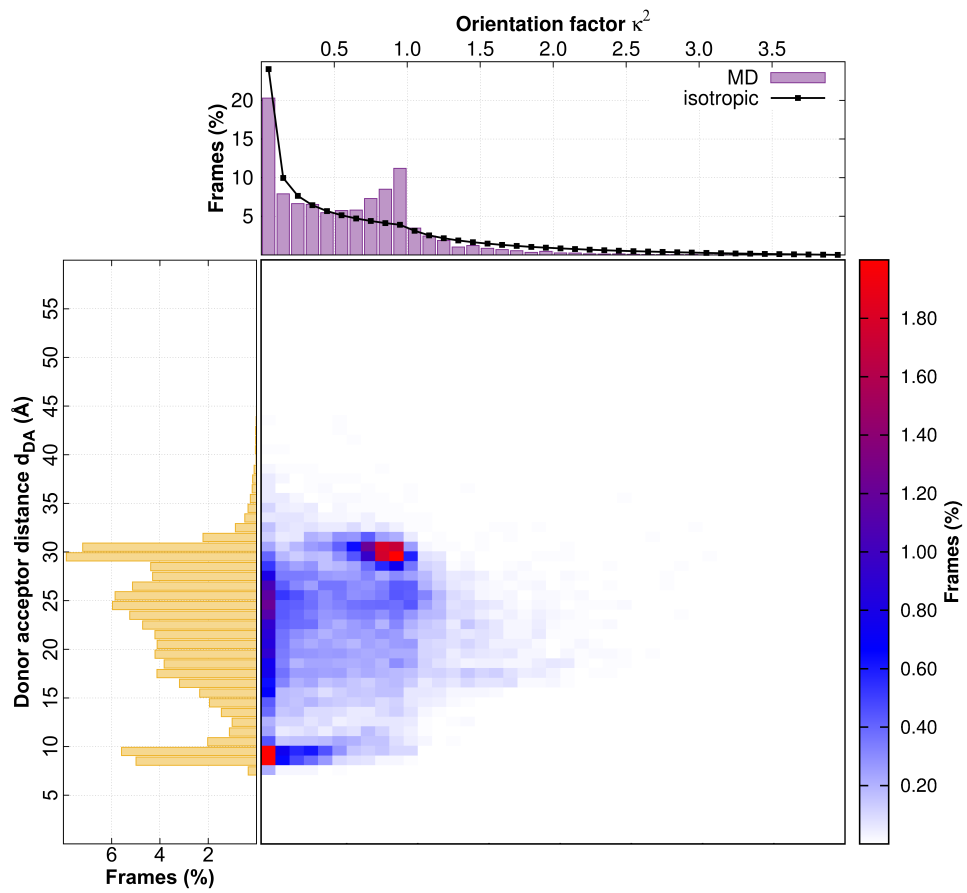


Figure S6: Distributions of the donor–acceptor distance and the orientation factor for dsRNA-8nt_nt22. The analysis is based on averaging all snapshots within distance intervals of 1 Å and intervals of 0.1 with regard to the orientation factor.

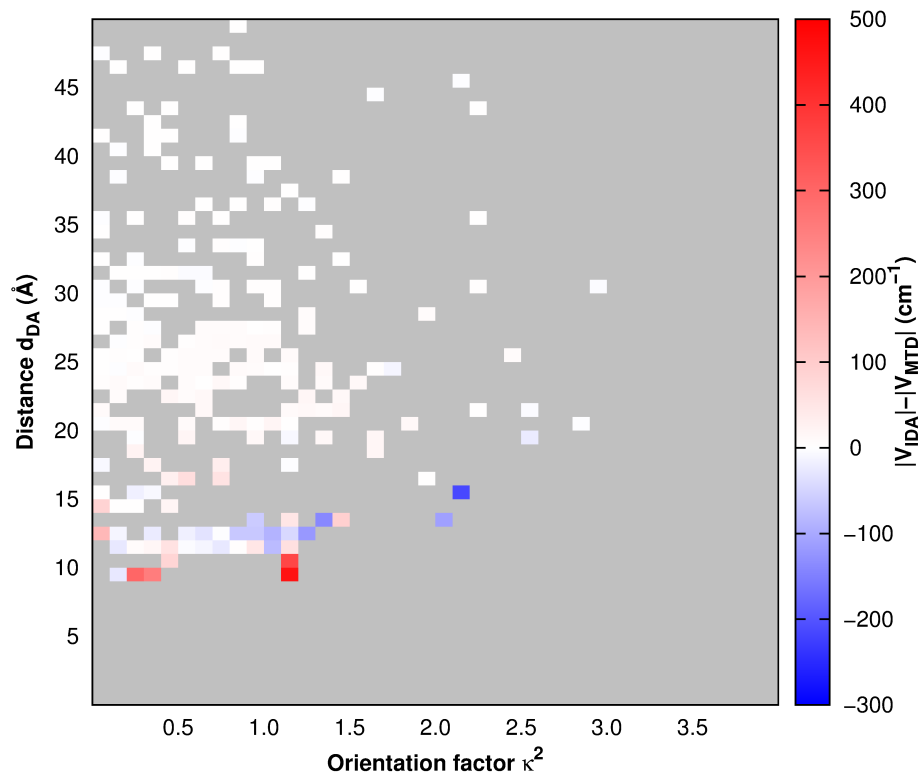


Figure S7: Deviation of the ECME calculated with IDA and MTD in dsRNA-8nt_nt23II considering every 50th snapshot. The analysis is based on averaging all snapshots within distance intervals of 1 Å and intervals of 0.1 with regard to the orientation factor. Grey-colored areas denote combinations of the donor–acceptor distance and the orientation factor for which no data points exist.

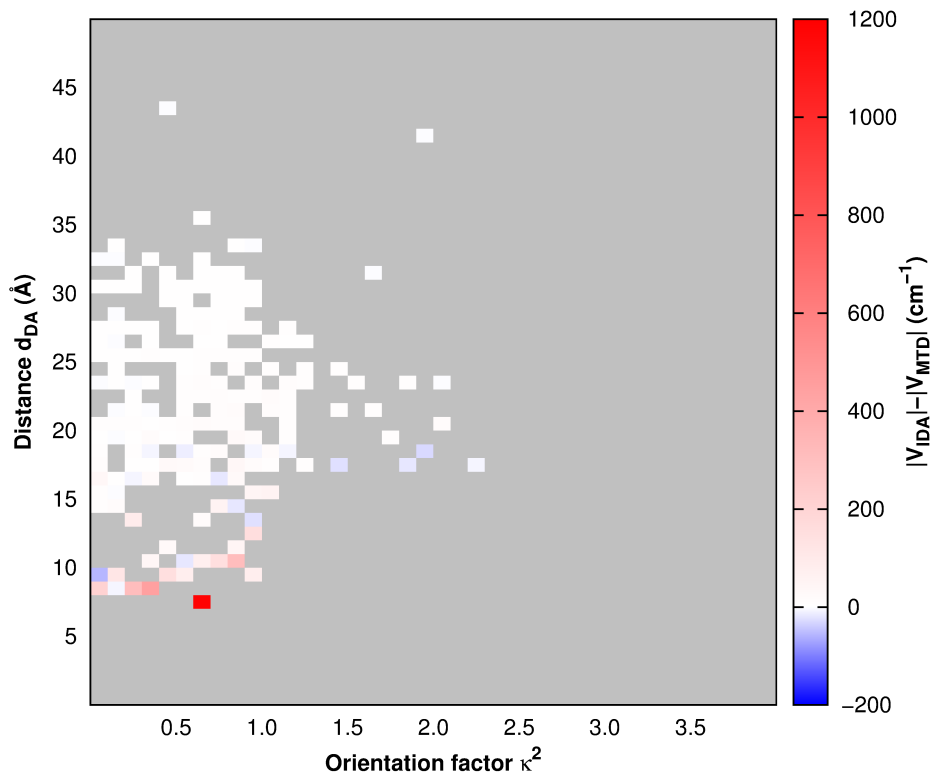


Figure S8: Deviation of the ECME calculated with IDA and MTD in dsRNA-8nt_nt22 considering every 50th snapshot. The analysis is based on averaging all snapshots within distance intervals of 1 Å and intervals of 0.1 concerning the orientation factor. Grey-colored areas denote combinations of the donor acceptor distance and the orientation factor for which no data points exist.

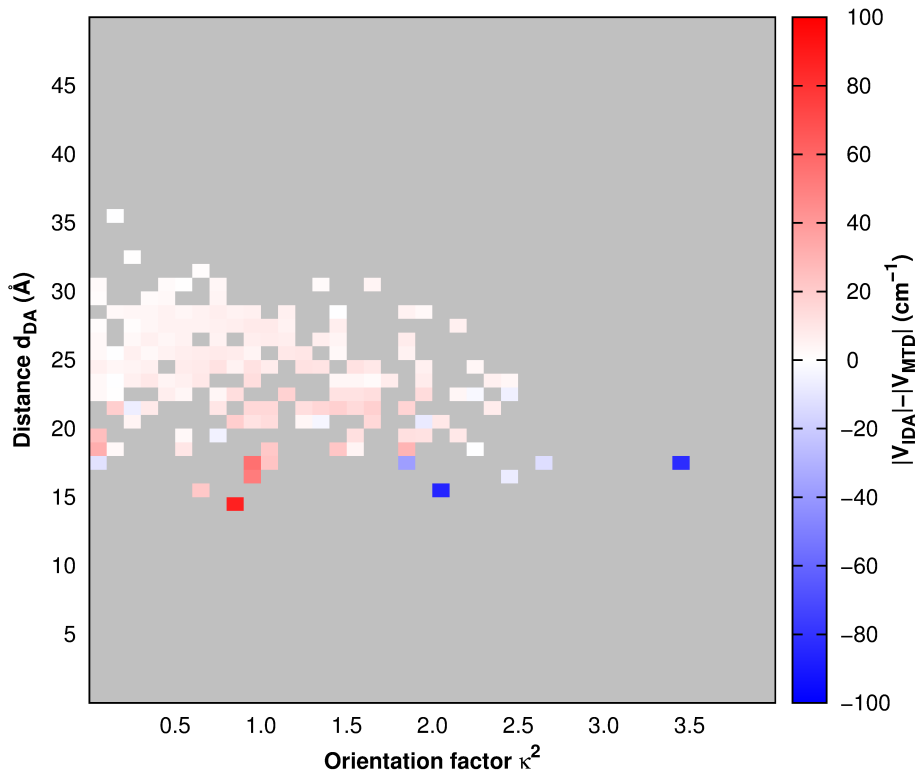


Figure S9: Deviation of the ECME calculated with IDA and MTD in dsRNA-8nt_nt14 considering every 50th snapshot. The analysis is based on averaging all snapshots within distance intervals of 1 Å and intervals of 0.1 with regard to the orientation factor. Grey-colored areas denote combinations of the donor acceptor distance and the orientation factor for which no data points exist.

References

- (S1) Gerloch, M.; Slade, R. *Ligand-field parameters*; Cambridge University Press, 1973.
- (S2) Diebel, J. *Representing attitude: Euler angles, unit quaternions, and rotation vectors*; 2006; (www.swarthmore.edu/NatSci/mzucker1/e28_f2015/reading/diebel2006attitude.pdf).